MECHANICAL, ELECTRICAL, MAGNETIC AND THERMAL ANALYSIS OF HIGH TEMPERATURE SUPERCONDUCTING MAGNETIC ENERGY STORAGE (SMES) DEVICES USED FOR SMART GRID APPLICATIONS

A

Thesis

Submitted to

For the award of

DOCTOR OF PHILOSOPHY (Ph. D)

in

Mechanical Engineering

By

Abhinav Kumar

(11617228)

Supervised by

Dr. JV Muruga Lal Jeyan

Co-Supervised by

Dr. Ashish Agrawal

LOVELY FACULTY OF TECHNOLOGY & SCIENCES
LOVELY PROFESSIONAL UNIVERSITY
PUNJAB
2019

dedicated to my Parents

and

younger brother Princy

Declaration

The work presented in this dissertation was carried out at School of Mechanical Engineering, Lovely Professional University between August 2016 to November 2019 under the supervision of Dr. JV Muruga Lal Jeyan and Dr. Ashish Agrawal.

I hereby declare that, except for where specific references are made to the work of other authors or specially indicated in the text, the contents of this dissertation are his own work. This report has not been submitted in parts, or in whole to any other university for a degree, diploma or other qualification. The work is purely done by me and includes nothing which is the outcome of work done in collaboration. This dissertation is within the word limit of 50,000 words, including bibliography, appendices, table and equations, and does not contain more than 150 figures.

Abhinav Kumar

November 2019

Certificate

This is to certify that **Mr. Abhinav Kumar** has completed the Ph.D. Mechanical Engineering titled, **"Mechanical, Electrical, Magnetic and Thermal Analysis of High Temperature Superconducting Magnetic Energy Storage (SMES) Devices used for Smart Grid Applications"** under my guidance and supervision. To the best of my knowledge, the present work is the result of his original investigation and study. No part of this thesis work has ever been submitted for any degree.

This thesis is fit for the submission for the partial fulfilment of the condition for the award of degree of Ph.D. in Mechanical Engineering.

Signature of Supervisor

Dr. JVM Lal Jeyan
Professor
School of Mechanical Engineering
Lovely Professional University
Punjab

Signature of Co- Supervisor

Dr. Ashish Agrawal
Assistant Professor
Department of Mechanical Engineering
Madanapalle Institute of Technology and Sciences
Andhra Pradesh

Abstract

Efficient energy storage is one of the future aspect where research communities are focussing their attention due to green and sustainable environment while minimizing the pollution and factors affecting global warming potential. International Energy Agency (IEA) has reported that major causes of pollutions are associated with the electricity production using coal and oil products. Thus, almost all countries are willing to opt renewable energy production using solar and wind power plants. The challenges associated with such technologies is that their output power is intermittent and needs some secondary or supportive power source that can handle the load efficiently at the time of uneven plant's output. The other issue that needs attention is power blackouts which can affect the daily lives of many peoples and even the overall GDP of any country. This implies, for both the situations energy storage systems will be the only possible and immediate solution. Among various available energy storage systems, it has been found that Superconducting Magnetic Energy Storage (SMES) systems have merits over the others as they can provide much higher power densities and response time is also better than other bulk energy storage systems like hydro and CAES.

Therefore, in this dissertation, the possible designs of SMES has been studied where the previous development related to the SMES design has been classified nationally and internationally. The high temperature superconducting tape has been identified on the basis of available manufacturers and current carrying capacity. Tape chosen for the present study has non-magnetic substrate material. Further, mechanical design of the 1 MJ of SMES at 77 K temperature has been studied thoroughly where all design parameters have been identified along with the constraints and input parameters involved. Solenoidal configuration of the magnet has been selected for the study where reference field of 3 Tesla has been chosen for the design. Effect of operating currents or different load factors, solenoid thickness and operating temperature on the magnet topology has been studied.

Effect of self-field on the critical current of the superconducting tape wounded as a coil has been studied. 2D model has been developed where the stacked tapes along with the

number of turns has been modelled using COMSOL MultiPhysics software. For the validation of the model, previous studies done by Grilli et al. has been reproduced. The gap among the adjacent tapes has also been considered while modelling and its effect on the critical current of the tape and the magnetic flux density has been studied. It has been found that self-field can affect the critical current of the coil significantly and this aspect cannot be ignored while designing the SMES system for large scale applications.

AC loss analysis for a 2D homogenous model has been studied for different operating currents and number of turns around the pancake coil. Certain assumptions have been made in order to reduce the complexities. H-formulation modelling has been used in order to evaluate the AC losses. Mapped meshes has been incorporated in order to capture the AC loss variations smoothly. For the validation of the model, previous studies done by Zermeno et al. has been reproduced. It has been found that with the increase in the load factor or operating current and number of turns around the pancake coil for a particular tape at 77 K temperature, the average AC losses are found to increase exponentially. Further, it has been found that with the increase in the substrate layer thickness, the AC losses can be controlled however one has to sacrifice with the magnetic flux density.

Quench analysis on the tape has been performed however, in this study model has been developed for the straight superconductor of length 10 cm. Effect of interfacial resistance on the Normal Zone Propagation Velocity (NZPV) has been studied and it has been found that with the increase in the resistance, the NZPV is increasing thus tape can be prevented from the quench if the interfacial resistance among the stabilizer and superconducting layer is kept more and this system can act as flux flow diverter.

At last overall conclusions from the present study has been presented along with the future scope available with this study.

Acknowledgements

There are a number of people who have contributed, either directly or indirectly, to the work presented in this thesis and for their contributions I am extremely thankful.

Firstly, I would like to express my utmost gratitude to my supervisors, Dr. JV Muruga Lal Jeyan and Dr. Ashish Agrawal, for their advice, guidance and support throughout the duration of my research. They taught me the skills required for independent research and allowed me the freedom to explore my own ideas, whilst providing appropriate guidance and criticism to ensure that I carried out my research professionally and completed my work on time.

I would like to thank Dr. Victor Rodriguez-Zermeno, Dr. V.R Ramanan, Dr. P.M. Sarun, Mr. Lorenzo Bortot and Mr. Siddhartha Shankar for his continuous technical assistance throughout my work. I must also thank the Dr. Francesco Grilli for his indirect support through excellent research articles those motivated me to keep myself attentive to my research work.

I attended a number of conferences and workshops during my PhD, and I am extremely grateful to those who I have collaborated with or who have provided comments and constructive criticism of my work. I must also thank to CEC/ICMC organizers who have chosen my profile for student full registration fee waiver award under ICMC student category.

I would like to thank Dr. Ramesh Chand Thakur, Dr. Rekha, Dr. Reji Thomas, Dr. Niti Kant, Dr. Vijay Kumar Singh, Dr. Ramandeep Singh, Mrs. Shilpa Rana, Mr. Vishnu Saini, Mr. Vikas Salaria, Sh. Mayadas Sharma, Sh. Joginder Singh, Mr. Naresh Chopra, Mr. Akash Bhardwaj, Mr. Abhishek Sahai and Mrs. Tanu Kaistha for their continuous motivation and endless emotional support.

Finally, I must thank all of my friends and family for their love and support. My parents, Mr. Prem Kumar and Mrs. Ashok Kumari, have supported me in all of my pursuits and

encouraged me to set my goals for achievement high. My brother, Princy, has supported me wholeheartedly, and without his help and encouragement, I would not have achieved all that I have thus far. The emotional support required to complete a PhD is often underestimated.

Abhinav Kumar

05 March, 20120

List of Publications

Journal Papers

1. Numerical analysis on 10 MJ solenoidal high temperature superconducting magnetic energy storage system to evaluate magnetic flux and Lorentz force distribution. Physica C: Superconductivity and its Applications Volume 558, 15 March 2019, Pages 17-24.

2. Effect of Self-field and Loosening of Stacked Superconducting Tapes on Critical Current of a Single Pancake Coil. International Journal of Engineering and Advanced Technology, ISSN-2449-8958, Vol. 9, Issue-1S3, pp. 155-158, December 2019.

3. Effect of Substrate Layer Thickness on the AC Losses in Stacked Superconducting Pancake Coils using Direct H-formulations. International Journal of Engineering and Advanced Technology, ISSN-2449-8958, Vol. 9, Issue-1S3, pp. 150-154, December 2019.

4. Feasibility Studies on Cryogenic Properties of Supercritical Nitrogen to be used in the Cooling of Hg-Based High Temperature Superconductors for Electric Aircraft Propulsion. - International Journal of Engineering and Advanced Technology, ISSN-2449-8958, Vol. 9, Issue-1S3, pp. 106-110, December 2019.

5. Numerical Model to Calculate Magnetization AC Losses for Superconducting Strip used for Current Transport Applications in Electric Aircrafts. - International Journal of Engineering and Advanced Technology, ISSN-2449-8958, Vol. 9, Issue-1S3, pp. 150-154, December 2019.

Conference Papers

1. “A Numerical Model Comprising the Effect of Number of Turns on AC Losses in 2G HTS Coated Conductor at 77K using H-formulations”, IEEE Xplore, 2019.

Conference Attended

1. 2019 IEEE 2nd International Conference on Power and Energy Applications, April 27-30, 2019 Singapore.
2. COMSOL Conference- 9-11th August, 2018, Bangalore, India.
3. International Symposium on Functional Materials, Punjab University Chandigarh and IIT Kanpur, Chandigarh, 13-15 April, 2018.
4. International Workshop on Advanced Materials, Behrampur, Odisha, India, 17th-20th December, 2017.
5. International Conference on Recent Advances in Mechanical Engineering (ICRAME-2017), Punjab, India during 14th to 15th April, 2017, LPU Phagwara.

Table of Contents

List of Figures

List of Tables

Nomenclature

IEA	International Energy Agency
TWh	Trillion Watts hours
ZEVs	Zero Emission Vehicles
GDP	Gross Domestic Product
GPS	Global Positioning System
HEMP	High altitude electromagnetic pulse
IEMI	International Electro Magnetic Interference
AFRL	Air Force Research Laboratory
YBCO	Yttrium Barium Copper oxide
BSCCO	Bismuth Strontium Calcium Copper oxide
HTS	High Temperature Superconductors
LTS	Low Temperature Superconductors
FACTS	Flexible AC Transmission System
BNL	Brookhaven National Laboratory
HTS	High Temperature Superconductors
CSM	Critical State Models
LHC	Large Hadron Collider
ITER	International Thermonuclear Experimental Reactor
NMR	Nuclear Magnetic Resonance
MRI	Magnetic Resonance Imaging
PiT	Powder-in-Tube
PLD	Pulsed Laser Deposition
MOCVD	Metal Organic Chemical Vapor Deposition
SFCL	Superconducting Fault Current Limiters
VECC	Variable Energy Cyclotron Centre
SPC	Single Pancake Coil
IBAD	Ion Beam Assisted Deposition

HMD	Horizontal Mesh Density
VMD	Vertical Mesh Density
NZPV	Normal Zone Propagation Velocity

Symbols

μ_0	Permeability of free space
H_{c1}	Lower critical field
H_{c2}	Upper critical field
T_c	Critical Temperature
χ	Magnetic susceptibility
ξ	Coherence length
F_L	Lorentz force
λ	Characteristic length
f_p	Pinning force
H_{irr}	Irreversibility field
B	Magnetic flux density
J_c	Critical current density
B_x	Parallel magnetic flux density
B_y	Normal magnetic flux density
Γ	Anisotropic parameter
ρ_{sc}	Resistivity of superconductor
ξ'	Instantaneous AC loss (W/m)
n_c	Number of parallel conductors
Q_j	Joule heating losses
$C_p(T)$	Temperature dependent specific heat of SC tape
ρ_m	Mass density
Q	Heat flux

Chapter-1

Introduction

This chapter aims to present a concise preface to energy and energy storage systems and its significance into the modernization of the societies. The critical challenges related to energy production from primary sources have been identified and it has been found that coal along with oil products are widely employed in electrical energy generation which again contribute to excessive CO_2 emissions. The solution of this problem has been found in installing renewable and green energy generation plants. The other challenges like power blackouts have been identified as other major concern for the society and in this chapter, all possible situations of such blackouts have been identified. Energy storage systems will be the only solution for such outages and many of them has been compared on the basis of energy/power density, response time, efficiency and disposal effects. It has been found that Superconducting Magnetic Energy Storage is one of the finest technology that can handle all aforementioned power grids problems.

Keywords: Energy storage, power grid, renewable energy, global warming, power blackouts.

1.1. Basic Introduction to Energy

Energy can neither be created nor be destroyed it only transforms from one state to another however it can be stored in various forms. Energy is the basic need of the life and it becomes essential commodity of modern world's development. Energy can be classified in many ways however, in broader sense it can be classified in major two categories: primary and secondary forms of energy. Primary energy sources are those which are in existence naturally like coal, biomass, crude oil, solar, tidal, wind, geothermal, water springs, uranium, natural gas etc. On the other hand, secondary energy sources are generally extracted from the primary sources using various energy conversion technologies. Figure 1.1 shows the flow diagram that consists the association among the primary and secondary energy sources.

Secondary sources of energy are directly consumed by the society as they are easily available which includes diesel, gasoline, electricity, butanol, ethanol, hydrogen and heat. Table 1.1 illustrate the secondary energy forms that are extracted from primary energy sources along with the corresponding technology of conversion.

Besides energy conversion, energy consumption has been growing significantly over the years due to the population growth. Conferring to International Energy Agency (IEA), energy demand has been increased by 2.3% in 2018 which is the highest in last decades [1]. India, China and United States are responsible for nearly 70% of energy demand throughout the world. Demand of all type of fuels has been increased worldwide and fossil fuels alone reached 70% growth for the second year since 2017. Renewable energy supply resources like Solar has increased by 31% along with wind energy generation which is grew at double-digit pace [1]. However, these growths are not enough to match the world's energy needs and due to this, usage of coal has been increased by 0.3% globally and the developing countries like Asian continental are contributing maximum into it. As a result, CO_2 emissions has increased by 1.7% to 33 Gigatonnes which is the main contender in increasing global warming potential [1]. Figure 1.2 shows the CO_2 emissions by sector World statistics for year 1990-2017 and it can be observed that CO_2 emissions are huge for electricity and heat production followed by transport and industry which is has to be controlled in coming years in order to avoid drastic climate change.

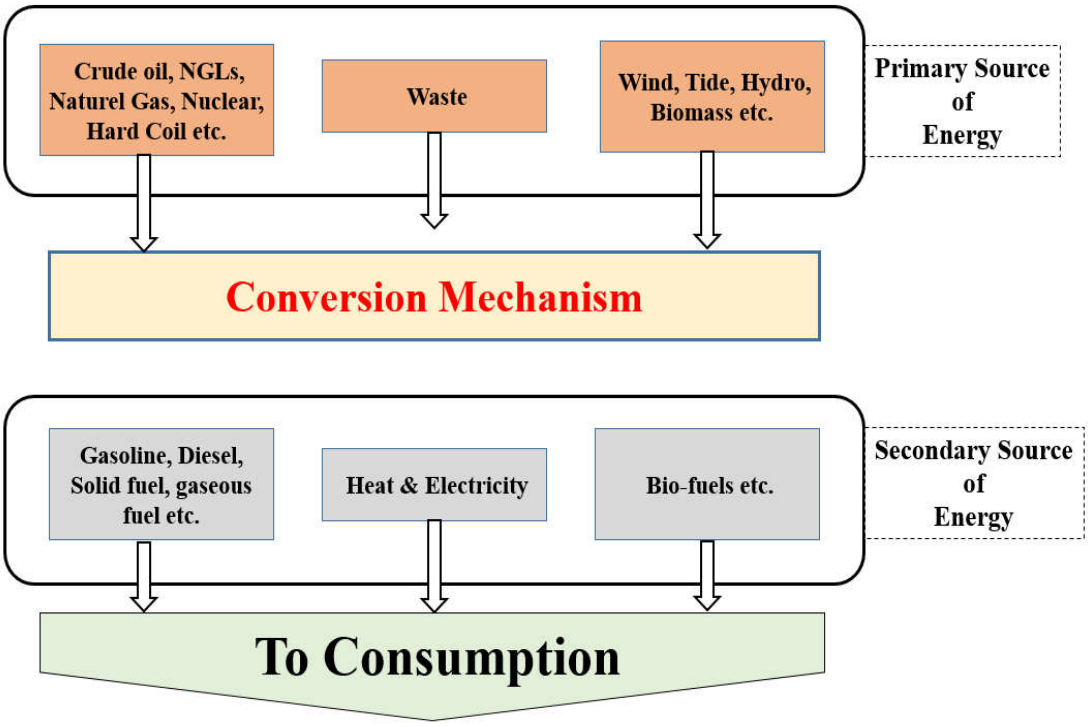

Figure 1.1 Association among the primary and secondary energy sources

Table 1.1 Conversion from Primary energy sources

Primary Energy Sources	Conversion Process	Secondary Energy Sources
Coal	Thermal Power Plant	Work, Heat, Electricity
Natural Uranium	Nuclear Power Plant	Work, Heat, Electricity
Crude Oil	Oil Refinery	Diesel, Gasoline
Wind Energy	Wind Turbine Farm	Work, Electricity
Tidal Energy	Tidal Power Plant	Work, Electricity
Solar Energy	Photovoltaic Plant	Heat, Electricity
Falling or Flowing Water	Hydro-power plant	Work, Electricity
Solar Energy	Solar Power Plant	Work, Heat, Electricity
Geothermal Energy	Geothermal Power Plant	Work, Heat, Electricity
Biomass	Bio-refinery	Work, Heat, Electricity, biofuel

These emissions are produced due to the use of coal and oil (Figure 1.3) in energy supply and developing Asian countries are contributing maximum in such emissions. The various statistics for the year 1990-2017 has been reported by IEA [2] and presented in Figure 1.2 to Figure 1.8. According to International Energy Agency (IEA) World Energy Balances 2019 report, total primary energy supply by source (1990-2017) in India is coal and oil products (Figure 1.4) both of which are

responsible for the pollution and global warming thus climate change due to the CO_2 emission.

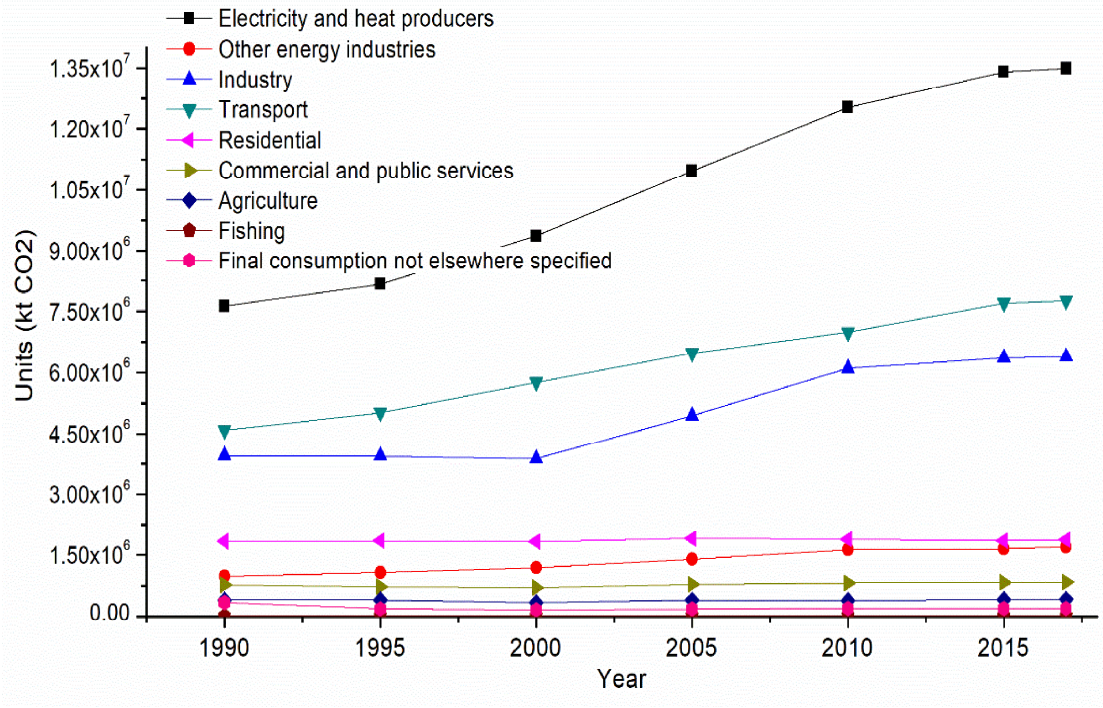

Figure 1.2 CO_2 emissions by sector, World 1990-2017

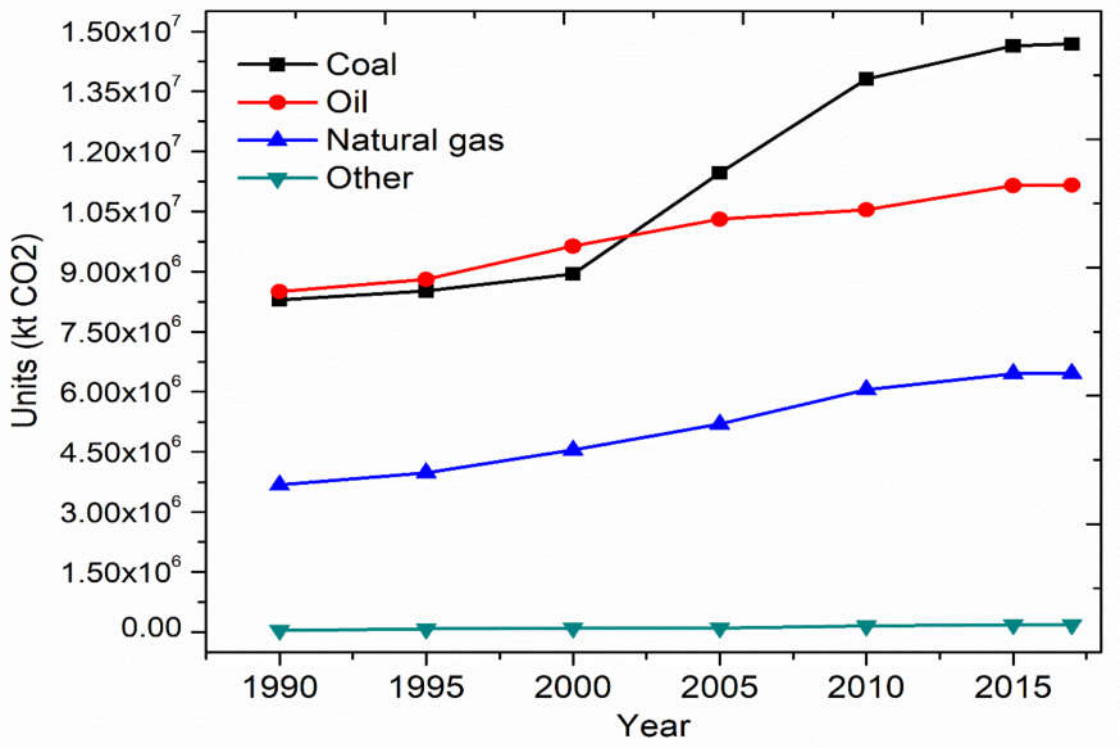

Figure 1.3 CO_2 emissions by energy source, World 1990-2017

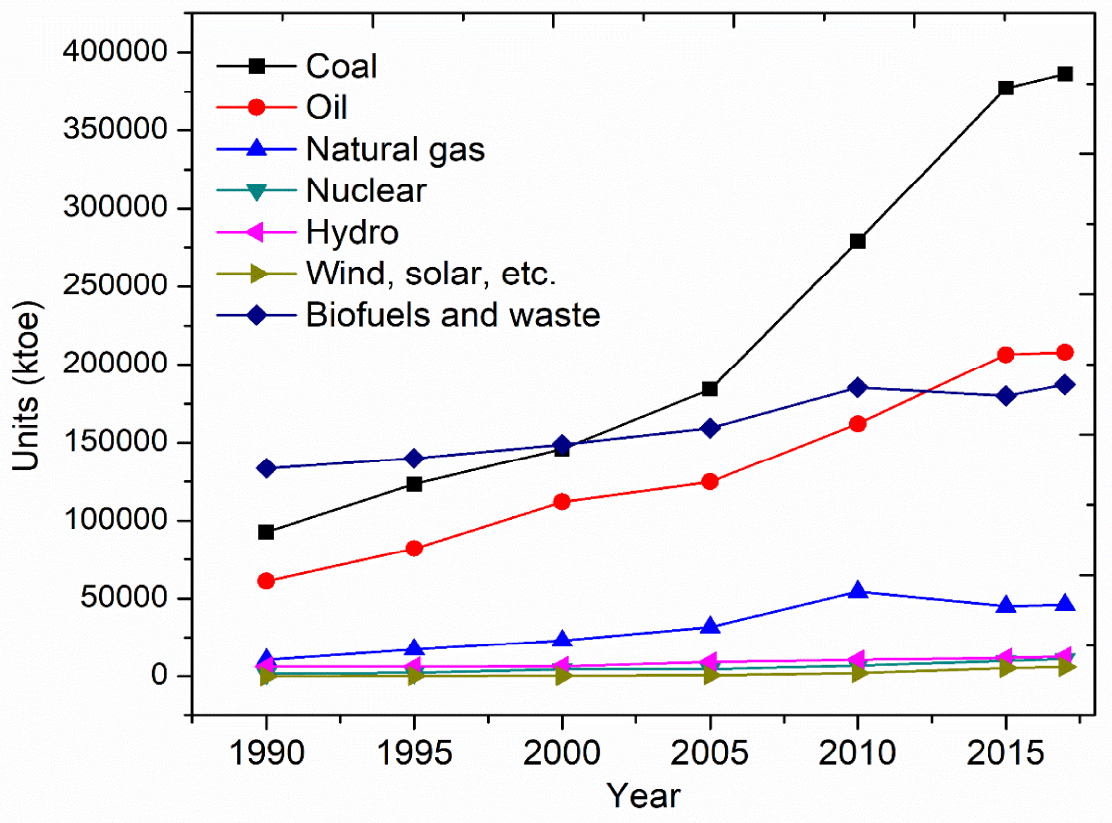

Figure 1.4 Total primary energy supply (TPES) by source, India 1990-2017

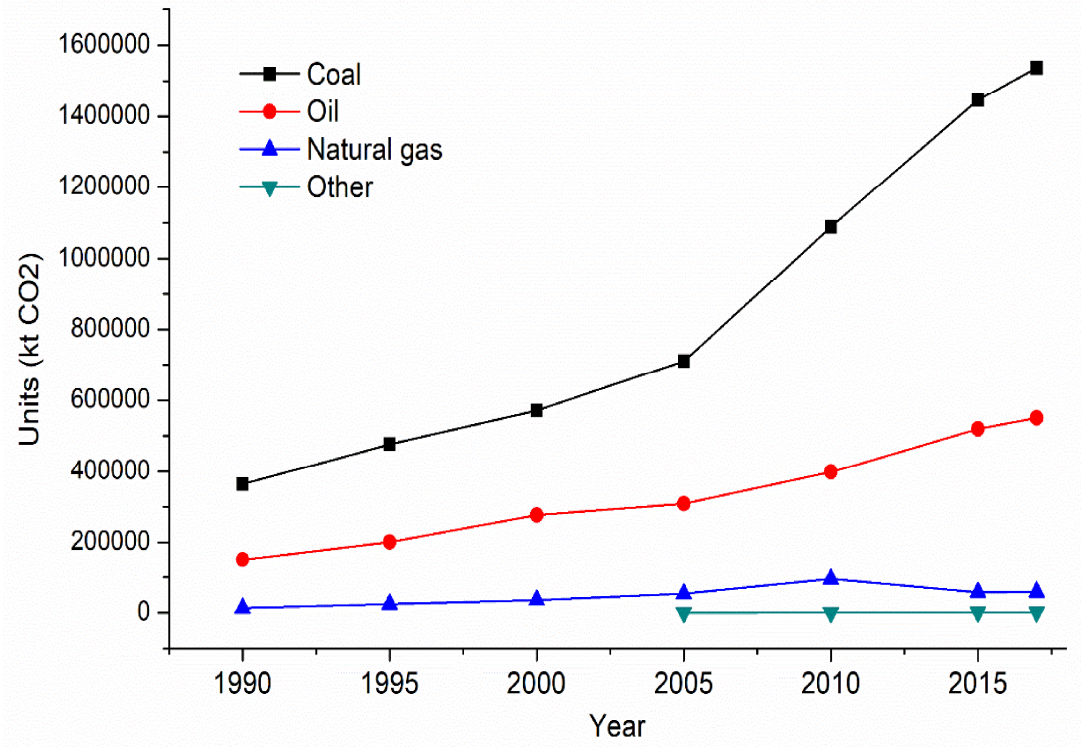

Figure 1.5 CO_2 emissions by energy source, India 1990-2017

IEA reports that the CO_2 emissions by energy source in India is due to coal and oil usage and these are increasing further day-by-day (Figure 1.5). Also, it has been reported by IEA that CO_2 emissions by sector in India is found to highest for electricity and heat production followed by industry and transport sector as described in Figure 1.6. Therefore, in order to avoid pollution challenges, there are two solutions, either there is a need to increase renewable energy resources so that electrical energy can be produced through such green innovative technologies such as wind, solar etc. to avoid pollution or there is a need to implement electric vehicles for the transportation which further adds to electrical energy consumption which automatically lower the emissions.

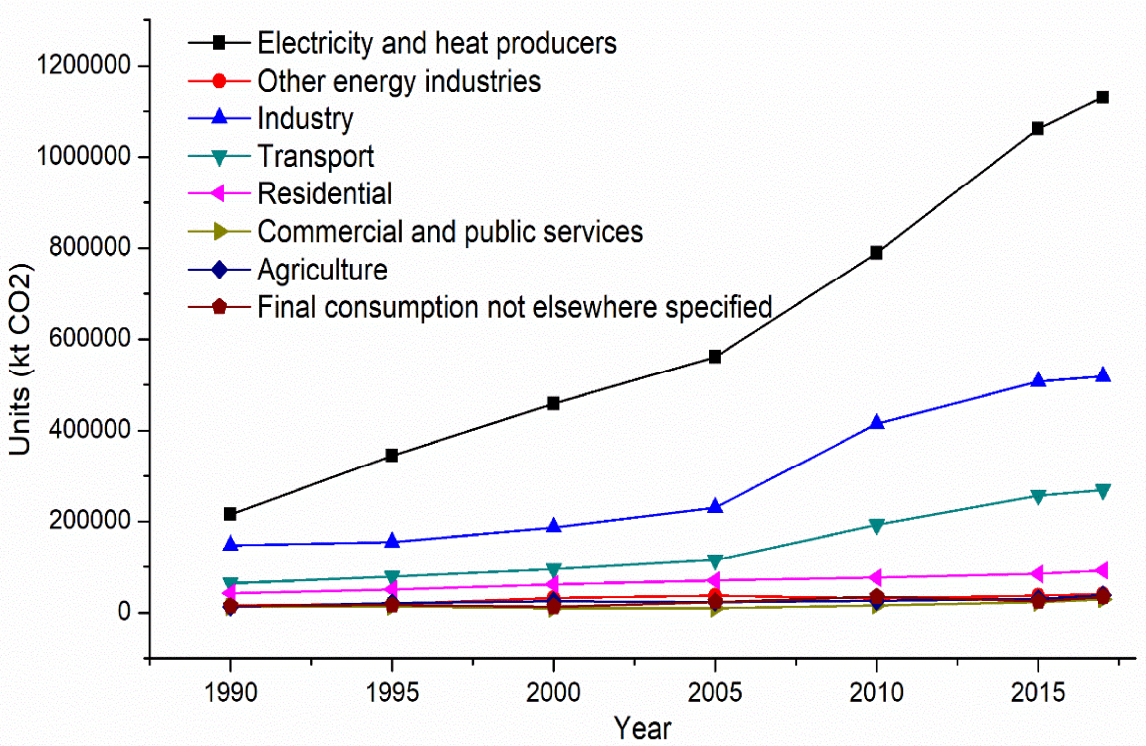

Figure 1.6 CO_2 emissions by sector, India 1990-2017

Energy consumption has reached to its all-time highest level and it is expected to increase further with faster rates due to the digitalization and automation of daily use products. Figure 1.7 illustrate the total energy consumption (1990-2017) by sector in India and it can be observed that the most of the energy reserves are consumed by industry and residential followed by transport. IEA has reported that the total energy

consumption (1990-2017) by source (Figure 1.8) is dominated by the oil products and biofuels and waste followed by electricity and coal [2].

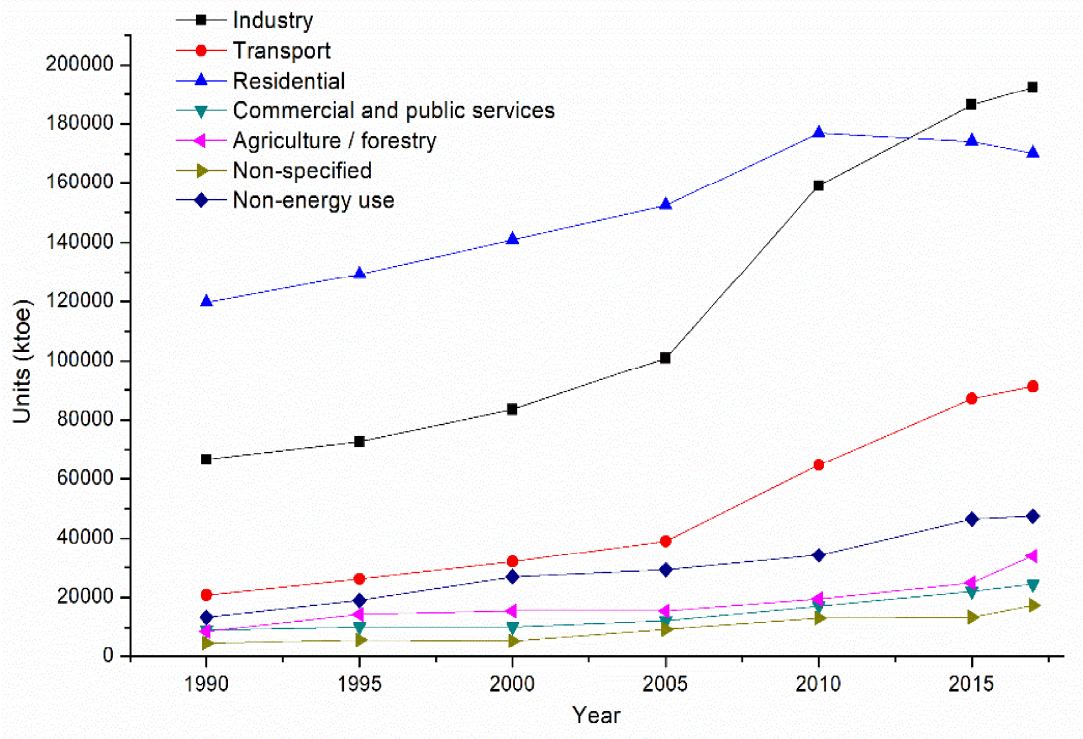

Figure 1.7 Total final consumption (TFC) by sector, India 1990-2017

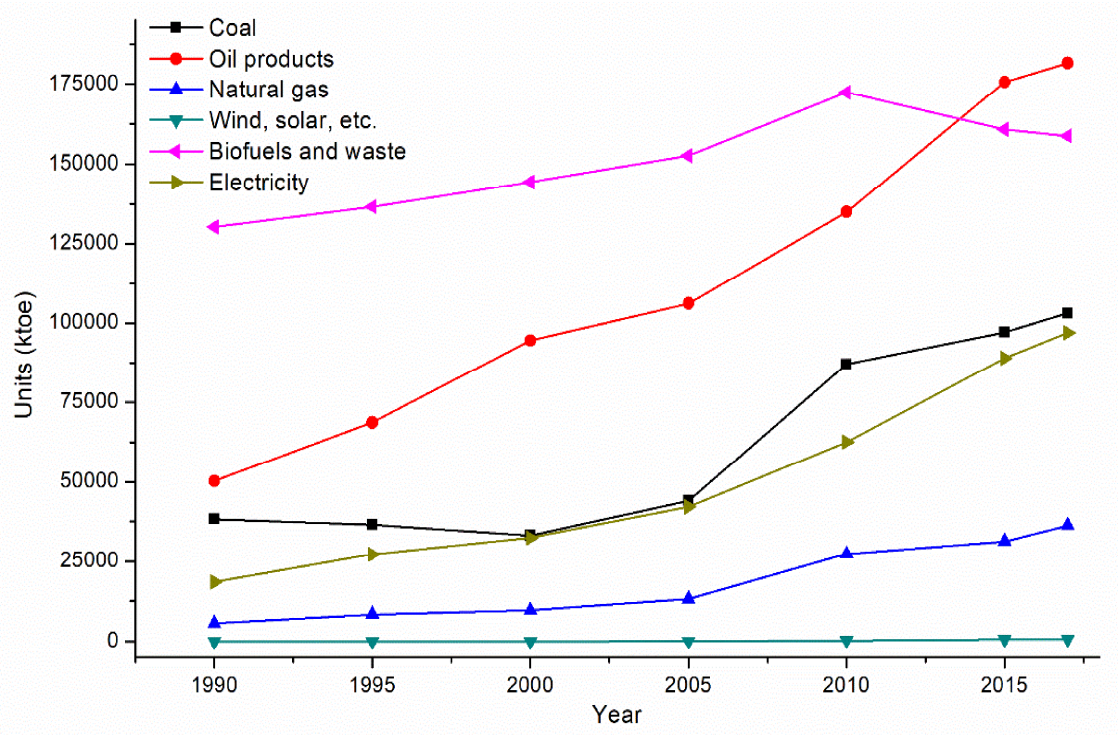

Figure 1.8 Total final consumption (TFC) by source, India 1990-2017

Electricity endures to place itself as “future fuel” as it has potential to limit global CO_2 emission reduction. The global electricity demand growing with a pace of 4% in 2018 [1] to more than 23000 TWh and the energy consumption through electricity is expected to increase due to the inclusion of electrical vehicle into the transport sector. This implies that constant energy input is required for such vehicles and which can only be possible if energy storage systems work efficiently.

Also, charging stations are required to develop for the energy unit charging like oil pumps in case of conventional gasoline or diesel vehicles. Thus, for charging purposes the energy/power bank must have high energy/power density and fast response properties in order to save dwell time while vehicle charging.

In order to avoid pollution and meeting energy demands, renewable energy resources can be considered for electrical energy production. Pollution issues can also be controlled by lowering the CO_2 emissions through limiting the usage of fossil fuels in the transport sector using electrical vehicles for transportation. Presently, Indian government is taking serious measures on this issue and already electrical motorbikes and cars has been launched in Indian market under Zero Emission Vehicles (ZEVs) program. However, energy production using renewable energy resources like wind and solar strongly depends upon the weather conditions and the overall output from such plants is intermittent. The other issue is with wind plants as such plants are effective if they have been installed at the remote locations near coastal regions to get better output thus it becomes clumsy to transmit or even distribute the power to the other grids. Recently, superconducting wind turbine generator of capacity 3.6 MW has been installed in Denmark and it has been reported that this superconducting machine delivered same power as that of conventional wind turbine generators with having half of the weight and volume [3]. The integration of wind power generation with SMES has been studied by many researchers and can be found in [4].

The other issue is with solar power plants and output for such plants is significantly depends upon the weather conditions thus in order to make up the power shortage, SMES system can be used as they consist high power and energy densities and can be used for micro-grid scale level. Highlighted region in Figure 1.9 shows the integration of the renewable energy power sources with SMES in order to get smoother

operation. The possible major factors behind increase in the energy demand and pollution have been identified and corresponding possible alternate has also been suggested in Figure 1.9.

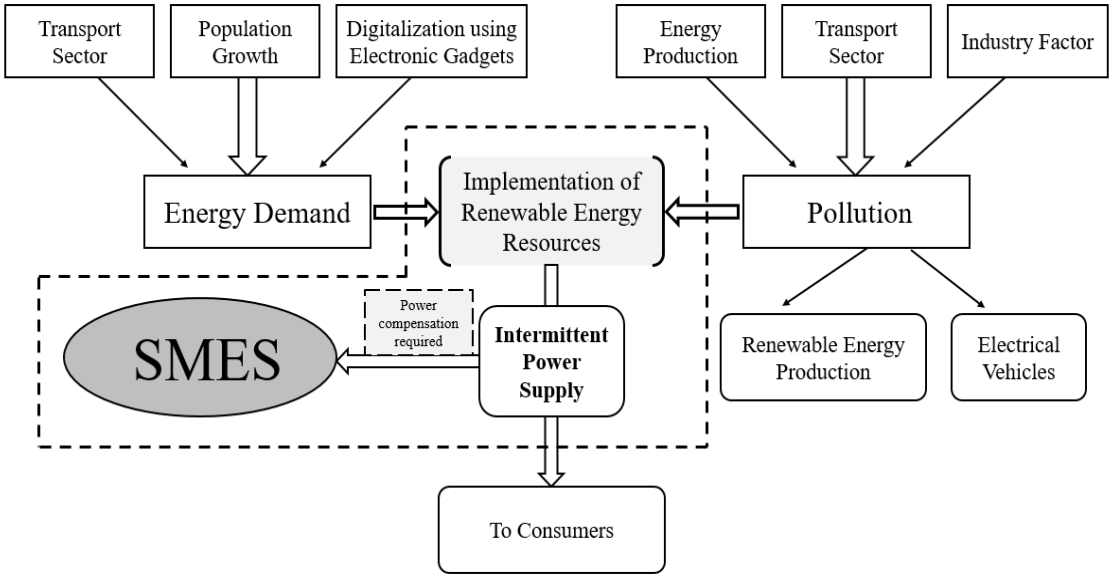

Figure 1.9 Integration of intermittent power grid with SMES

1.2. Power Blackouts

The other serious problem faced by the world's population is power blackouts. In this digital economy world, blackouts can damage the GDP of any country to a greater extent and leads to massive economic losses. They can appear due to the natural climate disasters like tsunami, earthquake or un-natural reasons like power interruptions due to power shortages at peak hours, voltage fluctuations, technical or human errors. Out of which damage done by natural phenomenon cannot be repairable easily and it need time and effort to resume lives of people to normalcy. However, un-natural facts of blackouts can be avoidable as they occur for smaller durations minutes to few hours. Figure 1.10 shows the number of blackouts worldwide per year and average duration of each blackout for the year 2009.

It can be noticed that most number of blackouts were happened in South Asia region and both India and China contributed the maximum in such blackouts [5]. Average duration of blackout is found to near 2.5 hours and the ultimate solution for controlling such happenings is to have an efficient, economical and environment

friendly energy storage backup that can be used in such situations thus economic losses can be avoided.

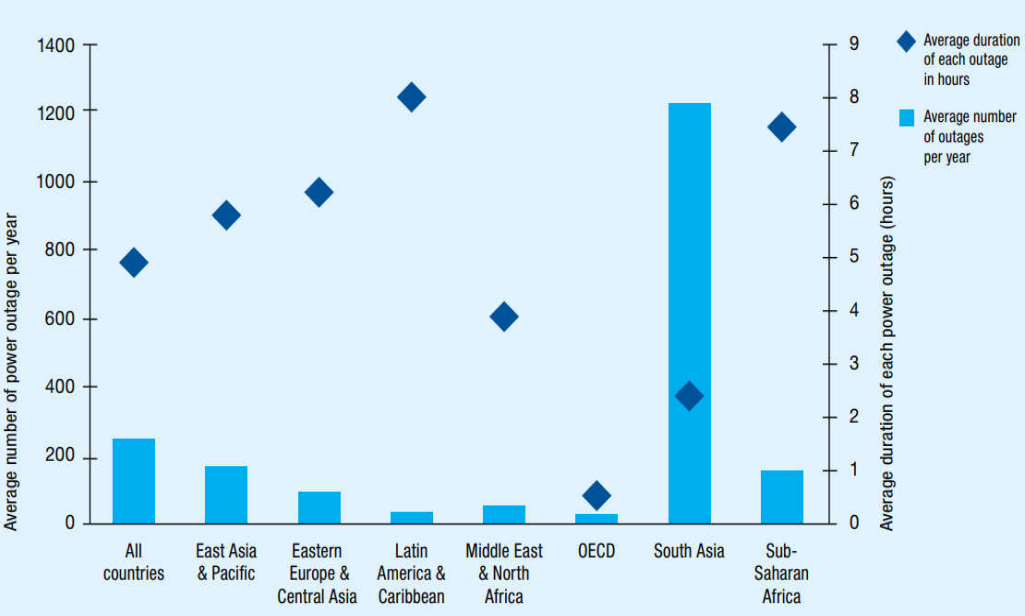

Figure 1.10 Worldwide Blackouts per year and average duration [5]

Figure 1.11 illustrate the possible reasons of power blackouts, where all catastrophic events have been enlisted that can result to blackout. Table 1.2 illustrate the ten major blackouts in terms of people affected and economic loss and it can be observe that the more common among all is happen due to the technical faults, human errors, heavy rains and power shortage problems causing overloading on the grid. In order to meet the demand, energy capacities should be enhanced to a higher level where renewable energy resources can be used as clean energy production however, one of the issue with such technologies is that the renewable energy plants are located very far from the demand centres and provide intermittent power output. Therefore, it becomes economically problematic to connect those remote areas with the power grid thus it would be beneficial if portable energy storage systems like SMES can be charged over there and transferred the same stored energy to the other locations.

Industry needs continuous power supply whether load is more or less, thus separate grids are always installed to meet their power requirements. Sometimes, due to power shortages or maintenance issues, power of the household or domestic consumer has

been deducted in order meet industry load requirement which is again leads to blackout for the common people.

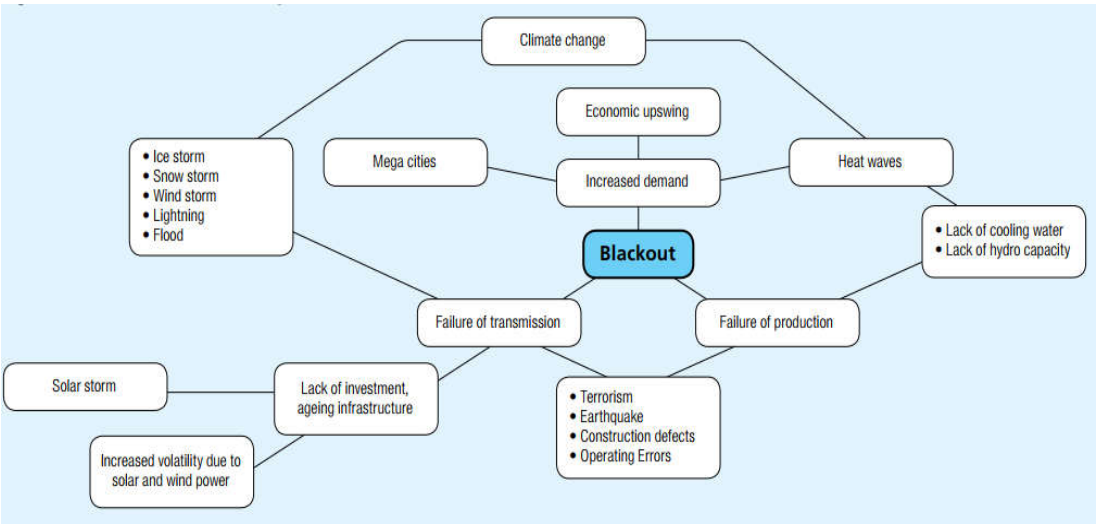

Figure 1.11 Probable reasons of Power Blackouts

Table 1.2 Ten most severe blackouts concerning affected population and duration

Country	Reason	Population Affected	Time of Blackout	Economic Loss
New Zealand 20-02-1998	Due to technical failure of the grid	70,000	4 weeks	
Brazil 11-03-1999	Due to lightning strike on electricity sub-station in Bauru causing tripping of almost all 440kV circuits. People faced heavy traffic jam and trains were out of running.	97,000,000	5 hours	-
USA & Canada 14-08-2003	Due to human error, maintenance ignorance and equipment failures caused an electricity outage for 4 days that influenced a larger area of Midwest and Northeast US and Ontario, Canada.	50,000,000	4 days	USD 6 billion
Italy 28-09-2003	Due to technical failure of the system led Italian system separate from rest part of Europe.	56,000,000	18 hours	-
Indonesia 18-08-2005	Due to technical failure of the electrical system led power cuts in Java, Bali and Madura.	100,000,000	7 hours	-

Spain 29-11-2004	Due to overloading of transmission line caused severe technical failure	2,000,000	5 blackouts in 5 days	-
South West Europe 04-11-2006	Due to human error lead to instabilities of frequency in the grid and overloading of the lines.	15,000,000	2 hours	-
Brazil 10-11-2009	Due to natural event caused by strong winds and heavy rains lead to short circuit in three main transformers and shut down of 20 turbines of world's 2nd largest hydroelectric dam.	87,000,000	25 min to 7 hours	-
Brazil 04-02-2011	System's technical failure of electronic components.	53,000,000	16 hours	-
India 02-01-2001	Failure of sub-station in Uttar Pradesh leads to a blackout of 12 hours where electric trains got affected and resulted in longer traffic jams in Delhi. Airlines also got affected and reserve generators were used to avoid interruptions among the flights.	226,000,000	12 hours	USD 110 million

1.3. Power supply as potential terrorism and military target

Power supply industry is the backbone for the military of any country in order to keep normalcy in the society. In modern era, due to the digitalization, all military bases are interconnected through wireless communication to have fast and accurate data or information transfer. Use of surveillance cameras have been increased due to the scarcity in the border regions which may be due to geographical locations or climate change. Other most important area on which earth, marine or air force of any country rely is the satellite communication systems like Global Positioning System (GPS), Radar etc. and such systems need continuous power supply at any cost. Minor failure of such systems can lead to an insecurity among the society and nations has to face drastic consequences.

Due to these reasons, power systems have always been on the targets in case of war and it is always desirable to protect such systems from terrorist attacks. In past many situations have been reported where terrorist groups or at war time, nations have

damaged the power supply, affected dams, thermal power plants, high voltage transmission line and substations. Some of them are briefed below:

- During 1952, U.S.- North Korean war, U.S. military has targeted many power plants and dams to wipe out the 90% power generation.
- In 2005, in Georgia, terrorists have damaged the high voltage transmission line.
- Since 9/11, many terrorist's groups have threatened U.S. to destroy their dams as a result U.S. has increased the security on some prone dams and some of them has been closed due to safety measures.
- As from last two decades, due to the expansion in computer and internet technology, it has been found that cyber-attacks increased where hackers have tried to attack the power systems. In 2007, hackers hacked the Idaho National Laboratory's USD 1 m diesel-electric generator remotely and destroyed it.
- Other type of threats has also been appeared due to the technological advancements. High altitude electromagnetic pulse (HEMP) and International Electro Magnetic Interference (IEMI) attacks can lead to entire power supply system failure as they can generate a voltage of 100s to 1000s V and have potential to destroy all electronic chips.

Aforementioned attacks damaged the power supply systems to a large extent and no country has any answer to such blackouts however, energy storage systems can help in emergency situations. Therefore, efficient energy storage systems are always desirable in such situations to ensure enough power backup.

1.4. Future transmission grid challenges

In order to achieve excellent energy management, usually conventional power grids are going to be interconnected through artificial intelligence where grid will work smartly in order have efficient production, transmission and distribution of power to the load and excess power can be made available to the other synchronized grids. However, such conventional grids have to be modernized globally and following are the few challenges that may face by the communities.

1.4.1. In other countries

German Energy Agency (Dena) [5] has published a study where agency has pointed out the critical issues (Figure 1.12) that should be taken into account while planning any future transmission grid that retorts to the sustainable energy/power supply and future needs of the smart power grid and increased ratio of renewable energy production.

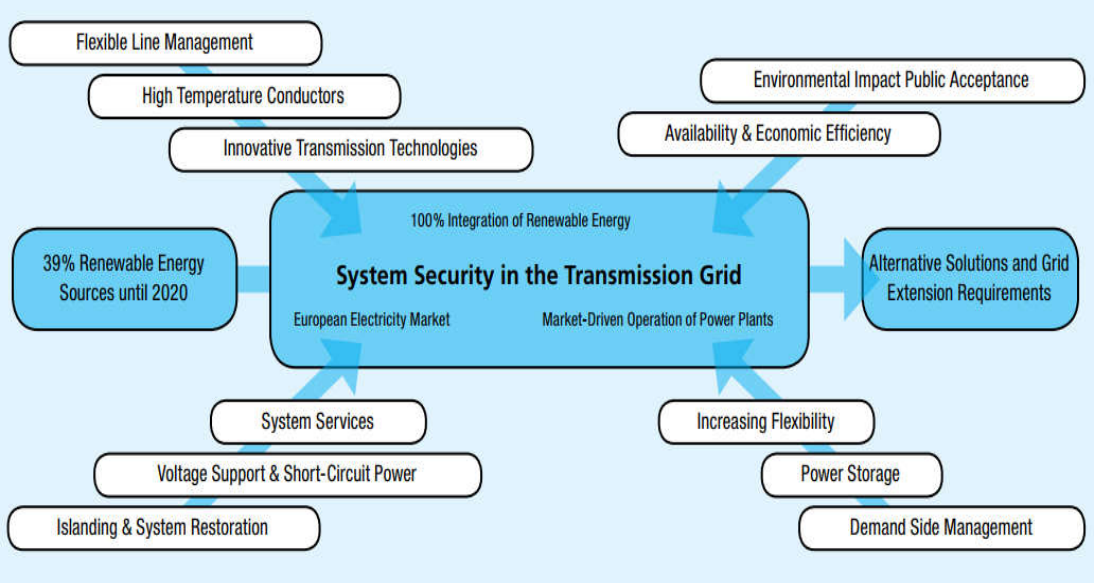

Figure 1.12 Future transmission grid challenges

The agency report concluded that for a reliable and healthy grid, Germany has to invest in bulk to extend the coverage of transmission lines to about 3600 km of 380 kV lines by near 2020. Report has also commented on the status of European Union grids that they have to invest about USD 23-28bn in coming five years. IEA has reported that an investment of USD 13.6 trillion is required by 2030 in order meet the demand of the modern world. Agency has also reported that 50% of total amount needs to be invested in the electricity generation and other part of 50% should be invested on transmission and distribution.

1.4.2. In Indian Context

Being an under-development country, India has still much to do in its power sector as energy/power supply demand is more than it is required as plotted in Figure 1.13 and Figure 1.14 [6]. It can be noticed that the demand is higher than the supply for both energy and power supply.

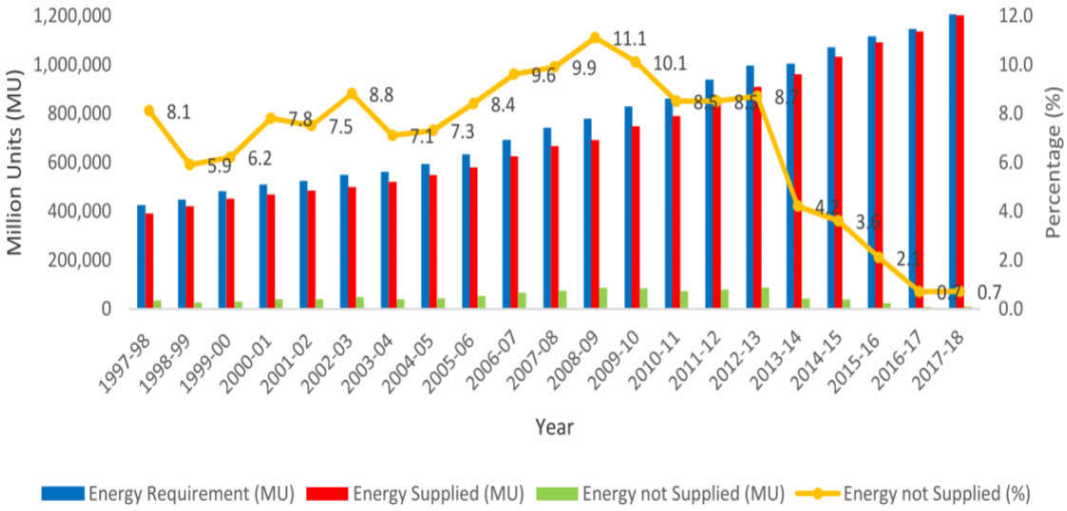

Figure 1.13 Power Supply Scenario (Energy)

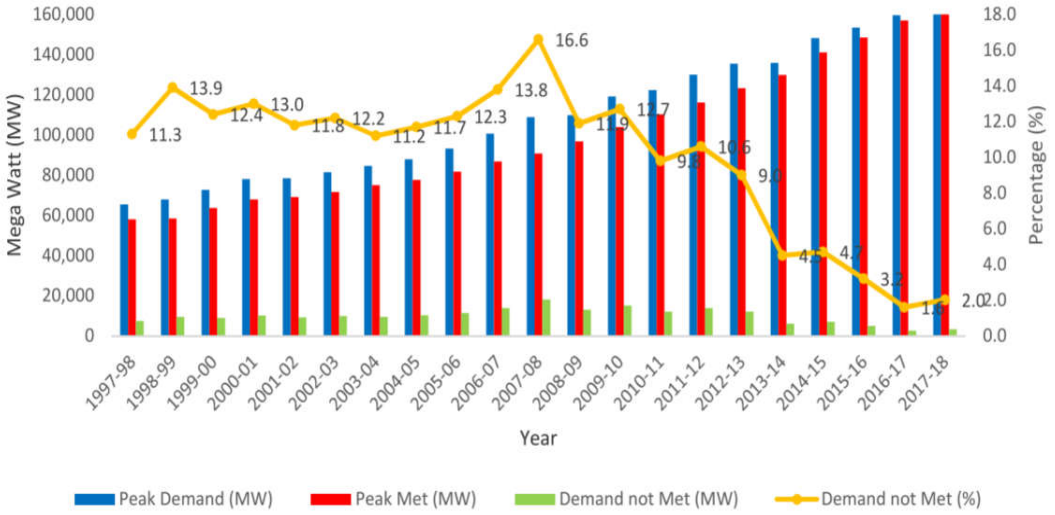

Figure 1.14 Power Supply Scenario (Load)

Government of India is still busy in electrifying the villages/houses of common people and it further adds to develop new smart power grid infrastructure for continuous power supply as all communication will be two-way. Another major programs like smart cities, 100 metro cities, and one nation one grid, initiated by government needs capital investment in installing new power plants based on green energy concept in order to meet the power requirements in future.

One nation one grid is another vibrant step in meeting the power supply demands and it will assist in maximum utilization of limited natural resources through transmission of power at various transmitting voltages of 765kV, 400 kV, 220kV, 132kV AC and ±500kV DC, and 400kV AC transmission lines from Resource centric grids to Load

centric grids thus need of energy storage systems will be increased to achieve continuous power supply. Figure 1.15 shows the one nation one grid concept where all five grids namely, north grid, northwest grid, east grid, west grid and south grid are synchronized to each other in order to use excess energy available at one grid at the other grid.

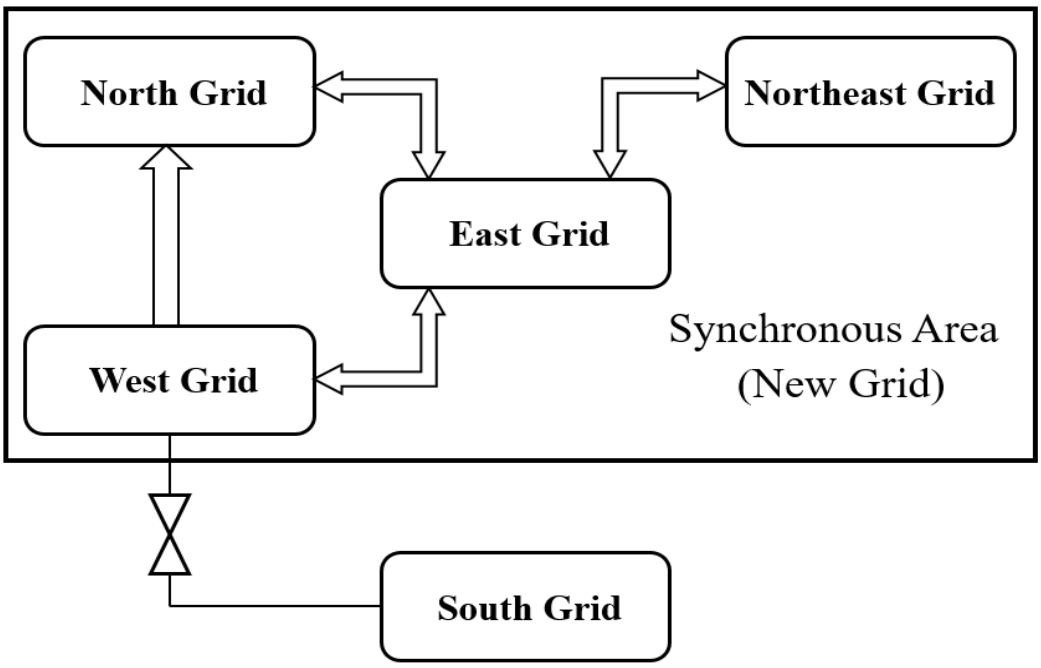

Figure 1.15 One Nation One Grid synchronization

1.5. Importance of energy storage systems

Continuous power supply becomes an essential element at present as almost every device is interconnected through electronic gadgets including electrical appliances, communication systems, data servers and many more. The primary source of energy is the power grid that distributes electricity from generation end to consumption end. Modern electrical power generation, transmission and distribution industry has to ensure continuous/uninterrupted power supply in order to achieve smart city concept in India, to avoid power blackout losses and to meet the increased power demand. Sometimes, there may be situations where power grid gets failed then there should be a secondary power system is required that can take the instantaneous load to keep a continuous power supply. Also, renewable power resources like solar, wind etc. are intermittent and they can produce power only as per the favorable climate conditions,

and thus interruptible at time without high density energy storage provisions. This implies it cannot supply continuous power to the grid and thus secondary power system is required to attain uninterruptible power supply. The work considered here "Superconducting Magnetic Energy Storage (SMES) Systems" is a small step towards achieving that technology in India.

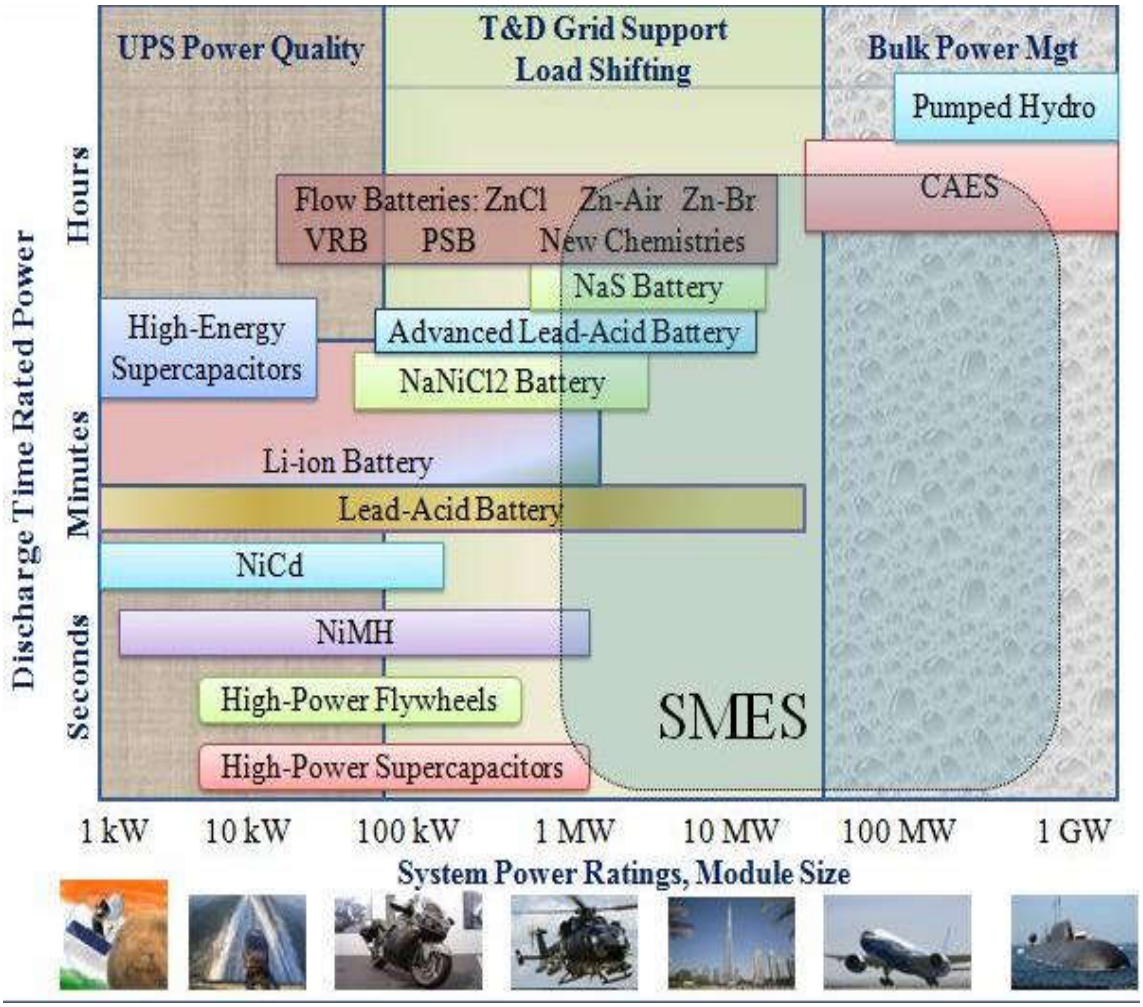

Figure 1.16 Various Storage System's Power Rating

The available options are very straight forward "store enormous energy' to be used upon requirement without depleting it instantaneously or store it fast. This storage 'the secondary power supply' is currently based on battery technology where electrical energy is converted and stored as chemical energy. Figure 1.16 shows the various energy storage systems along with their power ratings. From the Figure 1.16, it can be noticed that the battery storage systems are limited to low rate capability (how fast you can store and extract power). So for higher storage capacities one has

to choose between Pump hydro, (CAES) systems and super conducting magnetic energy storage (SMES) systems. However, implementing CAES and pumped hydro storage systems need large capital investment and require large area for installation. Whereas, SMES systems are flexible as they can be transported from one place to other and thus finds many applications like in charging of electrical vehicles, aircrafts, ship propulsion, electromagnetic launchers, Maglev trains etc.

Air Force Research Laboratory (AFRL), USA [7] have reported (Figure 1.17) the comparison between battery and SMES storage systems and they have concluded that SMES has more storage capacity per kg than battery storage systems, and hence in the present work, we consider a theoretical approach first "Computational Studies on Superconducting Magnetic Energy Storage (SMES) Systems for Power Grid Applications" to understand the right configuration to implement it for the practical application.

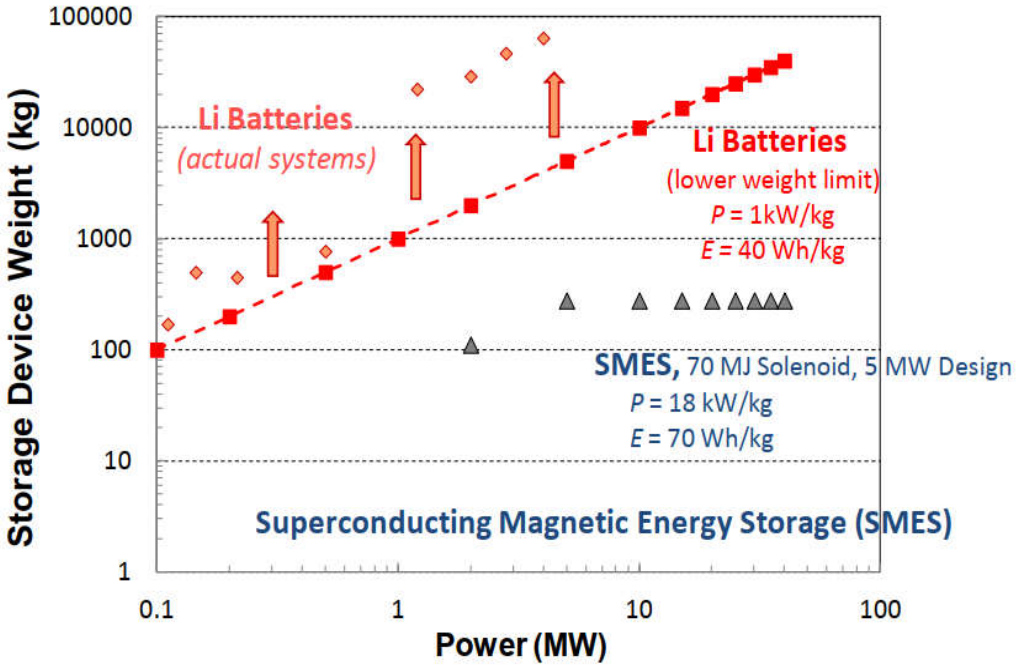

Figure 1.17 Storage Device Weight vs Power Storage [7]

Air Force Research Laboratory (AFRL), USA [7] (Figure 1.18) have done extensive studies and concluded that the Yttrium Barium Copper oxide (YBCO) superconducting tape can store energy in the range 10-200Wh/kg with specific power of 1-200kW/kg which is found to be much higher than battery storage systems,

Niobium-Titanium (Ni-Ti) based Low Temperature Superconductors and Bismuth Strontium Calcium Copper oxide (BSCCO) based High Temperature Superconductors.

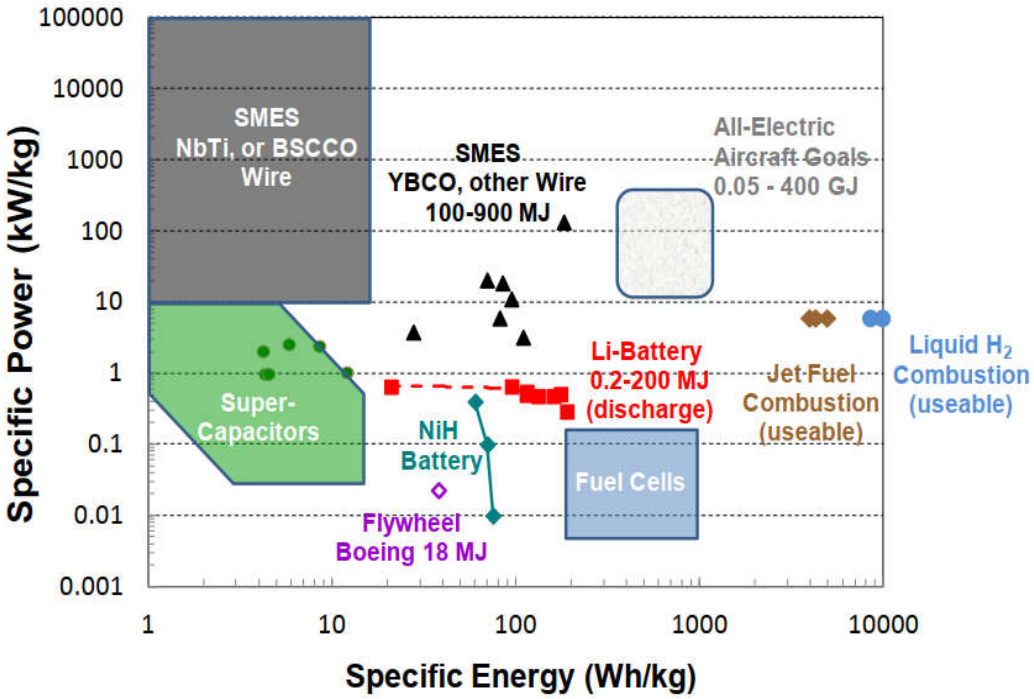

Figure 1.18 Specific Power vs Specific Energy [7]

Table 1.3 Different Energy Storage Systems

Mechanical	Electrical	Electrochemical
• CAES • Fireless Locomotive • Flywheel Energy Storage • Gravitational Potential Energy • Hydraulic Accumulator • Hydroelectric Energy Storage • Liquid Nitrogen • Pumped storage Hydroelectricity	• Capacitors • Superconducting Magnetic Energy Storage (SMES)	• Flow Batteries • Rechargeable Batteries • Supercapacitors • Ultra Batteries
Thermal	**Chemical**	**Biological**
• Brick Storage Heater • Cryogenic Liquid Air/Nitrogen • Eutectic System • Ice Storage • Molten Salt • Phase Change Materials • Seasonal Thermal Energy Storage • Solar Pond • Steam Accumulator • Thermal Energy Storage	• Bio-fuels • Hydrated Salts • Hydrogen • Hydrogen Peroxide • Power to Gas • Vanadium Pentoxide	• Glycogen • Starch

This implies it would be beneficial to use YBCO tapes (2nd Generation) in the construction of SMES systems as they possess excellent power handling capabilities than Low and High (1st Generation) Temperature Superconductors.

1.5.1. Need of energy storage in other major disciplines

In future, this aspect of energy storage will decide the future of electrical vehicle technology where only portable energy/power banks will be used for the charging of the electric cars and other vehicles. Also, from Figure 1.4 by source, it can be noticed that energy supply using hydro power plants is very less compared to coal and oil products.

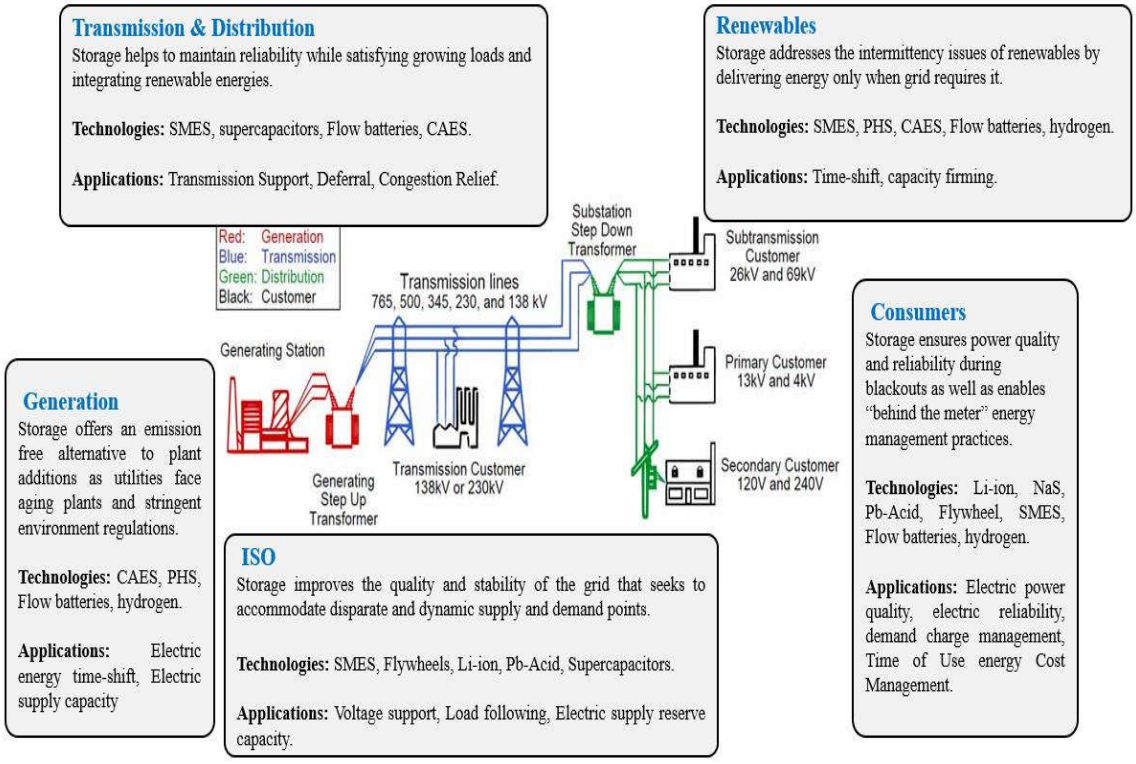

Figure 1.19 Energy storage across the power sector

Hydro-electrical grids are generally connected with the domestic power grids where power distribution to the public is done using step transformers and due to two-way communication, the electricity production will be done as per the requirement only. Sometimes, excess electrical power is distributed among the other grids synchronized with the parent grid. However, there are some situations where production can be increased to peak level during the rainy seasons and the excess energy can be stored using power banks that can store energy without or minimal losses. Such power banks

can be used in remote areas where transmission lines cannot install like military areas. Also, such power banks can be installed for the electrical vehicle charging, MagLev trains where such systems can be embedded with high temperature superconducting motors to achieve required traction force or can be used for electric aircraft take-off or landing situations. Figure 1.19 represents the energy storage technologies and applications at various levels of the power grid including generation, transmission, distribution and consumers level.

1.5.2. Immediate Need of Technology

Power grid instability is a serious concern all over the world as it results in voltage fluctuations, undesirable harmonics, momentary interruptions and voltage sags in the power system. Such instances would result in the instability of the power grid and it further adds to the drastic economic losses to any country of the world. In 2013, it has been reported that USA has suffered with a drastic economic loss of USD 220 billion due to power interruptions [8] as shown in Figure 1.20. Thus, high power quality and density along with fast response time to minimize interruptions are the two desirable characteristics required in the power grid stabilization.

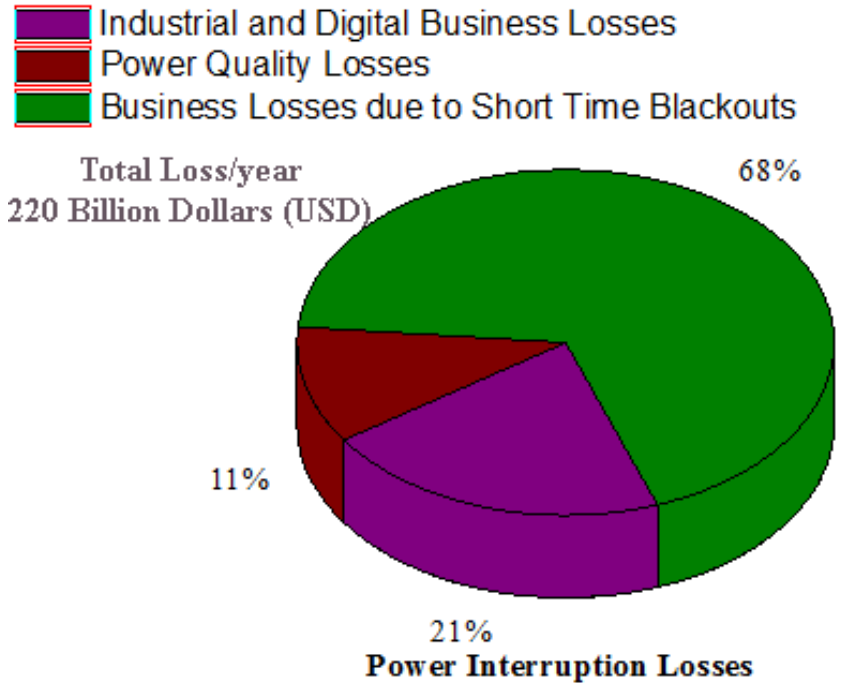

Figure 1.20 Power Interruption Losses in USA [8]

The other demand of this technology is coming from aviation and commercial transport sector as aviation sector is about to include electric aircrafts in the commercial flights in order to lower the pollution rates, on the other hand, transport sector is ready to deploy electric vehicles like buses, cars and motorbikes. These both technologies required high power density and high quality energy storage systems that can accomplish the targets of such industries. Figure 1.21 shows the all possible applications of SMES near future.

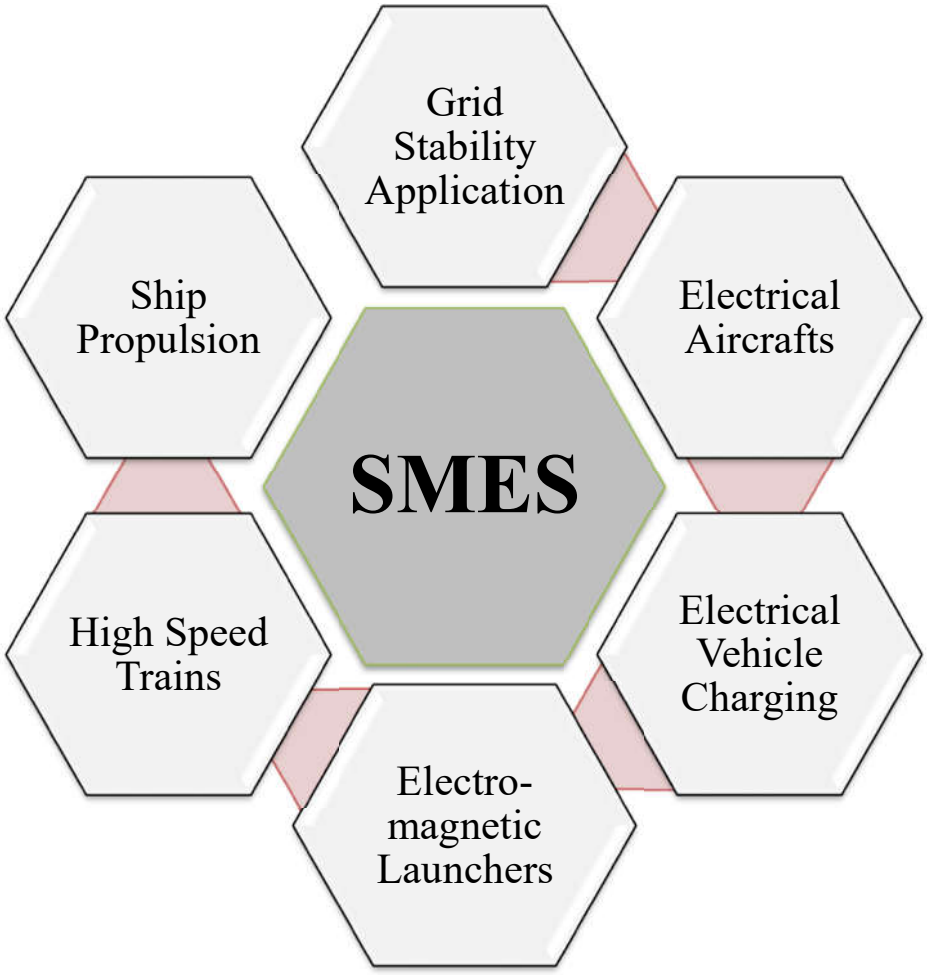

Figure 1.21 Possible applications of SMES in near future

There are numerous commercial storage systems such as mechanical, electro-chemical, thermal, electrical and chemical that can be used to mitigate above challenges. However, these energy storage systems have their own limitations related to cost, storage capacity, power density and response time. Figure 1.22 shows the technology maturity for grid storage applications and it can be noticed that SMES

technology is still under demonstration phase and not being deployed yet thus needs more research in order to lower the economic constraints.

SMES based technology has load leveling, dynamic stability, transient stability, voltage stability, frequency regulation, transmission capability enhancement, power quality improvement, automatic generation control, uninterruptible power supplies capabilities. In short, development of Superconducting Magnetic Energy Storage (SMES) technology as an electrical storage is considered due to:

a) SMES has the capability to store large amount of energy for longer periods.

b) Improves power quality for critical loads and provides carry over energy during momentary voltage sags and power outages.

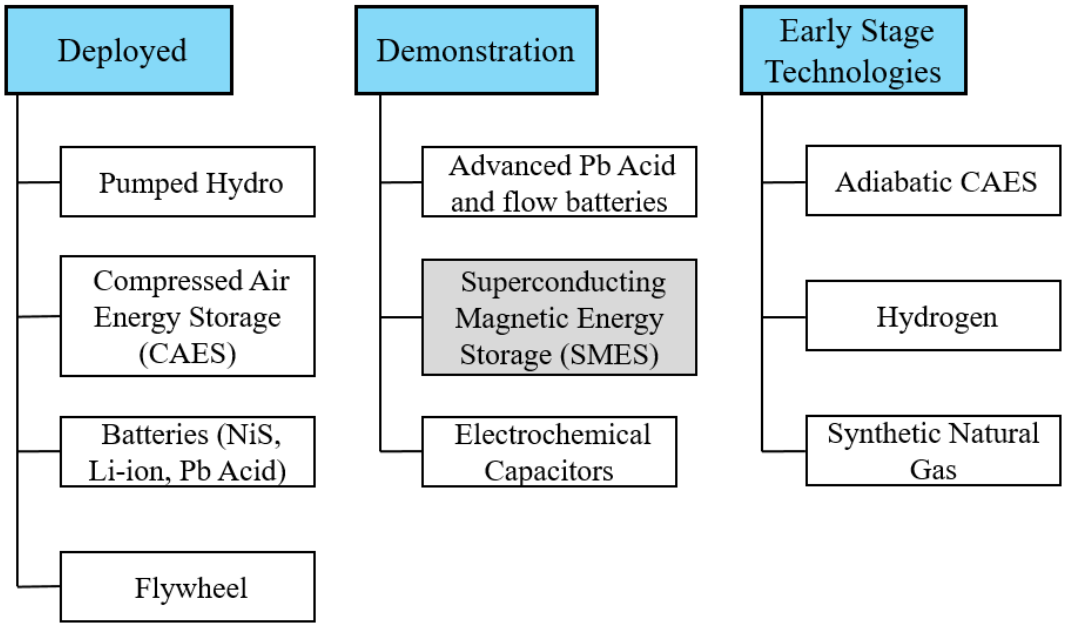

Figure 1.22 Technology Maturity for Grid Storage Applications

c) Improves load leveling between renewable energy sources (wind, solar) and the transmission and distribution network.

d) Environmentally beneficial as compared to batteries; superconductivity does not rely on a chemical reaction and no toxins are produced in the process.

e) Enhances transmission line capacity and performance – SMES features a high dynamic range, an almost infinite cycling capability, and an energy recovery rate close to 100%.

f) Discharges large amounts of power for a small period of time

g) Unlimited number of charging and discharging cycles.

Superconducting technology and power electronics development in recent years enhanced power systems performances by realizing high temperature superconducting magnetic energy storage systems (SMES) with rapid response (millisecond), high power (multi-MW), high efficiency, and four-quadrant control. The present work entitled "Computational Studies on Superconducting Magnetic Energy Storage (SMES) Systems for power grid applications" is about the design innovation of electrical energy storage with superconducting materials and simulation studies to know about the pre-requisites required before the development of actual prototype of SMES.

Technologies	Power rating (MW)	Storage duration (h)	Cycling or lifetime	Self-discharge (%)	Energy density (Wh/l)	Power density (W/l)	Efficiency (%)	Response time
Super-capacitor	0.01-1	ms-min	10,000-100,000	20-40	10-20	40,000-120,000	80-98	10-20ms
SMES	0.1-1	ms-min	100,000	10-15	~6	1000-4000	80-95	< 100ms
PHS	100-1,000	4-12h	30-60 years	~0	0.2-2	0.1-0.2	70-85	sec-min
CAES	10-1,000	2-30h	20-40 years	~0	2-6	0.2-0.6	40-75	sec-min
Flywheels	0.001-1	sec-hours	20,000-100,000	1.3-100	20-80	5,000	70-95	10-20ms
NaS battery	10-100	1min-8h	2,500-4,400	0.05-20	150-300	120-160	70-90	10-20ms
Li-ion battery	0.1-100	1min-8h	1,000-10,000	0.1-0.3	200-400	1,300-10,000	85-98	10-20ms
Flow battery	01-100	1-0h	12,000-14,000	0.2	20-70	0.5-2	60-85	10-20ms
Hydrogen	0.01-1.000	min-weeks	5-30 years	0-4	600 (200 bar)	0.2-20	25-45	sec-min
SNG	50-1.000	hours-weeks	30 years	negligible	1,800 (200 bar)	0.2-2	25-50	sec-min

Electrical Mechanical Electrochemical Chemical

Figure 1.23 Energy storage technology comparison

A comparison among the designated power ratings, storage duration, self-discharge, power density and response time has been shown in Figure 1.23 for the various electrical, mechanical, electrochemical and chemical energy storage technologies. It

can be noticed that SMES has much faster response time with lesser self-discharge rates. This means it can respond very fast whenever there is any voltage fluctuation or blackout situation. Also, the energy remains stored inside magnet for longer durations as self-discharge rating is low compared to other competitive technologies.

1.6. Historical Development of SMES

Many SMES systems have been employed in various power grid stability situations worldwide and now SMES is in its demonstration phase and all possible combinations have been tried to lower the overall cost of the system. However, many organizations have developed their prototype and demonstrated its working worldwide. Few of them related to power grid and pulse power applications have been discussed in the following sub-sections.

1.6.1. In Power Grids

Since the first idea to develop such systems, SMES systems have extensively studied from 1970. In 1970, the need is inspired from the fact that French scientists wanted to level the load in the electrical network [9]. However, this idea got failed due to large power requirements which can be achieved through pumped hydroelectric plants.

SMES systems have been evolved as Flexible AC Transmission System (FACTS) which is a static system which are generally installed in the electric grid to provide better control and power transfer capabilities. SMES as FACTS was the first device that has been operated in the power grid for the smooth operation. In 1980s, Bonneville Power Authority, USA [10] has implemented 30 MJ SMES in order to control the low-frequency power oscillations and this system was the first successful setup that has demonstrated the large SMES working in real power grid applications. This system was operated for one year in the real grid conditions for approximately 1200 hours of energy transfer. This system was shut down due to the problems occurred in power converter and cryogenic unit. No problems have been identified in the superconducting coil. Therefore, alternate solutions have been identified before the shutdown of the SMES system.

In 2000, American Superconductor Ltd. has installed six SMES units to increase the stability of the power grid in northern Wisconsin, USA [9]. This power grid has

experienced extensive voltage fluctuations with very large momentary voltage depressions. SMES units installed at different six locations in the power grid have injected reactive and real power when it was required to balance the grid and it was found that 15% of the transmission capabilities have been increased. Trailers have been employed for easy and rapid deployment.

1.6.2. In local power conditioning applications

Many MW rating SMES systems have been and still in operation for uninterruptible power supply applications. These are used locally for compensating critical loads required in highly sensitive applications like semiconductor chip fabrication or research and military based applications. American Superconductors have installed about 35 units of such systems after 2000 [9].

Many SMES systems has been built in Japan whose main focus was to protect the grids from voltage dips. In 2003, one liquid crystal manufacturing facility has been protected from voltage dips using a 5 MW-7 MJ SMES built in NbTi solenoidal configuration [11]. For load fluctuation compensations, a national program has been carried out in Japan where SMES systems have been built with high temperature superconducting tapes and tested a 1 MVA SMES made up with Bi-2212 1st generation tape constructed through Powder-in-Tube methodology and cooled at 4 K temperature [12].

In order to provide high quality power to synchrotron source to avoid beam loss due to voltage sags and momentary fluctuations, a 2.4 MJ SMES system has been installed at Brookhaven National Laboratory (BNL), USA [9]. SMES has protected Owens Corning's extrusion and production lines in North Carolina from voltage sags [13]. Similarly, a SMES system has protected a paper machine in South Africa, against 72 dips in 11 months [9].

Other category of SMES is among the pulse power sources where very high power is required for short durations like in magnetic forming and electromagnetic launchers. Due to higher power densities of SMES, these are used in electromagnetic launchers. SMES is a current driven device which is far better for such applications than capacitors which are usually voltage driven and thus can achieve very high efficiencies than capacitive systems. These systems can be used as railgun to launch

projectiles with a velocity of 2000 m/s and these are very useful in military applications. Also, such launchers can be employed to launch small payloads into lower earth orbital [9]. In Russia [14][15], such launching systems have been studied where pulse power SMES source using toroidal coil magnets are used.

1.6.3. Conclusions

From the earlier discussions, it has been concluded that energy storage is much needed technology to minimize power shortages or blackout challenges and SMES is one of the novel technological contender that will be going to contribute a lot in conquering such challenges. Thus, in the present work, study of SMES design has been performed where mechanical, electrical, magnetic and thermal aspects of SMES design has been addressed.

1.7. Research Gap

From the literature, it is found that there is a need for the development of large scale SMES for smart grid applications. The surges and spikes in the power generation and transmission can be balanced using the developed SMES.

- ✓ Research groups have not shared technical information among them in order to capture the global market and thus, the knowledge has not been shared properly. Also, design of 1 MJ of HT-SMES has not been identified in the literature properly.
- ✓ Effect of self-fields on the coil's critical current have been studied rarely for SMES systems. It has not been clearly found about the impact of self-fields on magnet topology.
- ✓ As varying magnetic fields are involved while charging and discharging of the magnet which can produce heat thus it becomes imperative to know the heat loads available. To our knowledge, detailed information on AC loss estimations in coils computationally has not been published.
- ✓ Design of thermal system is not studied properly till date and quenching of the superconducting tape is not well understood till date. Also, computational strategies that can be implemented for quench protection have not been found in literature.

1.8. Principle of Superconducting Magnetic Energy Storage

Superconducting Magnetic Energy Storage (SMES) systems store energy in the magnetic field when a direct current is allowing to flow through the superconducting coil which has been cryogenically cooled to a temperature below the critical temperature of the material used to form superconducting coil. The basic principal of the SMES is illustrated in the schematic drawn in Figure 1.24. Energy storage technology using superconducting coil mainly consists of a superconducting coil, power conversion unit, currents leads to transmit power and cryogenic cooling system.

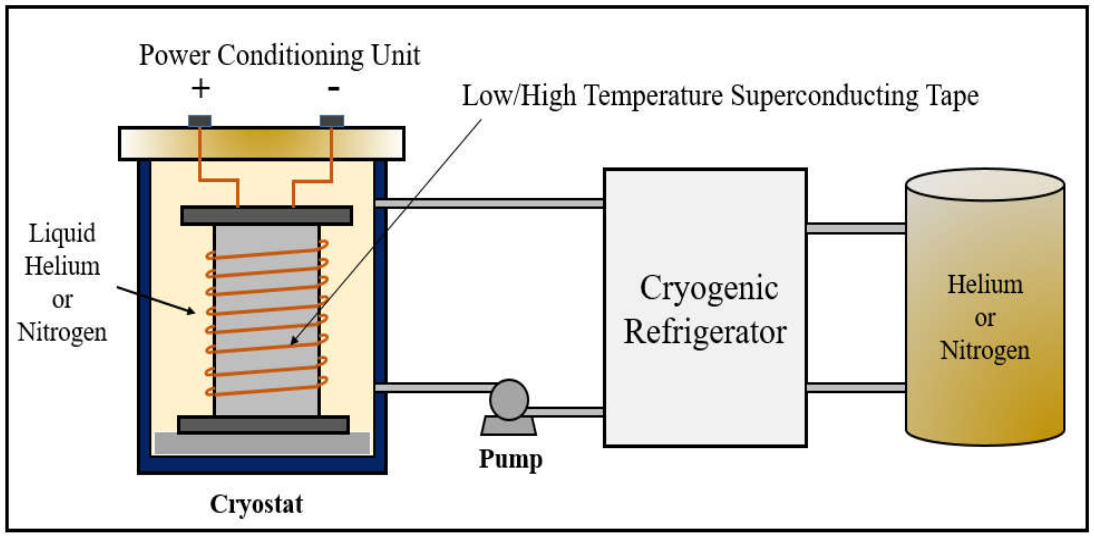

Figure 1.24 Basic Schematic of Superconducting Magnet

The energy stored inside the coil can be estimated using the same formula used for inductor given in Equation 1-1 where 'L' is inductance of the coil and 'i' is the current flowing the coil and 'B' is the magnetic field density associated with the coil due to the circulation of current.

$$\text{Energy stored within coil} = \frac{1}{2}Li^2 = \frac{1}{2\mu_0}\int_{Space}\int\int B^2 dxdydz \qquad 1.1$$

Once the superconducting coil gets charged, energy can be stored in the SMES device for longer time periods as current will not going to decay as superconductor has zero resistance. Power conversion/Conversion unit uses an inverter/rectifier to transform AC to DC or vice-versa. The losses associated with the SMES device are generally

occur during this conversion and from the literature study, it has been found that these losses limit to 2-3% in each direction.

Cryogenic refrigerator/Cryocooler is installed within the SMES unit in order to re-liquefy the boiled off cryogen. Depending upon the type of superconductor (low temperature or high temperature superconductor) used in the development of SMES; the cooling strategies are adopted.

The first step of present study is to identify the application of the SMES device. Comprehensive literature survey reveals that the device can be employed in the various energy sector applications including power grid systems, wind power energy storage, propulsion systems (Electromagnetic Launch Systems, Ship Propulsion etc.) and transmission systems (Magnetic Levitation Trains, Electric Trams, electrical aircrafts etc.).

Possible applications include load leveling, dynamic stability, transient stability, voltage stability, frequency regulation, transmission capability enhancement, power quality improvement, automatic generation control, uninterruptible power supplies, etc. as indicated in Figure 1.25. The one major advantage of the SMES coil is that it can discharge large amounts of power for a small period of time. Also, unlimited number of charging and discharging cycles can be carried out.

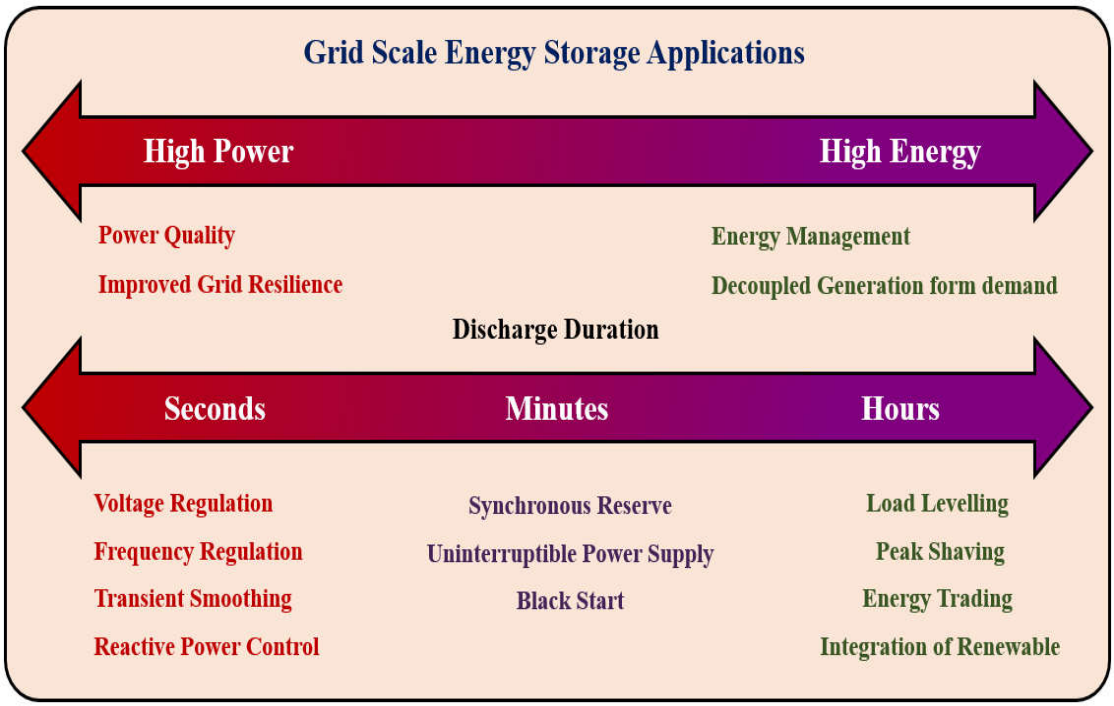

Figure 1.25 Grid Scale Energy Storage Applications

1.9. Objectives of the Present Study

Keeping the future challenges in mind, in the present work, mechanical, electrical, magnetic and thermal characteristics of the high temperature superconducting magnetic energy storage systems used in power applications have been studied. As whole SMES system design consist many sub-systems within however, in the present study attention is focused on the solenoidal magnet design parameters, self-field impacts on critical current of the HTS tape, AC losses estimation among the pancake coils to evaluate the heat load and thermal quench of the HTS tape. Therefore, the central objectives of the present proposed research work are enlisted as follows:

1. Mechanical design of 1 MJ superconducting magnet.
2. Investigation on the critical current due to self –field.
3. Estimation of AC losses to evaluate the heat load.
4. Quench analysis on the superconducting tape.

1.10. Structure of the Thesis Work

Present work is classified in 7 chapters, in chapter 1, energy crisis has been explained where it has been concluded that it is better to store energy in order to avoid blackouts

and thus heavy economic losses. Then, various energy storage technologies have been discussed on the basis of their energy density and power quality characteristics. It has been found that SMES has all the required capabilities such that it can be used for various applications as discussed earlier.

In chapter 2, the fundamental concepts on superconductivity has been explained, where discussions have been done on the principle of superconductivity along with the type of superconductors. In order to model the resistivity of superconducting, various critical state models have been explained including Bean's model and E-J power law. Mechanical, electrical and thermal properties of the coated conductors have been discussed.

Chapter 3 includes the mechanical design of the superconducting magnet where first of all criterion for the tape selection has been decided followed by the identification of design variables and constraints. Then, through design procedure for electromagnet has been discussed where numerous analytical relations have been used for the solenoidal magnet design. Then, effect of current, solenoidal thickness and operating temperature has been discussed.

In Chapter 4, effect of self-field on the critical current of the tape has been studied. Numerical scheme has been developed under some assumptions. Then, selection criteria for the critical current of the tape has been finalized. Effect of self-field on the various magnet design parameters has been discussed.

AC losses have been studied in chapter 5 where H-formulation model has been used for the AC loss evaluation. To evaluate the AC losses among the superconducting tape, various conceptual models like Norris, Brandt and H-formulations have been discussed. Certain assumptions have been made in order to minimize the geometrical complexities and computational time. Geometric modelling of homogenized domain has been performed in COMSOL MultiPhysics where AC/DC module has been incorporated to solve the partial differential equations. Effect of operating current magnitude and number of turns has been studied. In order to minimize the losses, effect of substrate layer thickness on AC losses has been studied.

In chapter 6, thermal quench analysis on the superconducting tape has been studied where effect of varying interfacial resistance on the normal zone propagation velocity has been studied.

Chapter 7 includes the overall conclusions and future scope of the present work followed by the appendix and references.

Chapter-2

Superconductivity and Theoretical Overview

This chapter is aims to present a concise preface to superconductivity along with its applications including low and high temperature superconducting systems. Further, the concepts related to the superconductors and superconducting systems have been presented. The critical state models have been studied in order to model the resistance of the high temperature superconductor. The theoretical principles and analytical techniques for modelling the electromagnetic behavior of HTS materials have been presented. Mechanical, electrical and thermal properties of the superconductors have been studied along with the applications of such tapes.

Keywords: Superconductivity, Meissner effect, high temperature superconductors, critical state models, Type-I and Type-II superconductors,

2.1. Introduction to Superconductivity

Superconductivity is an electronic phenomenon which comes into existence when a particular metal or alloy is cooled below its critical temperature and at this temperature the resistivity of the metal or alloy falls down to zero. Such materials oppose magnetic lines of forces and do not let them pass through and generates equal and opposite induced magnetic flux inside themselves. Before introducing this concept thoroughly, let us discuss about the resistivity of metal.

Two properties are directly related to the superconductivity;

i. Resistivity, which is found to approximate zero at transition temperature of the metal or alloy i.e. critical temperature,

$$\rho = finite\, at\, T > T_c \qquad and\ \rho = 0\, at\, T < T_c \qquad \Rightarrow Thermal\ Conductivity \to \infty$$

ii. At the same point of time, the magnetic susceptibility, χ, is found to change from slightly positive value (paramagnetic) to -1 i.e. perfect diamagnetism below T_c.

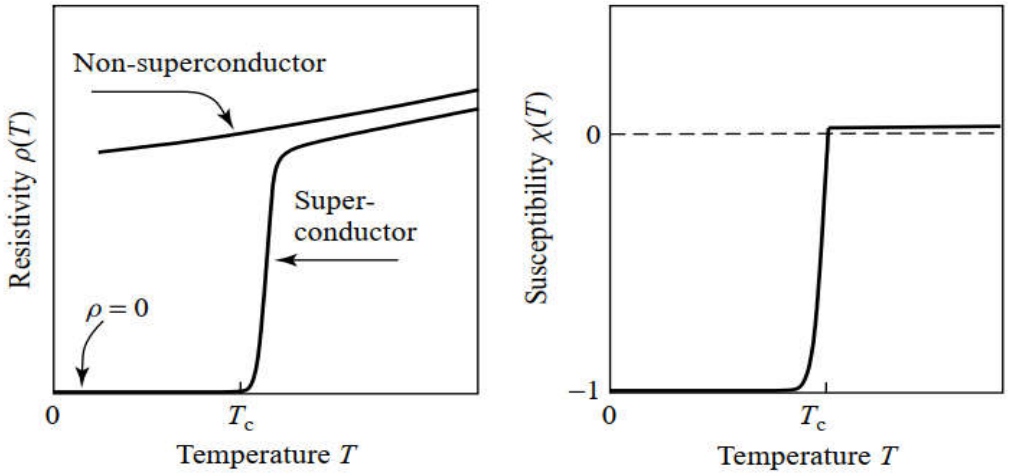

Figure 2.1 Resistivity of normal conductor and superconductor

Figure 2.1 illustrates the two basic characteristics of the superconductor where Figure 2.1 (a) describes the transition from normal phase to superconducting phase with $\rho \to 0$ and Figure 2.1 (b) defines the diamagnetic nature of the superconductor below T_c. Let us discuss the first property in this section. Figure 2.2 describes the transition temperature for Tl-Ba-Ca-Cu-O superconductor and it can be seen that at T_c, the resistivity is nearly becomes zero.

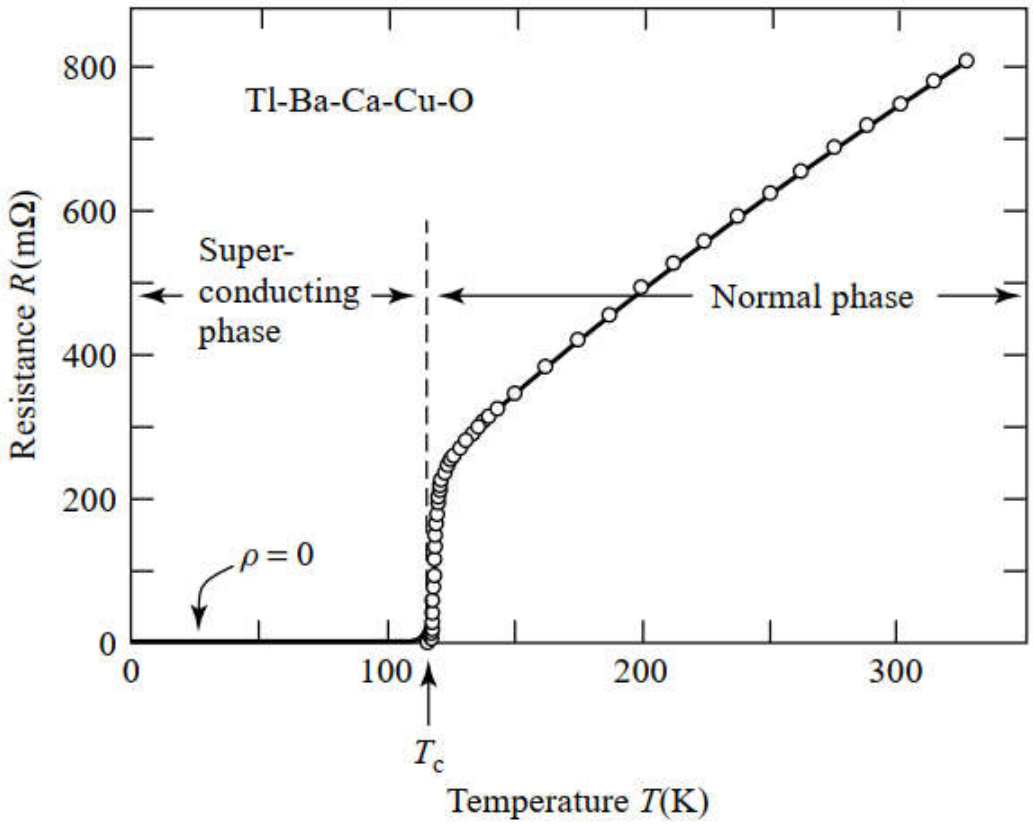

Figure 2.2 Resistance of superconductor above and below critical temperature

The conventional method to evaluate the resistance of any wire is by balancing a Wheatstone bridge where unknown resistance chosen as a sample resistance. Once it is balanced, the accuracy and precision of the measurement is as fine as that of the resistors present in the circuit or conceivably bounded by the galvanometer's zero-readout accuracy using balancing the bridge. Moreover, there is a limit on the measurement of the lower value of resistance; as zero resistance can never be measured or achievable with direct measurement. One can record the change in resistance to a certain order of magnitudes however, absolute resistance of any metal or wire can never be calculated in rea world.

If one can attempt to measure the resistance through inverse quantity i.e. conductivity $\sigma = 1/\rho$, even with this one cannot evaluate resistance or conductivity as no method is available that can measure infinite physical quantity. At the time of invention of Superconductivity, this was the only dilemma among the researchers. Even, Kamerlingh Onnes has faith on the "micro-resistance" which remains below T_c. This implies it can be concluded like $\rho \to 0$ or $\sigma \to \infty$.

In order to understand the concept and upper bound to resistivity of the material, an analysis has been performed where lower bound on decay of current has also been estimated for a closed loop coil as shown in Figure 2.3.

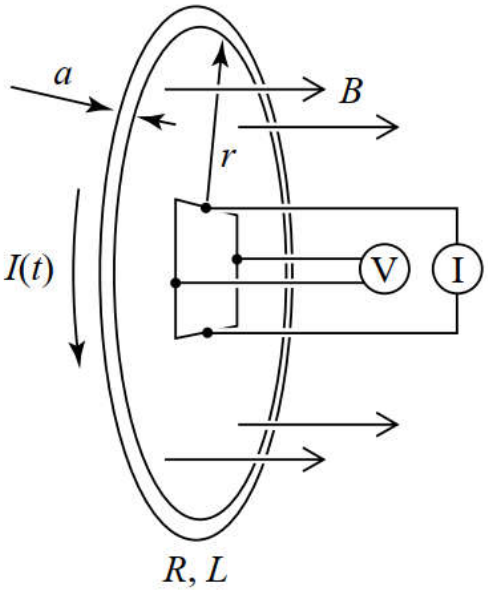

Figure 2.3 Closed loop coil

Let us assume a with diameter '*a*', loop radius '*r*', resistance '*R*', inductance '*L*' and a circulating current *I(t)*. Let us assume that a current I_0 is getting setup by induction in the superconducting closed loop coil at t=0, at a temperature below T_c. Thus, energy conservation equation for this closed loop coil can be written as:

$$\frac{d}{dt}\left(\frac{1}{2}LI^2\right)+RI^2=0 \qquad 2.1$$

Solution of above equation is:

$$I(t)=I_0e^{-(R/L)t} \qquad 2.2$$

where I_0 is the initial current at time t = 0. The decay time constant can be calculated using $I(t)=I_0e^{-(R/L)t}$. Let B be the corresponding magnetic induction which surrounds the closed loop coil and if it found to same after one year i.e. at t_1 then I (t_1= 1 year) = I (t = 0) = I_0, and similar results can be applicable for corresponding B-field. Since B-field, which is a result I (t), is measured through the instruments which further depends on the precision of the instrument. Let the resolution of the instrument to measure change in B-field is $\delta B / B_0 = 10^{-5}$, where δB is decay in B-field

corresponding decay of current δI. This implies that the measuring instruments can determine the maximum change in current *I* and field *B* and in actual situations, decay may have been lower as measured by the instrument. Thus,

$$\delta I > I_0 - I(t_1) = I_0\left(1 - e^{-(R/L)t_1}\right) \quad 2.3$$

and

$$\delta B > B_0 - B(t_1) = B_0\left(1 - e^{-(R/L)t_1}\right) \quad 2.4$$

Above expression can also be written as

$$\frac{\delta I}{I_0} = \frac{\delta B}{B_0} > 1 - e^{-(R/L)t_1} \quad 2.5$$

After solving the equation for resistance, *R*, the expression is modified to

$$R < -\frac{L}{t_1}\ln\left(1 - \frac{\delta B}{B_0}\right) = -\frac{L}{t_1}\ln\left(1 - \frac{\delta I}{I_0}\right) \quad 2.6$$

If all quantities of right side known then resistance, *R*, of the sample can be calculated.

If r >> a, then inductance formula for a single loop can be written as:

$$L \approx \mu_0 r \ln(r/a) \quad 2.7$$

Thus expression for *B*-field upper bound can be described as;

$$R < -\frac{\mu_0 r \ln(r/a)}{t_1}\ln\left(1 - \frac{\delta B}{B_0}\right) \quad 2.8$$

For a loop radius of 50 mm and wire diameter 1 mm, the resistance, $R<10^{-19}$ **Ω**, when 1 year is chosen for the observations i.e. $t_1 \approx 3\times10^7 s$. Resistivity can be calculated as;

$$\rho < R\left(\frac{A}{l}\right) \approx 2.5\times10^{-25}\,\Omega m$$

This implies it is a fairly justified in treating superconducting state as a state zero resistivity. This value of resistivity of Al below T_c drops about 10^{13} than the normal state. For $\tau = L/R$, using the aforementioned values, $\tau = L/R >$ 5.8 $\times10^{13}$ s. Thus, the lower bound on the decay time is about 2 million years. All these calculations are strongly affected by the instrument resolution and it may or may not happen that we

have over-estimated the values. Since, present work is only dealing with computational studies thus such aspects have not been taken into account.

2.2. Meissner Effect

In 1911, Kamerlingh Onnes has discovered that below T_c, the resistivity of Mercury (Hg) is approach to zero. Meissner and Ochsenfeld has found after 22 years from the discovery of Superconductivity that such materials possesses perfect diamagnetism property in the superconducting state. Meissner and Ochsenfeld observed that when a magnetic field was applied to the material (above T_c), it expelled all the magnetic lines of force (Figure 2.4) as it becomes superconductor when it was cooled below T_c. This implies that the magnetic field inside the superconductor is zero for such situations. Let us apply conservative laws for a magnetic system such that:

$$B = \mu_0 \left(H + M \right) = 0 \qquad 2.9$$

This implies that within the superconductor, $M = -H$

Thus, the magnetic susceptibility is given by

$$\chi = \frac{dM}{dH} = -1 \qquad 2.10$$

This showed that the magnetic susceptibility for a superconducting material is –ve which means the material is perfect diamagnetic. It happens due to the presence of screening currents inside the superconductor's surface. Generally, current create a field on both sides, inside and outside of the superconductor, such that the induced field cancels the effect of the externally applied field (Figure 2.4), however on outside it adds to the total field. On the other hand, for normal conductor when temperature is greater than T_c, the magnetic lines of force or Faraday lines would pass straight through the metal. Near the equator, highest flux density can be found as magnetic lines are being expelled by the superconductor. Also, low flux zone can be found near poles compared to the normal conductor.

A superconductor can be characterized by its critical temperature, critical magnetic field and critical current density. These three components define the upper limits for the superconductivity in any material and represents the state of a superconductor for a given set of conditions as shown in Figure 2.5.

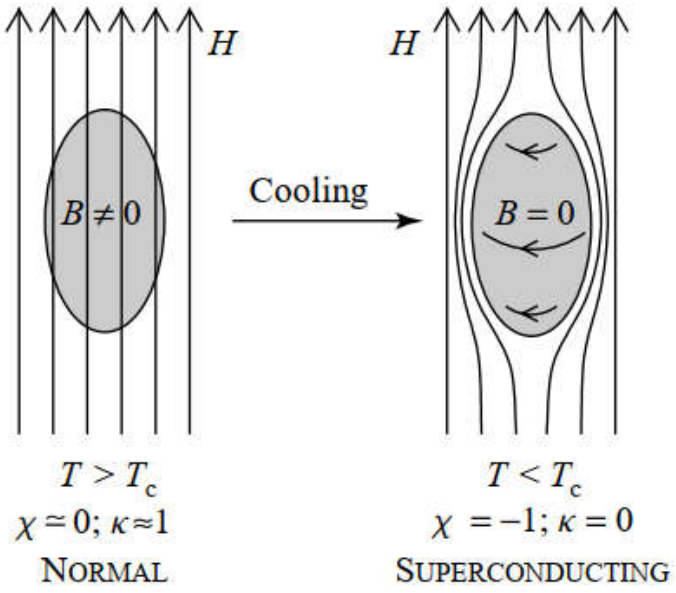

Figure 2.4 Process of Meissner effect

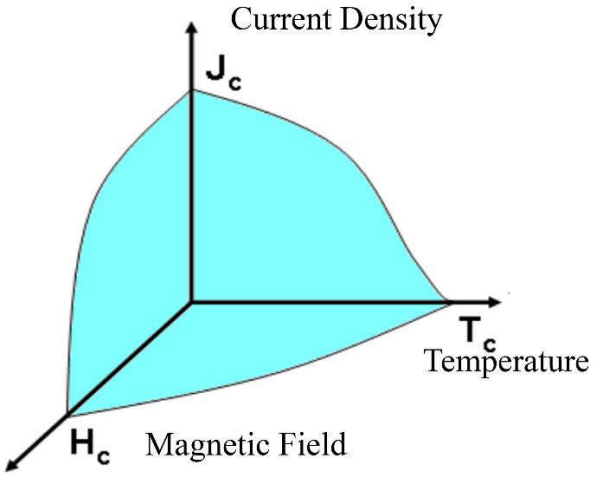

Figure 2.5 Characteristic curve of superconductor

2.3. Type-I and Type-II Superconductors

The superconductors are broadly classified into two categories namely; Type-I and type-II superconductors. This classification is based on the fact that how the resistivity of the superconducting material is going to behave in the presence of magnetic field. Any superconductor that has a tendency to have zero resistivity below the critical magnetic field (H_c), are characterized as Type-I superconductors. Moreover, if the field exceeds critical magnetic field, the superconducting nature of the material is abruptly destroyed by a first order phase transition. There is only one

upper bound is available for the Type-I superconductors and beyond this bound the superconductor changes to normal conductor.

However, for type-II superconductors, two critical magnetic field bounds (H_{c1} and H_{c2}) are there. The magnetic flux starts penetrating the superconducting material when magnetic field exceeds the lower critical field, H_{c1}, without disturbing the superconductivity of the bulk material. With the increase in the magnetic field, more magnetic flux lines start penetrating the superconductor until the normal state is reached at the upper critical field (H_{c2}), as shown in Figure 2.6 and Figure 2.7. Figure 2.7 represents the variation among critical field as a function of temperature. Figure 2.7 (a) represents Type-I superconductors and Figure 2.7 (b) represents Type-II superconductors thus the later has larger area under the curve which indicates such superconductors can holds superconductivity in the presence of larger fields than Type-I superconductors.

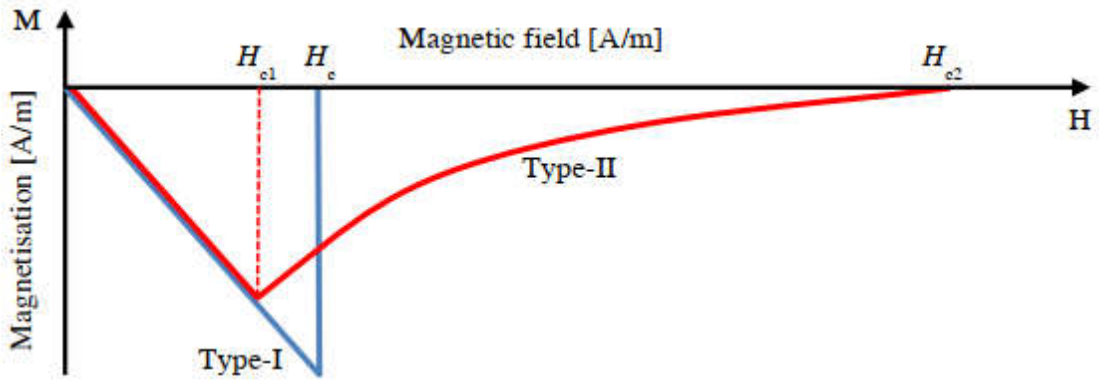

Figure 2.6 Magnetization curve for Type-I and Type-II superconductors

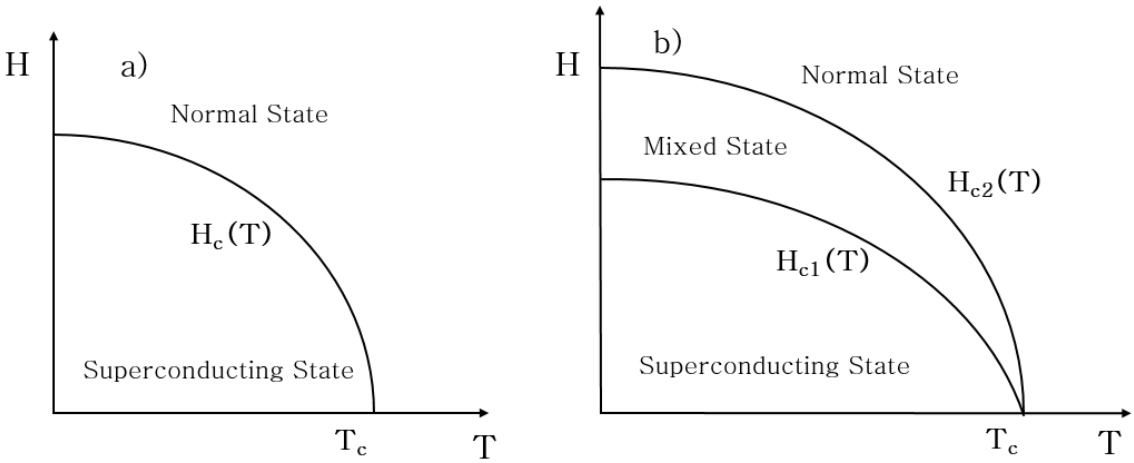

Figure 2.7 Critical magnetic field vs temperature

All low temperature superconductors (LTS) exhibit the properties of Type-I superconductors which are generally pure metals. However, all high temperature superconductors' (HTS) falls under type-II superconductors those are further divided into 1st generation and 2nd generation superconductors. The detailed information on superconductors is given in the upcoming sub-sections in this chapter.

It has been found that for type-I superconductors, the critical current density ($\mu_0 H_c$) is usually less than 1 Tesla even near the 0 K temperature and due to this reason these are less used for the practical applications. Whereas for type-II superconductors, the upper critical fields generally much higher which leads to high energy densities in case of superconducting magnetic energy storage systems and capable of producing large fields magnet.

2.3.1. Flux Vortices in Type-II Superconductors

In case of type-II superconductors, the magnetic flux starts penetrating the surface of the superconductor when the magnetic field exceeds lower critical fields (H_{c1}) in discrete flux fluxons/quanta whose value can be calculated as

$$\phi_0 = \frac{h}{2e} \approx 2.07 \times 10^{-15}\, Wb$$

A cylindrical shaped vortex or fluxon can penetrate the superconductor whose axis is usually parallel to the applied field. The vortex/fluxon radius is related with a parameter coherence length ξ which was introduced in the Landau-Ginzburg theory [16]. Generally, the fluxon core is not superconducting though the neighbouring material has superconducting nature. The model has been designed in such a way that the magnetic field should decay within the superconductor with a characteristic length of λ. Figure 2.8 illustrates the isolated flux lines, flux density distribution *B(r)* and Cooper pair's density *n(r)*. The decay can be achieved through circulating current around each fluxon (Figure 2.8). Abrikosov [17] firstly estimated from Landau-Ginzburg equations the outcomes of that the flux lines form a regular hexagonal lattice due to the presence of mutual repulsion in pure or defect free superconductors. A Lorentz force (F_L) per unit volume has been experienced by flux lines when a current is passed through the superconductor.

$$\kappa = \frac{\lambda}{\xi} > \frac{1}{\sqrt{2}} \qquad 2.11$$

$$\kappa < \frac{1}{\sqrt{2}} \Rightarrow Type - I\ Superconductor$$

$$\kappa > \frac{1}{\sqrt{2}} \Rightarrow Type - II\ Superconductor$$

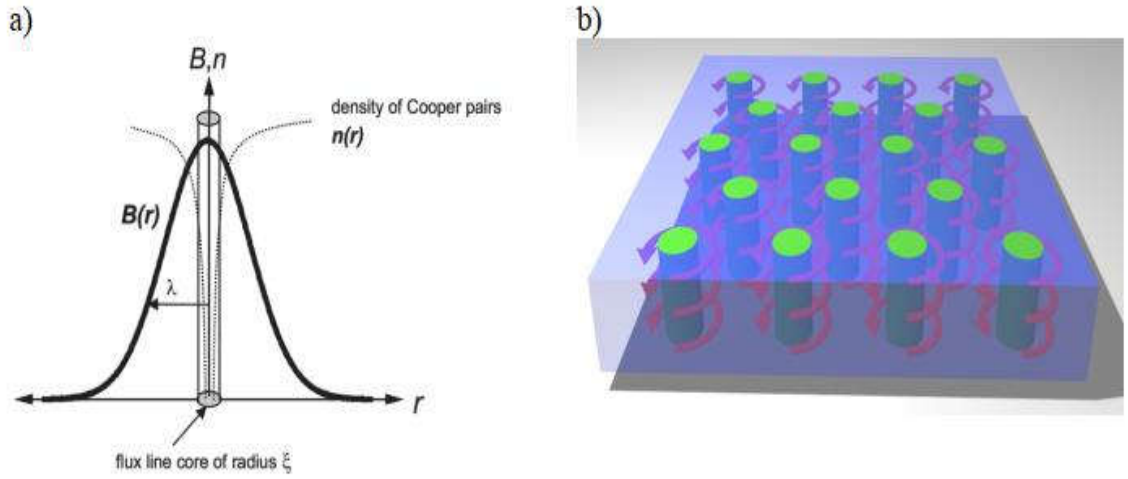

Figure 2.8 (a) Isolated flux line [18], Flux line lattice (green) in Type-II superconductors shielded by circulating currents

$$\mathbf{F}_L = \mathbf{J} \times \mathbf{n}\phi_0 = \mathbf{J} \times \mathbf{B} \qquad 2.12$$

where '*n*' is the flux line density. The changing magnetic flux can produce electric field whose direction is same as that of transport current, which results in to heat dissipation *Q* without changing superconductor into normal state and that can be calculated using following equations:

$$\nabla \times \boldsymbol{E} = -\frac{d\boldsymbol{B}}{dt} \qquad 2.13$$

$$\boldsymbol{Q} = \boldsymbol{E}.\boldsymbol{J} \qquad 2.14$$

This implies that at a field above the H_{c1}, the superconductors with defect free crystals cannot transport a current without heat dissipation. However, due to the presence of defects, flux lines can be pinned in the crystal lattice. Figure 2.9 illustrated that in order to minimize free energy, the flux lines preferentially fix up themselves on pre-existing defects. Therefore, this implies that flux pinning plays essential role in getting current transport with zero loss above lower critical field bound which the

basic assumption of Bean's critical state model as explained later in this chapter (Section 2.4.1, Page-46).

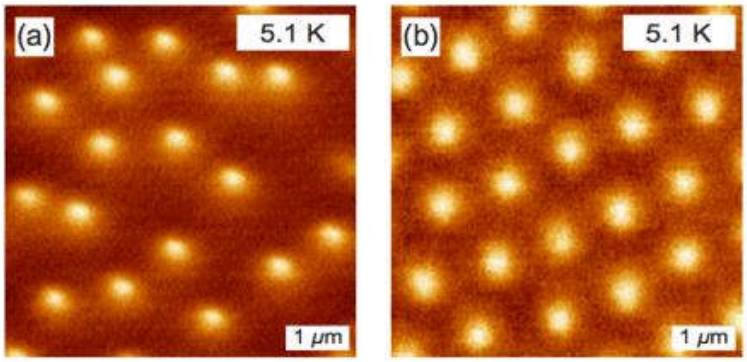

Figure 2.9 (a) Magnetic force microscopy image of flux lines in a neutron irradiated sample, (b) defect free BSCCO sample showing hexagonal arrangement

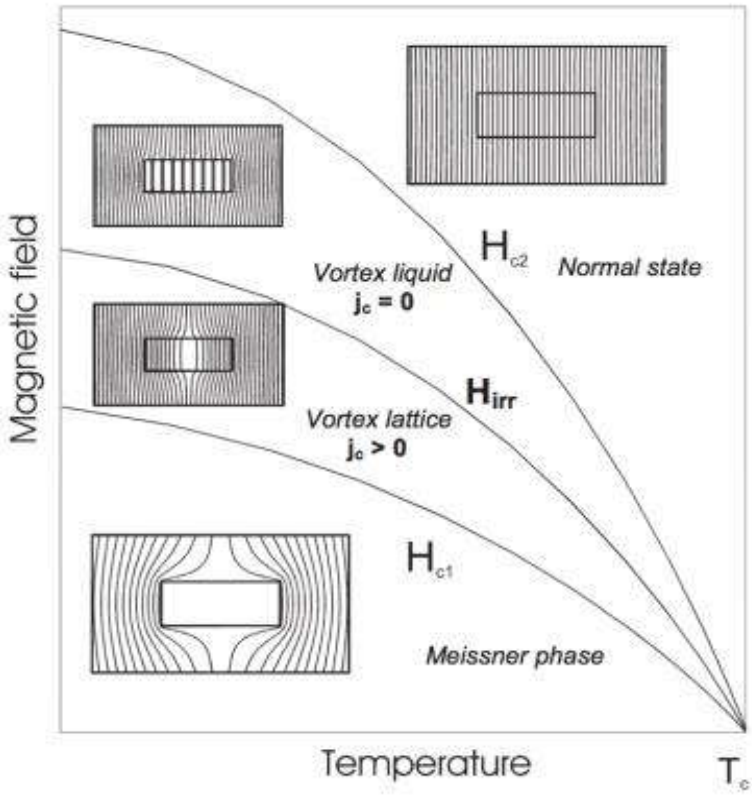

Figure 2.10 Magnetic phase diagram of Type-II superconductor [18].

The pinned flux lines are said to be in a vortex glass phase when pinning force f_p is lower than the Lorentz force F_L. A situation may arise when f_p is more than F_L due to the increase in magnetic field and as a result superconductor no longer can hold a current transport without losses. This magnetic field bound is known as irreversibility

field H_{irr} such that $H_{c1} < H_{irr} < H_{c2}$. This implies above this field the flux lines are free to move thus altering from vortex glass to vortex fluid (Figure 2.10). Therefore, it concludes that H_{irr} is the limiting factor for the practical applications instead of H_{c2}.

2.4. Critical State Models

High temperature superconductors are coming under type-II category of superconducting materials and thus magnetic flux enters type-II superconductor in the form of vortices (discrete fluxons). In order to shield the fluxons from superconducting matrix, usually Cooper pairs flow around it. It has been found that such fluxons penetrate through the sample from the edges of the material. As discussed earlier, the pinning sites like lattice defects, grain boundaries, non-superconducting precipitates and dislocations hindered the fluxons inward motion [19]. These pinning sites actually assist to trap the magnetic field within type-II superconductor otherwise the magnetization of such superconductors would be reversible in the absence of pinning sites and no magnetic field would be trapped inside superconductor. Interaction forces among the fluxons from the pinning sites would result in magnetic flux trapping and the force is given by Lorentz force. If pinning force is lesser than the Lorentz force only then the fluxon can pass the pinning site otherwise it remains locked. In order to predict this interactional behaviour of fluxons, generally Critical State Model (CSM) is often used which predicts the different operating modes for different operating conditions. As discussed in the previous section as magnetic field increases, the flux lines are starting penetrating the superconducting sample and they experience a force on them as a result flux lines reorganize themselves until f_p balances F_L. If Ampere's Law and Lorentz force equations combined, then;

$$\mathbf{F}_{\mathrm{L}} = \mathbf{J} \times \mathbf{n}\phi_0 = \mathbf{J} \times \mathbf{B} \qquad 2.15$$

$$\nabla \times \mathbf{B} = \mu_0 \mathbf{J} \qquad 2.16$$

$$\mathbf{F}_{\mathrm{L}} = \mathbf{J} \times \mathbf{B} = \frac{1}{\mu_0}\left(\nabla \times \mathbf{B}\right) \times \mathbf{B} = \mathbf{f}_{\mathrm{p}} \qquad 2.17$$

For instance, if applied field is in *z*-direction and the current transport is in *y*-direction such that

$$\frac{\partial B_z}{\partial x} = -\mu_0 J_y \qquad 2.18$$

$$f_p = J_y B = -\frac{1}{\mu_0}\frac{\partial B_z}{\partial x} B \qquad 2.19$$

This implies that the maximum current that can be transported through the superconductor for a known pinning force f_p with zero loss is called the critical current density J_c. This means;

$$\frac{\partial B_z}{\partial x} = -\mu_0 J_c \text{, } within\ regions\ penetrated\ by\ magnetic\ field$$

$$\frac{\partial B_z}{\partial x} = 0 \text{, } for\ no\ magnetic\ field$$

CSMs are worked on the macroscopic behavior of superconducting materials, resulting from experimental findings of the association among magnetic field and current density. In such models, the superficial layer is assumed to be in "critical state" for low applied magnetic field /or current. The critical state exists when the applied magnetic field surpasses the type-II superconductor's lower critical magnetic field H_{c1}. Magnetic flux fluxons/vortices with circulating supercritical screening currents pierce the material to shield the interior of the material from applied field/current. In the crystal lattice of the superconducting material, vortices are generally pinned at the defects locations and the applied current/field decides the depth of penetration. In order to trap the magnetic field within the superconductor, these defects are deliberately initiated inside superconducting domains e. g secondary phase Y211 in YBCO tape.

For normal conductors, electric field and current density are related by Ohm's law, however for superconductors, different expressions have been proposed in literature. For type-II superconductors, Bean's studies of ferromagnetic materials come up with classical CSM that successfully relate the critical current density (J_c) with electric field. This model is significant in two ways: as domain-like structure implemented for current density that can be resumed for modified models thus allow J_c to depend on magnetic field, and it has been found that it simplify the loss estimation. For type-II superconductors, CSM model is employed to evaluate J_c from magnetic hysteresis

curves as it results in appropriate solutions for simple problems and even for those where J_c is a function of magnetic field [20].

The Maxwell's equations (displacement term omitted) used to solve CSM model is as follows:

$$\nabla \times \mathbf{H} = \mathbf{J} \qquad 2.20$$

$$\nabla \times \mathbf{E} = -\frac{\mathrm{d}\mathbf{B}}{\mathrm{dt}} \qquad 2.21$$

where $\mathbf{B} = \mu_o \mathbf{H}$, this is found to be an excellent approximation for realistic problems where $H_{c1} < \boldsymbol{H} < H_{c2}$, and $\nabla.\mathbf{J} = 0$ which implies there is no time dependent free charge allotments. A Lorentz force of $\mathbf{F} = \mathbf{J} \times \mathbf{B}$ is experienced by the magnetic field vortices if a current is flowing through superconductor. The vortices become de-pinned if large Lorentz forces appear and they start moving in the direction of force with a velocity $\boldsymbol{v}$. Due to this vortex motion, induced electric field is generated, $\mathbf{E} = \mathbf{B} \times \mathbf{v}$, and **E** is parallel to $\mathbf{B} \times (\mathbf{J} \times \mathbf{B})$. If **B** is perpendicular to **J**, which is always true for 2D models, then **E** is parallel to **J**. Thus,

$$\mathbf{E} = \rho(\mathrm{J})\,\mathbf{J}$$

where $\rho(\mathrm{J})$ is the resistivity function depends upon current density **J** and highly non-linear in nature and $\mathrm{J} = |\mathbf{J}|$. The equation above is similar to the Ohm's law for normal conductor except in this equation resistivity is a non-linear function of **J**. All critical state models are stated that the current density in the superconductor should not exceed critical current density.

2.4.1. Bean Model

It is the simplest model among available all CSMs and it states that the current density magnitude for a superconductor is either '0' or 'J_c' which is critical current density. It assumes a non-vanishing electric field with current density in the direction of the electric field. Moreover, it also assumes that the current density is equal to zero in the regimes within the superconductor which have never experienced an electric field. The model describes that the superconductor is considered to be in critical state when entire superconductor is penetrated with $\pm \mathrm{J_c}$.

The field starts penetrating the boundary of superconductor when an external field is applied on it. The value of J_c and external field decides the penetration depth. According to the Bean's model, external field can penetrate through superconductor in the form of moving vortices without vortex or fluxon pinning and in this situation critical current density, J_c is zero. A gradient of vortex density is preserved by the pinning using vortex pinning and resulted gradient density is defining by J_c. This implies Bean's model consists following assumptions:

1. The electric field **E** is parallel to the current density **J**.
2. The superconductor is considered to be in critical state when $\pm J_c$ flows through it.

$$J(x) = \pm J_c \quad \text{if } |E(x)| \neq 0$$
$$J(x) = 0 \quad \text{if } |E(x)| = 0$$

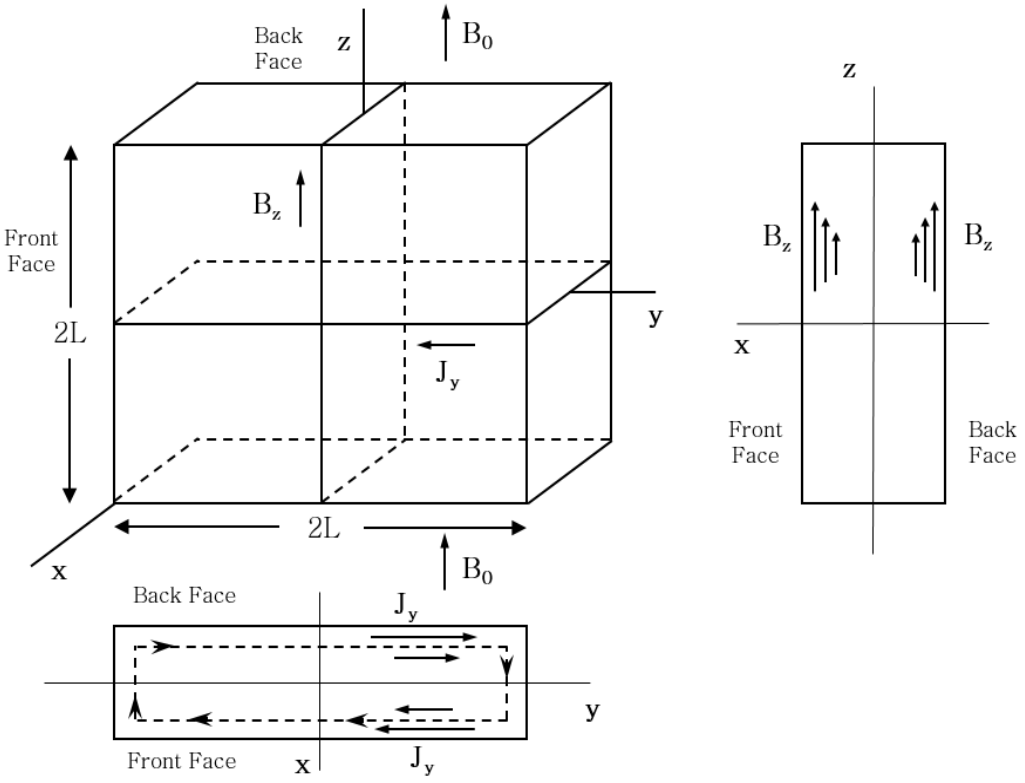

Figure 2.11 Superconducting slab in externally applied field

If AC current is flowing through the superconductor, then the current distribution at the peak AC current is same as that of occurs for DC current. When the shielding current produced by the transport current or external field, is large enough then the

current ‘sheath’ reaches the centre of the superconductor and it is called as ‘full penetration’. Losses depend on the direction of applied fields and the values above and below full penetration.

For example, an external field is applied on a superconducting slab having a thickness ‘2*L*’ as shown in Figure 2.11. The slab is orientated in *y*-*z* plane where an external magnetic field B_0 has been applied in *z*-direction. Inside back and front faces, the induced shielding current density, J_y flows in *y*-direction.

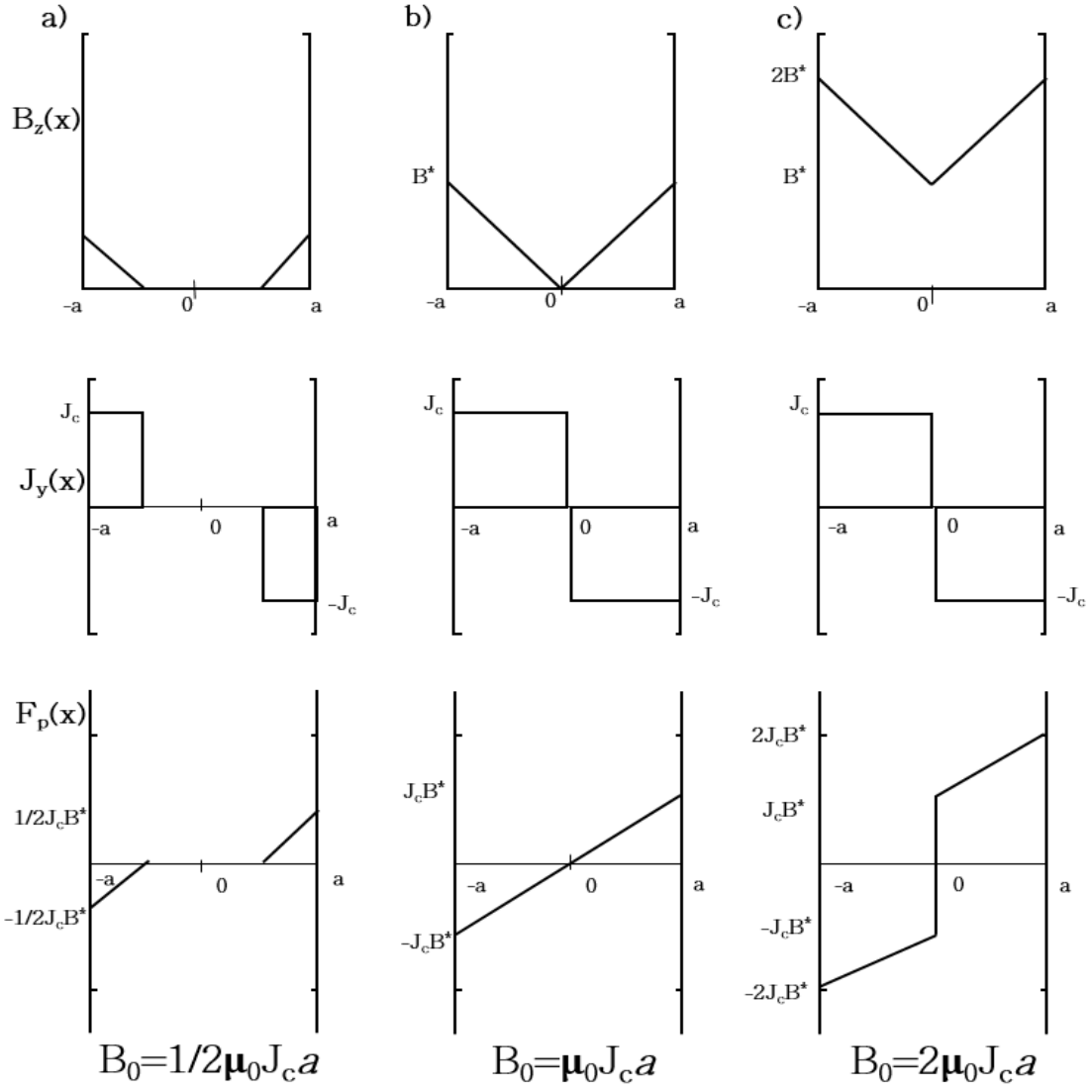

Figure 2.12 Dependence of the internal magnetic field B_z(x), current density J_y(x), and pinning force *Fp*(x) on strength of applied magnetic field B_0 for normalized applied fields.

The corresponding Bean's model for this case for different conditions is represented in Figure 2.12. From Figure 2.12, B^* is the full-penetration field and for a wire of radius '*a*' it is given by $B^* = \mu_0 J_c a$. this model can be applied to transport current, and for both transport current and magnetic field and the individual results for transport current and screening current can be superposed. Kim [21] and Anderson [22] have proposed a modified model where the dependency of critical current density on local magnetic field has been considered. In the upcoming sections, these models are discussed in detail.

2.4.2. Superconducting Strip Model

Brandt [23][24] has realised that Bean's model was only appropriate to long length superconductors in parallel field where demagnetization effects were insignificant, nearly all realistic researches used flat superconductors in a perpendicular field, for which demagnetizing effects are critical. Brandt done analysis on superconducting strips in the presence of perpendicular magnetic fields and/or transport currents and brief results are presented below. For coated conductors, superconducting strip is a fine estimation for the superconducting layer. Results obtained from this analysis are generally used to compare the results of finite element models and these are explained later in this chapter.

For a magnetic field perpendicular to tape width with magnitude H_0, Brandt illustrates that the flux penetrates from the edges of the tape having width *'2a'* (x-axis) and thickness *'d'* (y-axis) such that

$$J(x) = \frac{2J_c}{\pi}\arctan\left(\sqrt{\frac{a^2-b^2}{b^2-x^2}}\left(\frac{x}{a}\right)\right) \qquad \text{for } |x| < b$$

$$= J_c d \qquad \text{for } b < |x| < a$$

$$b = \frac{a}{\cosh\left(\frac{\pi H_0}{J_c d}\right)}$$

where *'b'* is penetration depth and the magnetic field strength along the tape can be calculated from the following relation, where H_c is the characteristic field.

$$H(x) = 0 \qquad \text{for } |x| < b$$

$$= H_c \arctan\left(\sqrt{\frac{x^2-b^2}{a^2-b^2}}\left(\frac{a}{|x|}\right)\right) \qquad \text{for } b<|x|<a$$

and $$H_c = \frac{J_c d}{\pi}$$

The results obtained are found to significantly different from that of Bean's model for slab where magnetic flux penetration is linear while for superconducting strip, the flux penetration is quadratic. Moreover, the penetrating flux front has a vertical slope for superconducting strip; however, for Bean model it is constant and finite. When a critical state with $J = J_c$ has established near the edges of the strip and the flux has somewhat penetrated, then the current flow is over the entire width of the strip to shield the central flux-free region, however in the Bean's model the flux-free region is current free. When a critical state with $J = J_c$ has achieved, the screening current density is a continuous function with a vertical slope at the flux front, however for Bean's model it is a piecewise constant function.

Current density for a transport current I_0 is given by

$$J(x) = \frac{2J_c d}{\pi}\arctan\left(\sqrt{\frac{a^2-b^2}{b^2-x^2}}\right) \qquad \text{for } |x| < b$$

$$= J_c d \qquad \text{for } b< |x| < a$$

where I_0 and penetration depth (b) is given by

$$I_0 = 2J_c d\sqrt{a^2-b^2}$$

$$b = a\sqrt{1-\left(\frac{I_0}{I_c}\right)^2}$$

Critical current, $I_c = 2aJ_cd$ and Magnetic field strength along the tape is given by

$$H(x) = 0 \qquad \text{for } |x| < b$$

$$= \frac{H_c x}{|x|}\operatorname{arctanh}\left(\sqrt{\frac{x^2-b^2}{a^2-b^2}}\right) \qquad \text{for } b< |x| < a$$

where H_c is the characteristic field, $H_c = \frac{J_c d}{\pi}$, AC loss calculations will be discussed in the coming sections on AC loss.

2.4.3. E-J Power Law

A step liaison among the electric field and current density in a superconductor assumed by Bean's model, based on the known well-defined values J_c as a function of magnetic field. Bean's critical state model works very well for to low temperature superconductors and somewhat to high temperature superconductors too [25]. However, there are few HTS materials where critical current is ill-defined. A flux creep theory has been proposed by Anderson [22], which illustrate that the association among current density and electric field is not discontinuous. This theory tells that due to thermal activation, flux moves slowly at currents lower than the critical value which results losses as an electric field appears. A non-linear relationship proposed by Rhyner [25] known as E-J power law;

$$E = E_0 \left(\frac{J}{J_0} \right)^n \qquad 2.22$$

where n is the index of the relationship and its magnitude is dependent on the material properties and microstructure. Rhyner [25] found that this non-linear relationship fits well with the *I-V* experimental findings for DC input and for most of the HTS materials. For the extreme values of '*n*', we have [26],

$$\text{if } n = 1, \text{ then } E = \rho J \rightarrow \text{Ohm's Law}$$
$$\text{if } n = \infty, \text{ then } J \text{ is either zero or } J_c \rightarrow \text{Bean's Model}$$

$$\text{if } n = 5, \rightarrow \text{Strong Flux Creep}$$
$$\text{if } n = 15, \rightarrow \text{Weak Flux Creep}$$
$$\text{if } n = 50, \rightarrow \text{Limiting Value between HTS and LTS values}$$

For $n > 20$, it turns out to be a fine approximation of Bean's CSM model. Figure 2.13 shows the *n*-value variations from Ohm's law ($n=1$) to Bean's model ($n=\infty$).

2.4.4. Kim Model (magnetic field dependency of J_c)

The internal factors like type of material concentrations of defects, twinning, and granularity and so on will decide the magnitude of the critical current density for a particular superconductor. As we know, critical current density is a function of

temperature and magnetic field. It has been found that *I-V* characteristics of few type-II superconductors are strongly depends upon strain that may arise due to twisting or bending of the superconductor for example in case of HTS cables, motor/generator coils and so on. therefore the factor like magnetic field temperature and strain *'r'* important while modelling superconductors handset factors and such factors are referred as external factors in order to get the better performance material scientist are trying their best to optimize internal factors whilst peoples from engineering background are trying to optimize external factors in this dissertation magnetic field dependency of critical current density has been considered by assuming temperature of the coil as constant that is the rate at which heat is generated due to losses is exactly balanced by the rate at which heat is rejecting from the system. It has also been assumed that the superconductor does not quenched for the applied current and its properties are not affected due to strain.

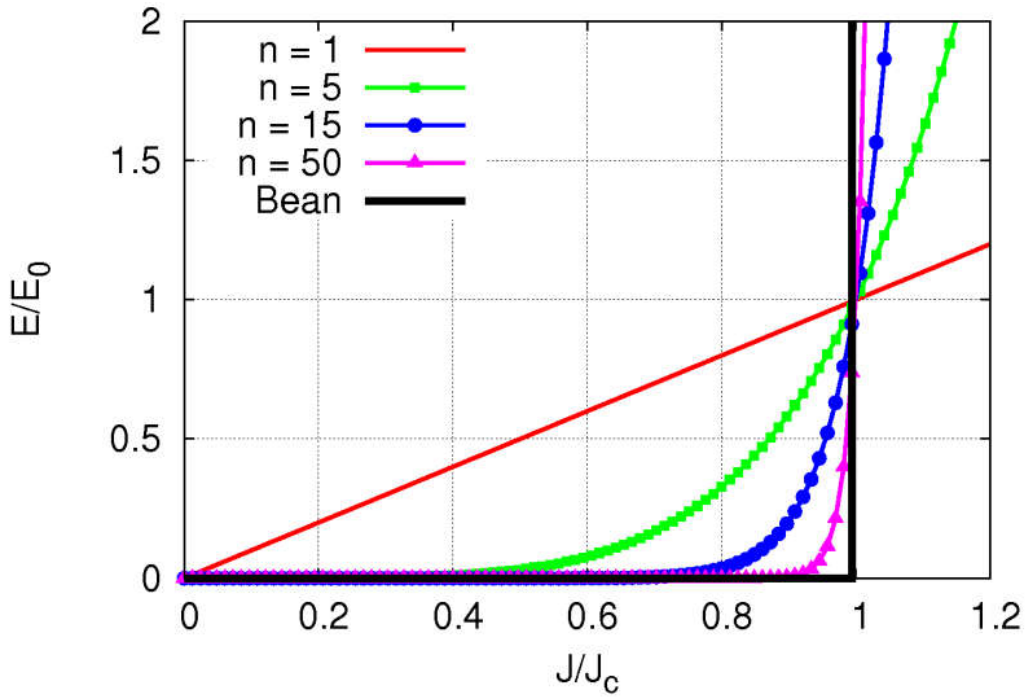

Figure 2.13 Power law model representation

Kim [21] and Anderson [22] found that for type-II superconductors critical current density has strong dependency on field and temperature. The empirical relation is given by

$$J_c(B) = \frac{\alpha(T)}{B_0 + B} = \frac{J_{c0}(T)}{1 + \frac{B}{B_0}} \qquad 2.23$$

$$J_{c0} = \frac{\alpha(T)}{B_0} \qquad \alpha = \frac{1}{d}(a\text{-}bT)\,, \qquad \frac{a}{b} \le T_c$$

where B0 is a constant and its magnitude depends upon the material used and d is significantly affected by the microstructure of the material. The magnetic field dependency of '*n*' and critical current density is given by [27],

$$J_c(B) = \frac{J_{c0}}{1 + \frac{|B_y|}{B_0}} \qquad 2.24$$

$$n(B) = \frac{n_{c0}}{1 + \frac{|B_y|}{B_0}} \qquad 2.25$$

where B_y is the *y*-component of magnetic field as this component contributes to AC losses more than the parallel/transverse component [28]. J_{c0} and n_{c0} are the critical current density and power index in self-field implies in the absence of applied magnetic field. B_0 can be calculated from I_c-B_{DC} experimental curve. HTS electromagnetic behavior can be modelled accurately with this formulation particularly for the models in which both magnetic field and applied current exist. Kim model [29][30] can be extended to simulate the electromagnetic behavior of high temperature superconductor where critical current density is significantly depending on parallel and perpendicular magnetic field components.

$$J_c\left(|B_x|, |B_y|\right) = \frac{J_{c0}}{1 + \frac{\sqrt{k^2 |B_x|^2 + |B_y|^2}}{B_0}} \qquad 2.26$$

This model has been extended recently [31][32] where angular and field dependency has also been considered two models are electromagnetic behavior of superconducting tape. In this dissertation, only the dependency of perpendicular magnetic field component has been considered and angular variations of critical current density are not taking into account.

2.5. Technical details of low and high temperature superconductors

2.5.1. NbTi, Nb_3Sn

NbTi is one of the widely used superconductors for various high field magnetic applications such as magnetic resonance imaging (MRI) magnets and particle accelerators Large Hadron Collider (LHC) [33]. NbTi is an alloy of Niobium and Titanium, where it is used as fibres in copper matrix. The critical temperature for this superconductor is 9.2 K and the upper critical field is ~ 15 T. Its superconducting nature was confirmed in year 1962 and due to the easy manufacturing it is well known as the workhorse of the superconducting magnet industry.

Nb_3Sn is an alloy of Niobium (Nb) and Tin (Sn) and it has a critical temperature of 18.3 K which is quite higher than NbTi. The upper critical field for Nb_3Sn is ~30 T which is twice as that of NbTi. The magnets are needed to be wound with insulating materials to avoid reaction with precursor materials as Nb_3Sn is a brittle inter-metallic compound and also it is more expensive than NbTi. Due to high upper critical fields such superconductors are used in high magnetic field applications like fusion plasma confinement in International Thermonuclear Experimental Reactor (ITER) and Nuclear Magnetic Resonance (NMR). Generally, Powder-in-Tube (PiT) manufacturing is used to develop such superconductors [34]. The major challenge in using such low temperature superconductors is that they have to be cooled around liquid helium temperatures that make the operation relatively expensive.

2.5.2. MgB_2

Akimitsu et al. [35] have confirmed the superconducting nature of magnesium diboride in 2001; however, the compound was synthesized in 1953. Critical temperature of this superconductor is ~39 K astonishingly high for a binary compound. The merits of MgB_2 superconductors are notable due to following reasons: MgB_2 is more isotropic than 1st and 2nd Generation superconductors with longer coherence length that eliminates the requirement of textured materials and the precursor materials are cheap and widely available. The other advantage with such superconductors is that they can be manufactured through various processes like wires using PiT techniques [36], Magnesium diffusion method [37] or infiltration to

produce bulk samples having arbitrary shapes. As the critical temperature is quite higher this implies liquid hydrogen (20.3 K) can also be employed along with the helium cooled commercial cryocoolers for the cooling of such superconductors. A comprehensive review on the properties and fabrication methods of MgB_2 can be searched from article by Buzea et al. [38].

2.5.3. Bismuth Strontium Calcium Copper Oxide (BSCCO)

Bismuth Strontium Calcium Copper (BSCCO) is a category of cuprate superconducting compounds having two compounds; BSCCO-2212 and BSCCO-2223. The general formula for such compounds is $Bi_2Sr_2Ca_{n-1}Cu_nO_{2n+4+x}$. The critical temperature is found to increase with '*n*' [39];

$$For$$
$$n = 2 \Rightarrow Bi2212 \rightarrow T_c = 93\,K$$
$$n = 3 \Rightarrow Bi2223 \rightarrow T_c = 108\,K$$

It has been found that both critical temperature and irreversibility field line are significantly depending upon oxygen content for BSCCO superconductors. Also, the coherence length is found to small (of the order 1.6 nm in *ab* plane at 0 K) for these superconductors which results in grain alignment to permit the route of supercurrents. However, the critical temperature of BSCCO superconductors is high; they are infrequently employed at temperatures more than 77 K since the irreversibility field line is low due to the decoupling of the flux lines [40]. Figure 2.14 illustrates the different pinning situations where (a) indicates negligible pinning as vortices are forming hexagonal lattice, (b) illustrates strong pinning as vortices are separated into pancakes which are further joined through Josephson vortices between layers, and (c) shows strong pinning with small anisotropy unlike case (b) where anisotropy is higher, here vortices are forming distorted lattice in order to accommodate the bulk pinning sites they bend slightly. Due to this, 2nd generation (RE)BCO coated conductors are prominently preferred over BSCCO tapes as the former show better performance at high magnetic fields and temperatures.

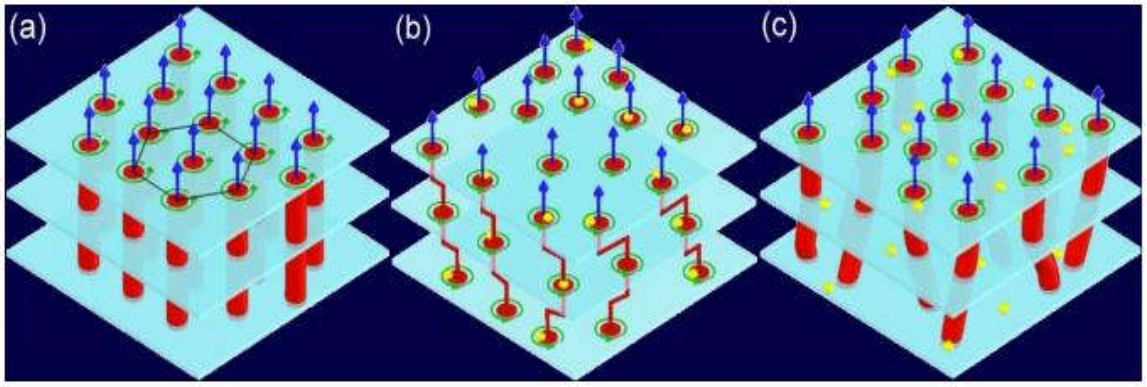

Figure 2.14 Possible flux pinning situations

2.5.4. (RE)BCO coated conductor

$(RE)Ba_2Cu_3O_{7-\delta}$ are the ceramic compounds where (RE) signifies the rare-earth elements, having perovskite structures and exhibits superconductivity at relatively high temperatures. The most extensively studied and manufactured compound of (RE)BCO family is YBCO, Yttrium Barium Copper Oxide or Y123 or RE123.

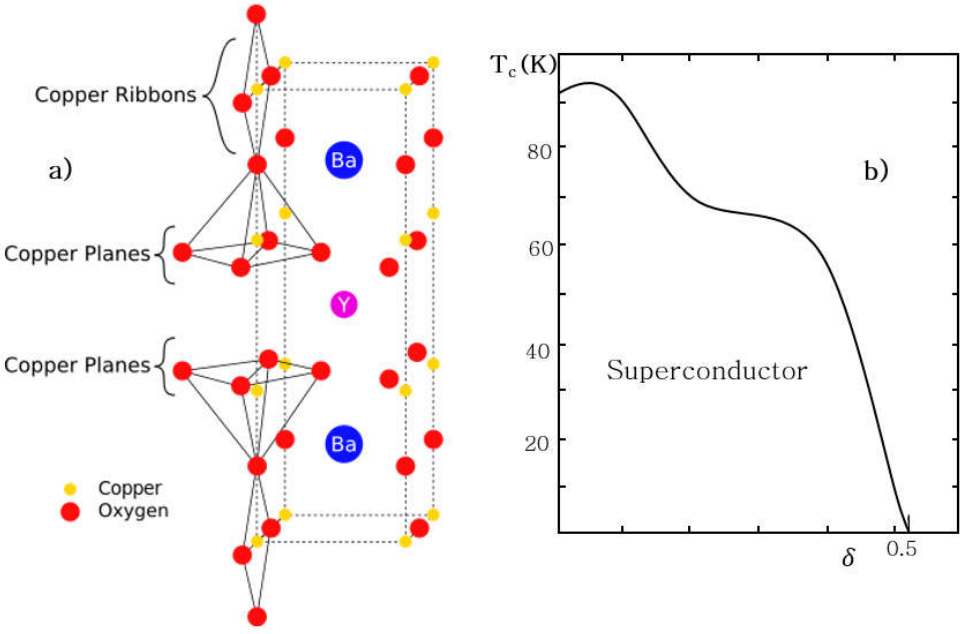

Figure 2.15 (a) YBCO (Y123)-Orthorhombic unit cell (b) Transition temperature of YBCO for different oxygen content

It has a critical temperature of 92 K, thus can be cooled using liquid nitrogen (77 K). The structural details of the Y123 unit cell are given in Figure 2.15. It can be seen from the Figure 2.15 that the crystal structure is exceedingly anisotropic as the majority of the current transport is allied with Cu-O planes this implies that the

critical current is found to higher in crystallographic *ab* plane than *c* direction. Coherence length is also a measure of the anisotropy and for YCBO crystal structures, it is about 2nm in *ab* plane and 0.4nm in *c* plane at 0 K temperatures [18]. The ratio $\Gamma = \xi_{ab} / \xi_c$ is known as anisotropy parameter. The properties of the Y123 vary significantly with oxygen stoichiometry. It has been seen that for $\delta > 0.6$, it shows semiconducting behavior at low temperatures whereas at $\delta \approx 0.07$, optimal superconducting properties have attained (Figure 2.15).

In case of low temperature superconductors, the grain boundaries act as pinning centers whereas for HTS it severely reduces the current carrying capacities. Also, the magnitude of coherence length is small for HTS than LTS. Therefore, in order to have useful engineering current densities, usually grain boundaries with lower angle can be considered or a disorientation of 4^o can be tolerated [41]. Thus is the reason for the texturing of such superconductors either by deposition on textured substrate or top seeded melting growth method. Although, YBCO superconductors is still having few challenges however it is being manufactured in coated conductors and bulk form.

2.5.4.1. (RE)BCO coated conductor manufacturing

2^{nd} generation superconductors are widely employed in various applications including transmission cables, generators, transformers, flywheels, motors, magnetic energy storage etc. The operating temperatures may also vary between liquid helium to liquid nitrogen temperatures depending upon the applications required. It has been found that at lower temperatures, the irreversibility field line shows better performance for YBCO superconductor [42]. (RE)BCO can be manufactured as bulk or a thin film on metallic substrate. Bulk superconductors can be used in levitation applications, motors or generators and coated conductors are mainly employed in current transport applications. Many researchers have shown that YBCO tape can be employed in trapped field applications [43]–[45] at liquid helium and nitrogen temperatures.

Many manufacturing companies have evolved from past few years where the coated conductors are being manufactured using various processes intended to improving the overall performance of the YBCO superconductor [46]. There are two ways to manufacture a trapped field magnet either by using bulk superconductor or a stack of coated conductors. Magnets using bulk sample are older technique and a concept of

stack of tapes is relatively new and thus needs more investigation in order to understand the constructional and computational challenges involved with this technology [47].

2.5.4.2. Bulk Superconducting Magnets

There are generally two ways through which (RE)BCO bulk superconductor can be manufactured either top seeded infiltration and melt growth [48] or top seeded melt growth [49]. In both the situations, texture is incorporated through a small (RE)BCO seed among rare-earth metal which has to be chosen in such a way that the peritectic temperature should be higher than that of (RE)BCO compound that is being grown. The seed materials used for YBCO are; $SmBa_2Cu_3O_{7-\delta}$ *or* $NdBa_2Cu_3O_{7-\delta}$. (RE)BCO bulk superconductors have no-uniform properties because of the processing methods. **Figure 2.16** represents the growth sector boundaries and regions for GdBCO bulk sample. Due to large pinning, the critical current density (J_c) is found to higher at grain growth boundaries and the texture declines going away from the seed. Using pulse field magnetization, such irregularities can be established in the trapped field performance. It has been concluded form the studies [50][51] that throughout pulse field magnetization, localized heat is generated at the growth sector regions where critical current density, J_c is lower.

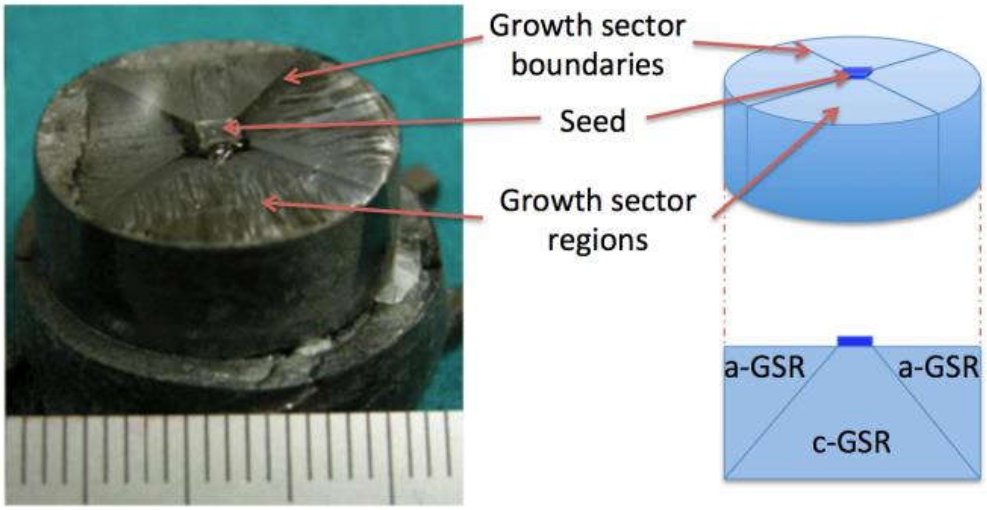

Figure 2.16 GdBCO Bulk Magnet

Due to this, trapped field profiles get distorted which leads to large diminution in the trapped field magnitude. This process also neglects supplementary defects such as

pores, cracks inside the bulk superconductors which are generally formed during the manufacturing [52]. Also, the weakening of the texture away from the seed locates a bound on the size of bulk and it is not going to contribute to the trapped field considerably as the distance between material and seed is large. However, manufacturers have fabricated the bulks of 10-15 cm size successfully.

On the other hand, researchers have suggested to use multi-seeding in bulk (RE)BCO, conversely, due to low quality of interfaces, the current transfer amongst the domains cultivated by the two seeds remains poor. However, for the large bulks fabricated using coated conductors (RE)BCO, it does not essentially result in higher trapped fields due to poor mechanical properties of ceramic materials. Furthermore, batch processes are involved in the fabrication of bulk (RE)BCO, which makes it less efficient. Also, to get optimum superconducting properties, there is a need to diffuse oxygen into large bulk samples to maintain its stoichiometry which is found to a longer process thus limits the practical implementations.

2.6. Coated conductors

In the present study, a coated conductor manufactured by SuperPower has been used as its substrate material (Ni based super-alloy) is non-magnetic whose structure is shown in **Figure 2.17**. By using ion beam assisted deposition (IBAD), a stack of buffer layers is deposited after the electro-polishing of Hastelloy. Buffer layers have biaxial texture which is used as a template for growing (RE)BCO. Then by incorporating either pulsed laser deposition (PLD) or metal organic chemical vapor deposition (MOCVD), (RE)BCO layer is deposited epitaxially. Texture of the superconducting layer is getting affected with the increase in thickness. Therefore, the thickness is typically kept to several microns to maintain the healthy texture of the layer. In order to provide the chemical protection, stabilization and electrical contact to the superconducting layer generally a silver over-layer is deposited using sputtering technique. Sometimes, to provide more protection generally, an extra layer of copper is deposited through electro-deposition. There are various methods through which these depositions can be achieved depending upon the manufacturer. One of them is to introduce the texture directly by the substrate. The texture is established on the

substrate using thermo-mechanical methods and then it is transported to the (RE) BCO layer through intermediate buffer layers.

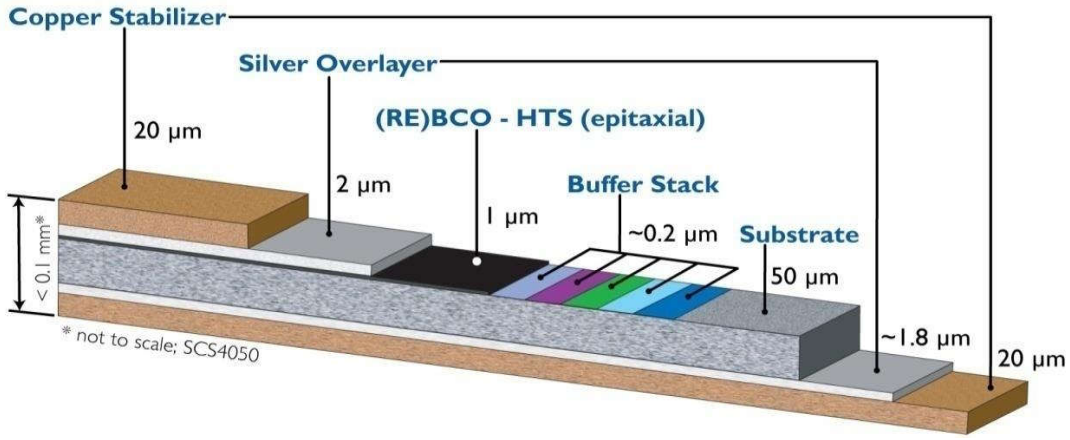

Figure 2.17 HTS tape with non-magnetic substrate

Due to their perovskite structure involved in such tapes, their behavior is highly anisotropic which leads to 2-dimentionality in its physical properties. YBCO exhibits comparatively low anisotropy compared to other HTS materials like Yb, Tm, Er, Ho, Dy, Gd, Eu, Sm, and Nd (in order of ionic size – smaller to larger), thus widely used in superconducting applications commercially.

In order to get better quality and uniform (RE)BCO coatings, generally, thin film deposition methods are employed which further results in high critical current densities, J_c that even of the order of 2-6×10^6 A/cm^2. The critical density scales obtained in coated conductors are one order higher than bulks (RE)BCO at 77 K in self-field. Although, this comparison is not that much simple as inconsistency is still there as for tapes, critical current density is limited by the weakest sector in the tape tested, whereas J_c is evaluated from the small cut sections in case of bulks. In actuality, the J_c may be lower for bulk material as they are having macroscopic inhomogeneities like pores and other defects discussed earlier. The engineering current density, J_e most significant parameter for trapped field applications and it involves the total volume of the superconductor. In general, the superconductor volume in a SC tape is of 1-6% of the total volume which further depends upon the thicknesses of silver, substrate and copper (if any) layers. For the tape used in this study, there is no additional copper layer and the other specifications are given in

Table 2.1. Due to small thicknesses, the engineering current density is found to higher in coated conductors.

Table 2.1 Parameters of HTS tape

Articles		Values
Bare Conductor	Tape width	12 mm
	Tape thickness	0.1 mm
	Substrate thickness	50 μm
	Stabilizer thickness	2 μm
Critical Current	77K, Self-field	330 A

Unlike bulk (RE)BCO conductors, manufacturing of coated conducting tape is a continuous (reel-to-reel) process which can be scaled to any level. Though, the manufacturing and application challenges for tapped field purposes are associated with the small width of the tape. Almost all the manufacturers have standardized the tape width to 12 mm for trapped field applications. Manufacturers have developed tapes with width 46 mm; however, the performance of this tape is not as good as 12 mm width tape. Also, many commercial manufacturers are developing superconducting tape with 100 mm width for scale-up purposes. Moreover, there are various configurations available which have different thicknesses and lengths of the tapes. Stacked tapes with zig-zag configurations (Roebel) are also being employed in various applications including power transmission, motors and trapped field magnets.

2.6.1. Mechanical Properties

(RE)BCO bulk superconductors are brittle materials which consist lower fracture strength due to the presence of pores and micro-cracks those acts as stress concentration sites. For YBCO superconductors, the tensile strength is about 25 MPa and fracture strength is in the range of 1.4-2.2 MPa [18]. There may be a situation arise when magnetic tensile stress exceeds tensile strength which may lead to direct failure of the superconducting tape. In the remanent state, the center of the sample has experienced maximum tensile stress [53] and is given by:

$$\sigma = 0.354 \frac{B_0^2}{\mu_0}$$

Where is σ tensile stress in *'Pa'* and B_0 is trapped flux density in Tesla. From the equation, it can be concluded that during magnetization, the stresses developed in bulk superconductor are much larger if the magnitude of external magnetic field exceeds B_0. It has shown in study [54] that the tensile stresses can be reduced or controlled by introducing compressive stress using metal ring around the bulk. By impregnating resins in the bulk YBCO, it has improved the tensile stress from 12 to 18 MPa. The fractural toughness is also found to increase as resins filled the open cracks and voids in the sample. Further, the fractural stresses were improved to 29 MPa by impregnating resins and wrapping the bulk sample in carbon fibres [55]. Using a shrink-fit steel band, a record of 17.6 T field was setup in pre-stressed bulk sample.

However, in HTS tapes, the mechanical properties are dominated by the metallic substrate layer whose volume fraction is about 90% of the tape in the absence of additional copper stabilized layer. Generally, Hastelloy C-276 is used as a non-magnetic substrate in YBCO tape manufactured by SuperPower and the yield stress is 670 MPa at 77 K which is far greater than bulk superconductor.

2.6.2. Thermal Properties

Table 2.2 shows the properties of YBCO and it can be noticed that the thermal conductivity of YBCO is much lower than most metals. The applications like current leads require low thermal conductivity however it can result to thermo-magnetic instabilities like flux jumps at low temperatures. Due to localized heating, the flux avalanches/jumps happen as a result of movement of individual flux lines.

Table 2.2 Properties of YBCO tape

Parameter	**Hastelloy**	**Silver over-layer≈**	**Bulk YBCO**
Density (kgm^{-3})	8890	10490	5900
Thermal Conductivity ($W\ m^{-1}\ K^{-1}$)	3-7.5	≈500-1500	6-20 ab-plane 1-4 c-axis
Heat Capacity ($J\ kg^{-1}\ K^{-1}$)	2-200	2-155	≈1-200
Tensile Strength (MPa)	670-760 (yield)	≈60 (yield)	≈30 (fracture)

Conversely, in superconducting tapes, (RE)BCO is composed with silver over-layer and copper layers (sometimes) which has high thermal conductivity and can rapidly homogenize the temperature stifling flux avalanches/jumps. In addition, the thicker substrate materials are generally employed as heat sink comparatively thinner materials [43].

2.7. Applications of trapped/high field cryomagnets

Such cryomagnets are cooled through liquid nitrogen mostly, due to the economic viability of the cryogen. There are various situations where stacks of the YBCO or (RE)BCO tape are employed in high field magnetic applications as that of bulk superconductors. The applications of such magnets are classified as follows:

1. Power Grid Stabilization
2. Medical Applications
3. Transportation Services
4. Energy Storage Applications

1. Power Grid Stabilization

Due to the increase in power demand, a network of power grids can be found all around on this planet where overhead high voltage transmission cables are employed for power transportation from one power station to other. All power generation units are combined to one common grid locally so that operations like load shifting or unit maintenance can be handled easily. Large currents and voltages are associated with such power grids and small interruption or faults may cause power instability or even failure of the grid. Power grid instability is a serious concern all over the world as it results in voltage fluctuations, undesirable harmonics, momentary interruptions and voltage sags in the power system. Such instances would result in the capital economic loss. To get rid of from such faults usually Superconducting Fault Current Limiters (SFCL) are employed which are installed within the grid to protect the grid from catastrophic events.

In order to match voltage fluctuations generally capacitors are employed at present however their capacity to handle such events is much low due to less response time and large specific weights of the unit for higher power ratings.

Superconducting Magnetic Energy Storage (SMES) systems are capable of not only handling such fluctuations but also the load shifting sequences. SMES systems have large response time and higher power densities and they can respond within few milliseconds to few minutes. Many countries have developed/tested both SFCL [56]–[59] and SMES [60]–[62] systems for power grid stabilization.

As discussed earlier in chapter-1, the other advantage of SMES system is that it can be used as a bridged energy reservoir among the distribution power grid and renewable energy plant like solar and wind as output of such plants is considerably intermittent. This device can be used to power blackouts and thus economic loss can be prevented.

2. Medical Applications

Advancement in medical science becomes possible after the discovery of superconducting machines like Magnetic Resonance Imaging (MRI) and Nuclear Magnetic Resonance (NMR). High magnetic fields are involved in MRI devices to capture the image of various parts of the body through recording hydrogen spin available in our body in the form of water.

3. Transportation Applications

Modern transportation sector is seeking for electric driven technology in order to avoid pollution and global warming challenges. Sectors like automobile and aviation are shifting their energy resources from conventional fossil fuels to electrically driven green technology. Already automobile sector has started their production on the basis of electrical technology and few of vehicles have been deployed recently in India under Zero Emission Vehicles (ZEVs). In aviation sector, research on electric aircraft concept has been started few years back and till now research is going on related to energy storage technologies. As discussed earlier, for such technologies superconducting energy storage systems are one of the strong and significant contender.

Chapter-3

Mechanical Design of Superconducting Coil

In this chapter, design of superconducting magnet has been studied at a temperature of 77 K and 14 K. Configuration of the superconducting tape has been identified among 1st and 2nd generation. The selection of the tape is done on the basis of large current carrying capacity or the critical current of the tape at 77 K and 14 K. Effect of operating temperatures has also been addressed in this chapter. In literature, many configurations are available for the magnet design however the configuration has been chosen which require less surface area and has an ability to minimize the length of superconductor used to store energy. The design, input and constraint variables have been identified for the electromagnetic design of superconducting magnet. Analytical correlations have been employed to evaluate the geometrical details like bore diameter, height of the magnet, thickness and number of turns around the pancake coil of the magnet. Effect of current and solenoid thickness on the topology of the magnet has been examined. A comparison has been done for the magnet design at 14 K and 77 K and it has been concluded that it is beneficial to cool magnet at low temperatures as it reduces the total length of the superconducting tape.

Keywords: Superconducting Magnet, Solenoid Magnet, Superconducting tape, Pancake Coil, Energy Storage.

3.1. Introduction

A superconducting magnet involved many sub-systems like main superconducting coil, current leads, cryogenic setup and supporting structure. Many research institutes have worked on the structural, thermal and magnetic design of the SMES. International and National status of superconducting magnet has been elaborated in the following sections.

3.1.1. Literature Survey (International Status)

Since superconducting magnetic energy storage technology is under development phase due to economic constraints it is not being commercialized yet. The most well-known experiment of superconducting magnet (NbTi superconductor) is installed in CERN, Geneva, where the magnet is being cooled at 1.9 K using superfluid Helium (Helium-3) [63]–[66]. Low Temperature Superconductors (LTS) (NbTi and Nb_3Sn) have been widely employed in the construction of the magnets [63]–[73]. After the discovery of High Temperature Superconductors (HTS), the research communities have employed HTS materials for the energy storage applications as these are found to be economical than LTS and also generate stable magnetic fields with high energy densities and compact size compared to LTS [74]. Many researchers have simulated the structural aspects of HTS SMES including shape or configuration of the magnet [75]–[78]. Various configurations like solenoidal [19], [20]–[27], toroidal [75][78][88][89]–[92][93][94]–[103][104], D-shaped [92] and race track coils [105], [106] have been employed in the design and development of the HTS magnet.

In the HTS technology, basically two types of HTS tapes are being employed in the development of the SMES viz. 1st Generation (1G) HTS Tapes (BSCCO-2212 and BSCCO-2223) [107]–[113] and 2nd Generation (2G) HTS tapes Yttrium Barium Copper Oxide (YBCO) [77], [114]–[121]. Literature showed that both tapes have been employed in the design of HTS magnet however 2G tapes are found to be better than 1G as they can carry more currents and provides excellent mechanical strength [122]. Many studies are devoted to the computational development of HTS SMES. Some of the research institutes have successfully developed their prototypes also viz. Korea Electro-Technological Research Institute, (KERI) Korea [123]–[128], Kyushu

Electric Power (KEP), Japan [129]–[132] and China Electric Power Research Institute (CEPRI) China [133]–[135].

3.1.2. Literature Survey (National Status)

In India, attempts have been made to develop such systems by using Low Temperature Superconducting technology (below 10K) at IIT Kharagpur [136] and Variable Energy Cyclotron Centre (VECC) (at Liquid Helium temperatures), Kolkata [98]. Very less work has been reported other than our previous work [121][137] where high temperature superconducting tapes have been incorporated in the development of SMES devices in India. Table 3.1 and Table 3.2 describes the computational and experimental studies performed on SMES having various energy capacities.

In this chapter, only design of superconducting coil has been focussed where HTS tape's design and constraints parameters have been identified before the actual start of the design procedure. The detailed procedure of electromagnetic design of magnet coil has been explained in the coming sections.

3.2. Selection of High Temperature Superconducting Tape

As discussed in chapter 2, HTS tapes can be specified into two categories a) 1st generation and b) 2nd generation tapes. Among these two, 2nd generation HTS tapes can carry more current densities under high magnetic field and possess higher critical currents than 1st generation tapes at 77 K. Yttrium Barium Copper Oxide (YBCO) is one of the widely used 2nd generation tapes where Yttrium (*Y*) is a rare earth metal due its advantages over 1G tapes. HTS tape manufactured by SuperPower (SCS 12050) [138] has been selected for the present study as it is basically designed for high magnetic field applications like magnets and is having non-magnetic substrate. The tape configurations are enlisted in Table 3.3 and schematic is given in Figure 3.1. Proposed HTS tape is 12 mm wide and 0.1 mm thick and is composed with non-magnetic substrate material (Hastelloy), YBCO layer, and stabilizer (silver) layer. The manufacturing details of such tapes have been explained earlier in Chapter 2 (page-54).

Table 3.1 Computational Studies of HTS SMES

High Temperature Superconducting Magnetic Energy Storage (Computational)					
Tape Used	**Shape**	**Capacity**	**Authors**	**Investigation Remarks**	**Location**
BSCCO-2223	**Solenoidal**	50kJ	Dai et al. [139]	Design of 50kJ HTS SMES for power systems	China
		150kJ	Kreutz et al. [140]	Design of 150kJ HTS SMES for 20kVA Power Supply	Germany
		200kJ	Korpela et al. [141]	Optimization of HTS SMES	Finland
		600 kJ	Seong et al. [128]	Development of a 600 kJ HTS SMES	KERI, Korea
			Kim et al. [142]	Design of HTS Magnets for a 600 kJ SMES	KERI, Korea
		1MJ	Xiao et al. [143]	Fabrication and Tests of a 1 MJ HTS Magnet for SMES	China
			Zhang et al. [144]	The electromagnetic analysis and structural design of a 1 MJ HTS magnet for SM	China
			Dai et al. [145]	Development and Demonstration of a 1 MJ High-Tc SMES	China
		72MJ	Noguchi et al. [115]	An Optimization Method for Design of SMES Coils Using YBCO Tape	Japan
YBCO		50MJ	Shintomi et al. [146]	Design Study of SMES System Cooled by Thermo-Siphon With Liquid Hydrogen	Japan
		5MJ	Morandi et al. [147]	Design and performance of a 1MW-5s HTS SMES	Italy

		16.2kJ Janowski et al. [148]		HTS winding in toroidal configuration for SMES coil	Poland
		34.8kJ Kozak et al. [149]		Test results of HTS magnet for SMES application	Poland
		2.5MJ Kwak et al. [97]		Design of HTS magnets for a 2.5 MJ SMES	Korea
	Toroidal	2.5MJ	Kim et al. [150]	Performance analysis of a toroid-type HTS SMES	Korea
			Kim et al. [151]	Stress Analysis for Toroid-Type HTS SMES Coil	Korea
		5MJ Lee et al. [152]		Design of HTS Toroidal Magnets for a 5MJ SMES	Korea
MgB_2		48GJ Sander et al. [153]		A 48 GJ Toroidal MgB2-SMES	Germany

Table 3.2 Experimental Studies of HTS SMES

High Temperature Superconducting Magnetic Energy Storage (Experimental)					
Tape Used	**Shape**	**Capacity/ Authors**		**Investigation Remarks**	**Location**
BSCCO-2223	**Solenoidal**	2.5kJ Hawley et al. [154]		Modeling and design of the electromagnetic and thermal aspects of the coil	Australia
		2.79kJ Hawley et al. [155]		Characterization and Control of a Prototype HTS SMES Device	Australia
		4kJ	Hayashi et al. [156]	Fabrication and Test of 4kJ SMES	Japan

			Iwakuma et al. [157]	Fabrication of 4kJ conduction cooled SMES	Japan
		7.3kJ Janowski et al. [158]		HTS magnet for 7.3 kJ SMES system	Poland
		10kJ Wang et al. [159]		Design and Fabrication of 10kJ SMES Device	China
		35kJ	Kozak et al. [160]	Performance test of 35kJ HTS Magnet	Poland
			Shi et al. [161]	Development of 35kJ conduction cooled HTS SMES	China
		600kJ	Park et al. [162]	Fabrication and test a 600 kJ SMES model coil	KERI, Korea
			Yeom et al. [163]	Experimental Study of the Conduction Cooling System for the 600 kJ HTS SMES	KERI, Korea
		1MJ Xiao et al. [143]		Fabrication and Tests of a 1 MJ HTS Magnet for SMES	China
Bi-2212		800kJ Tixador et al. [164]		First tests of a 800 kJ HTS SMES	France
		6.7MJ Koyanagi et al. [165]		Design of a high energy-density SMES coil with Bi-2212 Cables	Japan

The tape is having a critical current of 330 A at 77 K and 0 T self-field and in case of higher transport currents, more than one tapes can be stacked to achieve the required power requirements. As in the present study, six tapes have been stacked one over the other which results in a maximum current of 1620 A with 82% load factor.

Table 3.3 HTS tape parameters for mechanical design

Articles		Values
Bare Conductor	Tape width	12 mm
	Tape thickness	0.1 mm
	Substrate thickness	50 µm
	Stabilizer thickness	2 µm
Critical Current	77K, Self-field	330 A

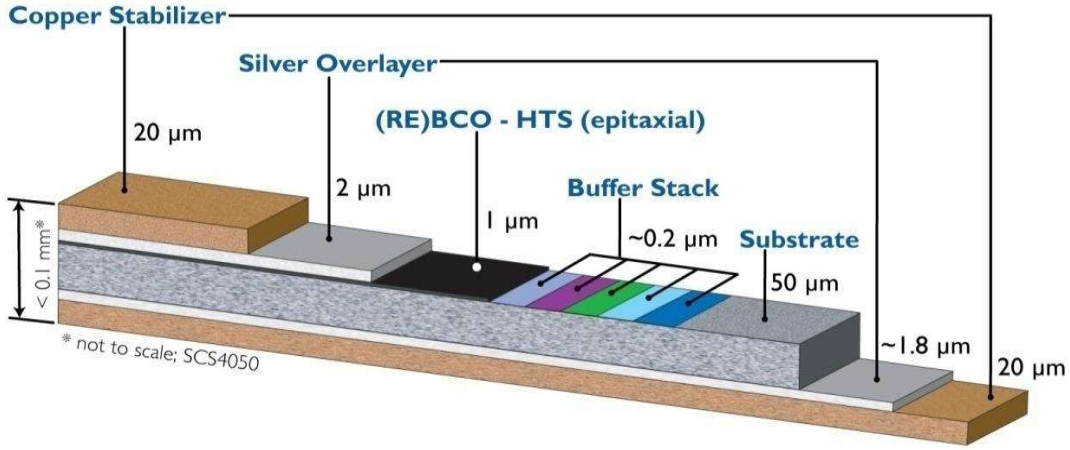

Figure 3.1 Schematic of HTS tape (manufactured by SuperPower)

3.3. Selection of Magnet Configuration

Selection of the SMES magnet cross-section is very important step while designing the magnet. The strength, space and robustness of the device are the preliminary requirements as large forces are associated with such devices. In the literature, various combinations have been employed till date in order to get efficient design for the HTS SMES device to store energy. Beginning with the Low Temperature Superconductors (LTS) namely Nb-Ti, Nb_3Sn etc. various attempts have been made to develop an economical and environmentally sound SMES magnets in past [62]. After the discovery of high temperature superconductors, researchers have preferred HTS technology over LTS in the development of superconducting magnets due to

economic issues and robustness. In the earlier stages, First Generation (1G) tapes (Bismuth Strontium Calcium Copper Oxide- BSCCO-2212 and 2223) are being utilized in the design and construction of magnets**.** These superconductors are manufactured by using "Powder-in-Tube" technology. However, it has been discovered that coated conductors (Yttrium Barium Copper Oxide-YBCO) i.e. Second Generation (2G) HTS tapes can carry more currents than 1G tape. Thus, in this study, YBCO tapes (manufactured by SuperPower® SCS12050) has been used for the design of superconducting magnet.

There are two geometrical configurations are available for the SMES- solenoid and toroid as shown in **Figure 3.2**. From literature, it has been found that the solenoidal arrangement is simpler to manufacture and allows an easier handling of the mechanical stress. Moreover, for isotropic superconductors, the solenoid configuration allows minimum wire consumption and signifies most economical solution [152]. However, 2G HTS coated conductors are anisotropic therefore in this work only isotropic properties have been considered. Despite the drawback of the high stray field, solenoidal geometry has been exploited in the past for the development of real-scale SMES systems based on low temperature superconductors [166]. More recently solenoidal geometries have also been used for the development of SMES based on first generation HTS wires [164]. However, when 2G HTS materials are considered, toroidal geometry is generally assumed [152], [77], [117], [167]. Since toroidal geometry reduces the perpendicular component of the magnetic field on the conductor, a lower material requirement can be expected due to the drastic dependence of its J_c vs. B performance on the orientation of the field. A presumably lower level of AC losses can also be expected due to the lower perpendicular field. However, a larger overall size of the toroidal SMES would result in larger external heat loads due to radiation. In fact, the area of the toroidal shaped magnet is about 300% that of the solenoidal [78]. Furthermore, a more complex support structure is also needed for holding the pancakes which in turn increase the overall manufacturing cost. Therefore, in the proposed work solenoidal magnet has been selected for energy storage.

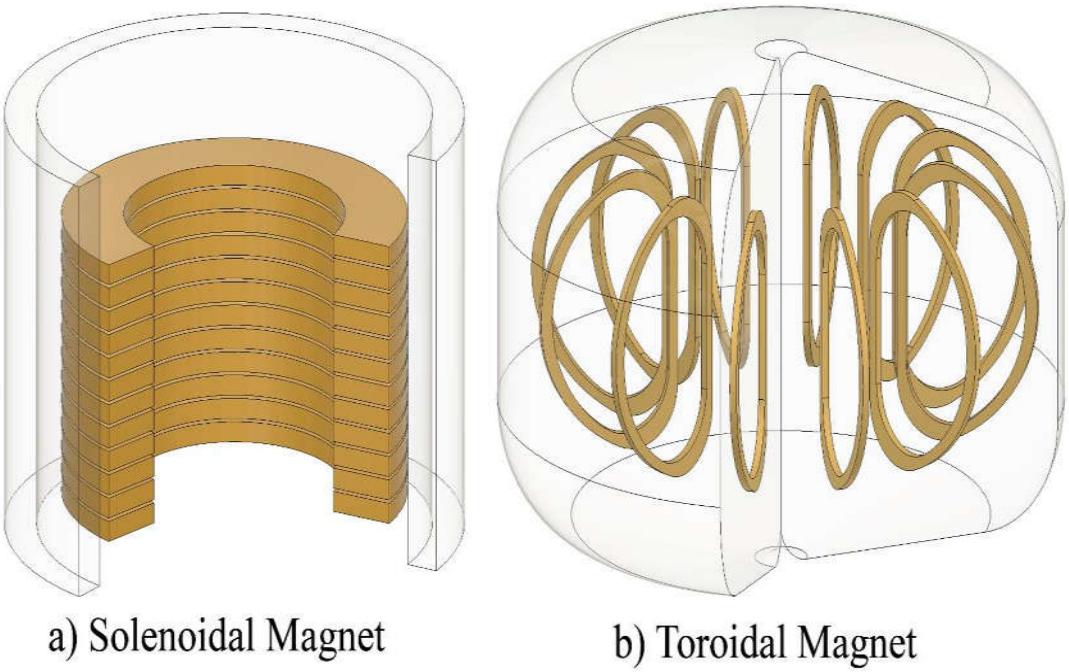

Figure 3.2 Schematic of Solenoidal and toroidal magnet

3.4. Design Variables and Constraints

In the design of superconducting magnet, various variables have been involved that can affect geometrical configuration of the magnet. For solenoidal magnet, the important geometrical parameters are bore diameter, aspect ratio, number of turns/thickness of the coil and supporting structure. Considering the design variables (bore diameter, number of single or double pancake coils, number of winding turns of superconductor etc.) and constraints (stray magnetic field, critical magnetic field, total length of superconductor etc.) into account, HTS tape having I_c 330 A has been chosen to store energy and higher load factors have been considered for maintaining the length of the HTS tape as minimum as possible so that maximum energy can be stored within the defined design constraints. The purpose of choosing minimum length is related to the cost of the superconductor which further strike on the economic constraints.

An optimum design for the storage of energy can be achieved choosing design constraints and variables cautiously. However, in the present study optimization of the magnet parameters has not been considered. The different types of design variables, constraints and input parameters are listed in Table 3.4 and Table 3.5.

Table 3.4 Design Variables and Design Constraints for the SMES design

Solenoidal	
Design Variables	**Design Constraints**
Operating Current	Length of the Superconductor
Number of single or double pancake coils (SPC/DPC)	Space for installation
Bore diameter of the solenoid	Max. Perpendicular Magnetic Field
Number of Turns of Single Pancake Coils	Critical Current and temperature

3.5. Assumptions

1. Gap among the adjacent single pancake coil (SPC) is assumed to be zero.
2. Reference magnetic field for the study is assumed to 3 T.
3. Optimization of the design variables has not been considered in the present work.

3.6. Electromagnetic Design of HTS Magnet

A solenoidal geometry has been considered for the design of 1 MJ HTS magnet. The solenoid is composed with multiple pancake coils piled up one top of the other in the axial direction as shown in Figure 3.3. A complete SMES system is having many sub-systems like pancake coil arrangement, current leads, supporting structure, vacuum shell, non-metallic structure and cryocooler ports for cooling operations or liquid nitrogen inlet/outlet ports. Generally, 2G HTS magnets are cooled with liquid nitrogen as the critical temperature of ReBCO tapes is higher than 77 K.

Table 3.5 Input Parameters for the design of SC coil

Parameter	Description
Aspect Ratio of the solenoid, a	Length to diameter ratio
J/J_c ratio of the SC conductor, c	Safety Factor
Operating temperature of the system, T	Useful in deciding the operating currents
Reference field for the solenoid, B_{ref}	Approximate field which is intended to be produced in the solenoid at the maximum current during normal operation
Distance between two SPC/DPC	For the cooling purposes

However, as discussed earlier, the current carrying capacity of HTS tapes is less at 77 K compared to 50 K or 20 K or liquid helium temperatures. Thus, to work at a temperature lower than 77 K generally liquid hydrogen (20 K), liquid neon (27 K), liquid helium (4.2 K) or cryocooler based cooling has been employed. For the present study, it has been considered that the magnet is cooled at 77 K using liquid nitrogen. The input parameters that are required for the design of superconducting magnet are enlisted in Table 3.5.

In the present work, operating temperature is assumed to 77 K, reference field is 3 T, J/J_c ratio is 0.9 and the distance among the SPCs is assumed to zero. All such parameters are crucial while magnet design and these are depending on each other in some or other way through the analytical relations discussed in the following section.

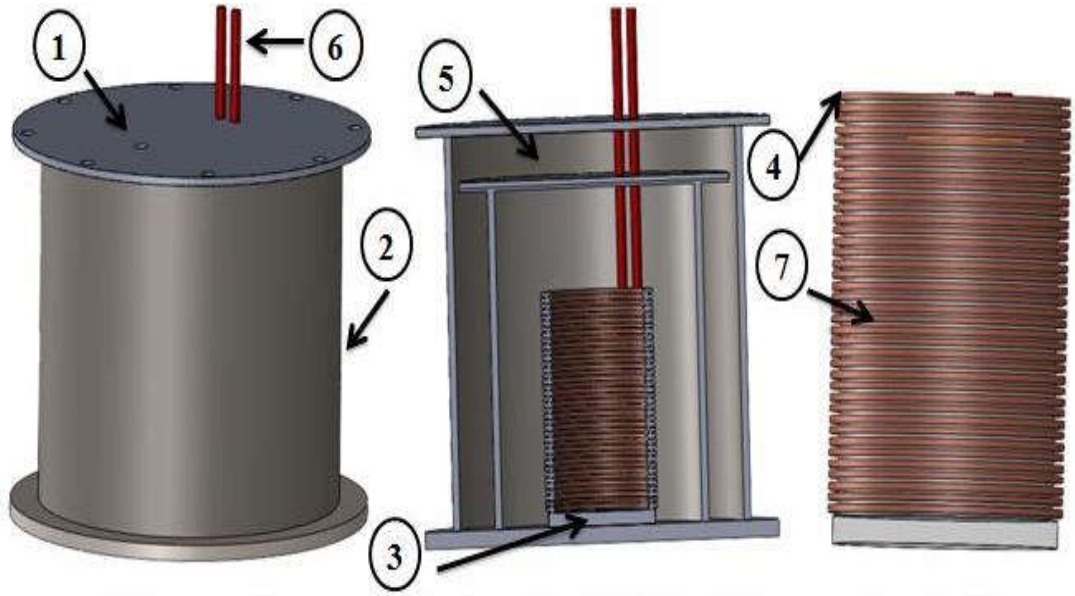

Figure 3.3 Components of Typical Solenoidal HTS Superconducting Magnetic Energy Storage Device.

The design of Solenoidal HT-SMES can be achieved using the following analytical relations:

1. The volume of the bore V_{bore} of the solenoid can be obtained based on the energy ΔE to be delivered and the energy density $e = B_{ref}^2 / 2\mu_o$ corresponding to the reference field (B_{ref}) by using following relation [168].

$$V_{bore} = 2\mu_o \Delta E / B_{ref}^2; \quad D_{sol} = \left(4V_{bore} / a\pi\right)^{1/3}; \quad H_{sol} = aD_{sol} \tag{3.1}$$

Where a is aspect ratio, D_{sol} is the bore diameter and H_{sol} is the height of the solenoid. μ_o is the magnetic permeability of free space $4\pi \times 10^7$ *H/m*.

2. The maximum allowable current density of the SC conductor is obtained as $J_{max} = c\, J_c$, where c is the allowable J/J_c ratio. The maximum allowable field B_{max} at the center of the solenoid is deduced based on J_{max}. The maximum energy E_{max} storable by the solenoid is also deduced based on J_{max}.

   The length of the SC conductor needed to build up the solenoid with thickness δ_{sol} is given by Equation 3-2, where S_{SC} is the cross section of the conductor and R_m is the average radius of the solenoid ($R_m = D_{sol}/2 + \delta_{sol}/2$), packing factor ($b$) is assumed to unity.

$$length_{SC} = 2\pi R_m H_{sol} \delta_{sol} / S_{SC} \tag{3.2}$$

3. A Lorentz force arises in the coil due to the magnetic field. This produces a stress distribution which must be withstood by the superconductor. The maximum tensile stress occurring on the superconductor in the case of a thick solenoid can be estimated by means of Equation 3-3, where r is the ratio between the outer and the inner diameter of the solenoid, that is ($r = 1 + 2\delta_{sol}/D_{sol}$). For the designed coil to be acceptable from a mechanical point of view the maximum stress should be well below the critical tensile stress of the superconductors.

$$\sigma_{max} = \frac{1}{2} J_{max} B_{max} D_{sol} \frac{1}{r-1}\left[\frac{2r(7r^2 + r + 1)}{9(r+1)} - \frac{5}{12}\left(2r^2 + r - \frac{3}{5}\right)\right] \tag{3.3}$$

4. The last step for the design of the solenoid is the choice of the number of turns (N). This is a crucial parameter in estimating the inductance 'L', and hence the

performance of the solenoid. The maximum current I_{max} and the deliverable energy ΔE of the solenoid are given by Equation 3-4 and Equation 3-5 [168]. Both these quantities depend on the thickness δ_{sol} and the number of turns N of the solenoid. Note that, as expected, the maximum storable energy $E_{max} = ½\ L\ I^2_{max}$ does not depend on N since L increases as N^2. Given a solenoid with assigned thickness δ_{sol} and maximum storable energy E_{max} a high number of turns, which leads to a high inductance L, is desirable since it implies a smaller maximum current I_{max} with reduced size and the heat load of current leads. A more relaxed sizing of the switches of the DC/DC converter is also obtained with a smaller maximum current.

$$I_{max} = J_{max} H_{sol} \delta_{sol} / N \qquad 3.4$$

$$\Delta E = \frac{1}{2} L \left(I_{max}^2 - I_{min}^2 \right) \qquad 3.5$$

Deliverable energy can also be calculated by using following relation:

$$\Delta E \approx \pi R_{sol}^2 H_{sol} B_{ref}^2 / 2\mu_o \qquad 3.6$$

In the following sections, effect of current, solenoid thickness and operating temperature on the magnet topology has been studied where aforementioned analytical relations have been used.

3.6.1. Effect of Current on the Magnet Topology

Effect of current on the magnet topological parameters like inductance, thickness of solenoid, number of turns around pancake coils and length of superconductor has been evaluated in this section. Operating current through single tape has been varied from 170 A to 270 A and its effect on the magnet design parameters has been studied.

Figure 3.4 shows the inductance variation with operating current varies from 170 A to 270 A. As six tapes are stacked one top of the other in order to increase the maximum current (I_{max}) and reduce the superconductor's length used to store 1 MJ of energy. The minimum transport current of tape has been varied from 170 A to 270 A simultaneously I_{max} also changed with respect to I_{min} from 1020 A to 1620 A.

Inductance of the coil is found to decrease with the increase in operating current to keep deliverable (ΔE) and maximum (E_{max}) energy constant.

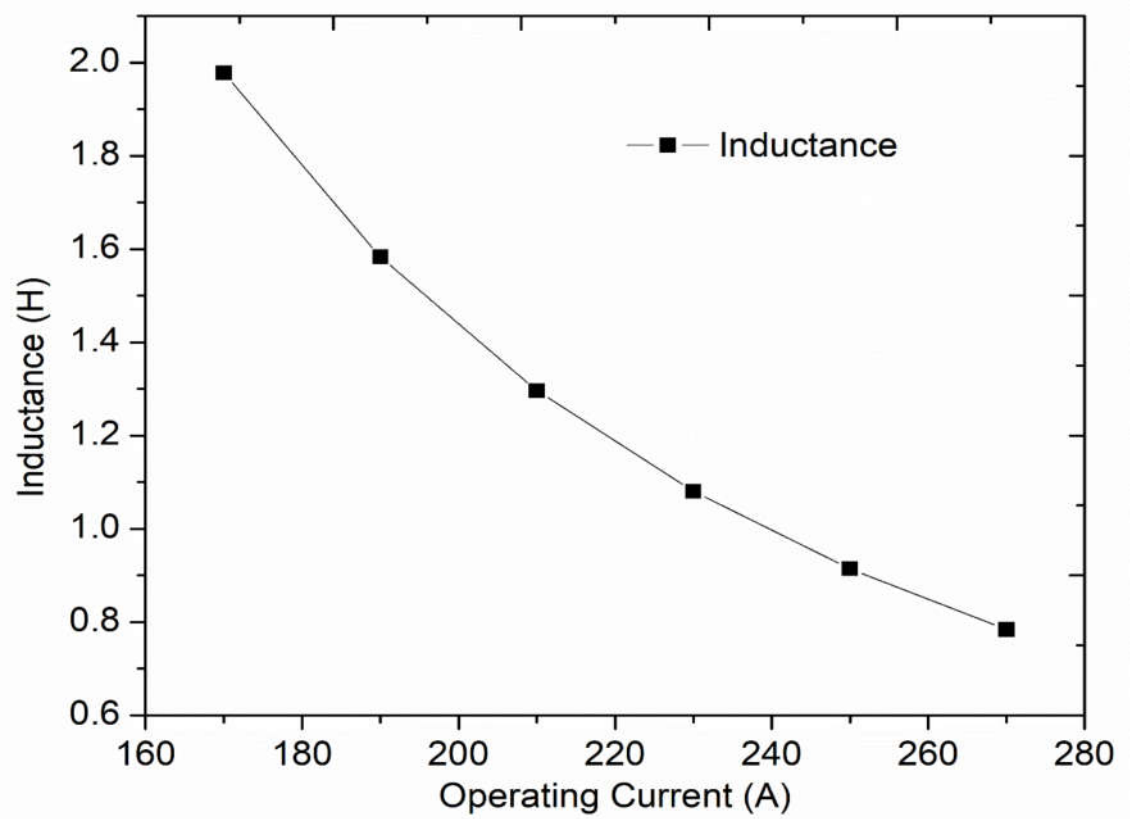

Figure 3.4 Operating current effects on Inductance

For a constant deliverable (ΔE) energy, maximum (E_{max}) energy and number of pancake coils, the solenoid thickness is found to decrease with increase in the operating current as explained in Figure 3.5. Similarly, the superconductor's length is found to decrease with increase in operating current (Figure 3.6). Solenoid thickness plays an imperative role as it is indirectly related to the bore diameter thus solenoid height which further affect the size of the magnet. As per the space requirement, many solenoid magnets can be designed where bore diameter and height of magnet can be controlled when it is required.

Figure 3.7 indicates the total number of turns around SPCs variation with operating current and it has been observed that with increase in minimum operating current, the number of turns are found to decrease for constant 1 MJ deliverable energy and 49 pancake coils (as zero gap among the adjacent pancakes has been considered thus there is a need of 49 pancake coils to match the solenoid height with 0.8 aspect ratio).

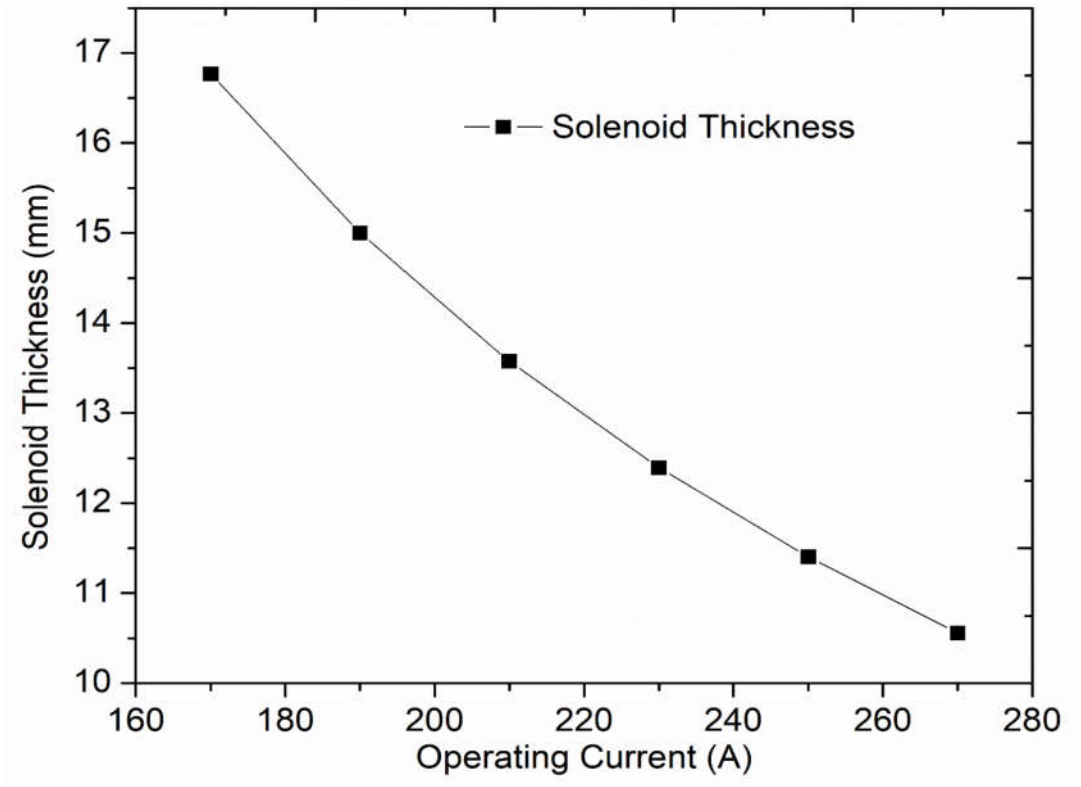

Figure 3.5 Operating current effects on solenoid thickness

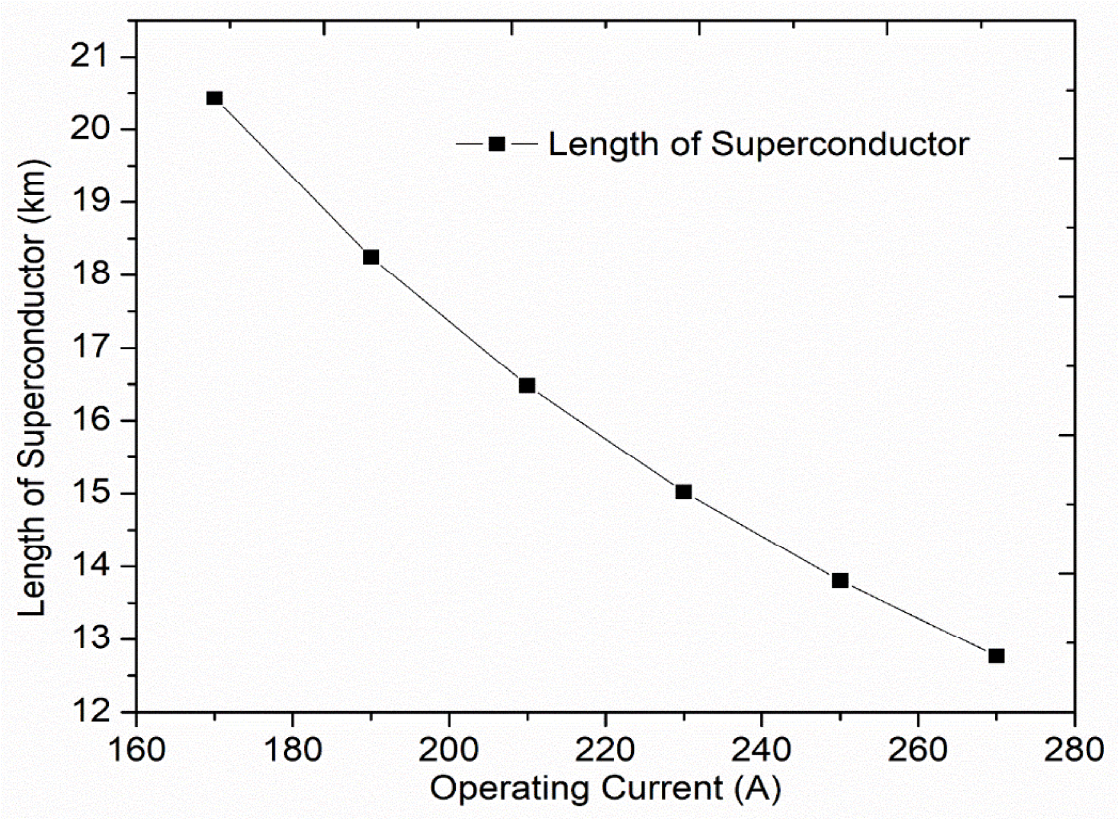

Figure 3.6 Operating current effects on length of superconductor

This implies that with the increase in the minimum operating current flowing through HTS tape the inductance, solenoid thickness, total number of turns and length of superconducting tape is found to decrease which further indicate that as SC tape contributes maximum part in the economic cost of the system thus with the increase in the minimum operating current magnitude the overall cost of the system can be controlled.

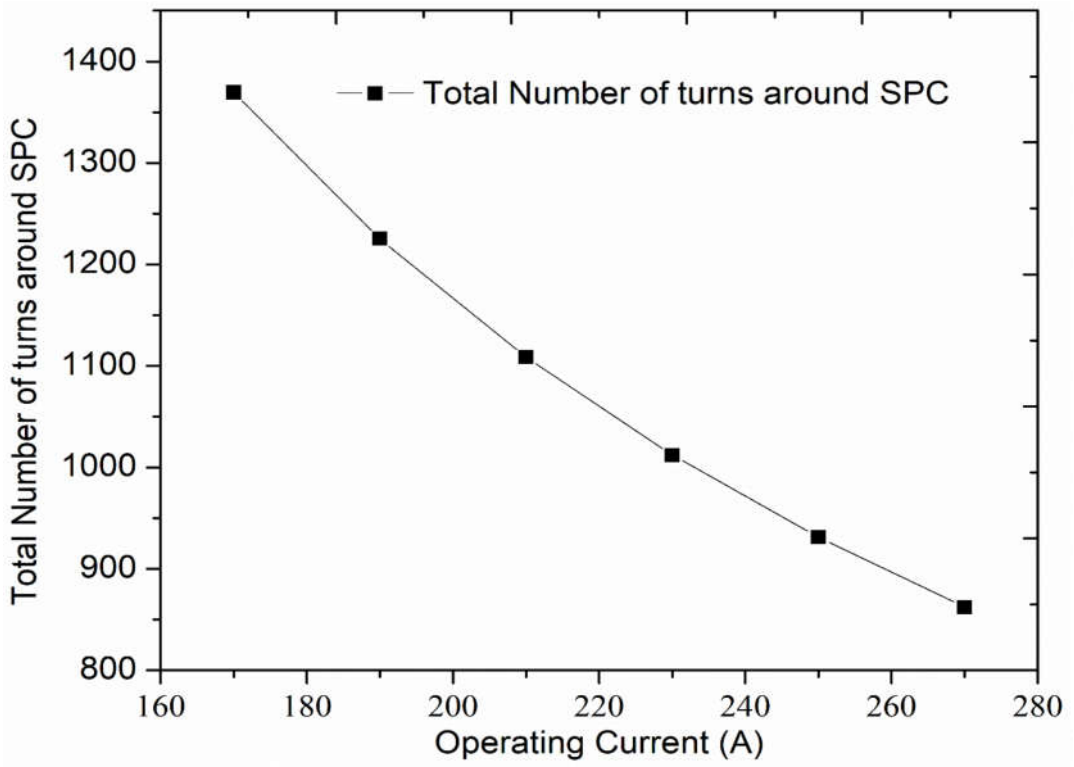

Figure 3.7 Operating current effects on number of turns around SPC

3.6.2. Effect of Solenoid Thickness on Magnet Topology

In this section, the effect of various solenoid thicknesses (5 mm to 35 mm) on the magnet design parameters like bore diameter, height of solenoid, number of turns/SPC, number of SPCs and length of superconductor. For a deliverable energy of 1 MJ and fixed maximum energy, in order to evaluate the effect of solenoid thickness on the magnet design parameters have been studied for a fixed minimum operating current of 270 A flowing through single HTS tape.

It can be observed from Figure 3.8 that the bore diameter is found to decrease drastically with thickness up to 20 mm and after this thickness the decline slope is lesser than the former. Bore diameter can affect the rest of the magnet topology alone

as it is related to all other design parameters directly or indirectly Equation 3-4 and Equation 3-6. Similar trend has been noticed for solenoid height Figure 3.9.

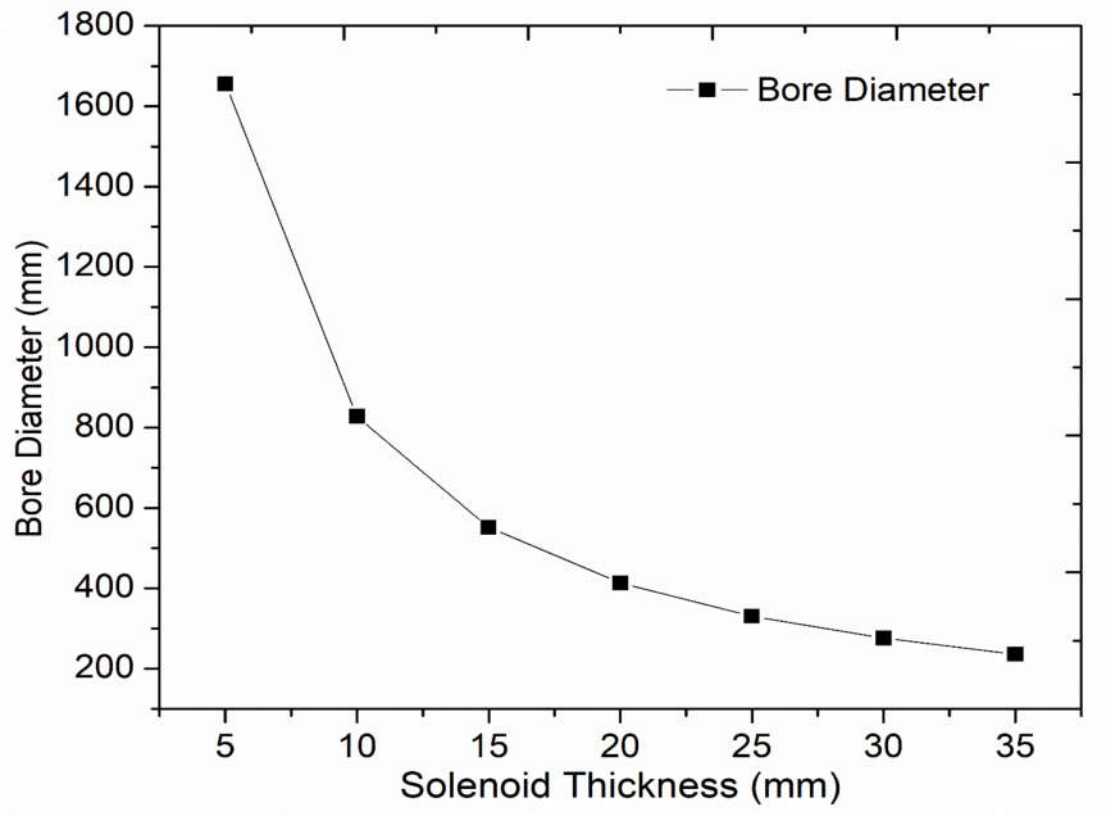

Figure 3.8 Effect of solenoid thickness on bore diameter

Number of SPCs and turns around single SPCs can also get affected by the solenoid thickness as described in Figure 3.10 and Figure 3.11. As the height of solenoid is varying with solenoid thickness thus number SPC required also varies. It can be noticed from Figure 3.11 that with increase in the solenoid thickness, number of SPC required to match the height of the magnet decreases as overall height of magnet decreases. With the increase in solenoid thickness from 5 mm to 35 mm, number of turns around the SPCs found to increase as described in Figure 3.11 as height is decreasing. Similar to bore diameter and solenoid height, the length of the superconductor is found to decrease rapidly up to 20 mm thickness and after that the decline slope is less steep than thickness varies from 5 mm to 20 mm (Figure 3.12). This implies that for thicker solenoid, less superconducting tape is required to store 1 MJ of energy than thinner magnet.

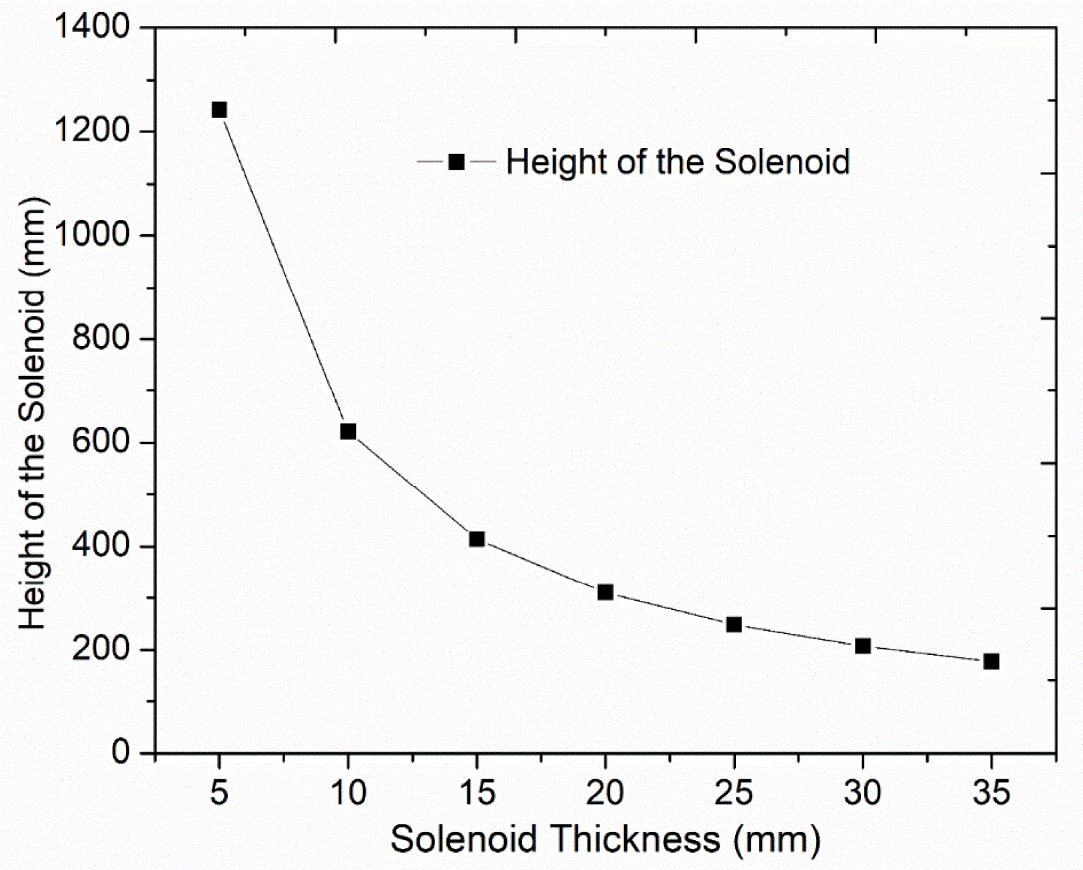

Figure 3.9 Effect of solenoid thickness on height of solenoid

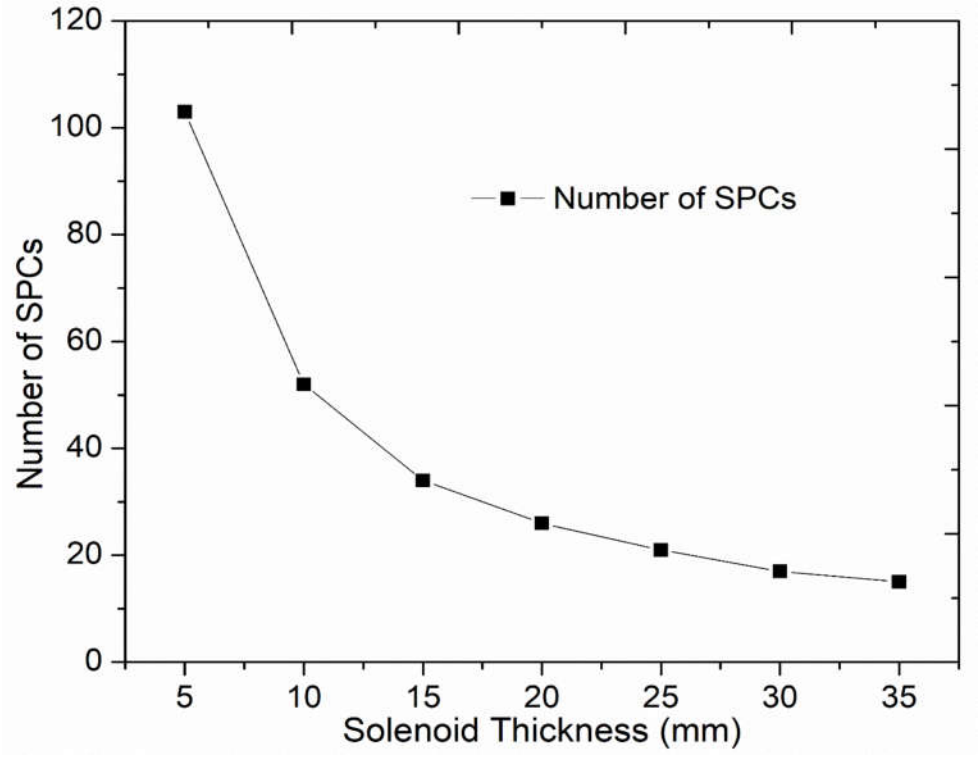

Figure 3.10 Effect of solenoid thickness on number of SPCs

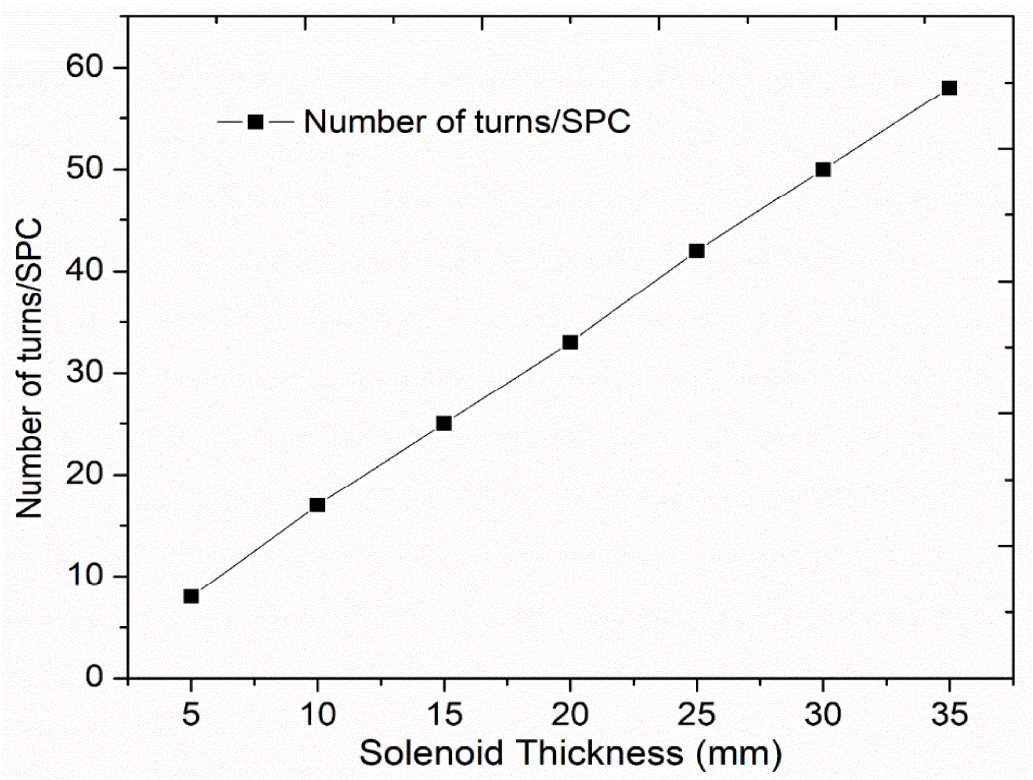

Figure 3.11 Effect of solenoid thickness on number of turns/SPC

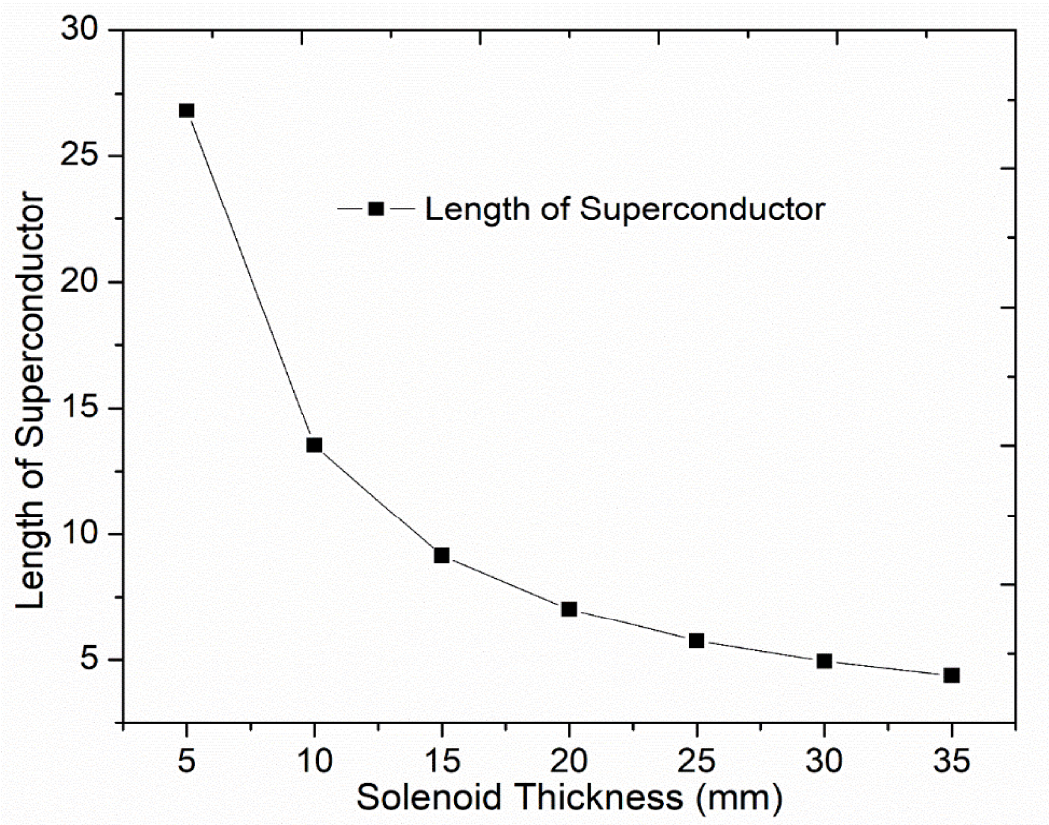

Figure 3.12 Effect of solenoid thickness on length of superconductor

3.6.3. Effect of Operating Temperature

In the present work, the magnet is assumed to be cool at 77 K however when the characteristic curve *B-T* has been drawn (Figure 3.13) for the tape at 14 K temperature, it has been found that perpendicular magnetic field has strong effect on the critical temperature of the tape which is around 330 A for 77 K at 0 T self-field. At 0 T self-field, the critical temperature of the tape is more than 10 times than that of at 77 K. In order to acquire the ratio for the critical currents (14K/77K) at different perpendicular magnetic flux densities, an attempt has been made to fit this curve with polynomial fit 3.7 and the coefficients of this fit are given in Table 3.6 with the standard errors done in estimating the correlation coefficients.

$$I_c\, Ratio(14K/77K) = \phi_1 + \phi_2 B + \phi_3 B^2 + \phi_4 B^3 + \phi_5 B^4 \qquad 3.7$$

Where *B* is the perpendicular magnetic flux density evaluated in Tesla (*T*), ϕ_1 , ϕ_2 , ϕ_3 , ϕ_4 and ϕ_5 are the correlation coefficients whose values are available in Table 2.

Table 3.6 Correlation Coefficients for Polynomial fit

Coefficients	Values	Standard Error
ϕ_1	10.30866	0.07595
ϕ_2	-5.50355	0.16249
ϕ_3	1.51155	0.08952
ϕ_4	-0.1916	0.01723
ϕ_5	0.00896	0.00107

It has been found that at 14 K, the critical current of tape is 3390 A which is 10.27 times more than that of what is available at 77 K @0 T self-field. If a load factor of 82% is used here which is equal to that has been used for 77 K @ 0 T, then, the minimum operating current that can be send through one tape at 14 K is 2780 A which is greater than the maximum current flowing through 6 stacked tapes at 77 K i.e. 1620 A.

This means 1.72 times current can be sent through single tape at 14 K thus there is no need of stacking of tapes to achieve higher currents. This implies, it is better to cool the magnet to lower temperatures as much as possible however this depends upon the

overall economic cost of the SMES system. Only after economic survey, the energy storage ratings can be finalized.

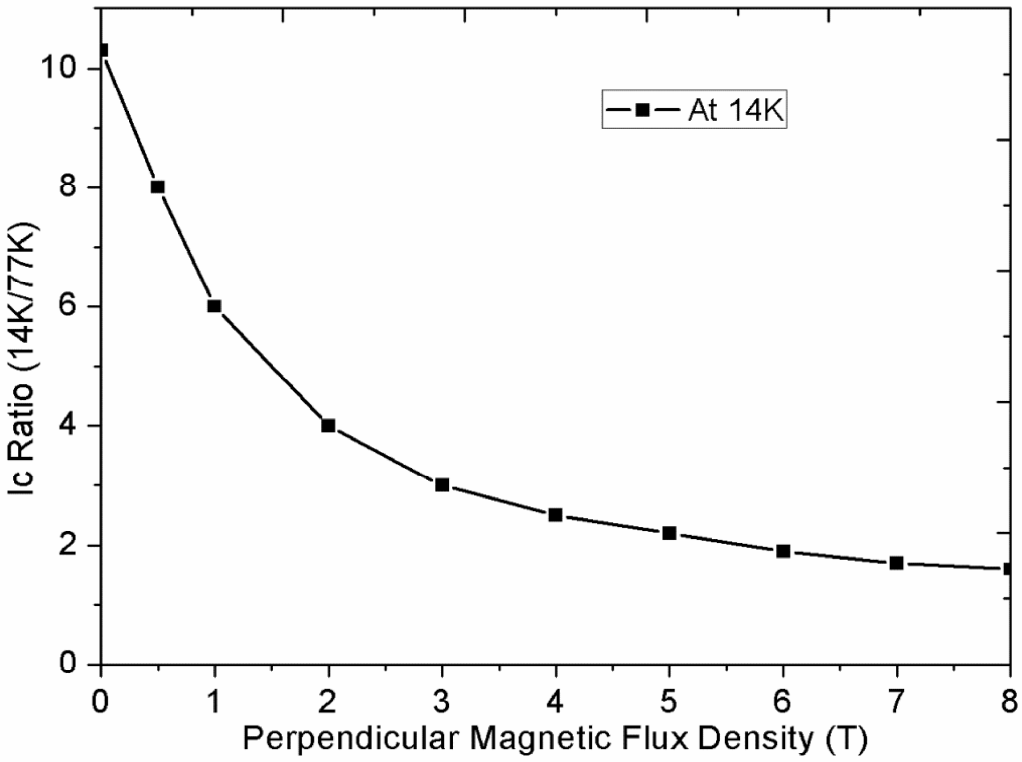

Figure 3.13 Critical current dependence on perpendicular magnetic flux density at 14K.

3.7. Conclusions

In this chapter, mechanical design aspects of the solenoid magnet have been studied where input, design and constraints parameters have been evaluated and the effect of operating current, solenoid thickness and operating temperature on the magnet topology has been examined. From the study, it can be concluded that higher currents have significant effect on the length of the superconductor used for energy storage which implies less superconducting tape is required for energy storage if the operating temperatures are low. Secondly, if large solenoid thicknesses used for magnet design then the overall height and bore diameter is found to decrease for same total number of turns.

Chapter-4

Effect of Self-field on Critical Current

In this section, effect of self-field on the critical current of the superconducting tapes, wounded on pancake coils, due to transport current has been evaluated using finite element methods. To compute the effective critical current (I_c) of the high temperature superconducting devices like magnets, it has been identified that there is a need to understand the critical current density (J_c) dependence on magnetic field (B) and orientation among the current direction and local magnetic field components i.e. J_c (B, θ). A 2D numerical model has been developed using critical state models (CSM) where the magnetic field dependency of critical current density (J_c) is considered. In the present model, the self-field developed due to current circulation through the superconducting tapes has been taken into account whereas the effect of orientation has not been considered in the present work. Since multi-turned pancake coils are involved in the design of solenoidal superconducting magnet this implies that the stacked tapes are interacting electromagnetically with each other thus the magnetic field dependency of J_c cannot be ignored. Mapped meshes are used within the superconducting tapes to achieve higher accuracies.

Keywords: Critical State Models, Self-field, Critical Current, Pancake Coils, Solenoidal Magnet.

4.1. Introduction

As discussed earlier, high temperature superconducting tapes are widely employed in various applications including high voltage power transmission, generators, motors, energy storage, and transformers etc. These superconducting systems can be implemented in various engineering fields like electric power transmission, power grid stabilization, ship propulsion, Maglev trains propulsion, electric aircrafts, solar and wind energy storage systems.

4.1.1. Literature Survey

Coated conductors can be used as long cables, single pancake coils and double pancake coils having circular or race-track configuration [78], [97], [99], [121], [169]–[174]. Coated conductors are frequently used due to their capability to handle large currents (helpful in power transmission cables) and magnetic fields (energy storage systems like SMES). Pancake coils are used in various applications including motor winding [175]–[177], magnets (solenoidal or toroidal) [121][128], [137], [178] where these are piled up one top of the other to generate the required field. In order to retain the superconducting nature of the tape, it has to be cooled below critical temperature which limits the amount of current (termed as critical current of the tape) that can carry by the tape. It has been found that this current is significantly affected due to the presence of either external magnetic fields or self-fields [170][179]–[182]. Thus, it becomes essential to know about the critical current (I_c) dependency on the magnetic field (B) as I_c magnitude can directly affect the design and optimization of the superconducting systems. Though, almost all superconducting tape manufacturers have defined the I_c characteristics with 0 T self-field. Also, there is lack of information on the effect of external field to the I_c of the tape. Moreover, the effect of neighboring tapes or coils has not been considered in the general information catalogue as the I_c can vary depending on the temperature and type of engineering applications. As large currents are involved in the magnet design, self-field can affect the I_c of the tape thus in the present work, a multi-turned pancake coil has been considered to evaluate such effects and I_c variations are evaluated for each strand. Magnets are generally designed to work near critical currents and thus, I_c can influence its geometrical parameters like height, bore diameter, thickness of magnet,

number of turns, inductance and length of the superconductor, an analysis has been done on solenoidal magnet in order to have a feel how significantly I_c can affect topology of superconducting magnet.

Many models and strategies have been tried in the past to evaluate the critical current of the single or multi superconducting tape's arrangement which can be found in [32], [179]–[181], [183]–[186]. Most of these studies considered power cables with low aspect ratios or having small circular cross-sectional area. Few studies have been performed where cable consisting superconducting tapes with high aspect ratios where critical current of Roebel cables (used in transformer windings) have been estimated [179][181]. These models have provided fair results however, they need comparative and iterative processes to evaluate the I_c and there is a need to consider uniform current distribution within each superconductor. A detailed report on ITER's solenoid coil is available in [187] where effect of self-field and current non-uniformity on the voltage-temperature relation of the ITER's central solenoid insert coil through numerical calculations has been studied. A more accurate way to estimate critical current of the tape formed as a coil or cable is to incorporate the critical current dependency of the superconducting tape or coil on the local flux density J_c ($\boldsymbol{B}$). Kim model [188] is usually used to describe the critical current density dependency on the local magnetic flux density J_c ($\boldsymbol{B}$). This model is also employed to estimate the AC losses among superconducting devices using various formulations [189]–[191]. In order to model the resistivity of the superconducting material, generally *E-J* power law is used. For the detailed description, one can refer to [31], [192] where three different numerical approaches have been explained. Few models [32][184] have considered numerous conductors to evaluate the current distribution however for this one needed to solve non-linear *E-J* power law relationship or an iterative estimation of the I_c which again required large computing time to get the numerical solution of the problem.

Therefore, in this work, a novel dc model has been introduced that can be implemented to estimate the critical current among the multi-turned pancake coil used to store 1 MJ of energy. Only inductance of the coil has been considered and no effect of mutual inductance taken into account. Like study available in literature [181], in

thus study a variable P has been developed in order to acknowledge the E-J relationship. This parameter is assumed to be uniform in each domain and provides simple, robust and fast numerical technique to evaluate the critical current of the stacked superconductors.

In this chapter, firstly assumptions have been made prior to the mathematical modelling of the superconducting tapes then the criteria required for the selection of I_c has been discussed. Further, the discussions on the critical current dependency on temperature has been described. Computational analysis has been done on the multi-turned pancake coil to evaluate the self-field critical current at 77 K. For the validation, the developed model was tested with previous studies. Final section provides the outcome of the study.

4.2. Assumptions

1. 2D model is considered for the study.
2. Time independent analysis has been performed.
3. Effect of mutual inductance has not been taken into account.
4. Analysis has been done on 2D model when viewed from the top and only one pancake coil has been considered for the analysis.
5. Tape bending effects have not considered.
6. Since current is flowing through the superconducting layer thus only this layer has been modelled as a computational domain along with vacuum domain which is assumed to be air.
7. Voltage drop is assumed to uniform across the cross-section of each conductor as infinitely long conductors have been considered.

4.3. Numerical Scheme

Figure 4.1 shows the 2D model of the stacked HTS tapes containing 108 tapes (18 turns and 6 stacked tape) of a pancake coil. **Figure 4.1** (a) comprises air and superconducting domain of the model and **Figure 4.1** (b) shows the magnifying view arrangement of the tapes. Only superconducting layer has been modelled among the HTS tape as current is assumed to flow through it. Table 4.1 comprises the modelling parameters used to evaluate the self-field effects on the critical current. Kim model

[188] has been used in order to consider the local field effects of self-field whose constant B_0 and k values are tabulated in Table 4.1.

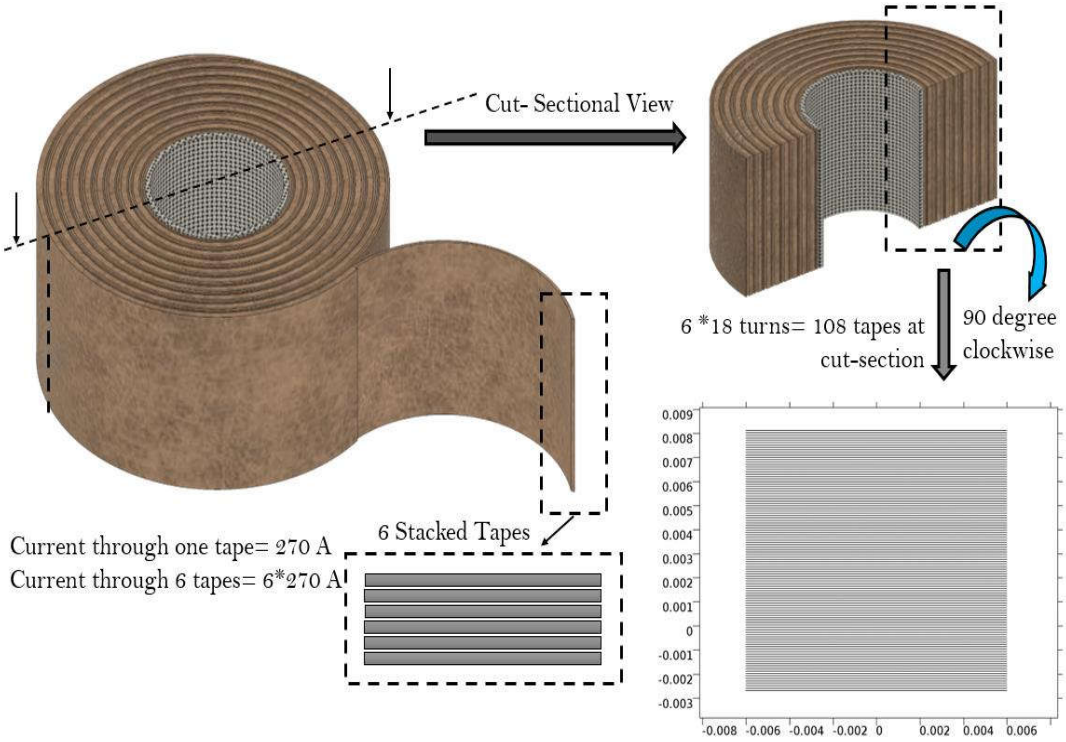

Figure 4.1 Arrangement of 108 tapes (6 stacked tapes with 18 turns)

Table 4.1 Model Parameters

Parameters	**Data**
Number of parallel tapes	108
Width of the tape	12 mm
Thickness of the tape	1 μm
Inter-distance among tape	1 to 3×10^{-4} m
Index, n	30
Critical Electric field	10^{-4} V/m
Constant, k	0.29515
Magnetic field, B_0	42.65 mT

The magnetic flux density **B** is expressed in terms of magnetic vector potential **A** thus $\mathbf{B}=\nabla\times\mathbf{A}$ and electric field can be represented as $\mathbf{E}=-\partial\mathbf{A}/\partial t-\nabla V$ where V is electric potential. Since DC currents are involved in superconducting magnet applications thus $-\partial\mathbf{A}/\partial t\rightarrow 0$ which means current density J has reached its steady state and magnetic field inside the superconductor is time independent. As steady

state conditions have been assumed which are identical to the practical DC current flow situations for most of the applications and this method can be used all such superconducting applications. This is apparently a simplified characterization of the actual physics transpiring within the superconducting tape where due to flux flow in flux percolation results in the dc voltage dispersed along the length of the tape.

Since the problem is 2D thus only one component of electric field which is parallel to current flow is taken into account in the present study. As magnetic field inside the superconducting tapes invariant with time $-\partial \mathbf{A}/\partial t \to 0$ thus electric field reduced to $\mathbf{E} = -\nabla V$, implies for the 2D problem, V should be uniform over the cross-section of each superconductor. Also, the voltage gradient ∇V is considered to be uniform across the cross-section of each conductor as infinitely long conductors has been assumed for the study which implicitly meaning that E (voltage drop/length) is also uniform within all superconducting tapes. Critical electric field (E_c) is the field value where current density reaches its critical value $J_c(\boldsymbol{B})$ and its relationship with current density is given in (Equation 4-1) [25].

$$E = E_c \frac{J}{J_c(\mathbf{B})}\left|\frac{J}{J_c(\mathbf{B})}\right|^{n-1} \tag{4.1}$$

$$J = J_c(\mathbf{B})\ P \tag{4.2}$$

where

$$P = \frac{E}{E_c}\left|\frac{E}{E_c}\right|^{\frac{1}{n}-1} \tag{4.3}$$

As discussed earlier, for DC inputs, electric field E is uniform over the cross section of superconductor which implies P is also uniform. It can also be noticed that when current reaches its critical value, $J=J_c(\boldsymbol{B})$ (Equation 4-2), P=1 (Equation 4-3) and $E=E_c$ (Equation 4-1). As evaluation of P does not involve solution of non-linear equation like E-J relationship thus problem can be solved in less time. As in the solenoidal superconducting magnet, the 49 pancake coils are having 18 turns (108 tapes locally) on each pancake and the individual turn is carrying a same current therefore a parameter P_i has been considered that will be constant in each turn and

which ensure that a current of I_a is flowing through each conductor. For a current I_a flowing through i^{th} conductor, automatically its corresponding P_i value will be chosen for the calculations as described below:

$$I_a = \int_{\Omega_i} P_i J_c(\mathbf{B})\,\mathrm{dxdy} \qquad 4.4$$

As P is constant therefore,

$$P_i = I_a / \int_{\Omega_i} J_c(\mathbf{B})\,\mathrm{dxdy} \qquad 4.5$$

The electric field E_i (voltage drop per unit length) in the i^{th} conductor can be estimated as

$$E_i = E_c P_i \left|P_i\right|^{n-1} \qquad 4.6$$

Ampere's law (Equation 4-7) has been used in the form of magnetic vector potential to estimate magnet field. The equations involved are given below:

$$\nabla \times H = J \qquad 4.7$$

$$B = \nabla \times A \qquad 4.8$$

$$\mathbf{B} = \mu \mathbf{H} \qquad 4.9$$

$$\rho_{HTS} = \frac{E_c}{J_c}\left|\frac{J}{J_c}\right|^{n-1} \qquad 4.10$$

$$\nabla \times \frac{1}{\mu}\nabla \times \mathbf{A} = \mathbf{J} = J_c(\mathbf{B}) P \frac{\mathbf{J}}{J} \qquad 4.11$$

For air/insulating domain P_i=0 whereas for superconducting domain its value can be found using (Equation 4-5). Thus the 2D problem is now reduced where the attention will be focused on solving equation (Equation 4-5) and (Equation 4-11) and by applying appropriate boundary conditions depending upon the number of turns; magnitude of transport current etc. the computational model can be solved using Comsol MultiPhysics.

4.4. Selection of the I_c criteria

When the voltage reaches its critical value, E_c, which is generally 1 $\mu V/cm$ for high temperature superconductors, then the current is called as critical current (I_c). For the pancake coils usually critical current can be evaluated by measuring the coil's end-to-

end voltage known as coil critical current (I_c^{coil}). In case of multi-turned coils, there may be a situation when the innermost turn achieves critical current at a value lower than I_c^{coil}, which is quite unsafe and can lead to over-critical situations, even at a current lower than actual I_c^{coil}. Thus, it is much important to know this condition as critical current is the maximum current that a superconducting system can carry without quench, therefore it becomes imperative to define this criterion with accuracy.

Therefore, for the present study, where 6 stacked tapes are wounded on the pancake coil having radius r, and turn spacing s, the I_c criteria is defined as follows:

i. I_c is the current at which the voltage drops per unit length of the superconductor $E_{i,j}$ has reached its critical value E_c in at least one conductor of the stacked tapes used to wind the coil, i.e. $P_{i,j}$=1.

It is easy to evaluate electric field from P_i by using (Equation 4-6) once the numerical model gets solved. Besides the merits of the model, this approach has one limitation also; present model describes the voltage drop V near the critical current density and it does not consider the real dynamics behind the voltage drop far from the critical current density.

4.5. Validation

To validate the computational procedure, Roebel cable composed with 10 strands has been considered from the literature [181]. Parameters used for the modelling are tabulated in Table 4.2 and schematic of the Roebel cable's strands is given in Figure 4.2.

The tested parameters are given in Table 4.3, where total 30 sets have been considered in order to evaluate the self-field effect on the critical current of the Roebel cable and Figure 4.3 represents the values obtained by the authors for more than 50,000 tests. Analysis showed that the nearest I_c achieved for Roebel cable is 534.83 A against 539 A with an error of 4.11 A for J_{c0} (A/m^2) = 4.75E10, B_c= 35 mT, b= 0.6 and k=0.25. The developed model has been tested for 30 different inputs and all obtained results lying among the feasible range as shown in Figure 4.4.

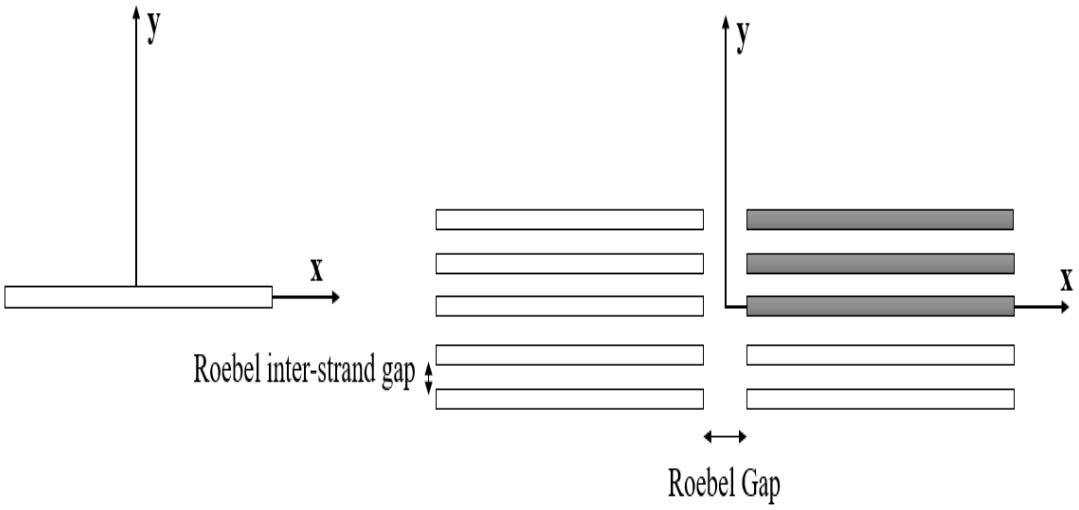

Figure 4.2 Tape arrangement

Table 4.2 Parameters for model validation

Parameters	**Value**
Number of Strands in Cable	10
Strand Width	1.8×10^{-3} m
Tape thickness	1×10^{-6} m
Roebel Gap	1×10^{-3} m
Roebel inter-strand gap	1×10^{-4} m
Exponent of E-J power Law	21
Critical Electric field	1×10^{-4} V/m

Table 4.3 Parameters used in computational validation

Parameters	**Tested Values**
J_{c0} (A/m^2)	[4.25, 4.5, 4.75, 5, 5.25] $\times 10^{10}$
B_c (mT)	25, 30, 35, 40
b	0.5, 0.6, 0.7
k	0.2, 0.25, 0.3

Mapped mesh has been used for the discretization of the superconducting domain and it has been found that results are matching with Zermeno et al. [181] findings. All calculated values are lying in the feasible region offered by the authors, thus this model can be directly used to evaluate the objectives of this thesis work.

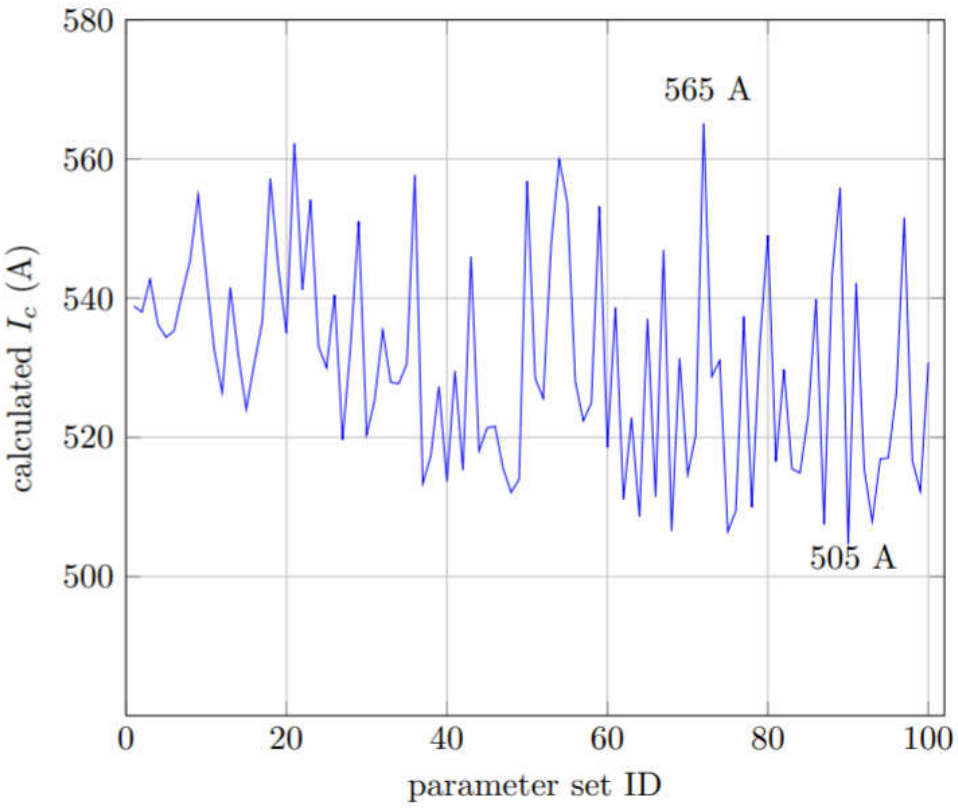

Figure 4.3 Calculated I_c for various input parameters

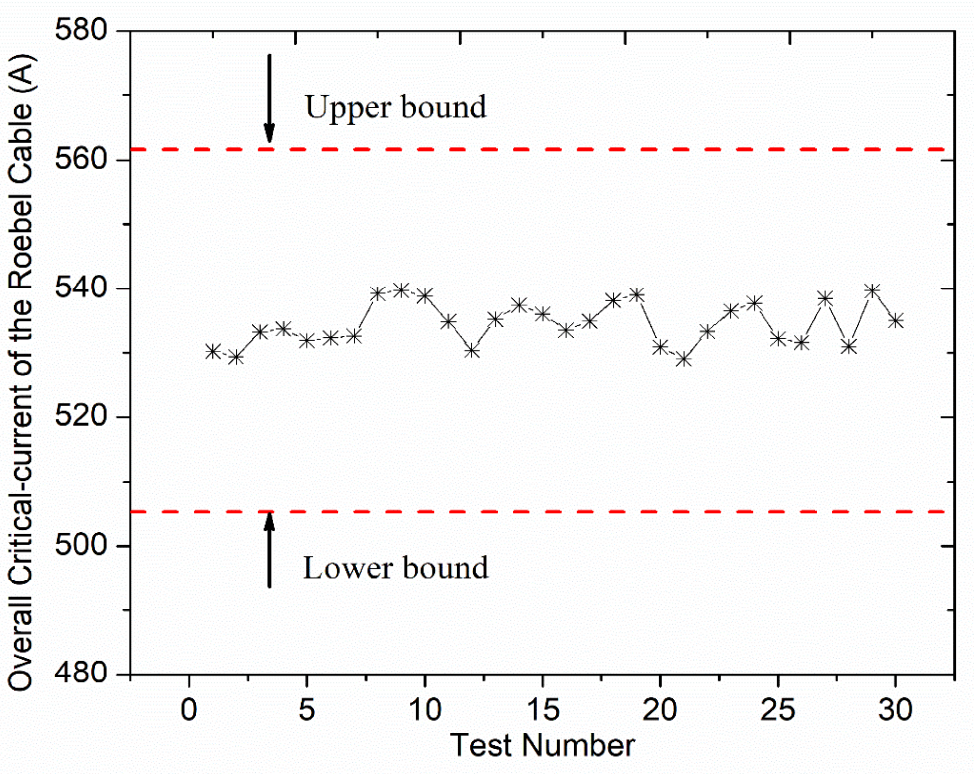

Figure 4.4 Calculated I_c for 30 different test parameters for validation

4.6. Model Description

Figure 4.5 shows the 2D computational domain of the stacked tapes where 108 superconducting layers have been drawn one top of the other with a minute gap among them in order to evaluate the effect of tight or loose winding.

To model the resistivity of superconducting layer *E-J* power law has been used with index, n=30. Time independent analysis has been performed using Comsol Multiphysics. An additional parameter P has been developed which ensures that at the critical current the voltage drop per unit length should reach its critical value E_c in at least one conductor.

$$\max_{i\in\{1,2....k_i\}} P_i = 1 \qquad 4.12$$

This model works very well for Zermeno and Grilli et al [181] and it is easy to implement in order to estimate the critical current of the multi-turned pancake coils. The methodology has been employed to evaluate the self-field effects on the critical current, magnet topology.

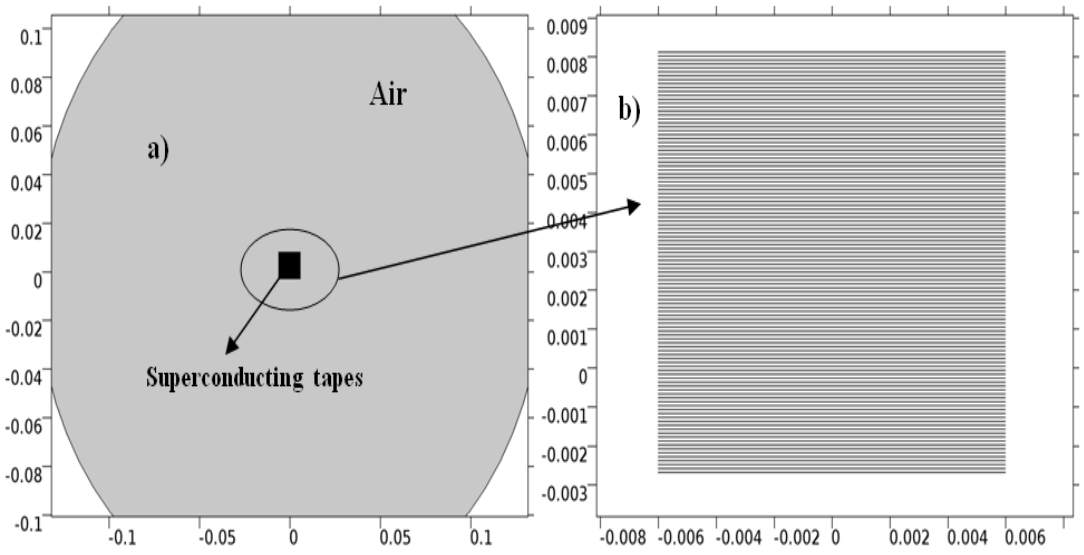

Figure 4.5 Geometrical representation of the 2D model

The transport current (I_a) flowing through the i^{th} individual turn of the coil can be calculated using (Equation 4-9). Using equation (Equation 4-10), the parameter P_i can be evaluated. The voltage drops per unit length E_i in the i^{th} superconductor can be calculated using (Equation 4-11). Ampere's law can be rewritten (Equation 4-12) in order to evaluate current densities and individual magnetic fields with the help of

magnetic vector potential. It has been noticed that the time required to solve the computational model is found to less than 90 seconds, this implies the model is quite quick to solve the problem. More than 2e5 degree of freedoms have been solved for each case.

4.6.1. Mesh Sensitivity Analysis

The computational domain is discretized by using mapped meshing where different number of elements have been employed for the discritization. Number of elements have been varied from 25 to 100 for the mesh sensitivity. Table 4.4 illustrate the effect of mesh density or number of elements on the critical current and time elapsed to solve the computational domain. Figure 4.6 represents the mesh density for six different number of elements and it can be noticed from the Table 4.4 that for case-5 i.e. for 100 number of elements, the results are same as that of case-6, thus this mesh has been used for the discritization of the superconducting domain and free triangular meshing has been used for the air domain with fine meshing. Number of domain elements, boundaries, degree of freedoms and time elapsed for computations are enlisted in Table 4.4. The system configurations were as follows: Intel Core i5-8250 CPU @1.6GHz, 8GB RAM, 64-bit operating system with Window 10.

Table 4.4 Mesh sensitivity studies

Sr. No.	Number of elements	Number of domain elements	Number of domain boundaries	Degree of freedom	Time (s)	I_c (A) of 108 tapes
1.	20	11962	4584	28402	51	33229
2.	40	30488	8904	69774	56	33223
3.	60	45966	13224	105050	61	33223
4.	80	76814	17544	171066	66	33223
5.	*100*	*95360*	*21864*	*212478*	*69*	*33222*
6.	120	139450	26184	304978	78	33222

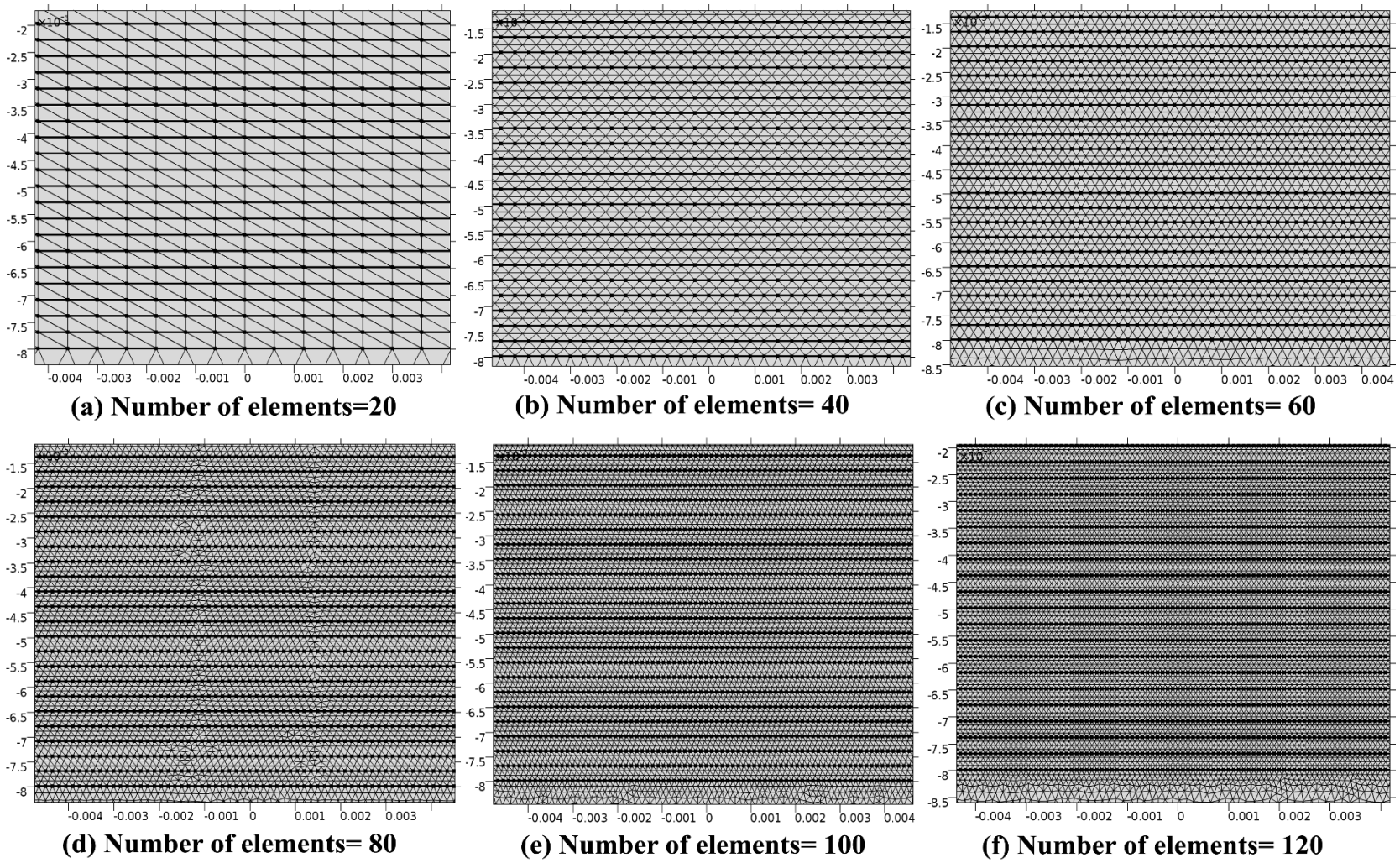

Figure 4.6 Mesh sensitivity for computational domain

4.7. Effect of Self-field on Critical Current of Tape

The critical current for the tape is 330 A and as 108 tapes are stacked around the coil thus the critical current for all tapes is equal to 35,640 A without considering self-field effect. The self-field analysis on multi-turned coil has been done using Comsol MultiPhysics software package. As multi-turns are involved thus the effect of tightened and loosened windings around the coil has also been studied in this work.

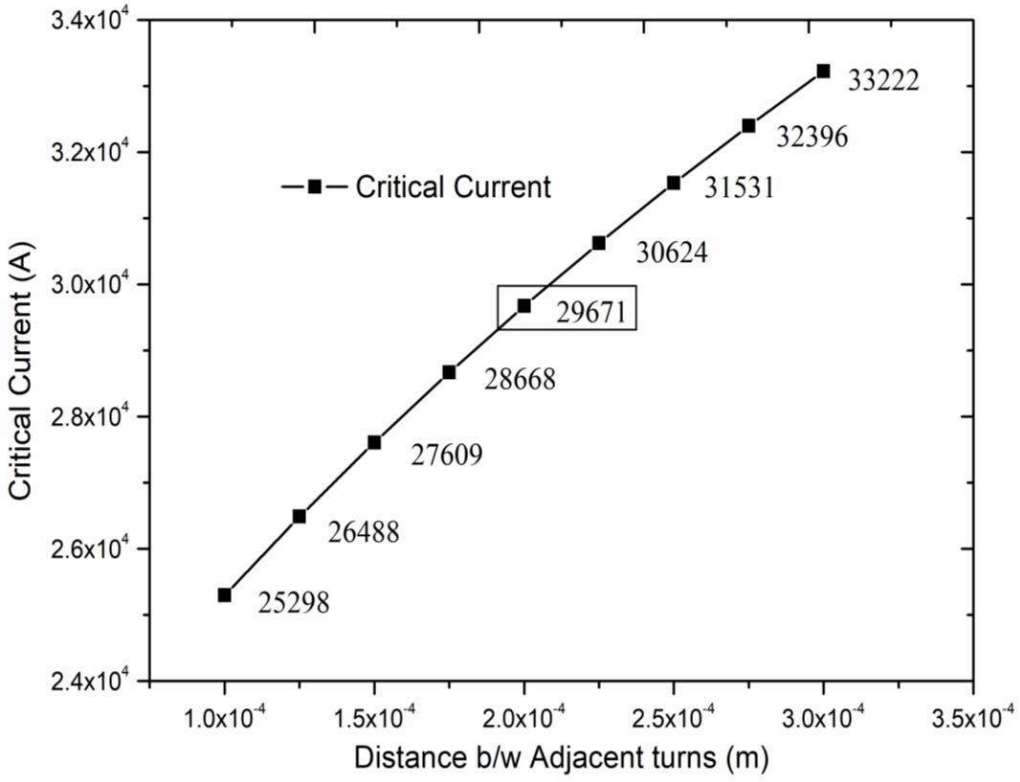

Figure 4.7 Critical current Vs inter-distance among tapes

The results showed that there is a significant drop in the critical current of tape (highlighted with rectangular box) which is nearly equal to 275 A for 108 tapes with 0.2 mm inter-distance among the turns against 330 A with no self-field. To evaluate the effect of tightened or loosened winding the analysis has been done by increasing and decreasing 0.1 mm gap among 0.2 mm initial gap.

Figure 4.7 shows that with the increase or decrease in the inter-distance among tapes, the critical current is found to increase or decrease respectively. However, the magnetic flux density is found to decrease with the inter-distance among tapes which results in less dense fields and vice versa as in Figure 4.8. The parallel and

perpendicular magnetic flux density component's (T) distribution for 108 turns is represented in Figure 4.9 and Figure 4.10 respectively. This implies that one has to sacrifice among the denser fields if the objective of the study is focused to achieve more transport currents. However, for the SMES or MRI applications where the sole motive is to have higher trapped fields, tapes are needed to be tightly wounded to ensure denser fields.

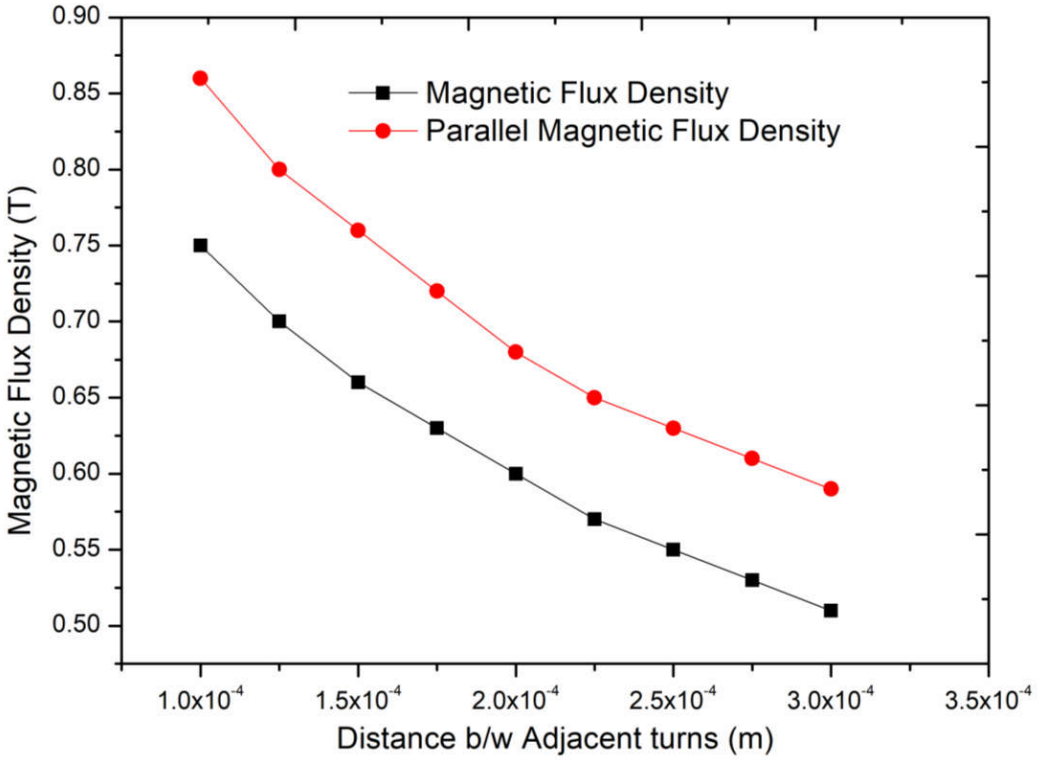

Figure 4.8 Magnetic flux density Vs inter-distance among tapes

Therefore, it has been concluded from here that the inter-distance among the tapes is a crucial factor as it can affect the magnetic flux density significantly. Such situations usually impact the performance of magnetic energy storage or MRI systems where high density fields are generally required to have higher power densities.

Also, number of turns around the pancake coils may also affect the critical current and magnetic flux densities due to self-field however in this work that aspect has not been taken into account.

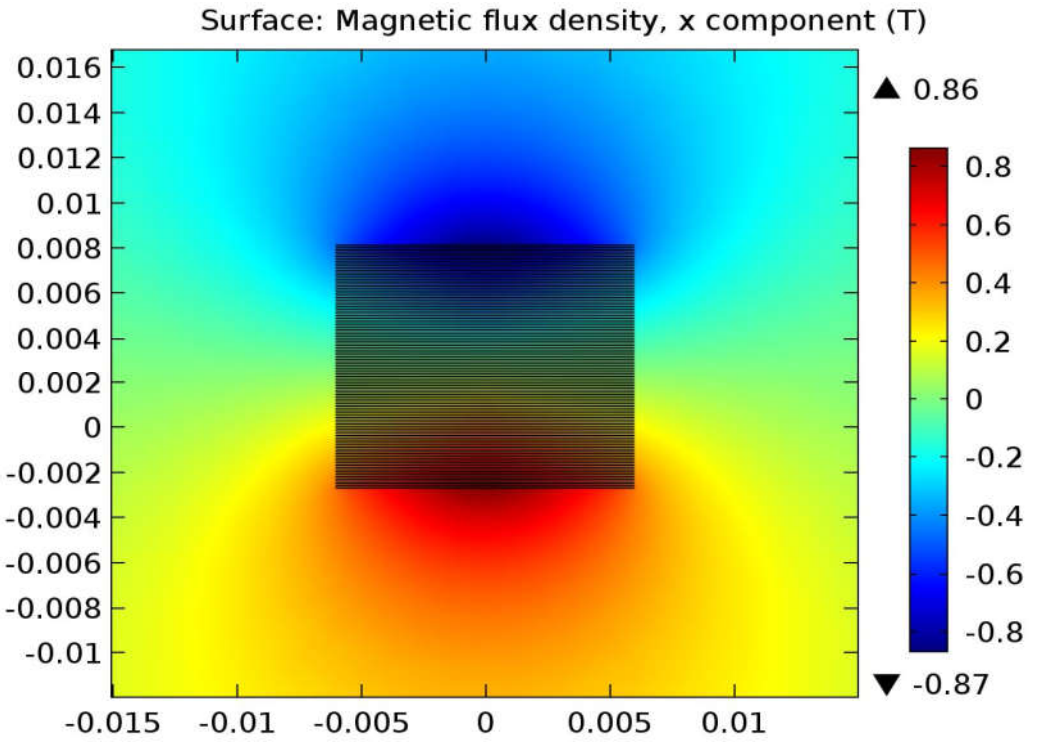

Figure 4.9 Parallel magnetic flux density component (T)

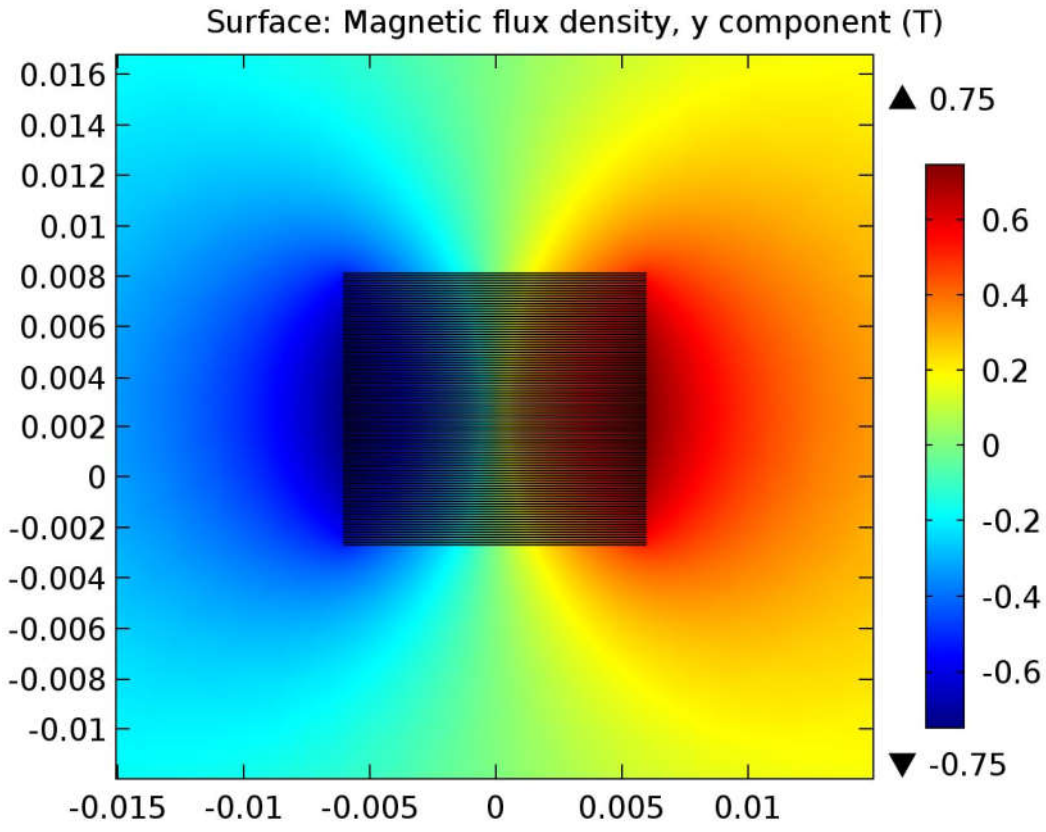

Figure 4.10 Perpendicular magnetic flux density component (T)

4.8. Self-field effects on Magnet topology for Single Pancake Coil

Superconducting magnetic energy storage can be achieved using superconducting tapes in solenoidal or toroidal configuration. In the present study, solenoidal configuration has been proposed and the effect of self-field on the energy storage parameters has been evaluated. Maximum energy (E_{max}) stored in an inductor when a current I_{max} is flowing through it can be calculated using (Equation 4-13) and deliverable energy can be estimated using (Equation 4-14). At 0 T self-field, the I_c of the tape is 330 A and the operating current is 270 A with 81% approximate load factor.

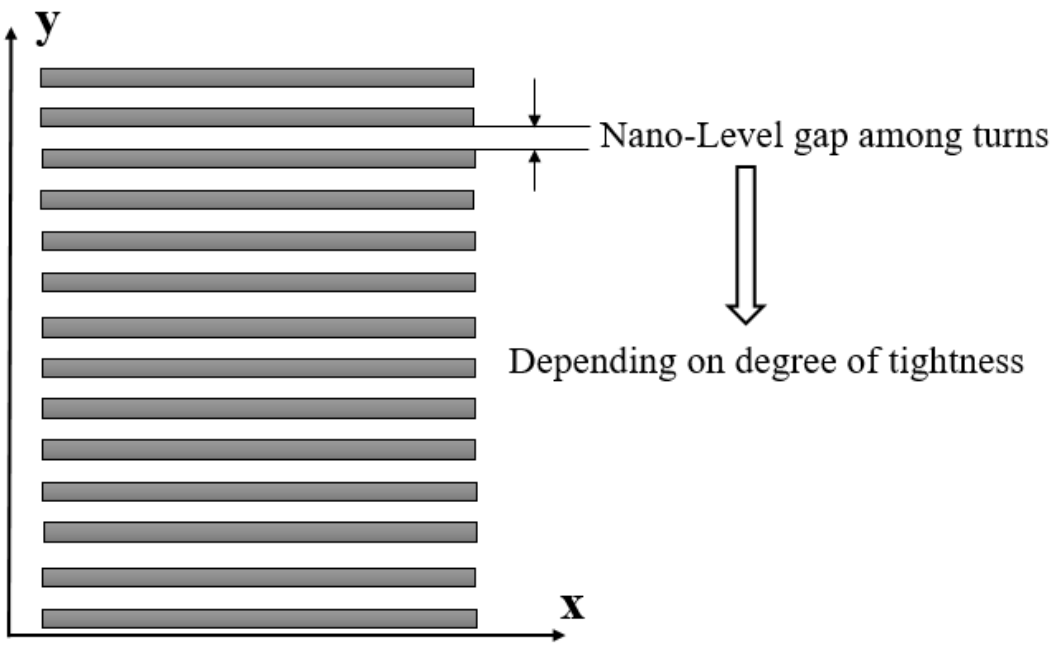

Figure 4.11 Tape arrangement

It has been assumed that the minimum current (I_{min}) is the current that is flowing through a single tape and minimum power requirement which also depends upon critical current (I_c) and load factor considered for the study. For this case 270 A is the minimum current flowing through a single tape and in order to achieve the minimum power requirement I_{max} should be 1.62 kA where six tapes are stacked together to ensure the minimum deliverable energy 1 MJ and having 0.784 H inductance of the coil. Figure 4.11 shows the arrangement of the tapes along with the adjacent gap among the tapes.

$$E_{\max} = \frac{1}{2} L I_{\max}^2$$

4.13

$$\Delta E = \frac{1}{2} L \left(I_{max}^2 - I_{min}^2 \right) \qquad 4.14$$

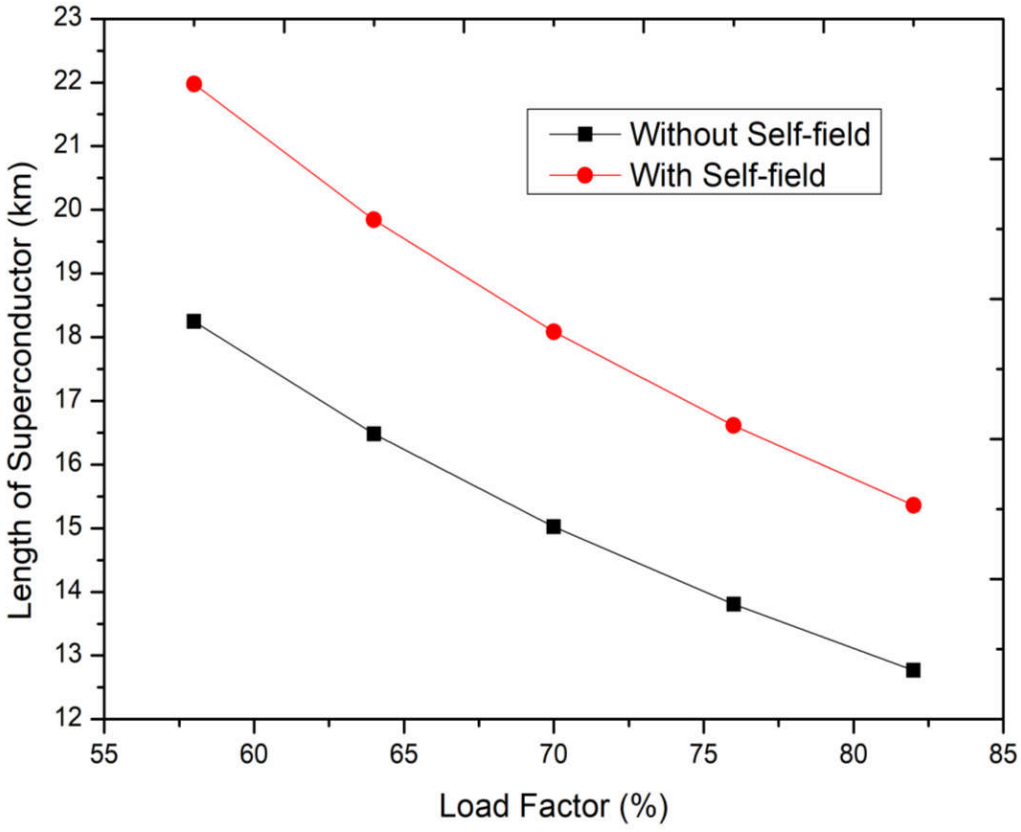

Figure 4.12 Load factor Vs Length of Superconductor

For lower load factor as in Figure 4.12, the superconductor length is found to increase for the same deliverable and maximum energy which implies it is better to operate near the critical current (high load factor) as less superconducting tape is needed for energy storage. Also, with decrease in transport current, the inductance (Figure 4.13) is found to increase which tells more time is required for the current to achieve its steady state. However, in this work, only steady state analysis has been performed where magnetic vector potential is independent of time $-\partial \mathbf{A} / \partial t \to 0$.

However, when self-field effects are taken into account, the I_c of the tape has been reduced to 275 A which is well below the I_c (330 A) at 77 K @ 0 T self-field. Keeping the load factor same as that of without self-field effect, the operating current

through a single tape reduced to 225 A. After keeping E_{max} and ΔE constant, it has been found that more superconductor is required to store same energy and the variation of superconductor's length with operating currents with and without self-field has been plotted in Figure 4.14. Where *A* and *A1* represents 0.81 load factor (LF) and *E* and *E1* represents 58% LF. It can be observed that the SC tape length required for energy storage (1 MJ) is found to increase from 12.8 km (I_c=330 A) to 15.4 km (I_c=275 A).

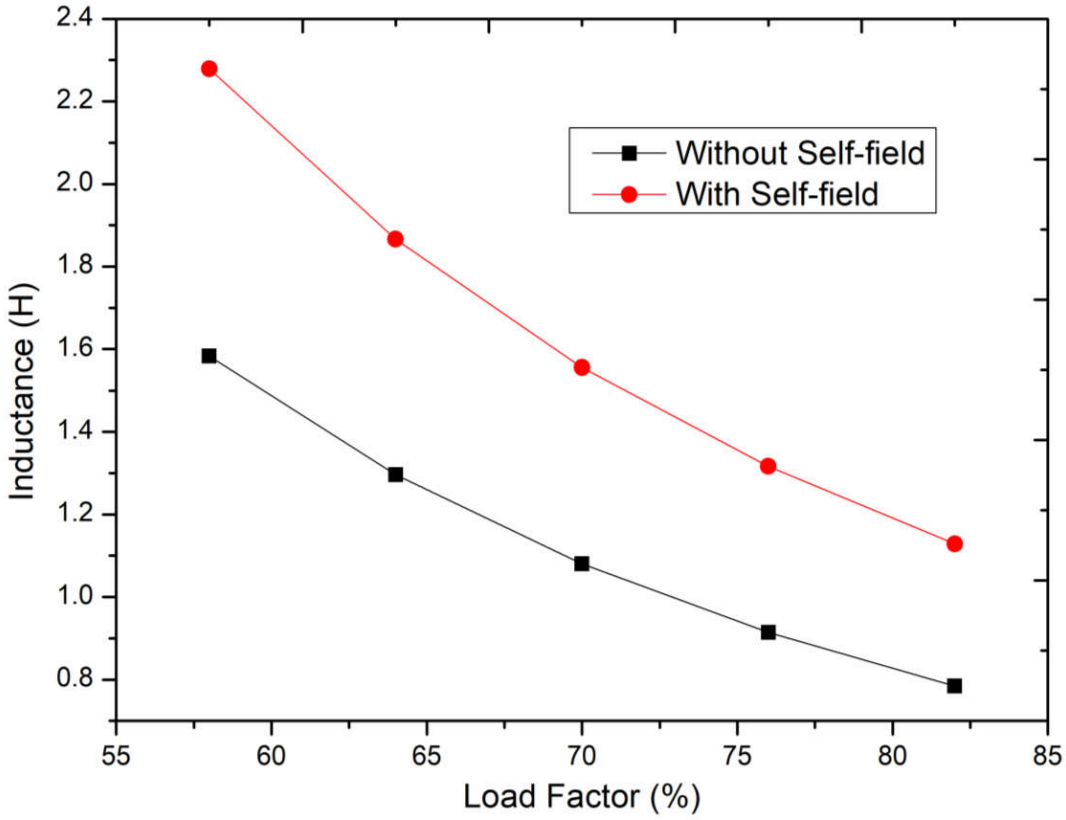

Figure 4.13 Load factor Vs Inductance of the coil

Due to the self-field, current reduces significantly and thus, more number of turns are needed to ensure the same stored energy capacity and this further results in increasing the overall thickness of the magnet Figure 4.15. This implies that self-field can influence the topology of the magnet to a great extent. However, in the present study fixed bore diameter and aspect ratios have been considered. If such geometrical parameters could also have considered under the influence of self-field, then it may affect the magnet topological parameters to even a broader extent. Meanwhile from

the present scenario, this is understood that the self-field contributions have to be considered while designing the superconducting magnet.

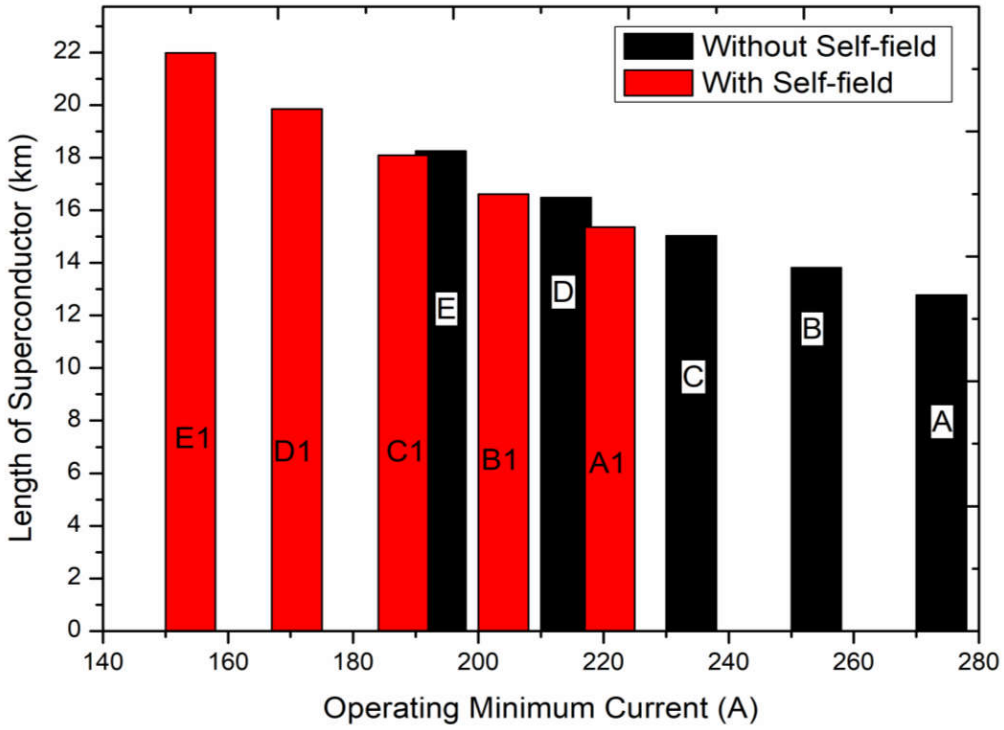

Figure 4.14 Operating current Vs Length of superconductor

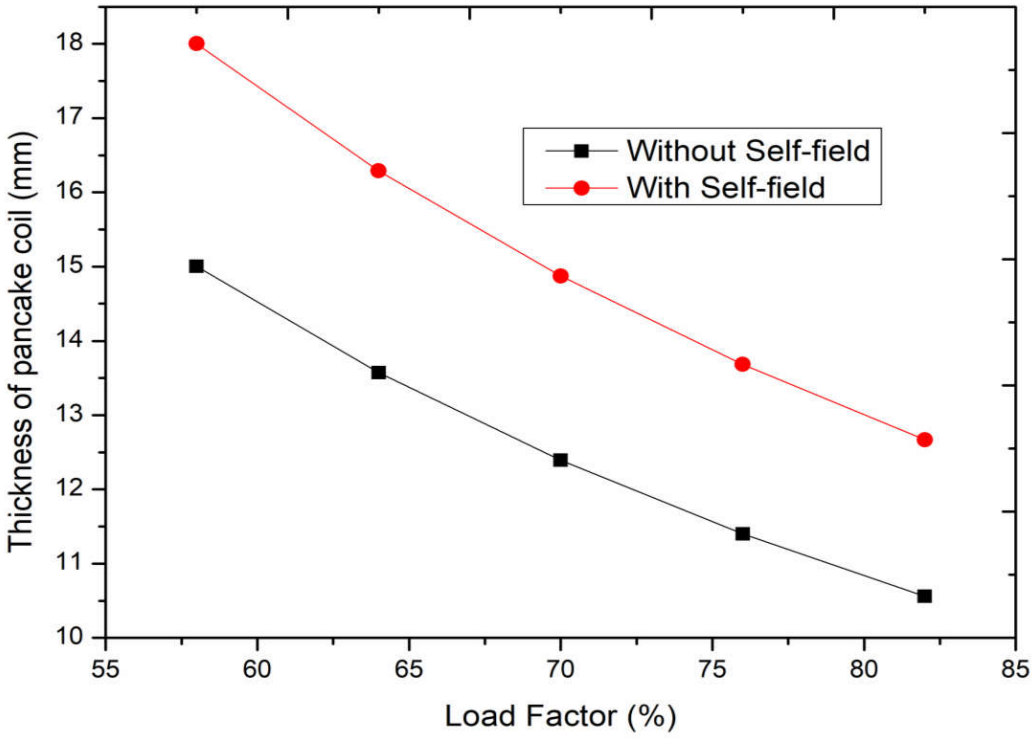

Figure 4.15 Load factor Vs Thickness of coil

4.9. Conclusions

In this chapter, the self-field effects on critical current have been studied for the magnet coils however in order to avoid the computational modelling difficulties various approximations have been considered. In order to identify the self-field effects, Kim model has been incorporated and a parameter *P* has been used to ensure the critical current existence in at least one tape out of 108 tapes of a pancake coil. It has been concluded that self-field has significant effect on the critical current of the coil and thus it can influence the magnet topology to a great extent. Thus, this aspect should be considered while designing the superconducting magnet.

Chapter-5

AC Loss Modelling of Superconducting Magnet

In this chapter, modelling of superconducting magnet is described by using finite element methods to evaluate the AC losses involved. As there are various methods are available to evaluate the AC losses in the superconducting tapes, therefore the selection of the method used in the present study is done on the basis of accuracy of the solution and computational time required. After presenting the computational domain of the magnet, the Maxwell's equations are solved using Comsol Multiphysics software package for 2D model implementing H-formulations. The assumptions are made to model the coil cross-section as number of individual turns in order to reduce the computational time. In order to further improve the accuracy and computational time, mapped meshing is implemented for meshing the computational domain. Local variations in the magnetic field have been considered by incorporating Kim model to estimate the critical current density. During investigation some interesting points are found for further analysis and a complete modelling of the stacked superconducting tapes is done.

Keywords: H-formulations, Kim-model, Comsol MultiPhysics, AC Losses, Superconducting magnet, Maxwell equations.

5.1. AC Losses in HTS conductors

In most of the electric power applications, generally at low frequencies it has been found that resistance arises in type-II superconductors due to flux flow and flux creep. As type-II superconductors can carry more current in the presence of larger magnetic field. However, losses may occur in type-II superconductors due to the appearance of electric field. Next generation superconductors are going to replace the normal conductors as the former produce negligible losses when compared with the later one. However, before coming into real life applications superconductors have to various requirements such as high critical current and low price. As superconducting devices work at very low temperatures (nearly at 77 K temperature) thus one has to consider economic aspects also while maintaining such low temperatures. Moreover, heat generated due to AC losses put an extra investment on the overall cost of the system, as this heating load has to be balanced by the cryogenic unit.

Therefore, before incorporating superconductors in the power devices financial constraints has to be considered such as material cost, energy cost, cryogenic unit cost, maintenance cost and the reliability of the system. As the resistance of the superconductor is almost negligible compared to normal conductor implies AC losses are found to be lower in superconducting systems then the conventional systems. Therefore, it is important to calculate the AC losses precisely in order to remove the heat load from the system economically and to retain the superconductivity of the system. The cooling can be done in two ways, convection cooling and conduction cooling. In the convection cooling, heat dissipation can be achieved by the evaporation of the coolant (helium, nitrogen). On the other hand, in case of conduction cooling a cryocooler is used to maintain the temperature of the system.

The detailed approach on the quenching of superconducting tape has been presented in Chapter 6. For each electrical power application, the AC losses are needed to be calculating as different time varying currents or magnetic fields are involved for different systems. AC losses can be obtained in two ways; transport current loss and magnetization loss. In the present study, attention has been focused on current losses only.

5.1.1. Types of AC loss

As discussed earlier, there are two types of AC losses; magnetization losses and transport current losses. Both of these losses results in power dissipation which increases superconductor's temperature. Due to this extra heat load, the cryogenic unit has to maintain the temperature of the system in order to avoid quenching of the superconductor.

Magnetization Loss (Q_m) this loss arises due to the application of alternating magnetic field to the superconductor. These losses are further classified into three categories; hysteresis loss, coupling loss and Eddy current loss. The source of energy for such losses is coming from the applied magnetic field.

Such losses are coming into picture due to the irreversibility caused by vortex pinning [20]. due to the pinning, the flux entered to the superconductor is not found to same as that of leaving it. The hysteresis loop is coming into existence when a plot between magnetic induction, B and magnetic field, H is drawn. in the absence of transport current, the energy loss per cycle is proportional to the area under the loop [193]. Such hysteresis losses will result into heat dissipation and thus increase the temperature of superconductor. Losses are proportional to the pinning i.e. stronger the pinning more will be the loss. This implies larger the critical current of the type-II superconductor more hysteresis losses are associated with it [19].

Coupling Losses For multi-filamentary conductors such as BSCCO (Bi-Sr-Ca-Cu-O), coupling losses are one of the challenges due to the presence of multiple superconducting filaments within a silver sheath [193][194]. Such losses can also be found in second generation superconductors (YBCO) if the tapes are striated into filaments. These losses occur when an eddy current induced due to varying magnetic field, flows partly through the silver and also through superconductor among the filaments. It happens when current flows from one filament to another, then the filament coupled together to form a single large magnetic system which offers significant resistance to the flow of current through the Silver matrix. Such Ohmic losses within the metal matrix are known as coupling losses [193].

5.1.2. Eddy Current Losses

Induced time-varying electric field can lead to flow of current when time-varying external magnetic field penetrates through a normal conductor [20]. This flow of current is known as eddy current in the tape and these currents may result into significant ohmic energy dissipation if the magnetic field is perpendicular to the tape surface [20]. Eddy current losses are sensitive to frequencies thus at low frequencies these losses can be calculated for many conductor geometries. By increasing the effective resistivity of the matrix such losses can be minimized. The present study, such losses have not been considered.

5.1.3. Transport Current Losses

Hysteresis Loss Such losses occur when AC current is flowing through the superconducting tape. Due to the circulation of large currents induced self-field may arise which plays an important role in such losses [193].

Flux Flow Loss With the increase in the transport current magnitude, the depinning of the flux lines increases and these lines start moving in the superconductor. The heat dissipation associated with such process is called flux flow loss [193].

5.1.4. Analytical Techniques to evaluate AC losses

Various studies have been available where magnetization and transport current AC losses are calculated using analytical techniques. AC losses calculated using such analytical equations can be used to compare the losses obtained through FEM techniques.

5.1.4.1. Norris Model

Norris proposed a method to estimate AC loss for self-field [195]. This analytical model is based on the idealized behavior of the superconductor which is equivalent to London model [196]. It is based on the fact that if current exceeds the critical values then the resistance of the superconductor is assumed to rise steeply and at constant current density its value is such that the ohmic voltage drop exactly balances the driving electromotive force (*emf*). This model assumed that the current density is not depends upon the ambient magnetic field however it is well known fact that it depends not only on the magnitude of the field but also on the direction of the field.

In order to compute the AC losses among the superconducting strip carrying a transport current, I_0, Norris proposed the following equation:

$$P_{strip}(W/m)=\frac{\mu_0 I_c^2 f}{\pi}\left[\left(1-\frac{I_0}{I_c}\right)\ln\left(1-\frac{I_0}{I_c}\right)+\left(1+\frac{I_0}{I_c}\right)\ln\left(1+\frac{I_0}{I_c}\right)-\left(\frac{I_0}{I_c}\right)^2\right] \quad 5.1$$

For different load factors and frequencies, a plot has been drawn in order finds the behavior of the AC losses. It has been found that the losses increase with frequency and load factor.

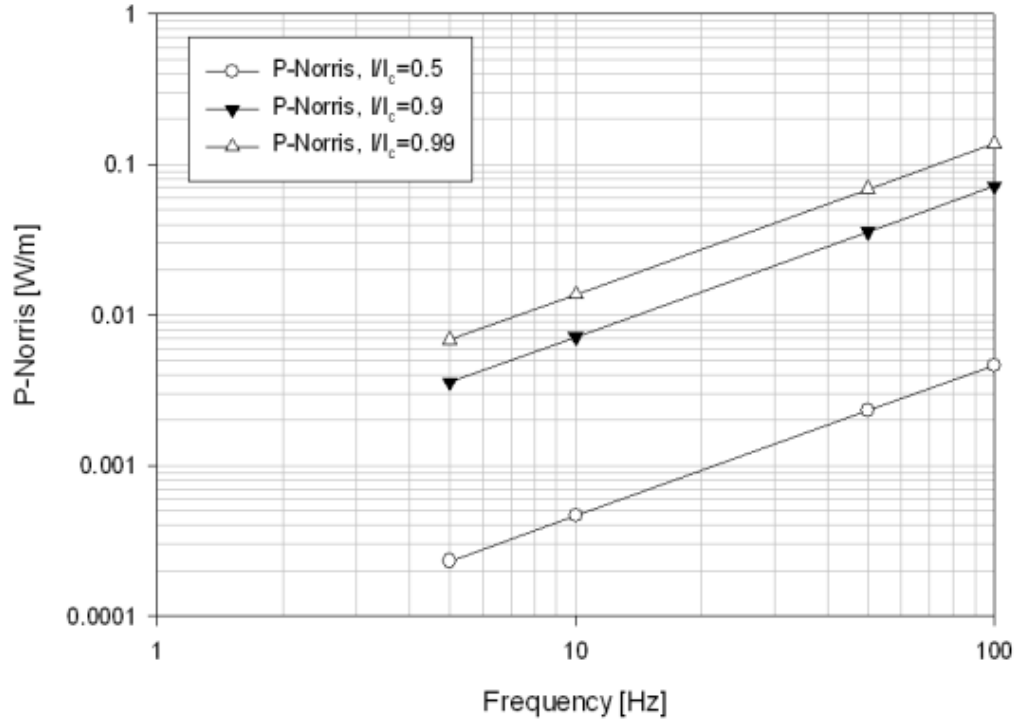

Figure 5.1 AC losses using Norris equation vs frequency of current

5.1.4.2. Brandt Model

Brandt proposed a model to estimate the AC losses in two dimensions where Maxwell's equations have been solved with E-J power law when a transport current is flowing through the strip or a perpendicular external magnetic field is penetrating the superconducting strip [23][24]. The involved equations (current and magnetic field distributions) in superconducting strip model have been discussed earlier. The magnetization loss for a strip of width '2a'and thickness 'd' for a perpendicular field having H_0 magnitude can be computed as follows:

$$P_m(W/m) = 4\pi\mu_0 a^2 H_0 H_c f\left[\frac{2H_c}{H_0}\ln\cosh\left(\frac{H_0}{H_c}\right) - \tanh\left(\frac{H_0}{H_c}\right)\right] \quad 5.2$$

For a transport current I_0, the above equation can be implemented to estimate the transport AC losses:

$$P_{trans}(W/m) = \frac{\mu_0 I_c^2 f}{\pi}\left[\left(1-\frac{I_0}{I_c}\right)\ln\left(1-\frac{I_0}{I_c}\right) + \left(1+\frac{I_0}{I_c}\right)\ln\left(1+\frac{I_0}{I_c}\right) - \left(\frac{I_0}{I_c}\right)^2\right] \quad 5.3$$

The above equation of transport AC losses is same as that of Norris equation.

5.1.4.3. The H-formulation

In order to solve the Maxwell equations for modelling the electromagnetic behaviour of the HTS in 2D, H-formulation are widely used as they provide accurate solutions in less computational time. Comsol Multiphysics 5.4 has been used to perform the analysis where PDEs have been incorporated to do H-formulation analysis. H-formulations are generally employed to evaluate the AC losses as it is easy to impose boundary conditions related to the externally applied magnetic fields and flow of current in superconductor and the solution is found to converge at faster rate than other methods.

Computational domain is divided into two sub-domains: air and superconducting domain. The inclusion of magnetic substrate materials has been not considered in the analysis and the tape (SCS 12050) manufactured by the SuperPower has been considered for the study. The same dependent variables are defined for both sub-domains by incorporating a few PDEs. By assuming that $\mathbf{B} = \mu_0 \mathbf{H}$ is applicable in both the superconducting and air sub-domains, the Maxwell's equations can be written as:

$$\nabla \times \mathbf{E} = -\frac{d\mathbf{B}}{dt} = -\mu_0 \frac{d\mathbf{H}}{dt} \quad 5.4$$

$$\nabla \times \mathbf{H} = \mathbf{J}$$

$$\mathbf{E} = E_0\left(\frac{J}{J_c(B)}\right)^{n-1}\frac{\mathbf{J}}{J_c} \quad 5.5$$

The E-J power law is used to model the behaviour of superconducting material by assuming:

- The electric field **E** is always parallel to current density **J**
- In the E-J relation, E_0 signify the threshold electric field which is generally used to define the critical current density, Jc is equal to 10^{-4} V/m.

Exploiting power law while modeling superconducting behaviour is more appropriate than that of original Bean model ($n \to \infty$) with a threshold voltage $E = 1\,\mu V/m$. The power index '*n*=30' is assumed which is a usual value for melt-processed YBCO tapes [63].

5.1.4.4. H-formulations in Cartesian Coordinates

In the 2D Cartesian coordinates, the space is considered to be infinite in *z*-direction and the tape is supposed to have infinitely long rectangular cross-section $w \times d$. The current density *J* is flowing in *z*-direction only and magnetic flux lies in the *x*-*y* plane. The schematic of the rectangular tape is shown in Figure 5.2.

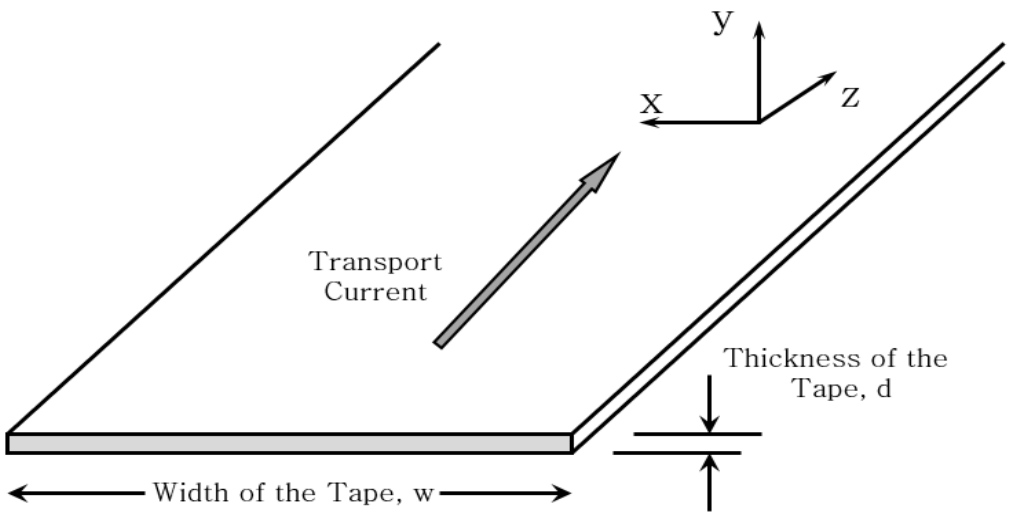

Figure 5.2 Schematic of the High Temperature Superconducting tape used for FEM model

Therefore, Maxwell's equations in Cartesian coordinates can be written as:

$$J_z = \frac{dH_y}{dx} - \frac{dH_x}{dy}$$

$$-\frac{dE_z}{dx} = -\mu_0 \frac{dH_y}{dt}$$

$$\frac{dE_z}{dy} = -\mu_0 \frac{dH_x}{dt}$$

Comsol Multiphysics is used to solve the PDEs mentioned above for two dependent variables H_x and H_y. Appropriate boundary conditions can be applied to model to solve PDEs. The non-linear PDEs can be written as

$$e_a \frac{d^2\mathbf{u}}{dt^2} + d_a \frac{d\mathbf{u}}{dt} + \nabla.\Gamma = F$$

$$\text{where, } \mathbf{u} = \begin{bmatrix} H_x \\ H_y \end{bmatrix}$$

Where *'e_a'* is mass coefficient matrix, d_a is the damping coefficient, u is a dependent variables vector, Γ is a flux vector and *F* is a source term. These all can be functions of spatial coordinates, space and time derivatives of **u** and the solution **u**. Thus, Maxwell's equations can be written as:

$$\begin{bmatrix} 0 & 0 \\ 0 & 0 \end{bmatrix} \frac{d^2\mathbf{u}}{dt^2} + \begin{bmatrix} \mu_0 & 0 \\ 0 & \mu_0 \end{bmatrix} \frac{d\mathbf{u}}{dt} + \nabla. \begin{bmatrix} 0 & E_z \\ -E_z & 0 \end{bmatrix} = \begin{bmatrix} 0 \\ 0 \end{bmatrix}$$

For the case where only transport current is flowing and no external magnetic field is there, a Dirichlet boundary condition can be applied at the infinity. At the interface between superconductor and air, a continuity equation $n \times (\mathbf{H_1} - \mathbf{H_2}) = 0$ is used. By applying Neumann boundary condition at the superconducting tape surface, this equation can be implemented in Comsol. In nutshell, it can be seen like that the magnetic field intensity's tangential components are conserved at either side of material interface and can be represented as follows:

$$\frac{dH_{t1}}{dn} = 0, \quad \frac{dH_{t2}}{dn} = 0$$

Where H_{t1} and H_{t2} are the tangential components. Using these boundary conditions, the PDEs are evaluated through Comsol. The scalar expressions like J_z are defined by "$d(H_y, x) - d(H_x, y)$", ρ_{sc} as $\frac{E_0}{J_c}\left(\frac{|J|}{J_c}\right)^{n-1}$. The expression $\rho_{sc}.J_z$ can be defined the electric field E_z for the superconductor and $\rho_{air}.J_z$ can be used to define the electric

field E_z for air (ρ_{air} =2E14 Ω-m). By incorporating a sub-domain integration variable I_{int}, it has been ensured that the current is flowing through superconducting domain only. The input current can be either of these; DC or AC. If '*s*' is the cross-section of the superconductor, then

$$I_{int} = \int\int J_z \, dxdy = \int_s J_z \, ds \qquad 5.6$$

This current value is imposed on the superconductor to ensure the current flow through it i.e. $I_{int,\ sub\text{-}domain} = I_{app}$. I_{app} is then applied as $I_0\left(1-e^{\left(-\frac{t}{\tau}\right)}\right)$ or $I_0 \sin(2\pi ft)$ or defined explicitly in the point/boundary setting.

5.2. Finite Element Method for Modelling of the Coil

The analytical models used for simple geometries have been discussed earlier, and many models have been proposed to evaluate the critical state of the superconductors. However, to solve the complex geometries, numerical models are needed to be developed. Usually, such numerical models (2D or 3D) are employed to solve the Maxwell's equations coupled with E-J power law by using finite element or finite difference methods. Finite element methods are popular for solving partial differential equations (PDEs). These models have been widely studied by many researchers before such as **T**-Ω (based on the current vector potential **T**) [197]–[201], **A**-V (based on magnetic vector potential **A**) [202]–[204], and **H-** formulations (based on directly solving the magnetic field components) [205]–[210]. While modelling, Maxwell's equations can be written using these formulations (having equivalent principles) however the outcomes of the equivalent PDEs can be differing from each other. As in the present work, H-formulations are used thus a detailed introduction to this numerical technique is presented in the next section.

5.2.1. Assumptions

1. 2D model has been used for the study.
2. Analysis has been performed on single pancake coil.
3. A homogenized domain has been used instead of using multi-turned coil in order to reduce computing time.

4. The turns are assumed to be a bundle of parallel conductors which consists both normal and superconducting materials.
5. External fields are not taking into consideration.

5.2.2. H-formulation modelling

The formulations using differential equations have been used earlier by Kajikawa et al [211] and Pecher et al [212] where magnetic field H has been considered for superconductor's modeling. Brambilla et al [213] and Hong et al [207] used H-formulations integrated with E-J power law where edge elements (explained in next section) are employed for the discritization of the superconducting homogeneous domain. In this research work, formulation used is same as that of Brambilla et al [213] where integral constraints have been employed to impose discrete currents to different conductors and no distinction has been made among the external and self-fields. H-formulations have been used in the present study as it is easy to implement and gives high degree of accuracy when zeroth-order edge elements have considered for the discretization of the domain. In the next section, a detailed study related to triangular and rectangular edge elements has been presented. Moreover, structured meshes have been used for the meshing of thin rectangular shaped domains. In order to model the stacked tapes or coils, its cross-section can be considered and that consists both normal and superconducting domains as a bundle which are parallel to each other. Dirichlet boundary condition can be used to impose the transport current at the domain boundary which are coupled at the ends. The boundary can be set at a distance of 8-10 times the maximum cross-sectional diameter of the conductor's bundle. Conversely, for a general case where current is known and it has to be enforced in each conductor, Dirichlet boundary condition cannot serve the purpose alone. For a cluster of n_c parallel superconductors (which carry a defined current), one integral constraint per conductor can ensure the transport current requirement.

As current density is considered in the direction out of x-y plane thus $J = \hat{e}_3 . \nabla \times H$ and where I_k (t) is the transport current in the conductor (C_k). If all parallel conductors or tapes carries same current, then I_k (t)= I (t). Thus, problem reduced to evaluate the magnetic field H i.e. [172]

$$\nabla \times \rho \nabla \times H = -\mu \frac{\partial H}{\partial t} \quad 5.7$$

$$H = H_{self} + H_{ext} \quad 5.8$$

$$H_{t=0} = H_0 \left| \nabla . \left(\mu H_0 \right) = 0 \right.$$

$$I_k(t) = \int_{C_k} J \, dxdy \qquad \forall k \in \{1, 2, ...n_c\} \quad 5.9$$

To calculate magnetic field H, Equation 5-1 has been employed with a boundary condition imposed on model as Equation 5-1

5.8. Magnitudes of J, E and B can be intended from H by using Ampere's Law $J = \nabla \times H$ and the subsequent constitutive relations $E = \rho J$ and $B = \mu H$ respectively. The resistivity of the HTS tape can be modeled by incorporating Power Law (5.10).

$$\rho_{HTS} = \frac{E_c}{J_c} \left| \frac{J}{J_c} \right|^{n-1} \quad 5.10$$

Here, E_c=1μV/cm is the electric field which can be attained when current density reached its critical value and n represents the index of *E-J* relationship. A Kim like model (Equation 5-5) for the J_c (***B***) dependence of HTS tape at 77 K was incorporated [188]. Instantaneous AC losses (W/m) can be estimated using following relation:

$$\xi = \int_{Inside\,domain} E.J \, dxdy$$

5.11

For periodic signals, average losses (*W/m*) can be evaluated using following relation:

$$Q = \frac{1}{T} \int_T^{2T} dt \int_\Omega E.J \, dxdy \quad 5.12$$

As zero initial condition has been chosen thus transient phase are expected. However, such phases will fade out once maximum magnitude has reached for the transport current or external fields if considered. Thus, second half of the cycle has been considered where most of the transient field fade out and to ensure the computational speeds, hence the integral changed to

$$Q = \frac{1}{T} \int_{T/2}^{T} dt \int_\Omega E.J \, dxdy \quad 5.13$$

5.2.3. Homogenization of the domain

As in the present study, six tapes have been stacked one over the other in order to reach a maximum current of 1620 A and for 1 MJ energy storage 49 pancake coils are required with having 18 turns each on single pancake. This implies there are total 108 conductors or tapes locally around one single pancake coil as shown in **Figure 5.3**.

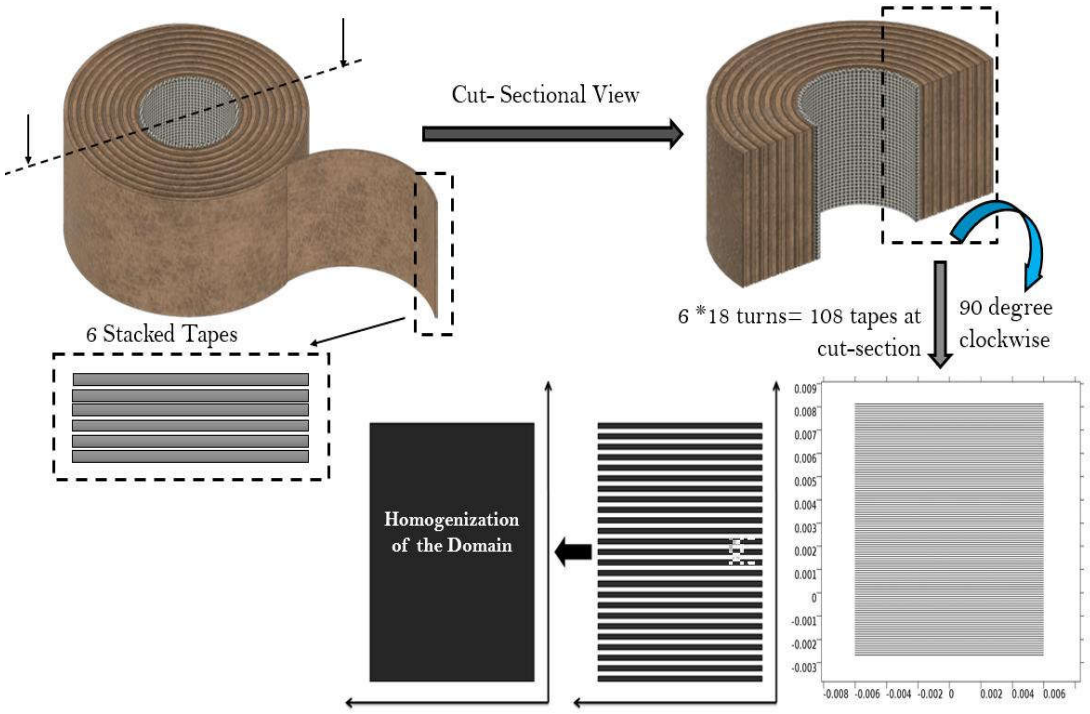

Figure 5.3 Details of the computation domain

Therefore, there is a need to draw 108 conductor's cross-section those are stacked over one another as shown in Figure 5.4 (b). Though, for practical situations, the thickness of one-unit cell (D) varies throughout the stack however for the present analysis it has been assumed to be constant and equal to 0.1mm.

Figure 5.4 (a) shows the schematic of model coil with all individual domains and Figure 5.4 (b) shows the exploded view of single tape. The superconducting tape is composed of insulator (indicating the minute gap among the adjacent layers), copper as substrate, silver as stabilizer, and YBCO tape whose geometrical details are available in Table 5.1. A current of 210 A to 330 A has been fed through each tape at a frequency of 50 Hz (assumed to be equal to AC current frequency).

The model shown in Figure 5.4 (c) describes the 2D representation of 108 turns where 6 stacked tapes roll one over the other for 18 turns. Figure 5.4 shows the periodic

linear arrangement of superconducting tapes (YBCO) constructed using Ion Beam Assisted Deposition (IBAD) [214][215] technique. Tapes manufactured with IBAD technique do not contain magnetic substrates therefore, relative permeability of many layers is considered to be equal to one.

Extended view Figure 5.4 (b) shows that a unit cell is composed with layers of copper, substrate, superconducting film, silver and insulation that separate the tape from the adjacent one. From the Table 5.1, it can be noticed that the resistivity of air and normal conductors is much larger than the superconductor in the mixed state. Therefore, in order to avoid complexities, homogenized model has been taken into account where only superconducting material's volume fraction is considered. In order to take care of the local field's J_c ***(B)*** effects, Kim [21] like model has been used. For homogenized bulk, the equivalent critical current density $J_{c,\,Eq}$ ***(B)*** = *Jc* ***(B)*** f_{HTS} is used; where f_{HTS} is the volume fraction of the superconducting material per unit cell. In order to avoid complexities, in the present study, for the case of homogenized stacks, J_c alone will be referred to the equivalent critical current density and J_c ***(B)*** for the superconducting layers of a tape.

In order to model the 108 stacked tapes as shown in Figure 5.4 (d) where each tape is carrying a predefined current equal to Equation 3 per conductor ensures the constraints is achieved. This can be achieved by introducing n_c Lagrange's multipliers, basically one for each conductor. Although, the present homogenized domain cannot be discretized through the described constraints therefore new set of constraints are required in order to assure the imposed transport current. For a special case of infinitely thin conductors with tightly packed configuration, Clem et al. [216] has expressed the condition as;

$$P(y,t) = \int_C J\left(x,y,t\right)dx \qquad 5.14$$

Here $P(\bar{y},t)$ represents the current density/height transported by the thin superconductor at $y = \bar{y}$ in the homogenized bulk of stacked conductors. For a situation when all stacked tapes carrying same current *I(t)* then $P(y,t)$ = *I(t)*/*D* will be the constraint in y-direction. Therefore,

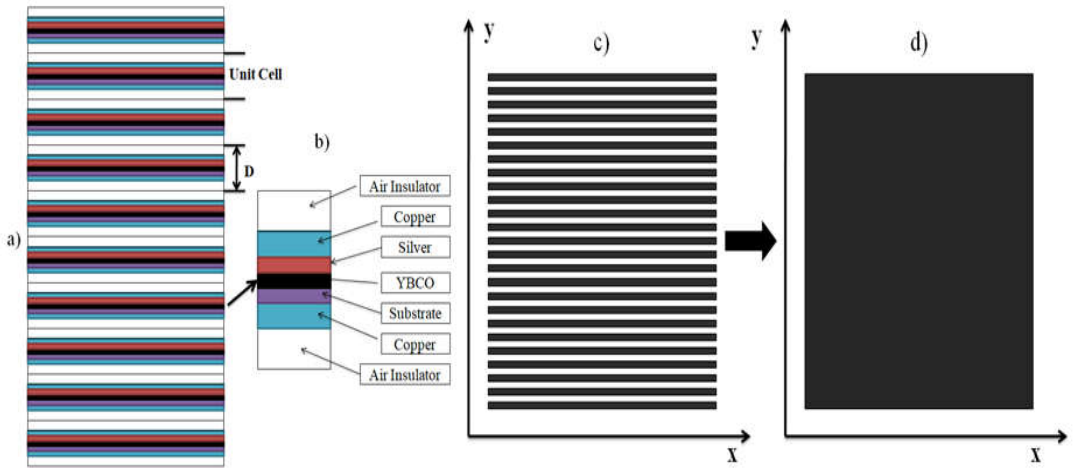

Figure 5.4 Computational Domain for the numerical model (a) Stacked HTS tapes, (b) Detailed view of unit cell, (c) Actual arrangement of the tapes and (d) Homogenized domain

$$\frac{I(t)}{D} = \int_C J(x,y,t)\,dx \qquad 5.15$$

Table 5.1 Parameters of the homogenized domain

Description	**Value**
Cu cover height (each side)	20e-6 m
Air gap and insulator height	2e-4 m
Ag cover height	4e-6 m
Substrate height	50e-6 m
HTS layer height	1e-6 m
Tape height	1e-4 m
Tape width	12e-3 m
Number of turns on pancake	108
n	30
Resistivity of Air	1 m*V/A
Resistivity of Ag	2.7e-9 m*V/A
Resistivity of Cu	1.97e-9 m*V/A
Resistivity of substrate	1.25e-9 m*V/A
Frequency of transport current	50 Hz
Critical Current Density, Jc	2.8E10 A/m^2

The above expression can be used to implement constraint numerically by making use of only one Lagrange's multiplier. As a result of which the computational time needed

to solve this homogenized bulk problem is now only depending upon the mesh density used to discretize the bulk computational domain and it completely independent of the number of original stacked tapes or conductors.

5.2.4. Edge Elements and its Significance

Edge elements are generally employed to signify curl conforming fields while solving rigorous PDEs with finite element methods. In order to evaluate AC losses, both rectangular and triangular elements have been used. These elements help in reducing computational time required to solve the problem.

5.2.4.1. Triangular Edge Elements

In order to discretize the magnetic field H= (H_x, H_y), triangular edge elements can also be used as shown in Figure 5.5. To solve this problem, area coordinates (L_1, L_2, L_3) has been considered which can be represented as follows:

$$L_j(x,y) = \frac{1}{2\Delta}(a_j + b_j x + c_j y) \qquad 5.16$$

Where Δ is the surface area of the triangular element and a_j, b_j, c_j are the coefficients whose values are as follows:

$$\Delta = \frac{1}{2}\left(x_1\left(y_2 - y_3\right) + x_2\left(y_3 - y_1\right) + x_3\left(y_1 - y_2\right)\right)$$

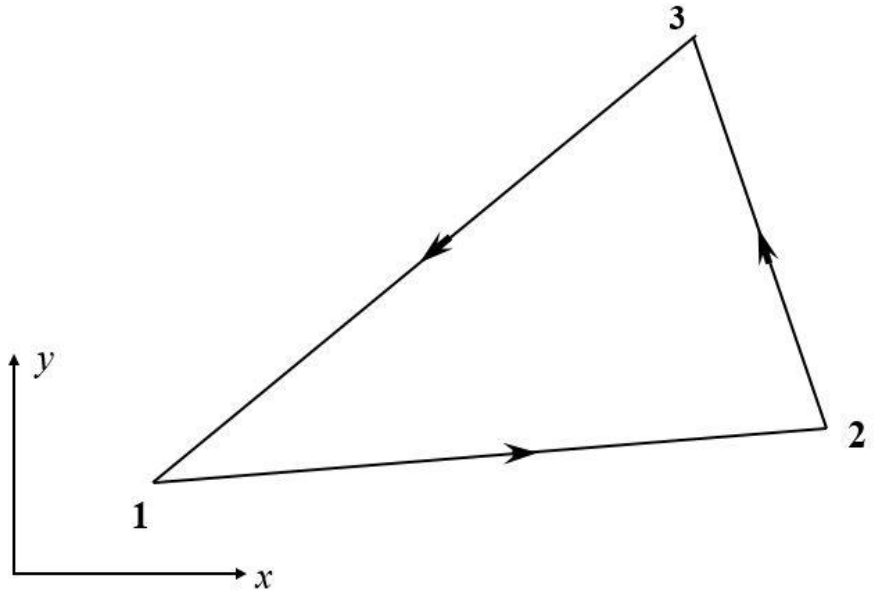

Figure 5.5 Triangular Edge Element

$$a_1 = x_2 y_3 + y_2 x_3 \qquad b_1 = y_2 - y_3 \qquad c_1 = x_3 - x_2,$$
$$a_2 = x_3 y_1 + y_3 x_1 \qquad b_2 = y_3 - y_1 \qquad c_2 = x_1 - x_3,$$
$$a_3 = x_1 y_2 + y_1 x_2 \qquad b_3 = y_1 - y_2 \qquad c_3 = x_2 - x_1.$$

Let N_1, N_2 and N_3 are arbitrary vector functions which can be represented as follows:

$$N_1 = \left(L_1 \nabla L_2 - L_2 \nabla L_1\right) l_{12},$$
$$N_2 = \left(L_2 \nabla L_3 - L_3 \nabla L_2\right) l_{23},$$
$$N_3 = \left(L_3 \nabla L_1 - L_1 \nabla L_3\right) l_{31},$$

Where l_{ij} is the length of edge joining the vertices i and j as represented in Figure 5.5. If H_i is the tangential component of the magnetic field on the i^{th} edge thus magnetic field within the element is given by:

$$H = \sum_{i=1}^{3} N_i H_i \qquad 5.17$$

Also,

$$\nabla . H = 0$$

$$\nabla \times H = \frac{1}{\Delta} \sum_{i=1}^{3} H_i l_i \hat{k}$$

Let the tangential components are space constants and thus by incorporating Ampere's law $\nabla \times H = J$, it can be obtained that current density J is constant within the element, i.e.

$$\frac{\partial J}{\partial (x, y, z)} = 0 \qquad 5.18$$

5.2.4.2. Rectangular Edge Elements

In order to discretize the magnetic field $H = (H_x, H_y)$, rectangular edge elements, as shown in Figure 5.6, have been considered. An elements of side lengths l_x and l_y have been drawn with its sides parallel to the coordinate axis in order to avoid complexity and loss of generality. The center of the rectangular element is chosen to (x_c, y_c).

Magnetic field inside the element can be described as (considering tangential components constant for each side of rectangular element):

$$H_x = \frac{1}{l_y}\left(y_c + \frac{l_y}{2} - y \right) H_{x1} + \frac{1}{l_y}\left(y - y_c + \frac{l_y}{2} \right) H_{x2} \qquad 5.19$$

$$H_y = \frac{1}{l_x}\left(x_c + \frac{l_x}{2} - x \right) H_{y3} + \frac{1}{l_x}\left(x - x_c + \frac{l_x}{2} \right) H_{y4} \qquad 5.20$$

Here, for edges 1 and 2, H_{x1} and H_{x2} are the tangential components of magnetic field H respectively. Similarly, for edges 3 and 4, H_{y3} and H_{y4} are the tangential components of magnetic field H respectively.

Using Equation 5-13 and Equation 5-14, we have

$$\nabla . H = 0$$

$$\nabla \times H = \left(\frac{(H_{y4} - H_{y3})}{l_x} + \frac{(H_{x1} - H_{x2})}{l_y} \right) \hat{k}$$

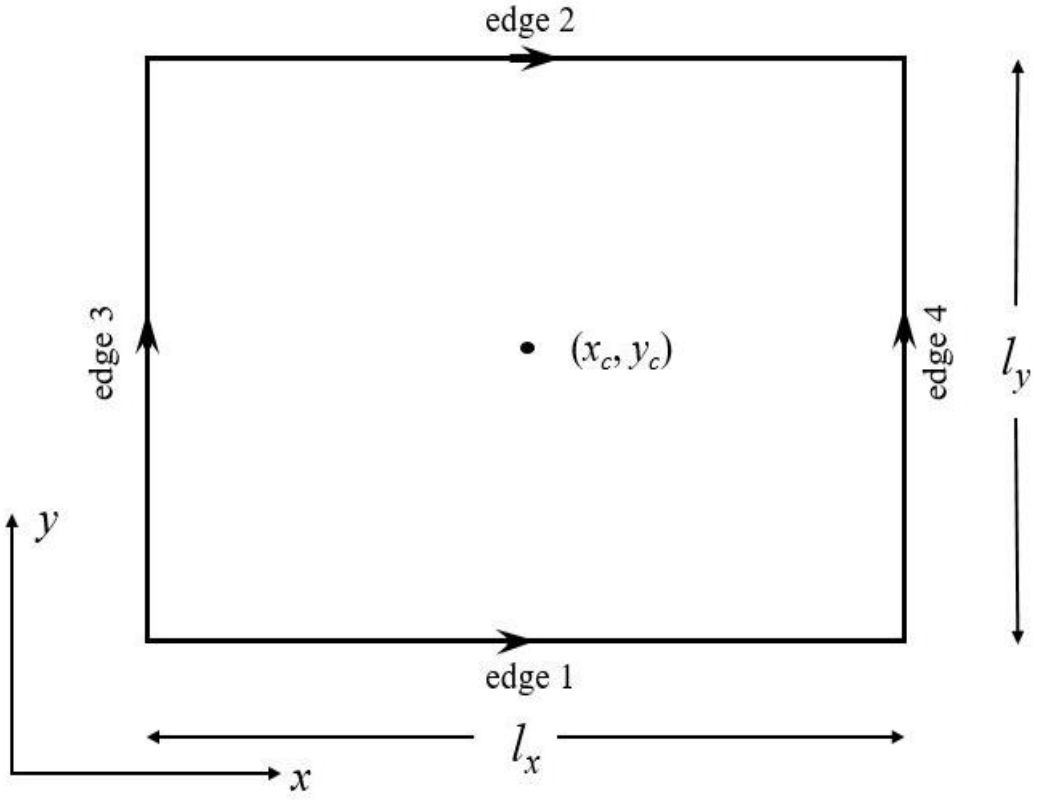

Figure 5.6 Rectangular Edge Element

Tangential components (H_{x1}, H_{x2}, H_{y3} and H_{y4}) are space constants and it can be obtained from the Ampere's Law $\nabla \times H = J$ that the current density is constant within the element i.e.

$$\frac{\partial J}{\partial(x,y,z)}=0 \qquad 5.21$$

Therefore, it can be concluded that for both rectangular and triangular meshes, implementation of zeroth-order edge elements to discretize the magnetic field results into following local properties:

$\nabla.H=0$

$\nabla\times H=J$

and

$$\frac{\partial J}{\partial(x,y,z)}=0 \qquad 5.22$$

Moreover, it can be concluded that use of zeroth-order edge elements provides direct computational solution for the current density from the calculated magnetic field components without the requirement of supplementary numerical differentiation, thus high accuracies can be achieved.

The expression $\nabla.H=0$ represents the local divergence free of the magnetic field ***H***, which holds only within each element. Edge elements offer continuity for the tangential component among the interfaces within elements, though for the normal conductors' discontinuities are permitted and due to this non-divergence free fields can also be characterized. In the present study, magnetic substrate free tapes have been considered for the AC loss calculations. For magnetic substrates, one can refer [217] and [218] in order to identify the magnetic substrates' influence on the AC losses for YBCO (RABiTS) coated conductors. Using non-linear ***B-H*** relation, usually magnetic materials have been modelled which indicates that one cannot apply Gauss law of magnetism $\nabla.B=0$ as it cannot implement $\nabla.H=0$ as it can only applicable for linear materials.

The expression $\nabla\times H=J$ and $\frac{\partial J}{\partial(x,y,z)}=0$ indicates that the current density inside the element is uniform thus the equation $\frac{I(t)}{D}=\int_C J\left(x,y,t\right)dx$ can be modified by discretizing the bulk computational domain **Ω** to sub-domains of Ω_i through

rectangular edge elements for structured meshing such that only one element is enough to represent the thickness of the element. This implies;

$\frac{\partial J}{\partial y} = 0$ and no such condition will be applicable for $\frac{\partial J}{\partial x}$

Therefore, now homogenized bulk computational domain can be sub-divided into n_s sub-domains then imposed current can be evaluated using following relationship:

$\bar{I}_i(t) = \int_{\Omega_i} J(x,y,t)\,dx \quad \forall i \in \{1,2,.....n_s\}$ where $\bar{I}_i(t)$ is the prescribed current in the i^{th} sub-domain. While expression $\bar{I}_i(t) = \int_{\Omega_i} J(x,y,t)\,dx$ and $I_k(t) = \int_{C_k} J\,dxdy$ are similar however, $n_s < n_c$ which represents that the number of constraints can be reduced in order to speed up the computational calculations at the expense of accuracy.

Table 5.2 Parameters used in validation

Description	**Value**
Cu cover height (each side)	20e-6 m
Air gap and insulator height	2e-4 m
Ag cover height	4e-6 m
Substrate height	50e-6 m
HTS layer height	1e-6 m
Tape height	1e-4 m
Tape width	12e-3 m
Number of tapes around pancake	32
n	38
Resistivity of Air	1 m*V/A
Resistivity of Ag	2.7e-9 m*V/A
Resistivity of Cu	1.97e-9 m*V/A
Resistivity of substrate	1.25e-9 m*V/A
Frequency of transport current	50 Hz
Critical Current Density, Jc	2.8E10 A/m^2

5.3. Validation of Computational Scheme

In order to verify the computational procedure, the results of Zermeno et al. [219] has been reproduced for the instantaneous and average AC losses using H-formulation at 77 K. Authors used homogenized approach in order to estimate the AC losses for coated conductors used for large scale applications where authors have performed study on 16 tapes, 32 tapes and 64 tapes at a frequency of 50 Hz. The critical current of the 4 mm wide tape used is 99.227 A and operating currents opted for the study was 50 A, 60 A and 70 A.

In order to consider local field effects Kim model has been considered, the parameters involved in their study are tabulated in Table 5.2. Computational analysis has been performed for 32 stacked tapes through which 60 A current has been transported at 50 Hz frequency. The results obtained from the analysis has been plotted in Figure 5.7.

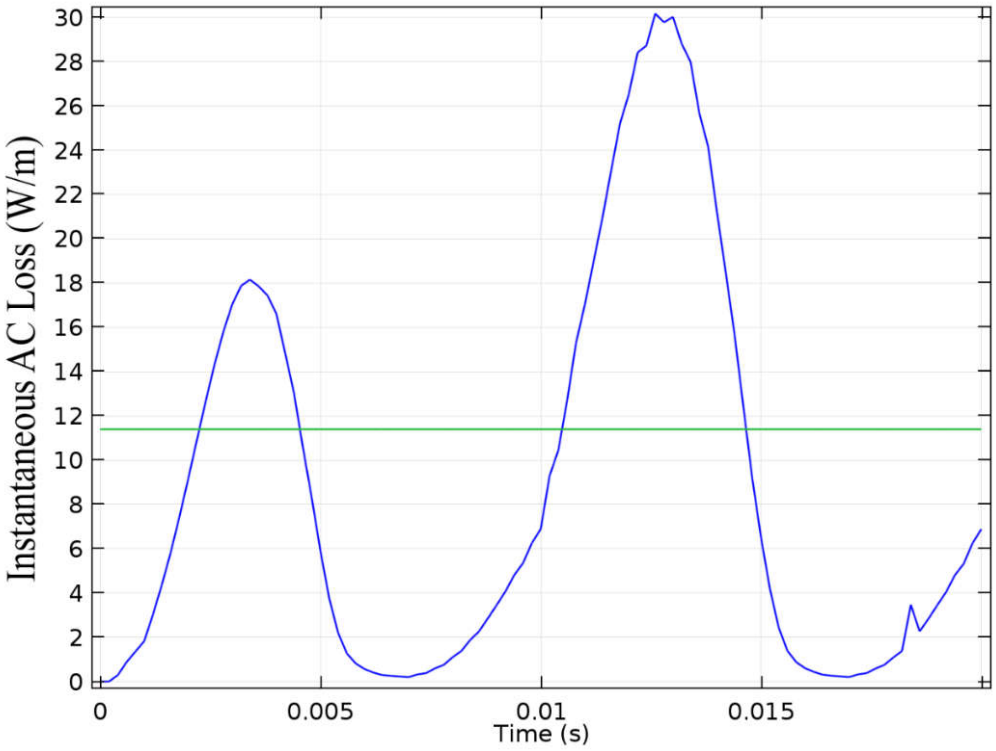

Figure 5.7 Instantaneous Losses Plot using present model

In order to validate the obtained simulated results with the Zermeno et al. [219] work, the instantaneous losses (W/m) have been identified through visual mapping using metric scale from the graph available in their research article whose values are tabulated in Table 5.3.

Table 5.3 Mapped data from the article

Time (ms)	Instantaneous Loss (W/m)	Time (ms)	Instantaneous Loss (W/m)
0	0	-	-
1	3.1	11	17
2	9.2	12	26.2
3	17.1	13	30
4	16.8	14	21.2
5	6	15	7
6	0.8	16	0.5
7	0.3	17	0.1
8	1	18	1
9	3.6	19	3.3
10	7	20	7

Data available in the Table 5.3 has been plotted in Origin 8.0 software and curve fitting has been done and it has been found that one correlation has fitted the data with more accuracy which is given by:

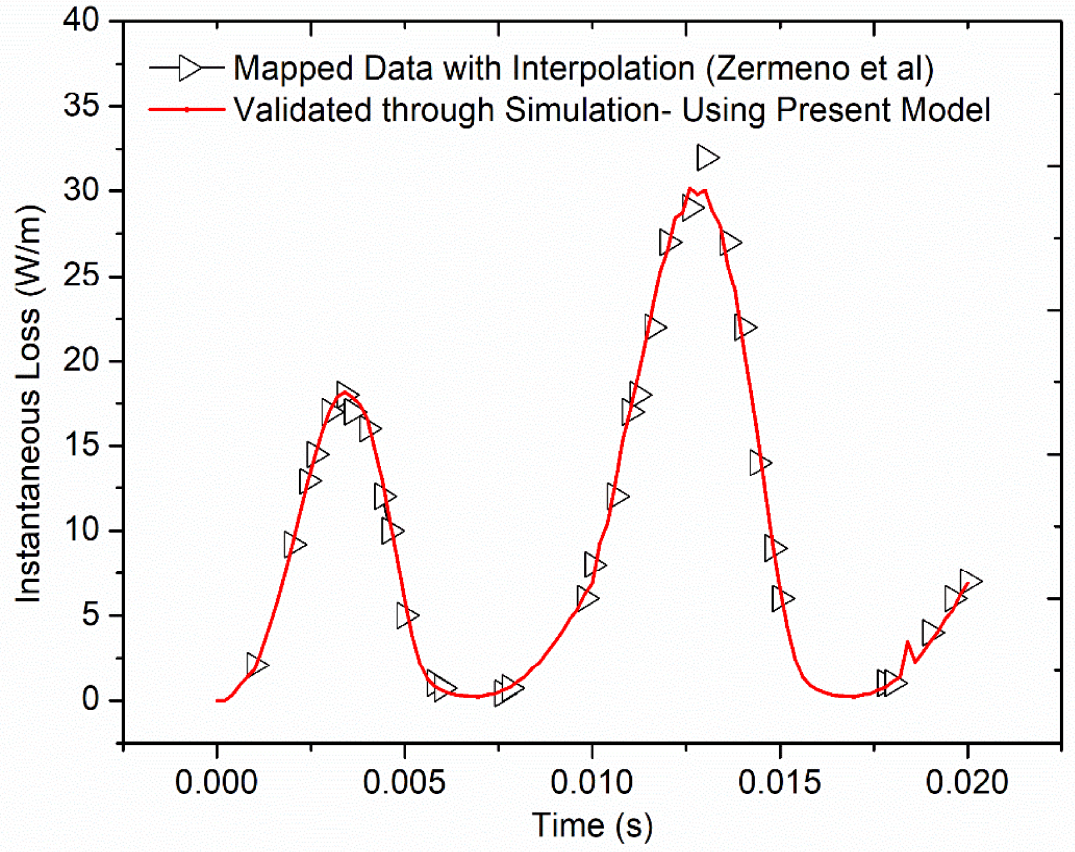

Figure 5.8 Instantaneous loss validation

$$Loss = a + \frac{b-a}{1+10^{(c-t)d}} \quad 5.23$$

Piecewise interpolation has been used in order to fit the curve whose coefficients are tabulated in Table 5.4. The results obtained for mapped data interpolation and simulated study has been plotted in Figure 5.8 and it can be observed that the simulated results are closely matching with the mapped data. Average AC loss for mapped data is 12.47 W/m and for simulated results it is 11.4 W/m which is showing a deviation of 9 %. This deviation has been accepted and the same developed model has been employed for the calculations of instantaneous and average AC losses of 1 MJ SMES.

Table 5.4 Correlation coefficients used to validate AC losses model

Time (ms)	R^2	Correlation Coefficients			
	0.9999	**a**	**b**	**c**	**d**
0 - 3.6		-0.63941	20.10227	0.00206	777.8357
	Error	0.12325	0.23464	1.48E-05	21.25464
3.6 – 7		0.10692	18.69893	0.0047	-1224.78
	Error	0.06557	0.16544	9.87E-06	29.20861
7 - 12.6		0.26312	35.23689	0.01107	518.3564
	Error	0.2634	1.1291	5.92E-05	28.29056
12.6 - 20		-0.3758	30.4145	0.01442	-948.354
	Error	0.23215	0.54242	2.1E-05	37.81676

5.4. Geometric Modelling

Superconducting magnet is having 49 pancake coils (Figure 5.9) piled up one over the other where a maximum current of 1.62 kA is flowing through the magnet to store 1 MJ of energy. The magnet is cooled at 77 K using convection cooling through liquid nitrogen and the critical current of the tape is found to 330 A at 77 K @ 0T self-field.

Equation 5-24 and Equation 5-25 are involved in finalizing the maximum current flowing through the magnet. For instance, in the present study, 2D numerical modeling has been performed in order to estimate the AC losses using H-formulation where 6 tapes are stacked one over the other and total 18 turns are there for one pancake coil. The actual arrangement of the stacked tapes and its turns around pancake coil is presented in Figure 5.3.

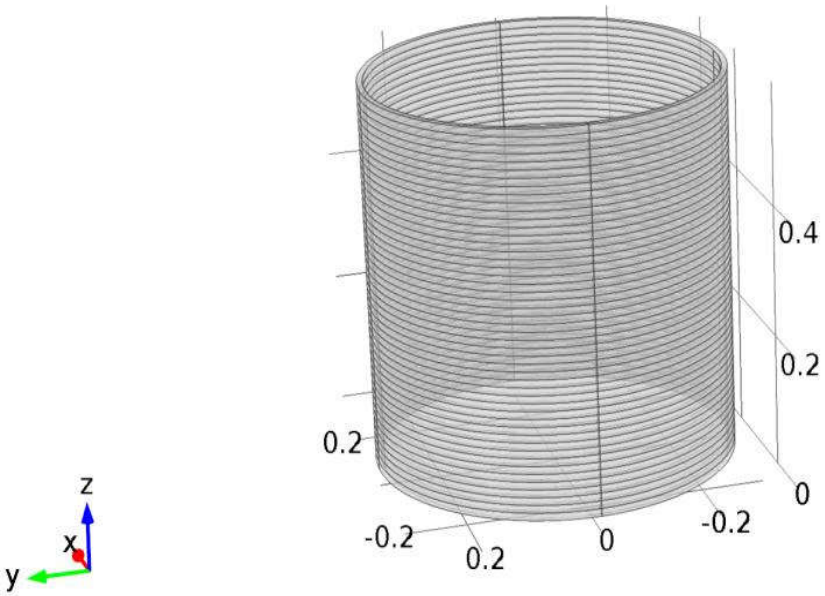

Figure 5.9 Schematic of Solenoidal Magnet consisting 49 pancakes

Table 5.5 Design Parameters of the Magnet

Description	**Value**
Stored Energy	1 MJ
Maximum Current	1.62 kA
Bore Diameter	779 mm
Coil Inductance	0.783 H
Index, n	30
Total number of turns	862
Cu cover height (each side)	20e-6 m
Air gap and insulator height	2e-4 m
Ag cover height	4e-6 m
Substrate height	55e-6 m
HTS layer height	1e-6 m
Tape height	1e-4 m
Tape width	12e-3 m
Number of tapes around pancake	108
Coil height	0.018 m
Resistivity of Air	1 m*V/A
Resistivity of Ag	2.7e-9 m*V/A
Resistivity of Cu	1.97e-9 m*V/A
Resistivity of substrate	1.25e-9 m*V/A
Frequency of transport current	50 Hz
Critical Current Density, J_c	2.75E10 A/m^2

$$E_{max} = \frac{1}{2} L\, I^2{}_{max} \quad 5.24$$

$$\Delta E = \frac{1}{2} L\left(I_{max}^2 - I_{min}^2\right) \quad 5.25$$

A Kim like model (Equation 5-20) for the J_c (***B***) dependence of HTS tape at 77K was incorporated where B_0=0.04265T, Jc (77K,SF)= 2.75×10^{10} A/m^2, k=0.29515, α =0.7 and B_{II} and $B_{\perp}$ are, respectively, the parallel and perpendicular components of magnetic field density with respect to tape's surface [188]. Here the J_c is used at 77 K (self-field) and the field dependence of parallel and perpendicular magnetic fields has been considered (Equation 5-20).

$$J_c(B) = \frac{J_c(77K, SF)}{\left(1 + \frac{\sqrt{k^2 |B_{II}|^2 + |B_{\perp}|^2}}{B_0}\right)^{\alpha}} \quad 5.26$$

$$normB = \sqrt{B_{II}^2 + B_{\perp}^2} \quad 5.27$$

The analysis has been done in order to evaluate the effect of transient transport current, frequency of current, number of turns around the pancake and thickness of stabilizer on the AC losses during unsteady phase.

5.5. Effect of operating current magnitude

At 77 K, YBCO coated conductor has a critical current of 330 A [138]. In order to evaluate the transport current's effect on the AC losses, a load factor of 63%, 69%, 75%, 81%, 87%, 93% and 100% has been considered. The magnetic flux and current density (J/J_c) distribution for all 7 load factors have been discussed in the upcoming sections.

5.5.1. Magnetic Flux and Current Density

Figure 5.10 to Figure 5.16 shows the J/J_c and normB distribution at 50Hz sinusoidal frequency and for different operating currents ranging from 210 A to 330 A. it can be noticed from the J/J_c plot that the local over critical currents have been attained as the E-J relationship specifying the superconducting behaviour of the tape.

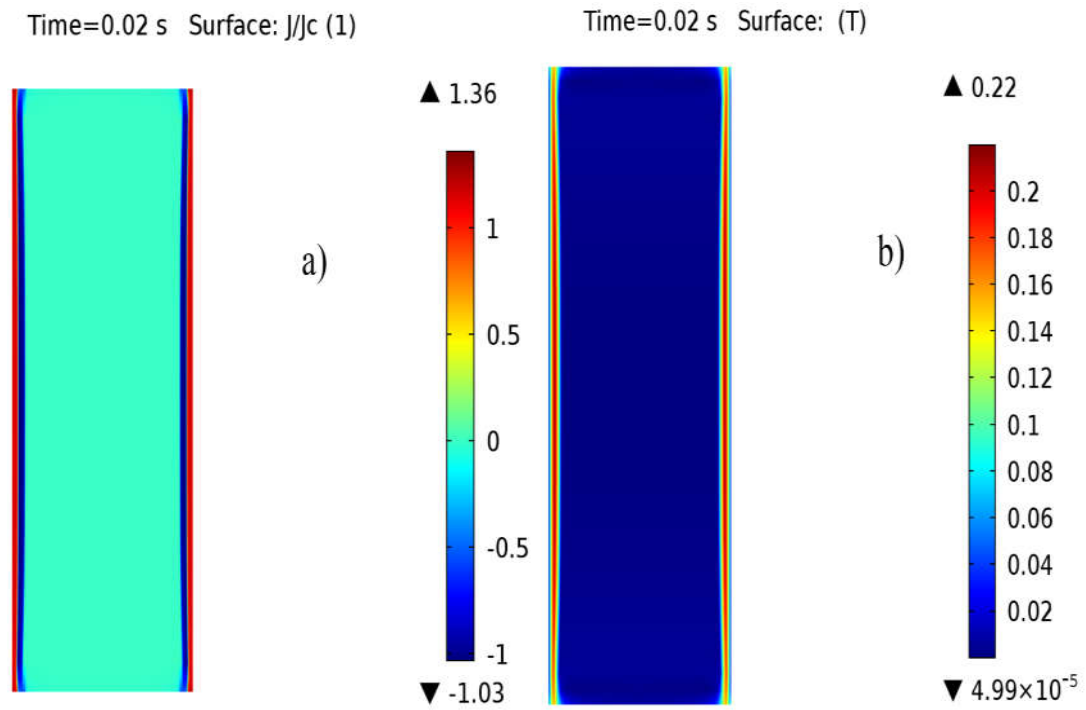

Figure 5.10 (a) J/J_c and (b) normB distribution at 210 A operating current. Plots are captured at time 0.02s and at 2π phase value.

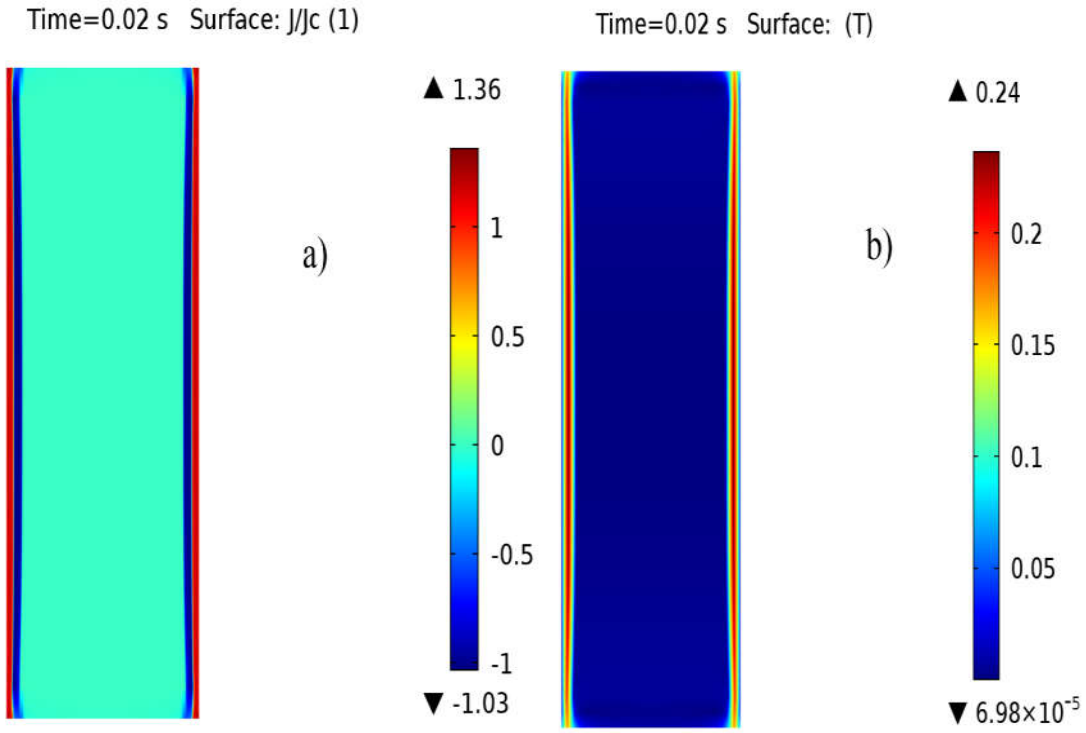

Figure 5.11 (a) J/J_c and (b) normB distribution at 230 A operating current. Plots are captured at time 0.02s and at 2π phase value.

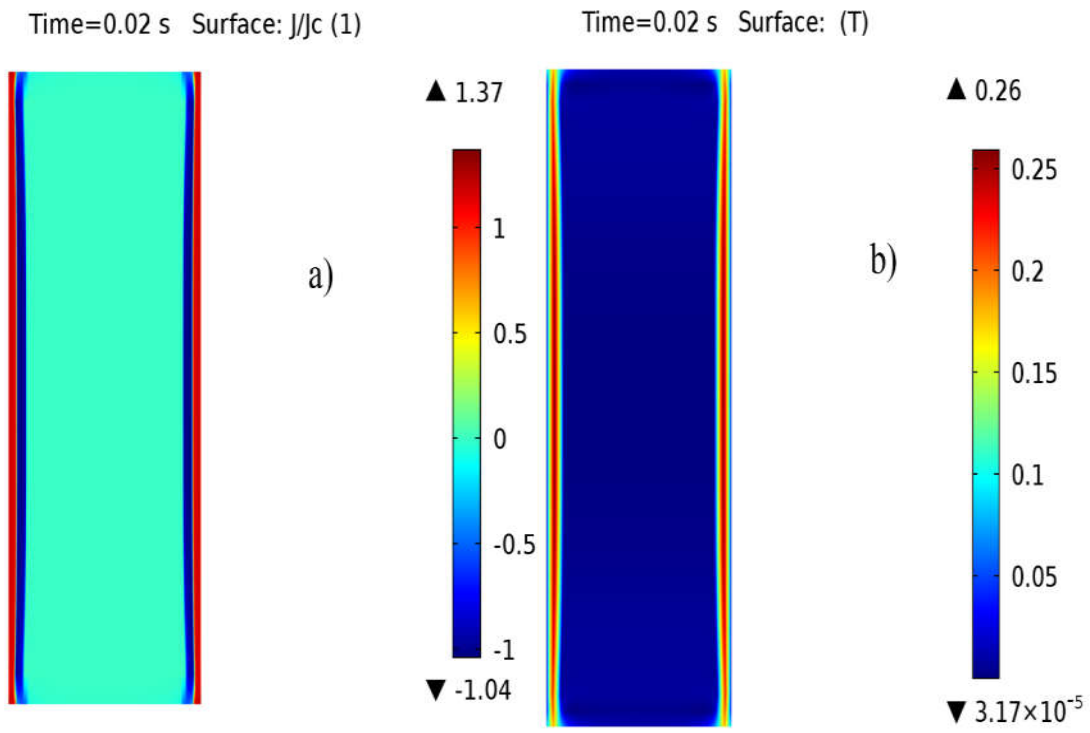

Figure 5.12 (a) J/J_c and (b) normB distribution at 250 A operating current. Plots are captured at time 0.02s and at 2π phase value.

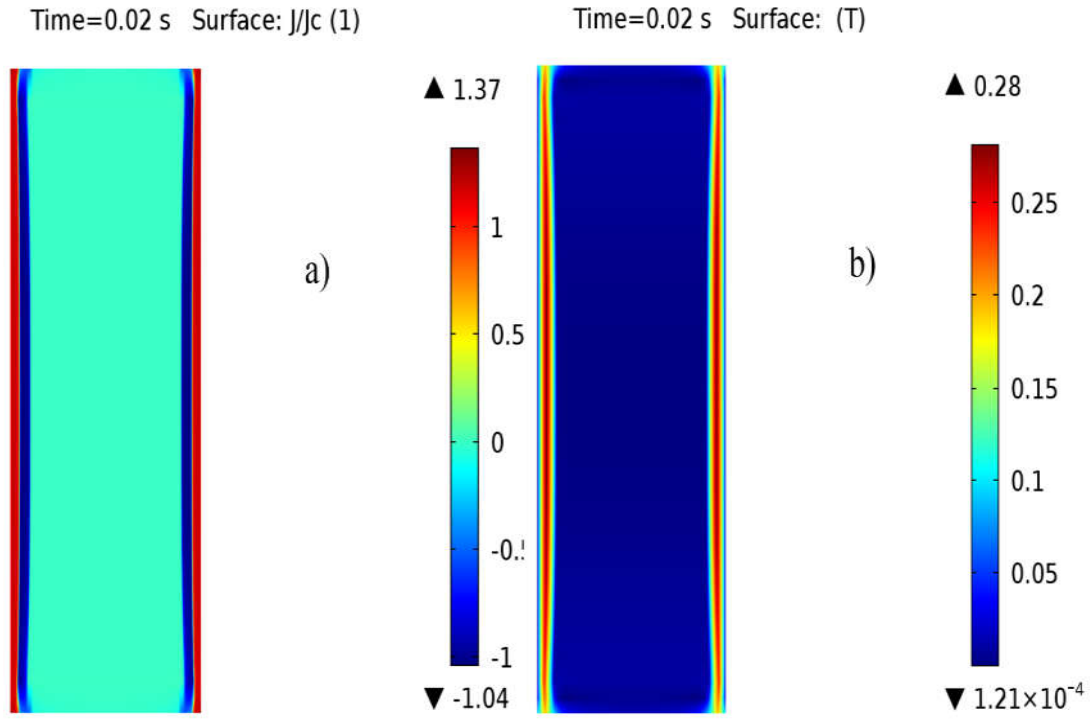

Figure 5.13 (a) J/J_c and (b) normB distribution at 270 A operating current. Plots are captured at time 0.02s and at 2π phase value.

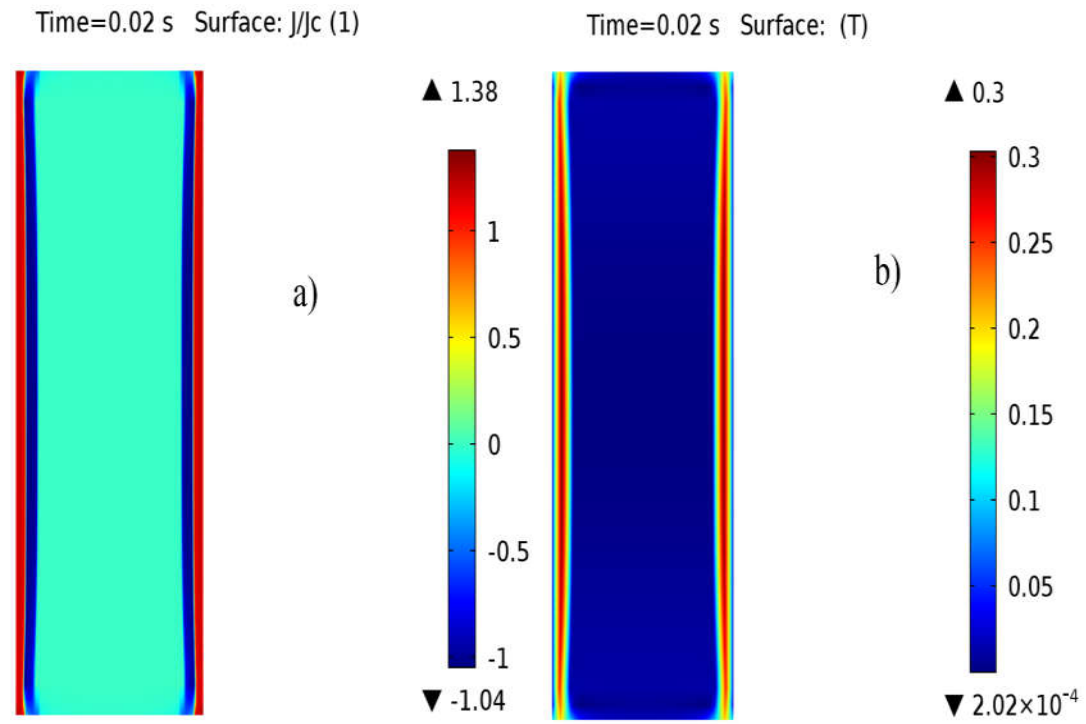

Figure 5.14 (a) J/J_c and (b) normB distribution at 290 A operating current. Plots are captured at time 0.02s and at 2π phase value.

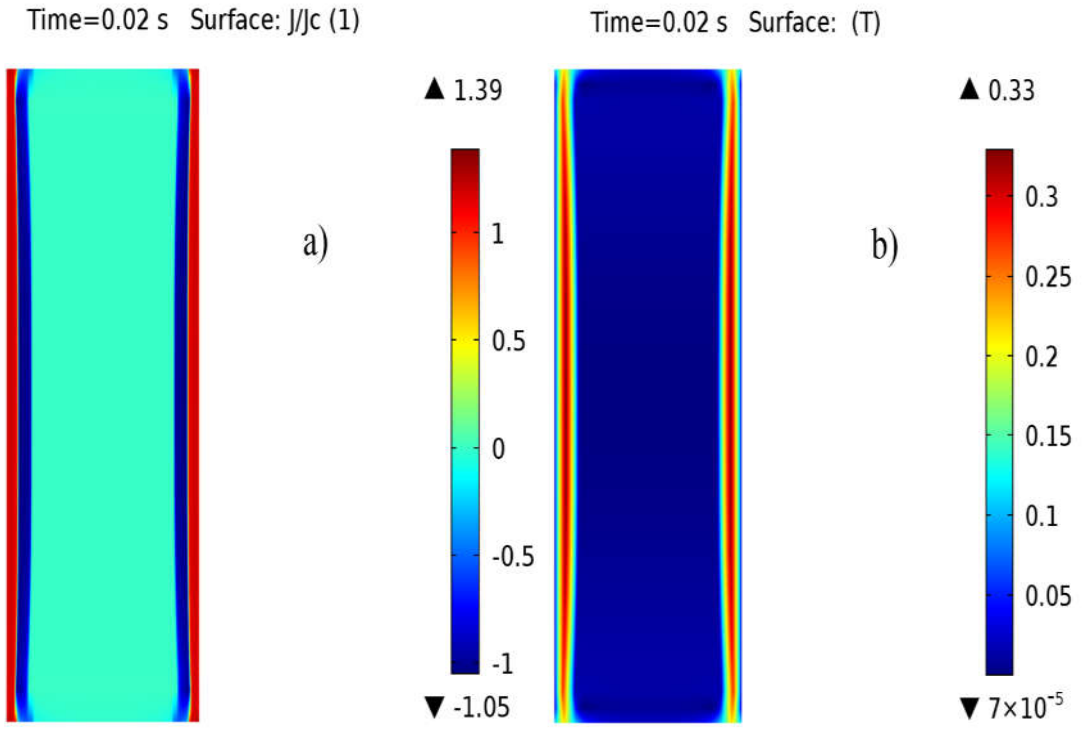

Figure 5.15 (a) J/J_c and (b) normB distribution at 310 A operating current. Plots are captured at time 0.02s and at 2π phase value.

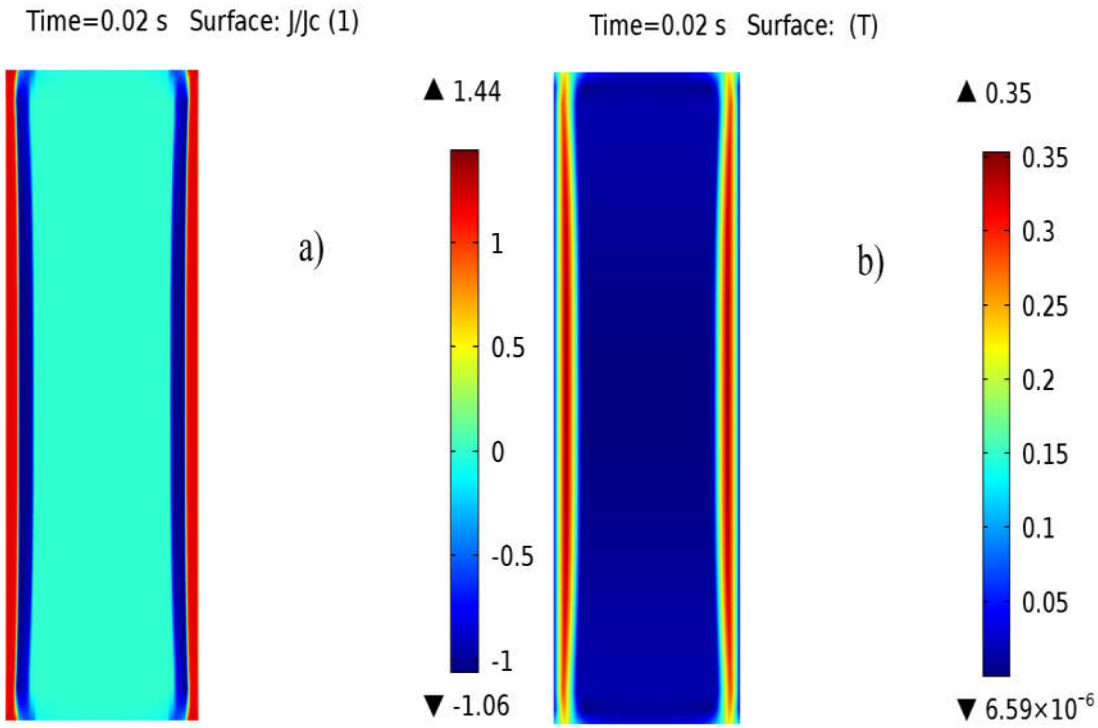

Figure 5.16 (a) J/J_c and (b) normB distribution at 330 A operating current. Plots are captured at time 0.02s and at 2π phase value.

It can also be worth noticing that the width of the influenced zone is increased with the increase in the operating current or load factor Figure 5.10 to Figure 5.16.

Also, normB distributions can also be observed among the stacked tapes Figure 5.10 to Figure 5.16 and it has been found that with the increase in the operating current or load factor the magnetic flux density is increased from 0.22 T (at 210 A) to 0.35 T (at 330 A). Thus, it is concluded from here that by increasing the current magnitude high dense fields can be achieved.

5.5.2. AC Losses

AC losses have been computed using Equation 5.5 where Figure 5.17 shows the instantaneous AC losses for different operating currents. It can be observed that the AC losses are found to higher at higher currents. It is also worth noting that the rate of increase in AC loss is found to higher at higher operating currents (270 A to 330 A) than at lower currents (210 A to 270 A).

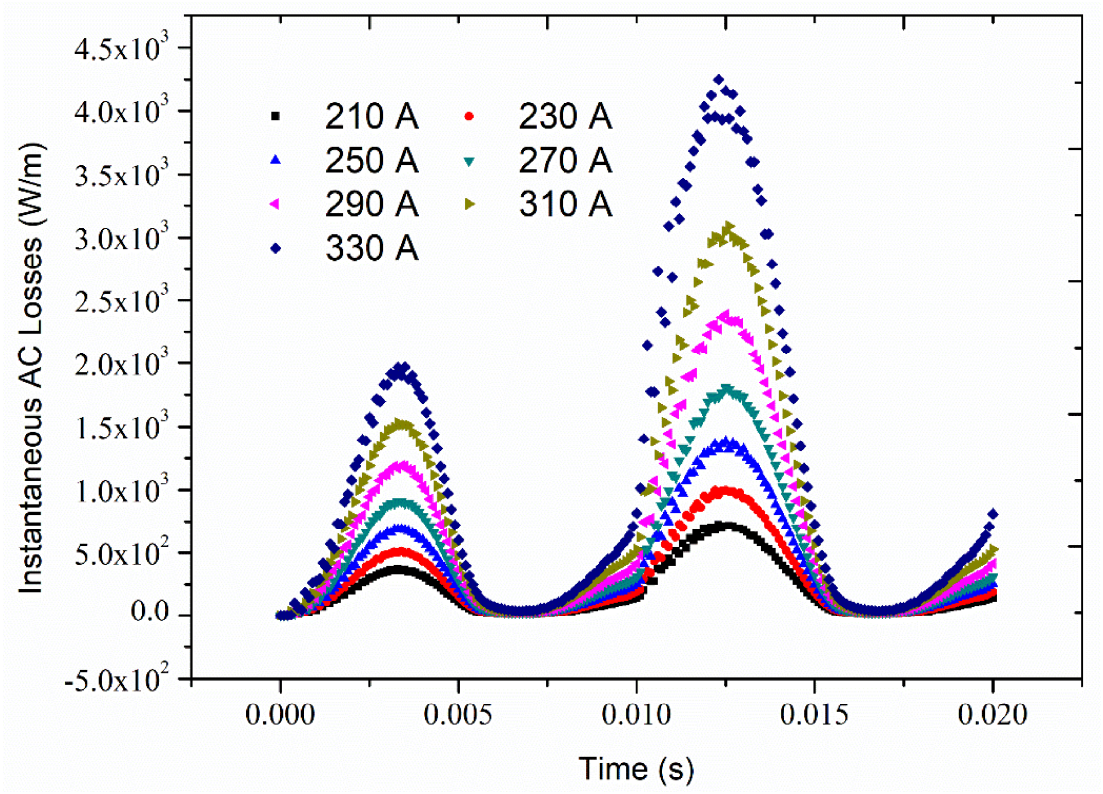

Figure 5.17 Instantaneous AC Losses (W/m) for different operating currents

Figure 5.18 shows the average loss variations with operating currents and the variation has been found exponential after fitting the data whose constants are tabulated in Table 5.6 along with standard errors, where I_{op} is the operating current. This exponential function can be used to estimate the AC losses among the operating current varying from 210 A to 330 A at 77 K temperature.

Table 5.6 Curve Fitting Parameters

Average AC Loss= exp (a + b*I_{op} + c* I_{op} ^2)		
Constants	**Values**	**Standard Error**
a	3.00049	0.68086
b	0.01156	0.00478
c	4.8495E-6	8.3043E-6

Average AC loss of 1.56 kW/m is found at 330 A operating and 268 W/m is at 210 A. Thus, the overall average AC loss at 210 A is 70 kW and at 330 A is 0.4 MW which means the losses are approximately 6 times more for 330 A. This implies that AC

losses are very sensitive to operating currents and found to increase with faster rates as operating current approaches to critical value.

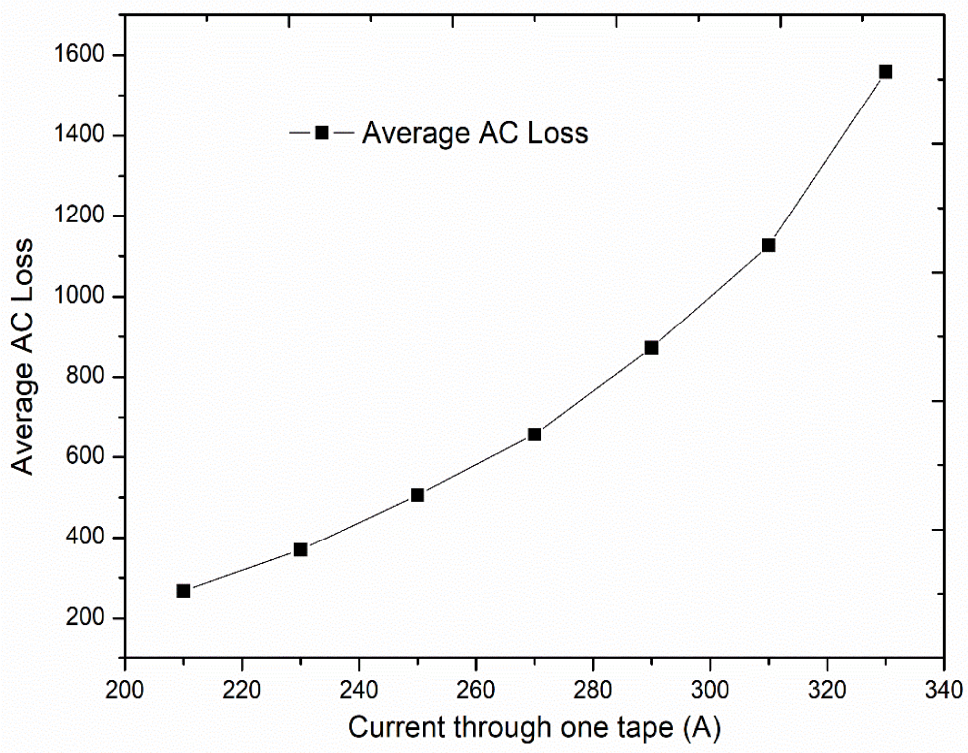

Figure 5.18 Average AC Loss at different operating currents

5.5.3. Mesh Sensitivity

In order to obtain the optimum mesh size, mesh sensitivity analysis has been performed where different mesh densities are used to estimate the AC losses as shown in Figure 5.19. It has been noticed that the horizontal mesh density (HMD) 500 and vertical mesh density (VMD) equal to 5 estimated same results as HMD=500 and VMD=10. The other parameters like degree of freedoms and computational time are tabulated in Table 3. The system configurations were as follows: Intel Core i5-8250 CPU @1.6GHz, 8GB RAM, 64-bit operating system with Window 10.

Table 5.7 Mesh Sensitivity Parameters

HMD	VMD	Degree of Freedoms	Computational Time
200	5	18613	47min
300	5	27151	62min 30s
400	5	35035	93min 23s
500	5	43345	110min 21s
500	10	48845	125min 33s

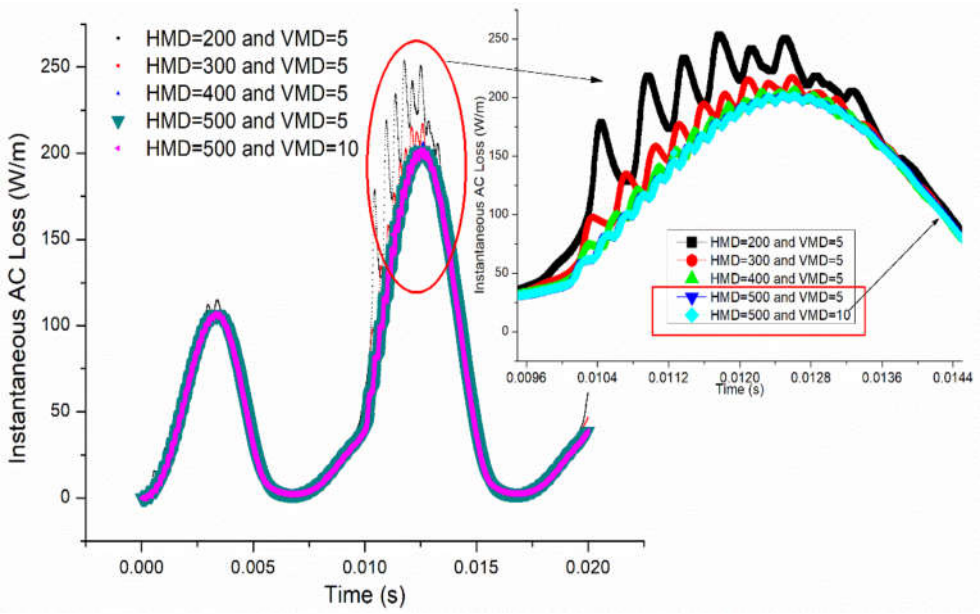

Figure 5.19 Mesh Sensitivity Analysis at different mesh sizes

5.6. Effect of number of turns on the AC losses

For a solenoidal magnet, using analytical correlations as explained in section 3.5 page-74, there are two types magnet configuration can be obtained, either by increasing the overall number of pancake coils (decreasing number of turns per pancake) or by increasing the number of turns per pancake (decreasing the overall number of pancake coils).

Table 5.8 Curve Fitting Parameters

Average AC Loss= exp (a + b*I_{op} + c* I_{op} ^2)		
Constants	**Values**	**Standard Error**
a	4.6525	0.84643
b	0.0187	0.01604
c	-1.40644E-5	7.54E-5

However, increasing number of turns per pancake coil is more feasible choice theoretically, as denser magnetic field can be generated which is needed to have larger energy densities (Equation 5-22) among the magnet. Thus, in this section, the effect of number of turns on the magnetic flux density and AC losses have been evaluated.

$$\text{Energy density} = \frac{B^2}{2\mu_0} \qquad 5.28$$

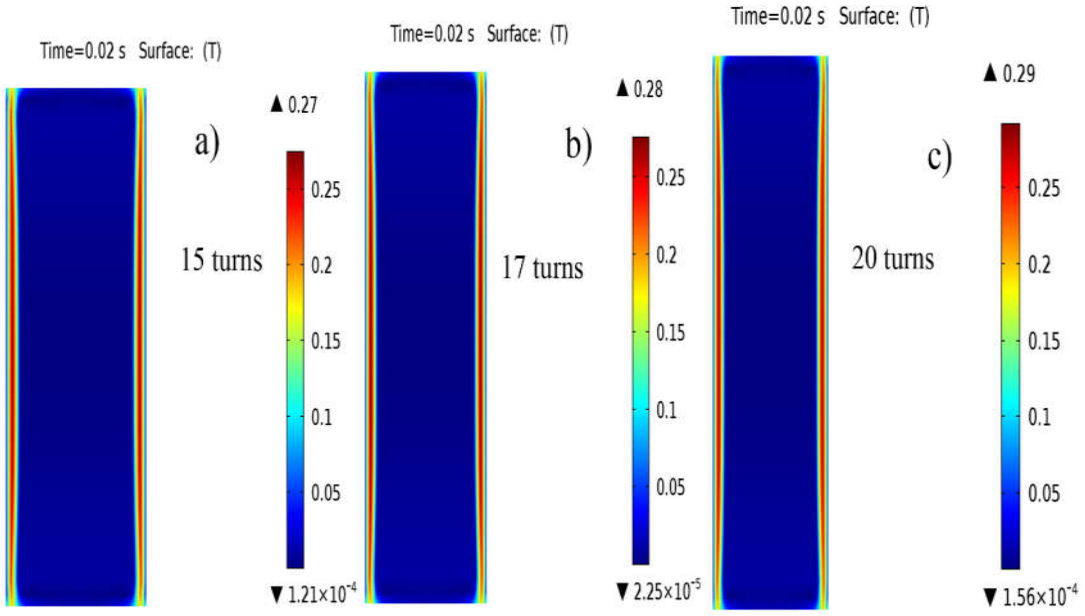

Figure 5.20 Magnetic flux density distribution (a) for 15 turns, (b) 17 turns, (c) 20 turns.

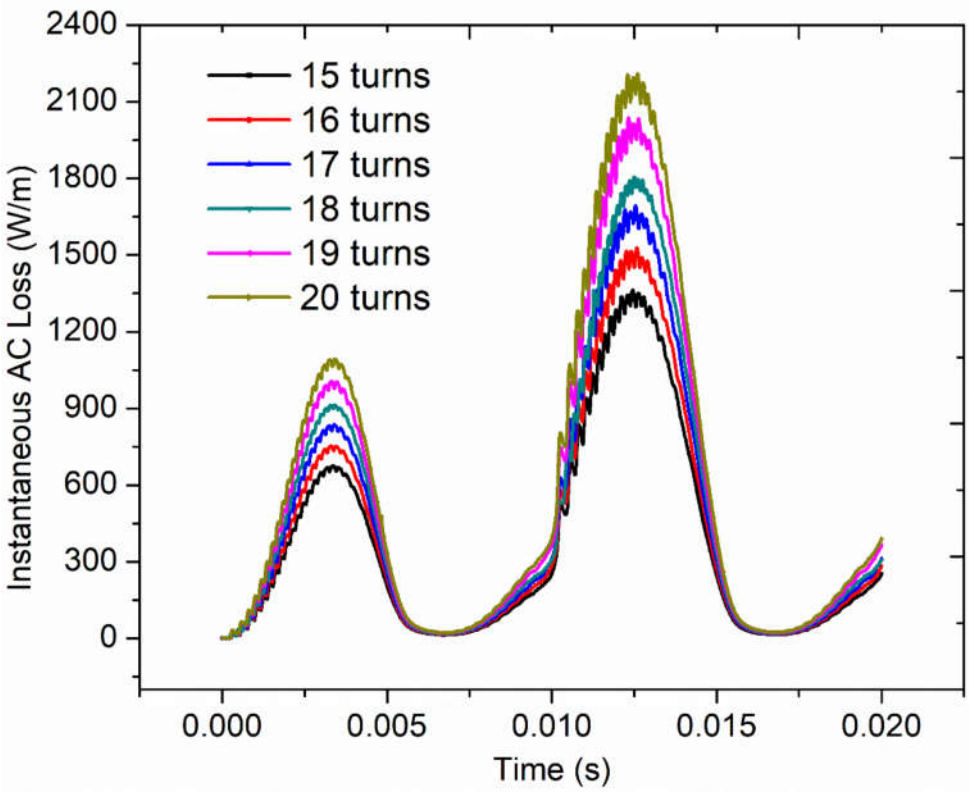

Figure 5.21 Instantaneous AC Loss variations for full cycle

For 1 MJ capacity magnet, 108 tapes (6 stacked tapes with 18 turns) are there around the pancake coil with 49 pancake coils mounted one over the other. In order to evaluate the effect of number of tapes around the coil, the turns varied from 15 turns

(15*6=90 tapes) to 20 turns (120 tapes). Figure 5.20 shows that with the increase in turns, magnetic flux density increased. However, it is clear from Figure 5.21 that with the increase in the number of turns instantaneous AC losses are also found to increase which implies one has to sacrifice in either way.

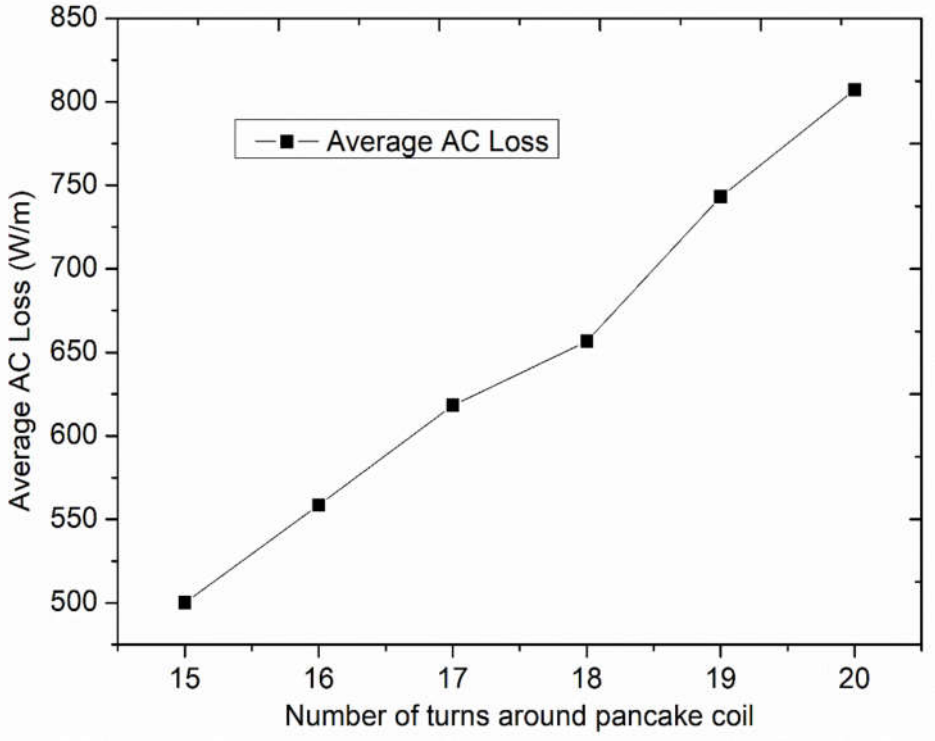

Figure 5.22 Average AC Loss variation with number of turns around the coil

Figure 5.22 shows the average AC loss variation with number of turns and this behaviour is found to exponential whose parameters are tabulated in Table 5.8. It has been concluded from this analysis that AC losses and magnetic flux density are found to increase with higher number of turns. Therefore, if one needs dense fields then compromise has to be make among losses and magnetic flux density. For the optimum design other parameters like length of the superconductor, height of the solenoid, stray fields, surface area etc. can also be taken into considerations.

5.7. AC Loss Control Strategies

5.7.1. Effect of substrate layer thickness on the AC losses

Mark D Ainslie [220] has discussed that AC losses can be controlled by increasing the substrate layer thickness thus overall thickness of the SC tape. Coated conductors manufactured with iBAD technique is independent from the magnetic substrate.

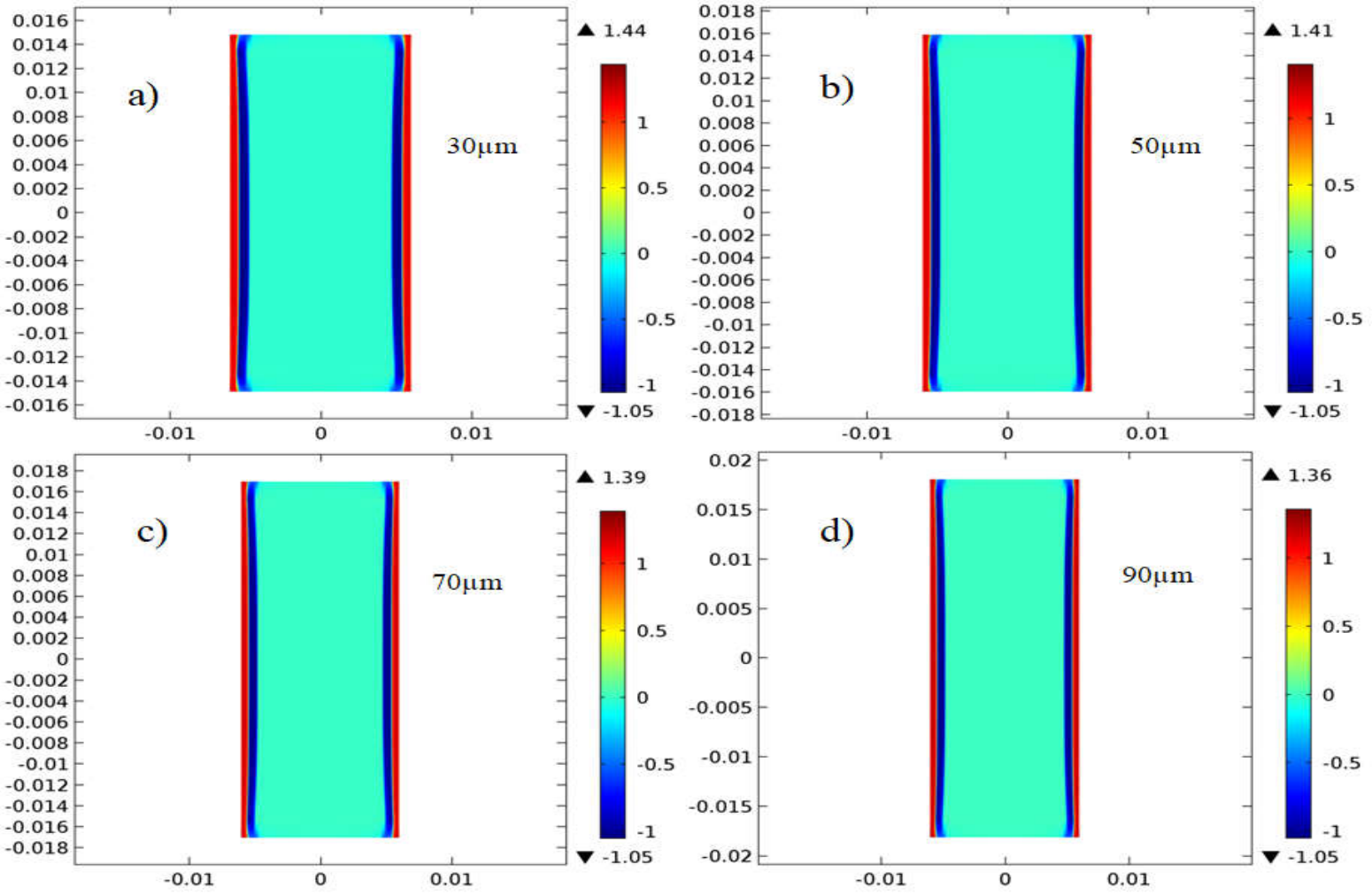

Figure 5.23 J/J_c distribution for different substrate thicknesses

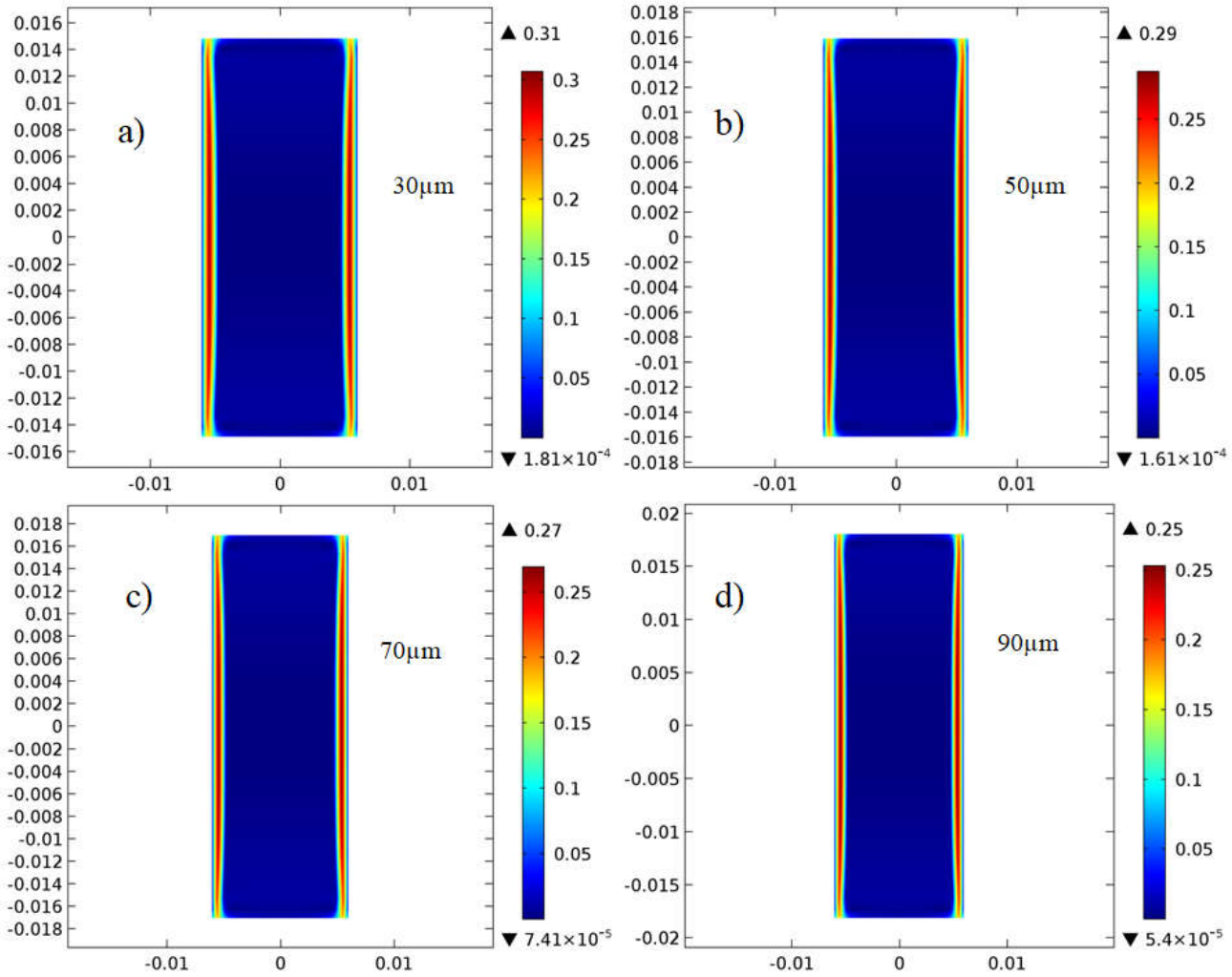

Figure 5.24 Magnetic flux density distribution for different substrate thicknesses

The thickness of the substrate material has been varied from 30µm to 90µm and the variation in J/J_c, magnetic flux density and AC losses has been evaluated and has been presented in following sections.

5.7.1.1. Magnetic Flux and Current Density Distributions

Figure 5.23 and Figure 5.24 shows the J/J_c and normB distribution for different substrate thicknesses (30 to 90 µm) at 50Hz sinusoidal frequency respectively. It can be noticed that the J/J_c ratio is found to reduce with substrate thickness. Same trend is repeated for magnetic flux density distribution which implies less dense magnetic flux is available at the core.

5.7.1.2. AC losses

Figure 5.25 and Figure 5.26 shows the instantaneous and average AC loss variation for various substrate thicknesses. It can be seen from Figure 5.25 that the losses are found to decrease with increase in substrate's thickness.

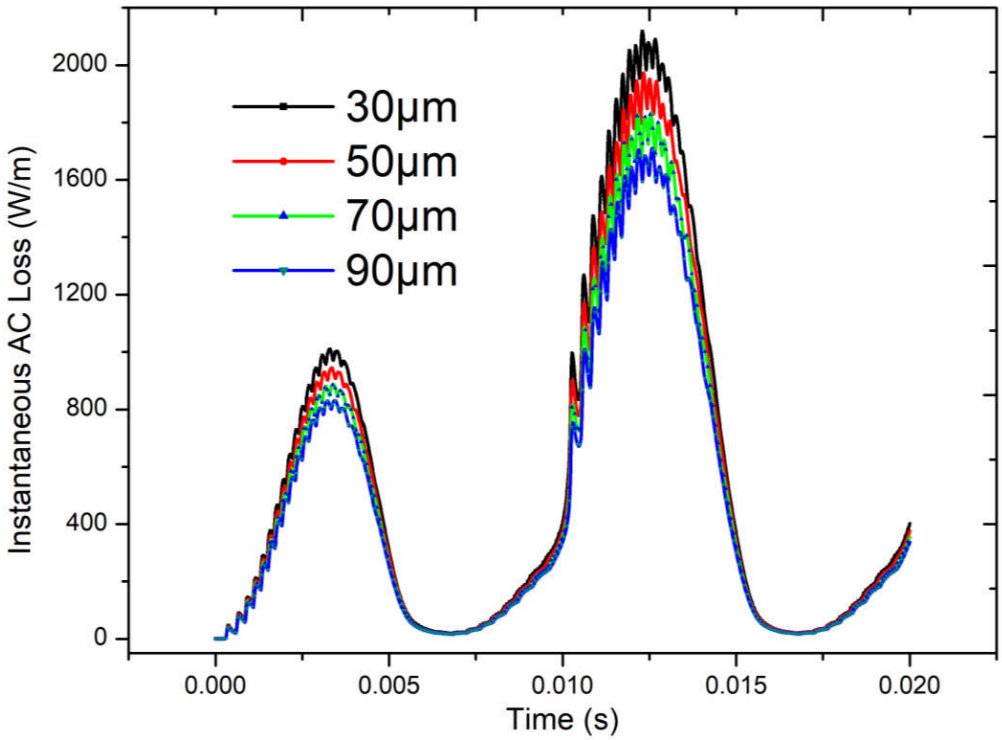

Figure 5.25 Instantaneous AC Losses (W/m) for different substrate thicknesses

Figure 5.26 indicates the average losses which found to decrease with thickness parabolically. To estimate the average losses within 30 to 90 µm, a correlation has been made whose parameters are given in Figure 5.26. Lower AC losses are always

desired in the superconducting applications which are generally appears for few fraction of seconds in the initial stages when current starts approaching to its steady state magnitude. The effect of substrate's thickness on the AC losses has been examined and results showed that there is a significant reduction in the AC losses with increase in thickness however at the cost of magnetic flux density which is also found to decline with thickness. This implies compromise has to make while choosing the substrate's thickness which further depends upon the type of applications (motors, energy storage, transformers, generators, fault current limiters etc.) where such superconducting pancake coils are to be used.

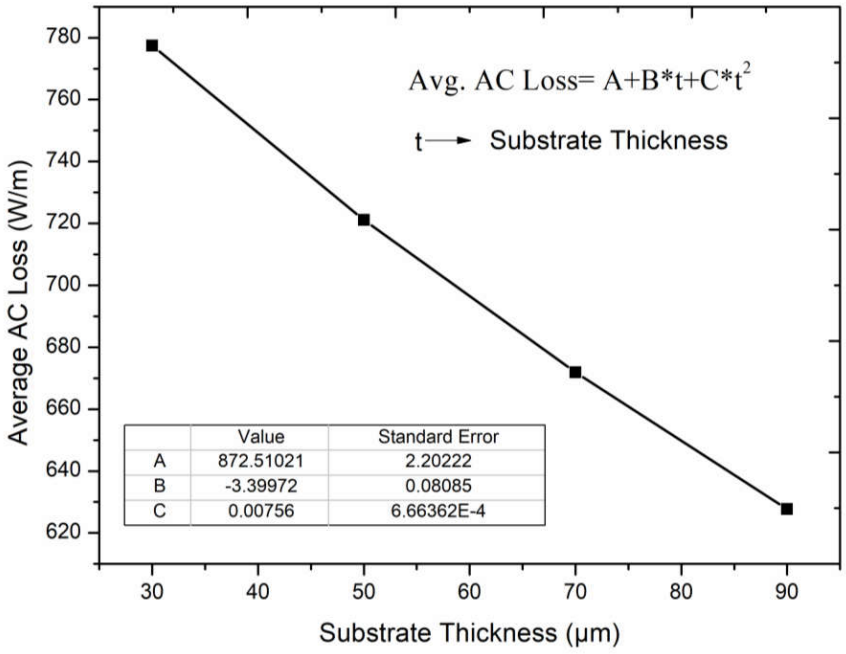

Figure 5.26 Average AC losses vs. substrate thickness

5.8. Conclusions

In this chapter, AC loss analysis on the multi-turned pancake coil has been performed. Maxwell equations have been solved using H-formulation computational technique. It has been observed that edge elements can reduce the computational complexities to a greater extent and can be used in AC loss estimation. In order to avoid complexities, 2D model has been solved for homogeneous domain. It has been concluded that number of turns has significant effect on the AC losses and such losses can be controlled by increasing the substrate layer thickness at the cost of magnetic density.

Chapter-6

Thermal Quench of Superconducting Tape

In this chapter, the electro-thermal computational studies have been performed on superconducting tape using COMSOL MultiPhysics software. The numerical model is approximated as two dimensional as buffer layers and interfacial resistance layer are approximated as infinitely thin domains which further implies that in-plane (J_x and J_y) current densities are taken as negligible and only normal component of current density (J_z) has been considered. Heat flux equation has been modelled using simple Fourier expression where temperature variation along z-axis has been considered. It has been found that with the increase in the interfacial resistance, the normal zone propagation velocity increases and thus in order to consider extra safety of the tape, larger resistances can be imparted to the interface.

Keywords: HTS tape, normal zone propagation velocity, interfacial resistance, quench, SMES, thermal analysis of HTS tape, electro-thermal studies of tape.

6.1. Introduction

Coated conductors are extensively used for power applications due to their capability to carry more currents and work efficiently near the critical currents. Almost in all power applications like cables, motors, generators, transformers, MRIs, NMRs, fault current limiters and magnetic energy storage systems coated conductors have replaced copper conductors as they are more efficient in handling currents and need less space than conventional devices. As fault current limiting and energy storage devices work near the critical currents so there may be situation arises when hot spots may come into existence which may lead to quench of the superconductor. The development of HTS cables is also receiving attention these days where design of current carrying cable is done with higher load factors in order to maximize its current carrying capacity. However, large currents can create unbalance due to heat generation which can lead to hot spots and further the thermal quench of the tape. This issue is still to be addressed and many research groups are working on this aspect theoretically/computer modeling [221]–[228] and experimentally [229][230].

Recently, second generation high temperature superconducting (HTS) tapes have been widely employed in design and development of Superconducting Fault Current Limiters (SFCL) and Superconducting Magnetic Energy Storage (SMES) systems. These systems are generally operated near the critical currents of the coated conductors to get the maximum energy and power densities thus there will be situations when the hot spots may occur due to the heat generation that may lead to quenching of the superconductor. Various studies have been proposed where attempts have been made to increase the normal zone propagation velocity (NZPV) to avoid such hot spots initiation. Large NZPV can be achieved by varying the interfacial resistance among the superconductor and stabilizer layer.

When a current, '*I*' is applied to such devices is found to near critical current I_c then there may be some locations where hot spots (due to thermal instabilities) can appear in the weaker zones of the superconducting tape. Inhomogeneities in the superconducting materials can be arises due to manufacturing defects at micro-scale levels that can affect the I_c of the tape or any other phenomena such as existence of external magnetic field results into the arbitrary increase in the temperature of the

superconducting tape locally which further leads to hot spots. Such hot spots can damage the whole system if local temperature exceeds the critical value. Thus, it becomes essential to avoid hot spots among the superconductors used for any application in order to prevent the failure of the system.

Quenching is a phenomenon when temperature of superconducting tape exceeds critical value (T_c) and as discussed earlier it may arise due to hot spots. Hot spot concerns subsist in all superconducting devices however they are more prominent in SMESs and SFCLs systems as in the former, the operating currents are generally chosen as close as to I_c to maximize the field generated [231] and in the later, their main functionality is based on the quenching of superconductor [232][233]. Studies reveal that for coated conductors, NZPVs are low which makes them prone to hot spots and this result into the drastic increase in the temperature before sufficient voltage drop develops and detecting the quench in case of superconducting magnets [234].

Various strategies have been adopted to mitigate hot spot challenges and among them increasing the thickness of stabilizer or substrate layer are commonly used in order to increase the thermal mass [235]. However, only over-sizing the tape by increasing copper's thickness not serves the purpose and a marginal current (temperature) is required to provide the enough time before the detection of the quench and to modify or stop the input current before the system failure. Therefore, it is better to work near 80% of load factor which provide enough margins to take care such issues. However, this margin obviously reduces the maximum attainable magnetic field inside the magnet [231].

The other approach to diminish the temperature rise at hot spots is to increase NZPV; however, it reduces the stability margin of the superconducting tape. This factor can be enumerated by the minimum energy required to initiate a quench and this energy is generally known as minimum quench energy (MQE) [236], [237]. Numerous methods have been proposed by various researchers in order to enhance the NZPV in the coated conductors. For illustration, researchers have suggested to use sapphire as a substitute for Hastelloy whose electrical and thermal properties favors large NZPV [238]. Recently, researchers have suggested to intentionally increasing the interfacial

resistance among the stabilizer and superconductor to enhance the NZPV in coated conductors [239]–[241]. This increases the current transfer length (CTL) among stabilizer and superconductor. This concept is easy to implement and provides attractive solutions, however, the critical challenges exist in increasing the interfacial resistance is associated with the amount of heat generation at the interface of current leads connections as at this location the temperature increased drastically such that it may cause quenching of the superconductor.

In this work, keeping large interfacial resistances, simple superconducting tape architecture has been used to increase NZPV. Here, it has been assumed that the interfacial resistance is not uniform along the width of the tape, instead having a segment of very low interfacial resistance and the other segment with very high interfacial resistance. A 2D numerical model has been developed using Comsol MultiPhysics and a comparison has been made for NZPV among different interfacial resistances.

A slight modification has been done in the architecture of the tape (Figure 6.1) where different interfacial resistances have been employed to estimate the temperature distribution among HTS tape having 10 cm length. A numerical model has been developed to evaluate the NZPV and it has been found that more velocities can achieved with large interfacial resistances through which quenching of superconducting tape can be prevented.

6.2. Numerical Modelling

2D model has been developed in the Comsol MultiPhysics 5.4 where Joule heating module has been employed for the numerical solution of the model. Electro-thermal behavior of the coated conductor has been examined where interfacial resistance among the superconducting and stabilizer layer has been varied. The basic geometry and methodology followed has been explained in the following sections.

6.2.1. Assumptions

- Effect of external magnetic field has not been considered.

- The interfacial resistance is not uniform along the width of the tape, instead having a segment of very low interfacial resistance and the other segment with very high interfacial resistance.
- The electrical conductivity of normal state while transition from superconducting state can be modelled by assuming two resistances in parallel.
- The temperature gradient at the both ends of the tape is zero.

6.2.2. Geometrical details

Coated conductors have been used for the present study whose geometry is given in Figure 6.2 where length of the tape assumed to be 10 cm and other parameters are tabulated in Table 6.1. The width of the tape is 12 mm and the thickness of superconducting (SC) layer is 1 μm. Generally, SC tape consists of four layers viz; stabilizer, superconducting layer, substrate and buffer layers. For the tape that has been chosen in the present study, the stabilizer layer is composed as silver (Ag), superconducting layer as ReBaCuO, substrate as Hastelloy and buffer layer using MgO. The architecture of the tape has been given in Figure 6.1 where longitudinal arrangement of the different layers has been presented. The marked arrows represent the virtual probe locations which are generally used to evaluate the electric field variations with time those are separated by a distance of 1 mm. Multi-colors are used to distinguish the different layers and Figure 6.1 represents that from left end current has been supplied and the other end is grounded which consists low J_c region at the end of the superconducting tape. The highly resistive layer can be termed as current flow diverter as it is responsible for diverting the current from SC region to stabilizer in order to ensure the safety of the superconducting tape from quenching. most of the tape's temperature dependent properties has been taken from [242]–[247]. A detailed information is available on the properties like thermal conductivity, specific heat and electrical resistivity/conductivity of buffer layer (MgO), stabilizer (Ag), Substrate (Hastelloy) and SC tape (ReBCO for $T>T_c$) is present in [242]–[247]. As the tape is required to cool at 77 K thus all property data is extracted on this liquid nitrogen temperature.

A mathematical model with few modifications has been used as that of Lacroix et al. [228] in the present study, current densities are considered 100 times greater than that of Lacroix model and the tape width is considered to be 12 mm instead of 4 mm. Due to the non-linear behavior of resistivity below T_c, electrical conductivity is also behaving in the similar way thus power-law model is used to approximate the electrical conductivity of (Re)BaCuO in the flux creep and flux flow regions (σ_{sc}).

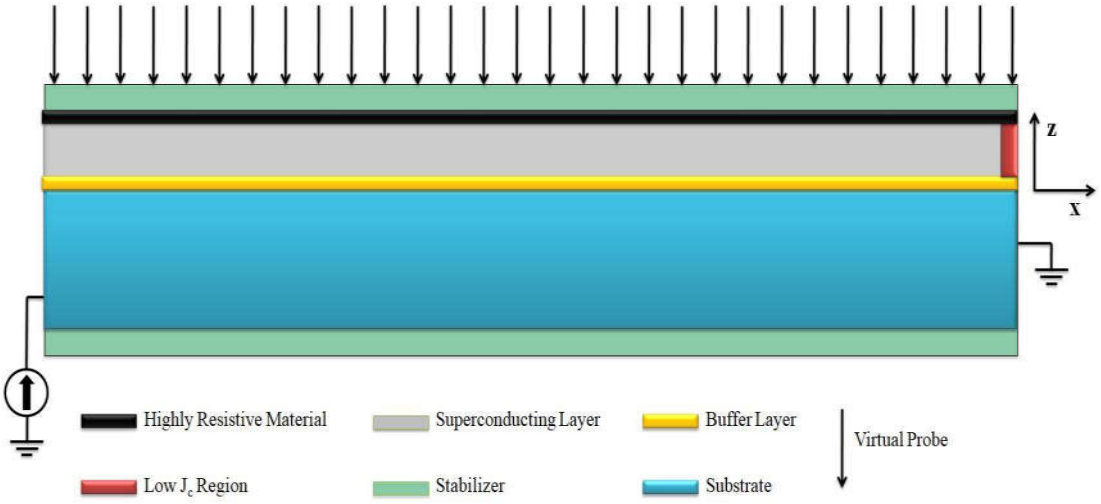

Figure 6.1 Tape Architecture

However, the electrical conductivity of normal state while transition from superconducting state can be modelled by assuming two resistances in parallel. The following expressions has been used for the present simulations:

$$\sigma_{sc}(T) = \frac{J_c(T)}{E_0}\left(\frac{\|E\|}{E_0}\right)^{\frac{1-n(T)}{n(T)}} \tag{6.1}$$

$$J_c(T) = \begin{cases} J_{c0}\left(\dfrac{T_c - T}{T_c - T_0}\right) & for\ T < T_c \\ 0 & for\ T_c \le T \end{cases} \tag{6.2}$$

$$n(T) = \begin{cases} (n_0 - 1)\left(\dfrac{T_c - T}{T_c - T_0}\right)^{1/4} + 1 & for\ T < T_c \\ 1 & for\ T_c \le T \end{cases} \tag{6.3}$$

Table 6.1 Modelling Parameters involved in quench analysis

Parameter	**Numerical Value**
Length	10 cm
Width	12 mm
Substrate thickness	50 μm
Buffer layer thickness	150 nm
Superconducting layer thickness	1 μm
Interfacial layer between superconductor and stabilizer thickness	100 nm
Current flow diverter thickness	100 nm
Stabilizer thickness- top	2 μm
Stabilizer thickness- sides and bottom	1 μm
Substrate thickness	50 μm

Table 6.2 Nomenclature

J_{c0}	Critical current density at T_0
T_0	Liquid nitrogen temperature
$\|E\|$	Norm electric field
T_c	Critical temperature
n_0	Fitting parameter
d	Width of the low J_c region
A	Amplitude of the low J_c region
l	Position of the low J_c region
$I(t)$	Applied transport current
Ω	Represents the surface at one end of the tape
n	Local unit vector perpendicular to the external surfaces of the tape
$\sigma(T)$	Electrical conductivity
ρ_m	Mass density of the tape
$C_p(T)$	Heat capacity
$k(T)$	Thermal conductivity

6.2.3. Electro-thermal modelling

In order to initiate the normal zone propagation, a low J_c region has been incorporated in the tape architecture highlighted by red area as mentioned in Figure 6.1. Same

model as that of Lacroix et al. [228] has been imitated in the present study where reduction in the critical current has considered by the following relation:

$$J_{c0} \rightarrow J_{c0}\left[1 - Ae^{\frac{-(x-l)^2}{2d^2}}\right] \qquad 6.4$$

It has been designed in such a way that whenever current density through the superconducting tape exceeded $J_{c0}(1-A)$ then heat is generated at low Jc region which further generates normal zone and that is expected to expand with time.

Potential V and the temperature T are the variables for the electro-thermal model of the superconducting tape. The governing equations used for electro-thermal modelling are as follows:

Electrical part

$$\nabla.(-\sigma(T)\nabla V) = 0 \qquad \textit{within the tape} \qquad 6.5$$

$$\int_{\Omega} -\mathbf{n}.(-\sigma(T)\nabla V)\,\mathrm{d}S = I(t) \qquad \textit{at left end of the tape} \qquad 6.6$$

$$V = 0 \qquad \textit{at the other end of the tape} \qquad 6.7$$

$$\mathbf{n}.\nabla V = 0 \qquad \textit{at the remaining boundaries of the tape} \qquad 6.8$$

Thermal part

For the thermal analysis, heat equation can be written as

$$\rho_m C_p(T)\frac{\partial T}{\partial t} + \nabla.(-k(T)\nabla T) = Q_j \qquad \textit{in the tape} \qquad 6.9$$

Joule heating losses can be evaluated using following coupled correlation:

$$Q_j = \sigma(T)(-\nabla V)^2 \qquad \textit{in the tape} \qquad 6.10$$

For the present study, it has been assumed that the temperature gradient at the both ends of the tape is zero as described by following equation:

$$\mathbf{n}.\nabla T = 0 \qquad \textit{at the both ends of the tape} \qquad 6.11$$

For the remaining boundaries, as superconducting tape is assumed to be through liquid nitrogen at 77 K therefore, the cooling power required by the nitrogen can be evaluated though the following relation:

$$\mathbf{n}.(k\nabla T) = h(T - T_0) \qquad \textit{at the remaining boundaries} \qquad 6.12$$

6.2.4. Numerical Approximations

For the 2D analysis, buffer layers and interfacial resistance layer are approximated as infinitely thin domains which further implies that in-plane (J_x and J_y) current densities are taken as negligible and only normal component of current density (J_z) has been considered. Therefore, after such approximations Equation 6-6 becomes:

$$J_z = \sigma(T)\frac{\partial V}{\partial z} = \sigma(T)\left(\frac{V_2 - V_1}{t}\right) \qquad 6.13$$

V_2 and V_1 are the potentials on each side of the infinitely thin layer and t is the thickness of the layer. Similarly, the heat flux (Q_z) flowing through infinitely thin layers can be calculated using following equation:

$$Q_z = k(T)\frac{\partial T_1}{\partial z} = k(T)\left(\frac{T_2 - T_1}{t}\right) \qquad 6.14$$

T_2 and T_1 are the temperatures on each side of the infinitely thin layer and $k(T)$ is the layer thermal conductivity.

Lacroix et al. [228] found that in the infinitely thin layer, both electric potentials and temperatures are discontinuous for such approximations and the values of the potentials and temperatures are not same on the both sides of the layer. This jump in the values can be handled using interface boundary conditions Equation 6-13 and Equation 6-14 which is a representation of the lumped approximation in continuous case and this significantly depends upon thin layer material properties i.e. electrical conductivity, thermal conductivity and thickness of the layer.

6.3. Validation

In order to validate the opted computational methodology, an attempt has been made to reproduce results of the research work done by Lacroix et al [228]. Parameters involved for the validation are tabulated in Table 6-3 and the schematic of the model

is given in Figure 6.2. The computational model used to validate the results is same as explained earlier in this chapter.

Table 6.3 Parameters of the tape for validation of the model

Parameter	**Numerical Value**
Length	5 cm
Width	1 cm
Substrate thickness	50 µm
Buffer layer thickness	150 nm
Superconducting layer thickness	1 µm
Interfacial layer between superconductor and stabilizer thickness	100 nm
Current flow diverter thickness	100 nm
Stabilizer thickness- top	2 µm
Stabilizer thickness- sides and bottom	1 µm

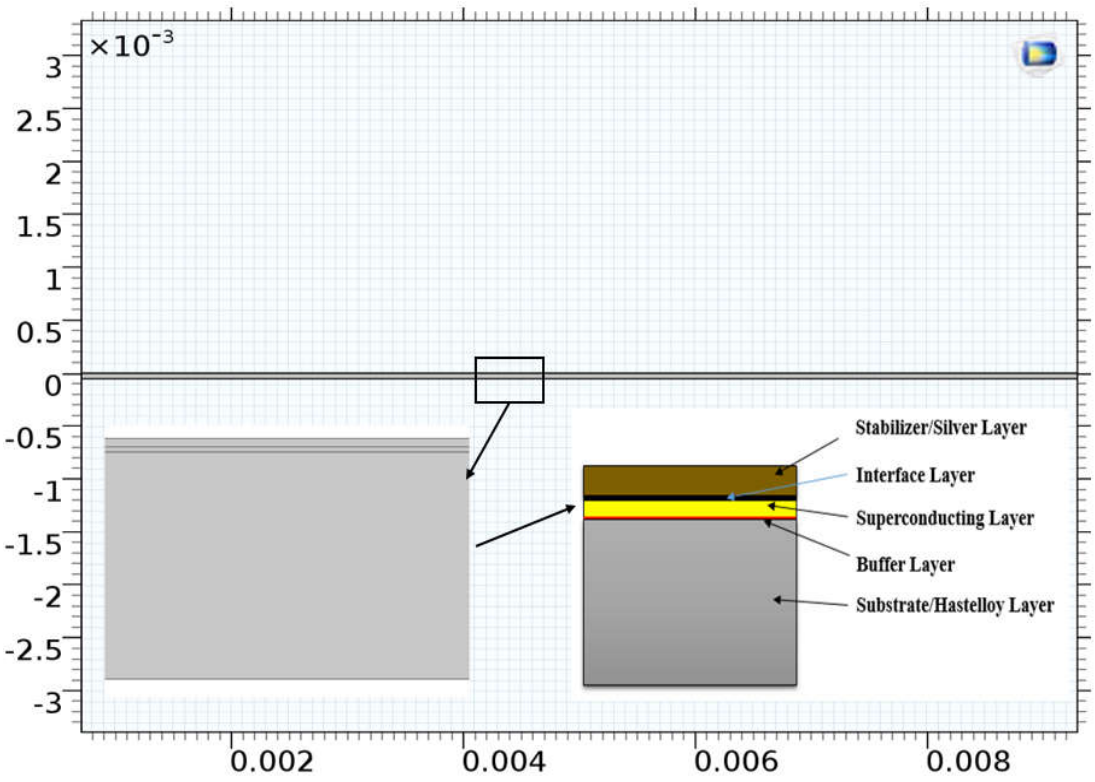

Figure 6.2 Electro-thermal model details

Normal zone propagation velocity (NZPV) has been evaluated in order to verify the computational integrity of the present model. In order to evaluate NZPV, point plot

for various probe locations have been captured for temperature distribution among the tape as shown in Figure 6.3.

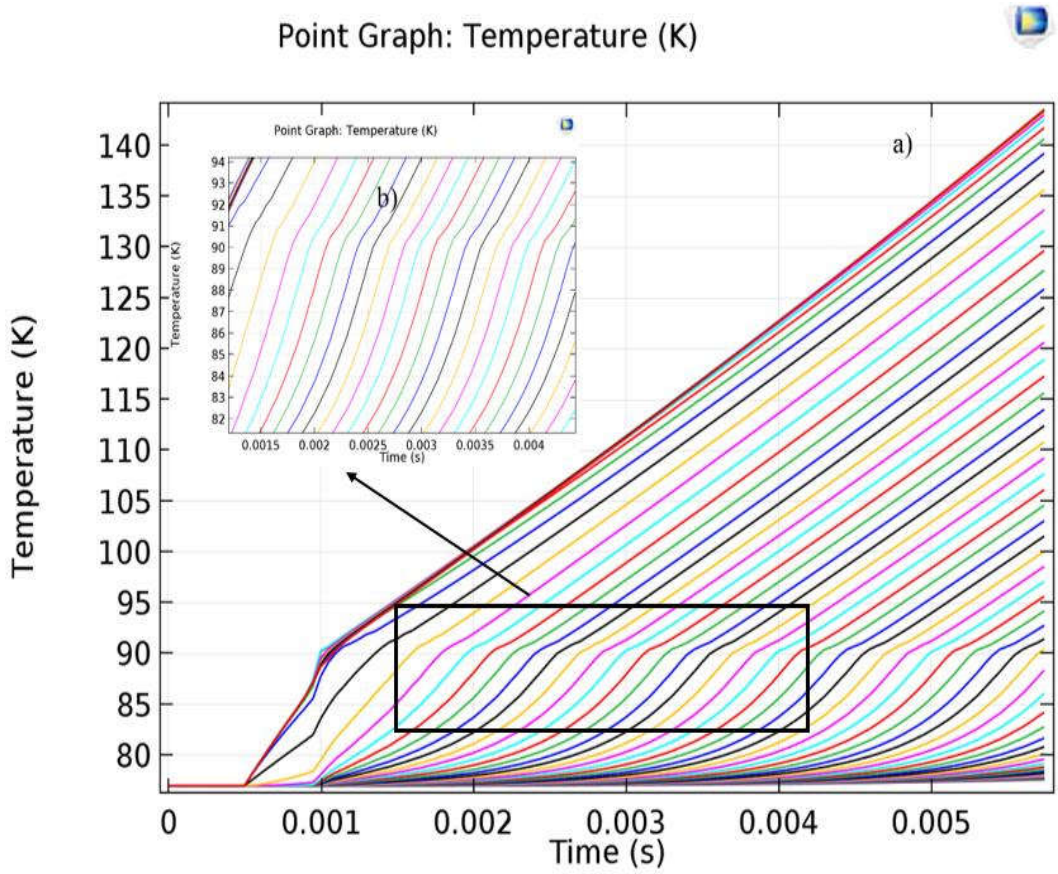

Figure 6.3 Temperature profile for different time steps

From the Figure 6.3, this can be noticed that the different curves representing the temperature distribution among the tape are almost parallel to each other and the NZPV can be calculated by taking the ratio of the distance between adjacent virtual probes to the time elapsed to reach the same temperature. Figure 6.4 shows that the calculated NZPV for the validated model is 741 cm/s against the value obtained by Lacroix et al as 736 cm/s. As the calculated value is very close to the other work thus this model is used to evaluate the effect of interfacial resistance on the NZPV of the superconducting tape.

6.4. Mesh Sensitivity Studies

The computational domain is discretized with mapped meshing where each layer of the superconducting tape including stabilizer, substrate and superconducting layer is

sub-divided into small sub-domains using mapped meshing technique. Superconducting tape of 10 cm length is discretized in transverse direction using 100, 200, 300, 400 and 500 elements as shown in Figure 6.5.

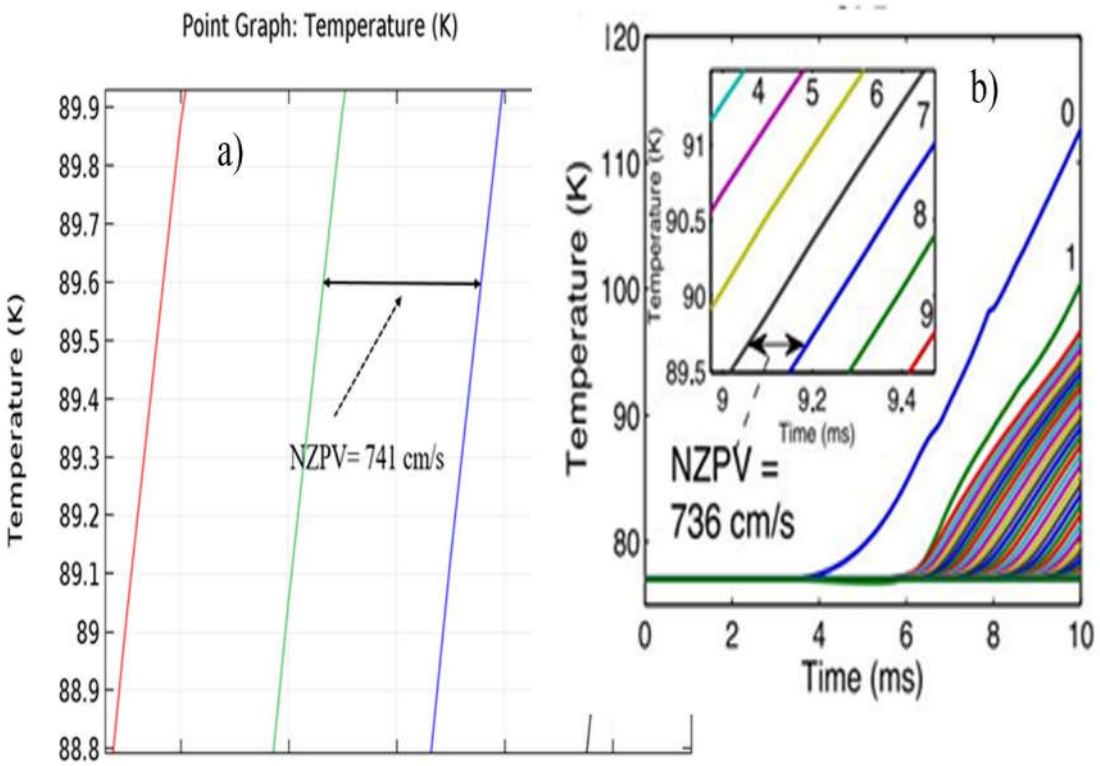

Figure 6.4 NZPV for model validation

It can be observed from Table 6.4 that for case-3, the maximum temperature rise within the tape for electrical conductivity 1e9 S/m is equal to case-4 and case-5. However, the computational time elapsed for analysis and degree of freedoms for case-3 are found to less thus this meshing has been used for rest of the studies. The system configurations were as follows: Intel Core i5-8250 CPU @1.6GHz, 8GB RAM, 64-bit operating system with Window 10.

Figure 6.5 (a) shows that there is one partition till 0.1 mm length of the SC tape and 5 partitions can be noticed in Figure 6.5 (e). However, Figure 6.5 (c) has been selected for the further studies due to the mesh density saturation has been found above this value.

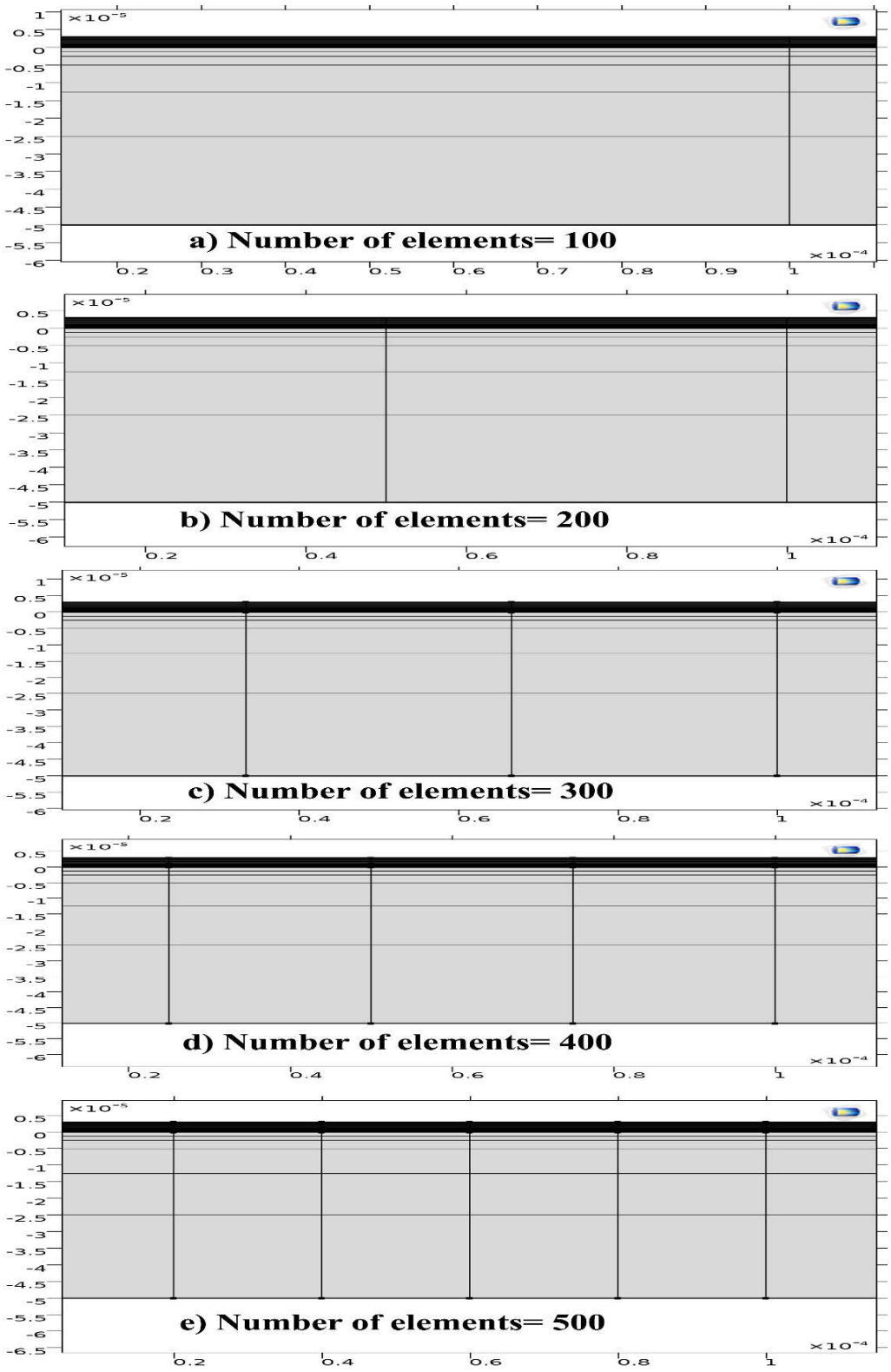

Figure 6.5 Mesh density analysis for 0.1 mm length of tape (a) 1 partition, (b) 2 partitions, (c) 3 partitions, (d) 4 partitions and (e) 5 partitions.

Table 6.4 Mesh sensitivity studies for electro-thermal analysis of the HTS tape

Sr. No.	Number of elements	Number of domain elements	Number of domain boundaries	Degree of freedom	Time (s)	Max. Temp. (K)
1.	100	3000	460	25327	22m 56s	95
2.	200	6000	860	50527	42m 47s	94.9
3.	*300*	*9000*	*1260*	*75727*	*1h 4m 37s*	*94.7*
4.	400	12000	1660	100927	1h 48m 32s	94.7
5.	500	15000	2060	126127	1h 56m 39s	94.7

6.5. Results and Discussions

The parameters involved in the quench dynamics are tabulated in the Table 6-1 where 2G HTS coated conductors have been tested for various interfacial resistance among the superconducting and stabilizer layer. For the modelling purposes, electrical conductivity has been used as input material property instead of resistivity. The right end of the tape is grounded and the effect of this has been tested for various electrical conductivities of the interface. More NZPV is required which implies the information regarding the fault has to dispersed uniformly to the left end so that uniform temperature distribution can be obtained in order to avoid instant gradients.

In order to evaluate the effect of interfacial resistance on the normal zone propagation velocity, a 2D model of a straight superconductor having length 10 cm has been drawn in Figure 6.2. Table 6.4 represents the different NZPVs achieved for various electrical conductivity input. To evaluate the NZPV, distance among the probes (shown in Figure 6.1) i.e. 1 mm is divided with the time elapsed to reach the same temperature as shown in Figure 6.6 and Equation 6-15.

$$Normal\ zone\ propagation\ velocity = \frac{1}{Time\ elapsed} \qquad 6.15$$

Figure 6.7 illustrate the temperature plots for different time steps and electrical conductivity and it can clearly visualize that with the increase in the interfacial resistance (from Figure 6.7 (a) to Figure 6.7 (f)), the NZPV is found to increase (Table 6-4). Further, it can be observed that the temperature gradient is found to less for higher resistances (Figure 6.7 (f)) compared to lower (Figure 6.7 (a)).

Thus, it has been concluded that higher interfacial resistances can increase the NZPV of the fault detection. It can further help in identifying the exact location of the fault.

Table 6.5 Normal Zone Propagation Velocity for various electrical conductivity

Electrical Conductivity (S/m)	NZPV (cm/s)
1e9	63.69
1e7	90.9
1e5	153.84
1e3	256.4
1e1	312.5
1e0	666.67

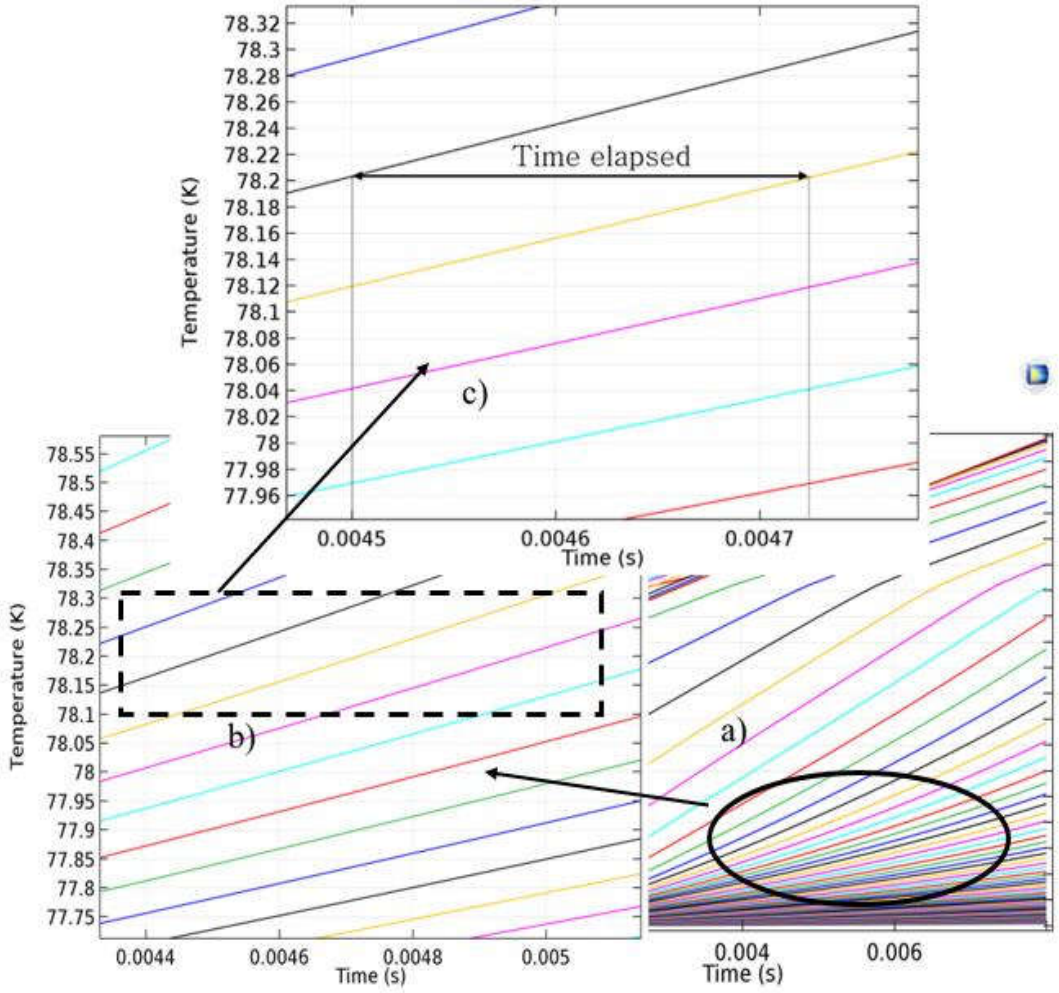

Figure 6.6 Temperature plot vs time

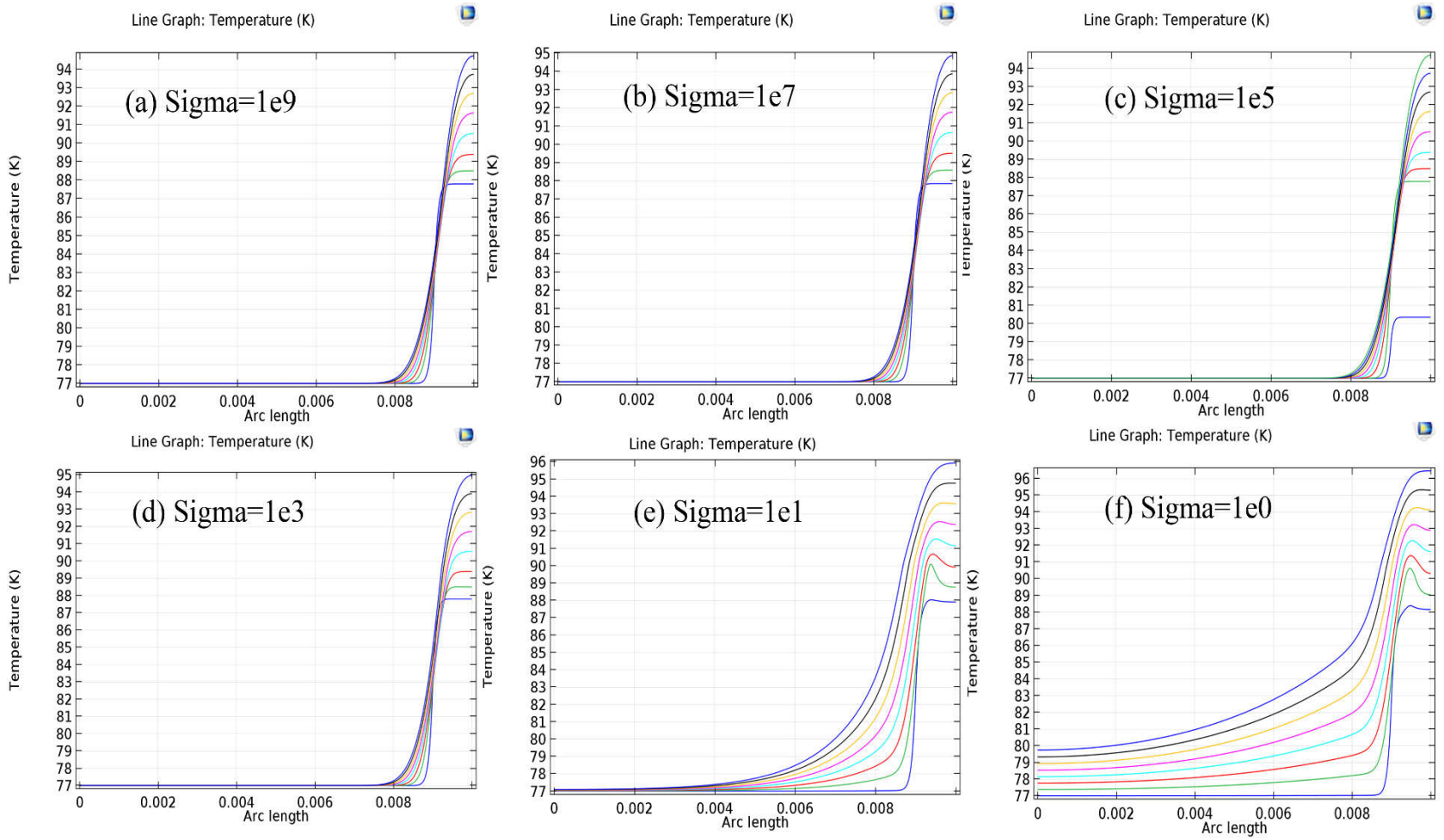

Figure 6.7 Temperature plot for various time steps and electrical conductivity

6.6. Conclusions

From the electro-thermal analysis of the superconducting tape, it has been concluded that with the increase in the interfacial resistance of the superconducting-stabilizer layer, the NZPV can be enhanced and which can assist in controlling the quenching of the tape. However, due to the increase in the interfacial resistance, the resistive losses may increase and thus, further studies are required in this regard.

Chapter-7

Conclusions and Future Scope

This dissertation is dedicated to the mechanical, electrical, magnetic and thermal studies of the superconducting magnetic energy storage systems which can be used in various applications like power/smart grid applications, power storage bank and propulsion applications etc. In chapter 3 to chapter 6, detailed studies has been presented related to mechanical design, self-field effects on critical current, AC loss estimation and quench of SC tape. In this chapter, overall conclusions have been made along with the future opportunities available in the further design and development of the SMES systems.

7.1. Overall conclusions

7.1.1. Mechanical Aspects

Mechanical design aspects of the solenoid magnet have been studied where input, design and constraints parameters have been evaluated and the effect of operating current, solenoid thickness and operating temperature on the magnet topology has been examined. From the study, it can be concluded that higher currents have significant effect on the length of the superconductor used for energy storage which implies less superconducting tape is required for energy storage if the operating temperatures are low. Secondly, if large solenoid thicknesses used for magnet design then the overall height and bore diameter is found to decrease for same total number of turns.

7.1.2. Electrical and Magnetic Aspects

The self-field effects on critical current have been studied for the magnet coils however in order to avoid the computational modelling difficulties various approximations have been considered. In order to identify the self-field effects, Kim model has been incorporated and a parameter P has been used to ensure the critical current existence in at least one tape out of 108 tapes of a pancake coil. It has been concluded that self-field has significant effect on the critical current of the coil and thus it can influence the magnet topology to a great extent. Thus, this aspect should be considered while designing the superconducting magnet.

7.1.3. AC Losses Estimation

AC loss analysis on the multi-turned pancake coil has been performed. Maxwell equations have been solved using H-formulation computational technique. It has been observed that edge elements can reduce the computational complexities to a greater extent and can be used in AC loss estimation. In order to avoid complexities, 2D model has been solved for homogeneous domain. It has been concluded that number of turns has significant effect on the AC losses and such losses can be controlled by increasing the substrate layer thickness at the cost of magnetic density.

7.1.4. Thermal Aspects

From the electro-thermal analysis of the superconducting tape, it has been concluded that with the increase in the interfacial resistance of the superconducting-stabilizer layer, the NZPV can be enhanced and which can assist in controlling the quenching of the tape. However, due to the increase in the interfacial resistance, the resistive losses may increase and thus, further studies are required in this regard.

7.2. Future Scope

In order to achieve the objectives of present study, many assumptions have been made out of which few can be consider while the design and development of SMES systems. Following are the further scopes of the present study that can be considered for the more realistic and practical feel of the SMES systems.

7.2.1. Mechanical Studies

- ✓ In the present study for the mechanical studies, the gap among the pancake coils has been assumed to zero however, in reality, for the cooling purposes this gap is always maintained greater than zero.
- ✓ The study is restricted to the design proposal only thus in future stress analysis on the SMES system can be done where design of supporting structure can also be included.
- ✓ A comparison among the operating temperature can also be performed computationally in future.
- ✓ A computational performance comparison can be done on solenoidal and toroidal magnets.

- ✓ Since, in the present study optimization of design variables has not been considered thus, in future, this aspect can also be considered for the full design of SMES system.

7.2.2. Electrical and Magnetic Studies

- ✓ Since, present study is restricted to 2D modelling thus, in future in order to have more clear physical insights of the computational modelling, 3D models can be used.
- ✓ Effect of mutual inductances can also be taken into account in the further studies related to the self-field effects on the critical current of the tape.
- ✓ Tape bending effects can also be considered in the future studies.

7.2.3. AC loss Estimation

- ✓ Since in the present work, 2D computational model has been studied, however, 3D model can predict the AC losses with more accuracy. Thus, in future attempts can be made in this regard.
- ✓ This work dealt with the single pancake coil studies only, however, SMES is having 49 pancake coils. Approach needs to develop that can either extrapolate or concisely predict the results for all 49 pancakes coils for more clarity of AC loss behavior.
- ✓ Study dealt with the homogeneous domain in order to avoid complexities associated with multi-turned modelling, however, modelling of multi-turned coils represents the actual arrangement of the coils. Thus, in future attempts can be made to simulate such complex problems.
- ✓ Effects of external magnetic fields have not taken into account, however, in reality, there may be some situations where external field can impede SMES performance. Thus, attempt can be made to model the problem with external fields effects.
- ✓ H-formulation technique has been employed in this study which is one of the simpler technique in evaluating the AC losses. In future, more advanced and complex techniques such as A-V formulations, can also be used as they can provide more generic results.

7.2.4. Thermal studies

- ✓ Effects of external fields can also be included in future studies.
- ✓ 3D modelling can provide more generous insights thus attempts can be made in future studies.
- ✓ This study only dealt with the quenching of straight tape however, in actual pancake coils, the tape is wounded on circular pancake coil thus radial components are required to be studied to reach physical insights of the problem.

Bibliography

[1] "World Energy Outlook- Annual Report 2019, International Energy Agency, https://www.iea.org/statistics/."

[2] "World Energy Outlook- Annual Report 2017, International Energy Agency, https://www.iea.org/weo2017/," 2017.

[3] A. B. Abrahamsen, N. Magnusson, B. B. Jensen, and M. Runde, "Large superconducting wind turbine generators," vol. 24, no. January, pp. 60–67, 2012.

[4] P. Mukherjee and V. V Rao, "Superconducting magnetic energy storage for stabilizing grid integrated with wind power generation systems," *J. Mod. Power Syst. Clean Energy*, vol. 7, no. 2, pp. 400–411, 2019.

[5] "Power Blackout Risks-Risk Management Options, A Techanial Report by CERO FORUM, Nov. 2011," no. November, 2011.

[6] "Ministry of Power, Central Electricity Power, Goverment of India, Annual Report 2012-13," 2012.

[7] T. J. Haugan, "Development of Superconducting and Cryogenic Power Systems and Impact for Aircraft Propulsion," *Air Force Res. Lab.*, no. April, 2015.

[8] M. Bruch, M. Kuhn, and G. Schmid, "Power Blackout Risks," *Cro Forum*, no. November, p. 32, 2011.

[9] P. Tixador, "Superconducting Magnetic Energy Storage : Status and Perspective," no. 3, pp. 1–14, 2008.

[10] H. J. Boenig and J. F. Hauer, "Commissioning Tests Of The Bonneville Power Administration 30 MJ Superconducting Magnetic Energy Storage Unit," *IEEE Trans. Power Appar. Syst.*, vol. PAS-104, no. 2, pp. 302–312, 1985.

[11] S. Nagaya *et al.*, "Development and performance results of 5 MVA SMES for bridging instantaneous voltage dips," *IEEE Trans. Appl. Supercond.*, vol. 14, no. 2, pp. 699–704, 2004.

[12] K. Shikimachi *et al.*, "Development of MVA class HTS SMES system for bridging instantaneous voltage dips," *IEEE Trans. Appl. Supercond.*, vol. 15, no. 2, pp. 1931–1934, 2005.

[13] J. Cerulli, G. Melotte, and S. Peele, "Operational experience with a

superconducting magnetic energy storage device at Owens Corning Vinyl Operations, Fair Bluff, North Carolina," in *1999 IEEE Power Engineering Society Summer Meeting. Conference Proceedings (Cat. No.99CH36364)*, 1999, vol. 1, pp. 524–528 vol.1.

[14] E. P. Polulyakh *et al.*, "Development of toroidal superconducting magnetic energy storages (SMES) for high-current pulsed power supplies," in *Digest of Technical Papers. 12th IEEE International Pulsed Power Conference. (Cat. No.99CH36358)*, 1999, vol. 2, pp. 1129–1132 vol.2.

[15] E. Y. Klimenko and E. P. Polulyakh, "Closed flux winding for smes," vol. 323, 2002.

[16] G. V. L. Landau, L., "On the Theory of Superconductivity .," vol. I, 1955.

[17] A. A. Abrikosov, "The magnetic properties of superconducting alloys," *J. Phys. Chem. Solids*, vol. 2, no. 3, pp. 199–208, 1957.

[18] G. Krabbes, G. Fuchs, W. R. Canders, H. May, and R. Palka, *High temperature superconductor bulk materials Fundamentals - processing - properties control - application aspects*. Germany: Wiley-VCH, 2006.

[19] A. A. Golubov, "Type II, Superconductivity," in *Handbook of Applied Superconductivity*, IOP Publishing, 1998, pp. 37–52.

[20] W. J. Carr Jr, *AC loss and macroscopic theory of superconductors*. CRC press, 2001.

[21] Y. B. Kim, C. F. Hempstead, and A. R. Strnad, "Critical persistent currents in hard superconductors," *Phys. Rev. Lett.*, vol. 9, no. 7, p. 306, 1962.

[22] P. W. Anderson, "Theory of flux creep in hard superconductors," *Phys. Rev. Lett.*, vol. 9, no. 7, p. 309, 1962.

[23] E. H. Brandt, "Superconductors of finite thickness in a perpendicular magnetic field: Strips and slabs," *Phys. Rev. B*, vol. 54, no. 6, p. 4246, 1996.

[24] E. H. Brandt and M. Indenbom, "Type-II-superconductor strip with current in a perpendicular magnetic field," *Phys. Rev. B*, vol. 48, no. 17, p. 12893, 1993.

[25] J. Rhyner, "Magnetic properties and AC-losses of superconductors with power law current—voltage characteristics," *Phys. C Supercond.*, vol. 212, no. 3–4, pp. 292–300, 1993.

[26] S. Stavrev *et al.*, "Comparison of numerical methods for modeling of

superconductors," *IEEE Trans. Magn.*, vol. 38, no. 2, pp. 849–852, 2002.

[27] N. Nibbio, S. Stavrev, and B. Dutoit, "Finite element method simulation of AC loss in HTS tapes with B-dependent EJ power law," *IEEE Trans. Appl. Supercond.*, vol. 11, no. 1, pp. 2631–2634, 2001.

[28] Q. Jiang, M. Majoros, Z. Hong, A. M. Campbell, and T. A. Coombs, "Design and AC loss analysis of a superconducting synchronous motor," *Supercond. Sci. Technol.*, vol. 19, no. 11, p. 1164, 2006.

[29] J. Šouc, E. Pardo, M. Vojenčiak, and F. Gömöry, "Theoretical and experimental study of AC loss in high temperature superconductor single pancake coils," *Supercond. Sci. Technol.*, vol. 22, no. 1, p. 15006, 2008.

[30] F. Gömöry, M. Vojenčiak, E. Pardo, M. Solovyov, and J. Šouc, "AC losses in coated conductors," *Supercond. Sci. Technol.*, vol. 23, no. 3, p. 34012, 2010.

[31] E. Pardo, M. Vojenčiak, F. Gömöry, and J. Šouc, "Low-magnetic-field dependence and anisotropy of the critical current density in coated conductors," *Supercond. Sci. Technol.*, vol. 24, no. 6, p. 65007, 2011.

[32] M. Vojenčiak, F. Grilli, S. Terzieva, W. Goldacker, M. Kováčová, and A. Kling, "Effect of self-field on the current distribution in Roebel-assembled coated conductor cables," *Supercond. Sci. Technol.*, vol. 24, no. 9, p. 95002, 2011.

[33] D. U. Gubser, "Superconductivity: an emerging power-dense energy-efficient technology," *IEEE Trans. Appl. Supercond.*, vol. 14, no. 4, pp. 2037–2046, 2004.

[34] J. G. Bednorz and K. A. Müller, "Possible highT c superconductivity in the Ba− La− Cu− O system," *Zeitschrift für Phys. B Condens. Matter*, vol. 64, no. 2, pp. 189–193, 1986.

[35] K. H. J. Buschow, *Concise encyclopedia of magnetic and superconducting materials*. Elsevier, 2005.

[36] B. A. Glowacki, M. Majoros, M. Vickers, J. E. Evetts, Y. Shi, and I. McDougall, "Superconductivity of powder-in-tube MgB2 wires," *Supercond. Sci. Technol.*, vol. 14, no. 4, p. 193, 2001.

[37] G. Giunchi, G. Ripamonti, T. Cavallin, and E. Bassani, "The reactive liquid Mg infiltration process to produce large superconducting bulk MgB2 manufacts,"

Cryogenics (Guildf)., vol. 46, no. 2–3, pp. 237–242, 2006.

[38] C. Buzea and T. Yamashita, "Review of the superconducting properties of MgB2," *Supercond. Sci. Technol.*, vol. 14, no. 11, p. R115, 2001.

[39] D. A. Cardwell and D. S. Ginley, *Handbook of superconducting materials*, vol. 1. CRC Press, 2003.

[40] C. Bernhard *et al.*, "Anisotropy and dimensional crossover of the vortex state in Bi 2 Sr 2 CaCu 2 O 8+ δ crystals," *Phys. Rev. B*, vol. 52, no. 10, p. R7050, 1995.

[41] D. Dimos, P. Chaudhari, and J. Mannhart, "Superconducting transport properties of grain boundaries in YBa 2 Cu 3 O 7 bicrystals," *Phys. Rev. B*, vol. 41, no. 7, p. 4038, 1990.

[42] A. Gurevich, "To use or not to use cool superconductors?," *Nat. Mater.*, vol. 10, no. 4, p. 255, 2011.

[43] A. Patel, K. Filar, V. I. Nizhankovskii, S. C. Hopkins, and B. A. Glowacki, "Trapped fields greater than 7 T in a 12 mm square stack of commercial high-temperature superconducting tape," *Appl. Phys. Lett.*, vol. 102, no. 10, p. 102601, 2013.

[44] A. Patel, S. C. Hopkins, and B. A. Glowacki, "Trapped fields up to 2 T in a 12 mm square stack of commercial superconducting tape using pulsed field magnetization," *Supercond. Sci. Technol.*, vol. 26, no. 3, p. 32001, 2013.

[45] M. Dürrschnabel, Z. Aabdin, M. Bauer, R. Semerad, W. Prusseit, and O. Eibl, "DyBa2Cu3O7− x superconducting coated conductors with critical currents exceeding 1000 A cm− 1," *Supercond. Sci. Technol.*, vol. 25, no. 10, p. 105007, 2012.

[46] S. Samoilenkov *et al.*, "Customised 2G HTS wire for applications," *Supercond. Sci. Technol.*, vol. 29, no. 2, p. 24001, 2015.

[47] A. Baskys, "Stacks of high temperature superconducting tape as trapped field magnets for energy applications," no. April, 2017.

[48] K. Iida, N. H. Babu, Y. Shi, and D. A. Cardwell, "Seeded infiltration and growth of large, single domain Y–Ba–Cu–O bulk superconductors with very high critical current densities," *Supercond. Sci. Technol.*, vol. 18, no. 11, p. 1421, 2005.

[49] N. H. Babu *et al.*, “Growth of large sized Y Ba2Cu3O7 single crystals using the top seeded melt growth process,” *Supercond. Sci. Technol.*, vol. 25, no. 7, p. 75012, 2012.

[50] M. D. Ainslie *et al.*, “Modelling and comparison of trapped fields in (RE) BCO bulk superconductors for activation using pulsed field magnetization,” *Supercond. Sci. Technol.*, vol. 27, no. 6, p. 65008, 2014.

[51] H. Fujishiro, T. Naito, and M. Oyama, “Three-dimensional simulation of magnetic flux dynamics and temperature rise in HTSC bulk during pulsed field magnetization,” *Phys. Procedia*, vol. 36, pp. 687–692, 2012.

[52] X. Chaud *et al.*, “Flux mapping at 77 K and local measurement at lower temperature of thin-wall YBaCuO single-domain samples oxygenated under high pressure,” *Phys. C Supercond.*, vol. 469, no. 15–20, pp. 1200–1206, 2009.

[53] M. Tomita and M. Murakami, “High-temperature superconductor bulk magnets that can trap magnetic fields of over 17 tesla at 29 K,” *Nature*, vol. 421, no. 6922, p. 517, 2003.

[54] H. Fujishiro, K. Yokoyama, M. Kaneyama, T. Oka, and K. Noto, “Effect of metal ring setting outside HTSC bulk disk on trapped field and temperature rise in pulse field magnetizing,” *IEEE Trans. Appl. Supercond.*, vol. 15, no. 2, pp. 3762–3765, 2005.

[55] M. Tomita, M. Murakami, and K. Yoneda, “Improvements in the mechanical properties of bulk YBCO superconductors with carbon fibre fabrics,” *Supercond. Sci. Technol.*, vol. 15, no. 5, p. 803, 2002.

[56] I. K. Okakwu, P. E. Orukpe, and E. A. Ogujor, “Application of superconducting fault current limiter (SFCL) in power systems: A review,” *Eur. J. Eng. Res. Sci.*, vol. 3, no. 7, pp. 28–32, 2018.

[57] B. C. Sung, D. K. Park, J. Park, and T. K. Ko, “Study on a Series Resistive SFCL to Improve Power System Transient Stability: Modeling, Simulation, and Experimental Verification,” *IEEE Trans. Ind. Electron.*, vol. 56, no. 7, pp. 2412–2419, 2009.

[58] B. C. Sung, D. K. Park, J. Park, and T. K. Ko, “Study on Optimal Location of a Resistive SFCL Applied to an Electric Power Grid,” *IEEE Trans. Appl. Supercond.*, vol. 19, no. 3, pp. 2048–2052, 2009.

[59] W. Park, B. C. Sung, and J. Park, “The Effect of SFCL on Electric Power Grid With Wind-Turbine Generation System,” *IEEE Trans. Appl. Supercond.*, vol. 20, no. 3, pp. 1177–1181, 2010.

[60] T. A. Coombs, “11 - High-temperature superconducting magnetic energy storage (SMES) for power grid applications,” in *Woodhead Publishing Series in Energy*, C. B. T.-S. in the P. G. Rey, Ed. Woodhead Publishing, 2015, pp. 345–365.

[61] N. Amaro, J. M. Pina, J. Martins, and J. M. Ceballos, “Integration of SMES devices in power systems - opportunities and challenges,” in *2015 9th International Conference on Compatibility and Power Electronics (CPE)*, 2015, pp. 482–487.

[62] M. H. Ali, S. Member, B. Wu, R. A. Dougal, and S. Member, “An Overview of SMES Applications in Power and Energy Systems,” vol. 1, no. 1, pp. 38–47, 2010.

[63] A. J. R and H. A. Snyder, “Comparison of different ways of using superfluid helium to cool superconducting magnets,” vol. 36, no. 3, pp. 209–214, 1996.

[64] H. Allain, R. Van Weelderen, B. Baudouy, M. Quintard, and M. Prat, “Investigation of suitability of the method of volume averaging for the study of heat transfer in superconducting accelerator magnet cooled by superfluid helium,” vol. 53, pp. 128–134, 2013.

[65] T. Koettig *et al.*, “Controlled cold helium spill test in the LHC tunnel at CERN,” *Phys. Procedia*, vol. 67, pp. 1074–1082, 2015.

[66] V. Benda *et al.*, “Cryogenic design of the new high field magnet test facility at CERN,” *Phys. Procedia*, vol. 67, pp. 302–307, 2015.

[67] R. Cable, *Superconducting Wires and Cables : High-Field Applications $*. Elsevier Ltd., 2016.

[68] S. Kundu, A. K. Singh, and M. M. Hussain, “ScienceDirect DEVELOPMENT OF Nb 3 Sn BASED MULTI-FILAMENTARY SUPERCONDUCTOR WIRES FOR FUSION REACTOR MAGNETS,” *Mater. Today Proc.*, vol. 3, no. 9, pp. 3045–3054, 2016.

[69] S. Pietrowicz and B. Baudouy, “Numerical study of the thermal behavior of an Nb 3 Sn high field magnet in He II,” *Cryogenics (Guildf).*, vol. 53, pp. 72–77,

2013.

[70] S. I. Bermudez, H. Bajas, and L. Bottura, “Quench modeling in high-field Nb 3 Sn accelerator magnets,” *Phys. Procedia*, vol. 67, pp. 840–846, 2015.

[71] Q. W. Hao, H. J. Liu, Y. Wu, and S. Guo, “Pressure drop test and analysis of Nb 3 Sn superconducting magnet,” vol. 497, pp. 58–61, 2014.

[72] M. Ghate, P. Raj, A. Singh, S. Pradhan, M. M. Hussain, and K. K. Abdulla, “Design , development and fabrication of indigenous 30 kA NbTi CICC for fusion relevant superconducting magnet,” *Cryogenics (Guildf).*, vol. 63, pp. 166–173, 2014.

[73] U. Bhunia, J. Akhter, C. Nandi, G. Pal, and S. Saha, “Design of a 4 . 5 MJ / 1 MW sectored toroidal superconducting energy storage magnet,” *Cryogenics (Guildf).*, vol. 63, pp. 186–198, 2014.

[74] J. C. Hernandez-llambes and D. Hazelton, “ADVANTAGES OF SECOND-GENERATION HIGH TEMPERATURE SUPERCONDUCTORS FOR PULSED POWER APPLICATIONS ∗,” no. 518, pp. 221–226, 2009.

[75] K. Kim *et al.*, “Stress Analysis for Toroid-Type HTS SMES Coil and Bobbin Structure Considering Large Parallel Magnetic Field,” vol. 21, no. 3, pp. 2275–2278, 2011.

[76] S. Nomura, D. Ajiki, C. Suzuki, and N. Watanabe, “Design Considerations for Force-Balanced Coil Applied to SMES,” vol. I, no. I, 2001.

[77] K. Higashikawa, T. Nakamura, K. Shikimachi, N. Hirano, S. Nagaya, and T. Kiss, “Conceptual Design of HTS Coil for SMES Using YBCO Coated Conductor,” vol. 17, no. 2, pp. 1990–1993, 2007.

[78] A. Morandi *et al.*, “Design and Comparison of a 1-MW / 5-s HTS SMES With Toroidal and Solenoidal Geometry,” vol. 26, no. 4, pp. 1–6, 2016.

[79] G. Schdnwetterl, C. Magele, K. Preis, C. Paul, W. Renhart, and K. R. Richter, “Optimization of SMES Solenoids with regard to their Stray Fields,” vol. 31, no. 3, pp. 3–6, 1995.

[80] G. Schonwetter, “SMES Solenoids with Reduced Stray Field,” vol. 30, no. 4, pp. 2636–2639, 1994.

[81] F. Trillaud and L. S. Cruz, “Conceptual Design of a 200-kJ 2G-HTS Solenoidal μ -SMES,” vol. 24, no. 3, 2014.

[82] G. Tomassetti, G. De Marzi, L. Muzzi, G. Celentano, and A. Corte, “Design and optimization of a HTS insert for solenoid magnets,” *Cryogenics (Guildf).*, vol. 80, pp. 419–426, 2016.

[83] S. Lim, J. Barc, Y. Jung, D. Youm, C. Park, and H. Kim, “Analyses of a solenoid magnet made of pancakes of coated conductors,” vol. 432.

[84] Y. Shiroyanagi, A. K. Ghosh, R. Gupta, and W. B. Sampson, “The Construction and Testing of YBCO Pancake Coils for a High Field Solenoid,” vol. 21, no. 3, pp. 1649–1652, 2011.

[85] A. Morandi *et al.*, “Design and Comparison of a 1 MW / 5s HTS SMES with Toroidal and Solenoidal Geometry,” vol. 8223, no. 1, pp. 1–6, 2016.

[86] X. Jiang *et al.*, “Development of a Solenoidal HTS Coil Cooled by Liquid or Gas Helium,” vol. 13, no. 2, pp. 1871–1874, 2003.

[87] B. Kondratowicz-Kucewicz, “The energy and the magnetic field in HTS superconducting magnetic energy storage model,” *2017 Int. Conf. Electromagn. Devices Process. Environ. Prot. with Semin. Appl. Supercond. (ELMECO AoS)*, no. 1, pp. 1–4, 2017.

[88] S. Lee *et al.*, “Design of HTS Modular Magnets for a 2 . 5 MJ Toroidal SMES : ReBCO vs . BSCCO,” vol. 20, no. 3, pp. 1324–1328, 2010.

[89] H. K. Yeom *et al.*, “Structural design of the toroidal configuration of the HTS SMES cooling system,” vol. 471, pp. 1390–1394, 2011.

[90] K. M. Kim *et al.*, “Heat characteristic analysis of a conduction cooling toroidal-type SMES magnet,” vol. 470, pp. 1711–1716, 2010.

[91] A. Kim *et al.*, “Performance Analysis of a Toroid-Type HTS SMES Adopted for Frequency Stabilization,” vol. 21, no. 3, pp. 1367–1370, 2011.

[92] H. Liu, X. Deng, L. Ren, Y. Xu, J. He, and Y. Tang, “Electromagnetic Design of HTS D-shaped Coils for a Toroidal-type Superconducting Magnet,” vol. 58, pp. 244–247, 2014.

[93] K. Yi and H. Jung, “A Design Methodology for Toroid-Type SMES using Analytical and Finite Element Method,” no. c, pp. 2–4.

[94] A. Dolan and F. Stefanescu, “Optimization of Modular Toroid Coil Geometry of a Superconducting Magnetic Energy Storage Device Using Design of Experiments and FEM,” 2014.

[95] M. Qiu, S. Rao, J. Zhu, S. Fu, and Z. Li, “Energy Storage Characteristics of MJ-Class Toroidal HTS- SMES Considering Maximum Value of Perpendicular Magnetic Field,” *Energy Procedia*, vol. 105, pp. 4179–4184, 2017.

[96] Y. Oga, S. Noguchi, and H. Igarashi, “Simulation of chain of quenches on toroidal HTS-SMES taking account of thermal and electromagnetic characteristics,” vol. 27, pp. 404–407, 2012.

[97] S. Kwak *et al.*, “Design of HTS Magnets for a 2 . 5 MJ SMES,” vol. 19, no. 3, pp. 1985–1988, 2009.

[98] U. Bhunia, J. Akhter, C. Nandi, G. Pal, and S. Saha, “Design of a 4 . 5 MJ / 1 MW sectored toroidal superconducting energy storage magnet,” *Cryogenics (Guildf).*, pp. 1–13, 2014.

[99] M. Park *et al.*, “Conceptual Design of HTS Magnet for a 5 MJ Class SMES,” vol. 18, no. 2, pp. 750–753, 2008.

[100] K. Kim *et al.*, “Design and manufacture of a toroidal-type SMES for combination with real-time digital simulator (RTDS),” *Cryogenics (Guildf).*, pp. 1–6, 2010.

[101] M. Fabbri, D. Ajiki, F. Negrini, R. Shimada, H. Tsutsui, and F. Venturi, “Tilted Toroidal Coils for Superconducting Magnetic Energy Storage Systems,” vol. 39, no. 6, pp. 3546–3550, 2003.

[102] K. Juengst, R. Gehring, A. Kudymow, H. Pfisterer, and E. Suess, “SMES Compensator with a Toroidal Magnet System,” vol. 12, no. 1, pp. 754–757, 2002.

[103] S. Lee *et al.*, “Design of HTS Toroidal Magnets for a 5 MJ SMES,” vol. 22, no. 3, pp. 5–8, 2012.

[104] S. Lee *et al.*, “Analysis of Eddy Current Losses and Magnetization Losses in Toroidal Magnets for a 2 . 5 MJ HTS SMES,” vol. 21, no. 3, pp. 1354–1357, 2011.

[105] J. Lee *et al.*, “Thermal Quench in HTS Double Pancake Race Track Coil,” vol. 17, no. 2, pp. 1603–1606, 2007.

[106] M. Zhang *et al.*, “AC Loss Measurements for 2G HTS Racetrack Coils With Heat-Shrink Tube Insulation,” vol. 24, no. 3, pp. 3–6, 2014.

[107] R. Kang and J. Zheng, “Stability study of Bi-2212 conductor based on

perturbation spectrum for hybrid superconducting magnet," 2017.

[108] K. Ohsemochi *et al.*, "Test Results of an Experimental Coil with Bi-2212 Rutherford Cable for High Energy-density HTS-SMES," vol. 43, pp. 825–828, 2006.

[109] D. Ha *et al.*, "Study on Bi-2212 Rutherford Cabling Process for SMES," vol. 18, no. 2, pp. 1192–1195, 2008.

[110] K. Ryu, H. J. Song, H. J. Kim, and K. C. Seong, "Transport Loss Characteristics of the Bi-2223 Tapes in an External AC Magnetic Field," vol. 16, no. 2, pp. 1011–1014, 2006.

[111] H. Hayashi, H. Kimura, Y. Hatabe, K. Tsutsumi, A. Tomioka, and T. Bohno, "Fabrication and Test of a 4 kJ Bi-2223 Pulse Coil for SMES," vol. 13, no. 2, pp. 1867–1870, 2003.

[112] S. S. Oh *et al.*, "Development of Bi-2223 HTS tape and its application to coil and current leads," vol. 42, pp. 377–382, 2002.

[113] S. Asulay, A. Friedman, Y. Wolfus, F. Kopansky, and Y. Yeshurun, "Electric Field in Bi-2223 Tape Carrying DC Current and Exposed to AC Parallel Magnetic Field," vol. 16, no. 2, pp. 1067–1070, 2006.

[114] Y. Ichiki and H. Ohsaki, "Numerical Analysis of AC Loss Characteristics of YBCO Coated Conductors Arranged in Parallel," vol. 15, no. 2, pp. 2851–2854, 2005.

[115] S. Noguchi, H. Yamashita, and A. Ishiyama, "An Optimization Method for Design of SMES Coils Using YBCO Tape," vol. 13, no. 2, pp. 1856–1859, 2003.

[116] L. Ren *et al.*, "Conduction-Cooled YBCO HTS Current Lead for SMES Application," vol. 20, no. 3, pp. 1737–1740, 2010.

[117] K. Shikimachi, N. Hirano, S. Nagaya, H. Kawashima, and K. Higashikawa, "System Coordination of 2 GJ Class YBCO SMES for Power System Control," vol. 19, no. 3, pp. 2012–2018, 2012.

[118] J. Zhu, W. Yuan, T. A. Coombs, and Q. Ming, "Simulation and experiment of a YBCO SMES prototype in voltage sag compensation," *Phys. C Supercond. its Appl.*, vol. 471, no. 5–6, pp. 199–204, 2011.

[119] U. B. Vetrella *et al.*, "HTS Coils Fabrication From Commercial 2G YBCO

Tapes : Measurements and Simulation," vol. 24, no. 3, 2014.

[120] H. Ueda *et al.*, "Quench Detection and Protection of Cryocooler-Cooled YBCO Pancake Coil for SMES," vol. 22, no. 3, 2012.

[121] A. Kumar and R. Kaur, "Electromagnetic analysis of 1MJ class of high temperature superconducting magnetic energy storage (SMES) coil to be used in power applications," vol. 050003, p. 050003, 2018.

[122] N. V. P. V.E. Sytnikov, V.S. Vysotsky, I.P. Radchenko, "1G versus 2G – comparison from the practical standpoint for HTS power cables use," vol. 012058, 2008.

[123] M.-J. Park *et al.*, "Analysis of magnetic field distribution and AC losses of a 600 kJ SMES," *Cryogenics (Guildf).*, vol. 47, no. 7–8, pp. 391–396, Jul. 2007.

[124] K. C. Seong, H. J. Kim, S. H. Kim, S. J. Park, M. H. Woo, and S. Y. Hahn, "Research of a 600 kJ HTS-SMES system," vol. 465, pp. 1240–1246, 2007.

[125] M. Park *et al.*, "Stress Analysis of HTS Magnet for a 600 kJ SMES," vol. 17, no. 2, pp. 1994–1997, 2007.

[126] M. Park *et al.*, "Analysis of magnetic field distribution and AC losses of a 600 kJ SMES," vol. 47, pp. 391–396, 2007.

[127] J. Choi, H. Cheon, D. Kwag, and H. Kim, "Study on electric insulation properties for development of conduction-cooled HTS SMES," vol. 47, pp. 397–401, 2007.

[128] K. C. Seong *et al.*, "Development of a 600 kJ HTS SMES," vol. 468, pp. 2091–2095, 2008.

[129] M. Iwakuma, K. Funaki, and K. Kajikawa, "Development of a 1T Cryocooler-Cooled Pulse Coil with a Bi2223 Superconducting Parallel Conductor for SMES," vol. 9, no. 2, pp. 928–931, 1999.

[130] T. Hamajima, K. Kitamura, M. Sakai, and T. Satow, "Specifications and performance experiences of internally cooled small-scale SMES," vol. 38, no. 11, pp. 1135–1143, 1998.

[131] K. Tasaki, Y. Sumiyoshi, M. Tezuka, H. Hayashi, and K. Tsutsumi, "Design study of a 3 . 6 MJ HTS-SMES Compact magnet design," vol. 360, pp. 1332–1335, 2001.

[132] T. Hamajima *et al.*, "Status Evaluation Method for SMES Used in Power Grid,"

Cryogenics (Guildf)., vol. 25, no. 2, pp. 3–6, 1999.

[133] J. Zhu, M. Qiu, B. Wei, H. Zhang, X. Lai, and W. Yuan, "Design, dynamic simulation and construction of a hybrid HTS SMES (high-temperature superconducting magnetic energy storage systems) for Chinese power grid," *Energy*, vol. 51, pp. 184–192, 2013.

[134] J. Zhu, H. Zhang, W. Yuan, M. Zhang, and X. Lai, "Design and cost estimation of superconducting magnetic energy storage (SMES) systems for power grids," 2013.

[135] L. Xiao and L. Lin, "Recent Progress of Power Application of Superconductor in China," vol. 17, no. 2, pp. 2355–2360, 2007.

[136] N. V. S. Rao, "Optimum Design of Superconducting Magnet Coil for a Micro SMES Unit," vol. 9, no. 2, pp. 350–353, 1999.

[137] A. Kumar, J. V. M. L. Jeyan, and A. Agarwal, "Numerical analysis on 10 MJ solenoidal high temperature superconducting magnetic energy storage system to evaluate magnetic flux and Lorentz force distribution," *Phys. C Supercond. its Appl.*, vol. 558, pp. 17–24, 2019.

[138] V. Lombardo, E. Barzi, D. Turrioni, and A. V Zlobin, "Critical Currents of YBCO Tapes and BSCCO Wires at Different Temperatures and Magnetic Fields," *IEEE Trans. Appl. Supercond.*, vol. 21, no. 3, pp. 3247–3250, 2010.

[139] T. Dai *et al.*, "Design study on 50 kJ HTS SMES for simulated dynamic experiment of electric power systems," *Phys. C Supercond. its Appl.*, vol. 412–414, no. SPEC. ISS., pp. 1239–1243, 2004.

[140] R. Kreutz *et al.*, "Design of a 150 kJ high-Tc SMES (HSMES) for a 20 kVA uninterruptible power supply system," *IEEE Trans. Appl. Supercond.*, vol. 13, no. 2 II, pp. 1860–1862, 2003.

[141] A. Korpela, J. Lehtonen, and R. Mikkonen, "Optimization of HTS superconducting," vol. 833.

[142] W. Kim, S. Kwak, J. Lee, K. Choi, H. Jung, and K. Seong, "Design of HTS Magnets for a 600 kJ SMES," vol. 16, no. 2, pp. 620–623, 2006.

[143] L. Xiao *et al.*, "Fabrication and Tests of a 1 MJ HTS Magnet for SMES," vol. 18, no. 2, pp. 770–773, 2008.

[144] J. Zhang *et al.*, "The electromagnetic analysis and structural design of a 1 MJ

HTS magnet for SMES," *IEEE Trans. Appl. Supercond.*, vol. 21, no. 3 PART 2, pp. 1344–1347, 2011.

[145] S. Dai *et al.*, "Development and demonstration of a 1 MJ high-Tc SMES," *IEEE Trans. Appl. Supercond.*, vol. 22, no. 3, p. 5700304, 2012.

[146] T. Shintomi, Y. Makida, T. Hamajima, S. Tsuda, D. Miyagi, and T. Takao, "Design Study of SMES System Cooled by Thermo-Siphon With Liquid Hydrogen for Effective use of Renewable Energy," vol. 22, no. 3, pp. 5–8, 2012.

[147] A. Morandi, B. Gholizad, and M. Fabbri, "Design and performance of a 1 MW-5 s high temperature superconductor magnetic energy storage system," *Supercond. Sci. Technol.*, vol. 29, no. 1, p. 15014, 2015.

[148] B. Kondratowicz-Kucewicz, T. Janowski, S. Kozak, J. Kozak, G. Wojtasiewicz, and M. Majka, "Bi-2223 HTS winding in toroidal configuration for SMES coil," *J. Phys. Conf. Ser.*, vol. 234, no. 3, p. 032025, 2010.

[149] J. Kozak *et al.*, "Test results of HTS magnet for SMES application," *J. Phys. Conf. Ser.*, vol. 234, no. 3, p. 032034, 2010.

[150] A. R. Kim *et al.*, "Performance analysis of a toroid-type HTS SMES adopted for frequency stabilization," *IEEE Trans. Appl. Supercond.*, vol. 21, no. 3 PART 2, pp. 1367–1370, 2011.

[151] K. Kim *et al.*, "Stress analysis for toroid-type HTS SMES coil and bobbin structure considering large parallel magnetic field," *IEEE Trans. Appl. Supercond.*, vol. 21, no. 3 PART 2, pp. 2275–2278, 2011.

[152] S. Lee *et al.*, "Design of HTS toroidal magnets for a 5 MJ SMES," *IEEE Trans. Appl. Supercond.*, vol. 22, no. 3, pp. 5–8, 2012.

[153] M. Sander, R. Gehring, and H. Neumann, "LIQHYSMES — A 48 GJ Toroidal MgB2-SMES for Buffering Minute and Second Fluctuations," vol. 23, no. 3, pp. 0–4, 2013.

[154] C. J. Hawley and S. A. Gower, "Design and Preliminary Results of a Prototype HTS SMES Device," vol. 15, no. 2, pp. 1899–1902, 2005.

[155] C. J. Hawley, D. Cuiuri, C. D. Cook, S. A. Gower, and T. P. Beales, "Characterisation and control of a prototype HTS SMES device," *J. Phys. Conf. Ser.*, vol. 43, no. 1, pp. 809–812, 2006.

[156] H. Hayashi *et al.*, “Fabrication and test of a 4 kJ Bi-2223 pulse coil for SMES,” *IEEE Trans. Appl. Supercond.*, vol. 13, no. 2 II, pp. 1867–1870, 2003.

[157] M. Iwakuma *et al.*, “Ac Loss Properties of a 4 kJ Conduction-Cooled Pulse Coil Wound With a Bi2223 6-Strand Parallel Conductor for SMES,” vol. 13, no. 2, pp. 1882–1885, 2003.

[158] G. Wojtasiewicz *et al.*, “HTS magnet for 7.3 kJ SMES system,” *J. Phys. Conf. Ser.*, vol. 43, pp. 821–824, 2006.

[159] Q. Wang, S. Song, Y. Lei, and Y. Dai, “Design and fabrication of a conduction-cooled high temperature superconducting magnet for 10 kJ superconducting magnetic energy storage system,” *IEEE Trans. Appiled Supercond.*, vol. 16, no. 2, pp. 570–573, 2006.

[160] J. Kozak, M. Majka, S. Kozak, and T. Janowski, “Performance of SMES System With HTS Magnet,” vol. 20, no. 3, pp. 1348–1351, 2010.

[161] J. Shi *et al.*, “Development of a Conduction-Cooled HTS SMES,” vol. 17, no. 3, pp. 3846–3852, 2007.

[162] M. J. Park *et al.*, “Fabrication and test a 600 kJ SMES model coil,” vol. 465, pp. 1247–1251, 2007.

[163] H. K. Yeom *et al.*, “An Experimental Study of the Conduction Cooling System for the 600 kJ HTS SMES,” vol. 18, no. 2, pp. 741–744, 2008.

[164] P. Tixador *et al.*, “First Tests of a 800 kJ HTS SMES,” vol. 18, no. 2, pp. 774–778, 2008.

[165] K. Koyanagi *et al.*, “Design of a High Energy-Density SMES Coil With Bi-2212 Cables,” *IEEE Trans. Appl. Supercond.*, vol. 16, no. 2, pp. 586–589, 2006.

[166] T. Kurusu, “Development of MJ-Class HTS SMES for Bridging Instantaneous Voltage Dips,” vol. 14, no. 2, pp. 770–773, 2004.

[167] J. H. Kim, S. Hahn, C. H. Im, J. K. Kim, H. K. Jung, and S. Hahn, “Design of a 200-kJ HTS SMES System,” vol. 12, no. 1, pp. 774–777, 2002.

[168] A. Morandi, B. Gholizad, and M. Fabbri, “Design and performance of a 1MW-5s high temperature superconductor magnetic energy storage system,” *Supercond. Sci. Technol.*, vol. 29, no. 1, p. 15014.

[169] T. Takematsu *et al.*, “Degradation of the performance of a YBCO-coated conductor double pancake coil due to epoxy impregnation,” *Phys. C Supercond.*

its Appl., vol. 470, no. 17–18, pp. 674–677, 2010.

[170] F. Grilli, M. Vojenˇ, A. Kario, and V. Zerme, “Estimation of Self-Field Critical Current and Transport-Magnetization AC Losses of Roebel Cables,” pp. 1–5, 2015.

[171] Q. Wang *et al.*, “High Temperature Superconducting YBCO Insert for 25 T Full Superconducting Magnet,” vol. 25, no. 3, pp. 3–7, 2015.

[172] V. M. R. Zermeno, F. Grilli, and F. Sirois, “A full 3D time-dependent electromagnetic model for Roebel cables,” *Supercond. Sci. Technol.*, vol. 26, no. 5, p. 52001, 2013.

[173] Z. Jiang *et al.*, “Magnetization Loss in REBCO Roebel Cables,” vol. 28, no. 3, 2018.

[174] E. Pardo and F. Grilli, “Numerical simulations of the angular dependence of magnetization AC losses : coated conductors , Roebel cables and,” vol. 014008, 2012.

[175] M. Furuse, M. Yoshikawa, Y. Itoh, S. Fukui, and T. Nakamura, “Fabrication and Testing of Racetrack-Shaped Double-Pancake Coil for Stator Windings of Induction-Synchronous Motor,” vol. 25, no. 3, 2015.

[176] W. Y. Li, X. J. Niu, H. Su, W. Chen, S. S. Peng, and J. Zheng, “A Study on HTS Double Pancake Coil for Electric Machine,” pp. 177–179, 2013.

[177] K. Nagao, T. Nakamura, H. Sugimoto, and T. Morishita, “Synchronous motor with HTS-2G wires.”

[178] A. Morandi, M. Fabbri, B. Gholizad, F. Grilli, F. Sirois, and V. M. R. Zermeño, “Design and Comparison of a 1-MW/5-s HTS SMES With Toroidal and Solenoidal Geometry,” *IEEE Trans. Appl. Supercond.*, vol. 26, no. 4, pp. 1–6, 2016.

[179] F. Grilli, V. M. R. Zerme, E. Pardo, M. Vojenˇ, and A. Kario, “Self-field Effects and AC Losses in Pancake Coils Assembled from Coated Conductor Roebel Cables,” pp. 1–5.

[180] F. Grilli, F. Sirois, S. Member, V. M. R. Zermeño, and M. Vojenˇ, “Self-Consistent Modeling of the I c of HTS Devices : How Accurate do Models Really Need to Be ?,” vol. 24, no. 6, 2014.

[181] V. Zermeño, F. Sirois, M. Takayasu, M. Vojenciak, A. Kario, and F. Grilli, “A

self-consistent model for estimating the critical current of superconducting devices," *Supercond. Sci. Technol.*, vol. 28, no. 8, p. 85004.

[182] J. Fleiter, A. Ballarino, L. Bottura, and P. Tixador, "Electrical characterization of REBCO Roebel cables," *Supercond. Sci. Technol.*, vol. 26, no. 6, p. 65014, 2013.

[183] F. Gömöry and B. Klinčok, "Self-field critical current of a conductor with an elliptical cross-section," *Supercond. Sci. Technol.*, vol. 19, no. 8, pp. 732–737, 2006.

[184] F. Sirois, D. R. Watson, W. Zhu, and J. R. Cave, "Development of a numerical method to determine the local EJ characteristics of anisotropic HTS from experimental VI curves," in *AIP Conference Proceedings*, 2002, vol. 614, no. 1, pp. 1118–1125.

[185] M. Zhang, J.-H. Kim, S. Pamidi, M. Chudy, W. Yuan, and T. A. Coombs, "Study of second generation, high-temperature superconducting coils: Determination of critical current," *J. Appl. Phys.*, vol. 111, no. 8, p. 83902, 2012.

[186] F. Gömöry *et al.*, "AC Loss in Pancake Coil Made From 12 mm Wide REBCO Tape," *IEEE Trans. Appl. Supercond.*, vol. 23, no. 3, p. 5900406, 2013.

[187] A. Nijhuis, H. G. Knoopers, Y. Ilyin, A. Godeke, B. ten Haken, and H. H. J. ten Kate, "Effect of self-field and current non-uniformity on the voltage–temperature characteristic of the ITER central solenoid insert coil by numerical calculations," *Cryogenics (Guildf).*, vol. 42, no. 8, pp. 469–483, 2002.

[188] K. P. Thakur, A. Raj, E. H. Brandt, J. Kvitkovic, and S. V Pamidi, "Frequency-dependent critical current and transport ac loss of superconductor strip and Roebel cable," vol. 065024, 2011.

[189] W. Yuan, A. M. Campbell, and T. A. Coombs, "A model for calculating the AC losses of second-generation high temperature superconductor pancake coils," *Supercond. Sci. Technol.*, vol. 22, no. 7, p. 75028, 2009.

[190] E. Pardo, J. Šouc, and J. Kováč, "AC loss in ReBCO pancake coils and stacks of them: modelling and measurement," *Supercond. Sci. Technol.*, vol. 25, no. 3, p. 35003, 2012.

[191] W. Yuan, A. M. Campbell, and T. A. Coombs, "Ac losses and field and current

density distribution during a full cycle of a stack of superconducting tapes," *J. Appl. Phys.*, vol. 107, no. 9, p. 93909, 2010.

[192] L. Rostila *et al.*, "How to determine critical current density in YBCO tapes from voltage–current measurements at low magnetic fields," *Supercond. Sci. Technol.*, vol. 20, no. 12, p. 1097, 2007.

[193] J. J. Rabbers, "AC loss in superconducting tapes and coils.," 2003.

[194] M. M. Farhoudi, "AC loss in Ag/Bi-2223 tapes in AC field," 2002.

[195] W. T. Norris, "Calculation of hysteresis losses in hard super- conductors carrying ac : isolated conductors and edges of thin sheets," vol. 489, 1970.

[196] F. London and H. London, "The electromagnetic equations of the supraconductor," *Proc. R. Soc. London. Ser. A-Mathematical Phys. Sci.*, vol. 149, no. 866, pp. 71–88, 1935.

[197] N. Amemiya, S. Murasawa, N. Banno, and K. Miyamoto, "Numerical modelings of superconducting wires for AC loss calculations," *Phys. C Supercond.*, vol. 310, no. 1–4, pp. 16–29, 1998.

[198] N. Enomoto and N. Amemiya, "Electromagnetic field analysis of rectangular high Tc superconductor with large aspect ratio," *Phys. C Supercond.*, vol. 412, pp. 1050–1055, 2004.

[199] T. Benkel, Y. Liu, E. Pardo, S. Wolfstädter, T. Reis, and F. Grilli, "TA formulation to model electrical machines with HTS coated conductor coils," *arXiv Prepr. arXiv1901.02370*, 2019.

[200] J. Dular, C. Geuzaine, and B. Vanderheyden, "Finite-Element Formulations for Systems With High-Temperature Superconductors," *IEEE Trans. Appl. Supercond.*, vol. 30, no. 3, pp. 1–13, 2019.

[201] E. Berrospe-Juarez, V. M. R. Zermeño, F. Trillaud, and F. Grilli, "Real-time simulation of large-scale HTS systems: multi-scale and homogeneous models using the T–A formulation," *Supercond. Sci. Technol.*, vol. 32, no. 6, p. 65003, 2019.

[202] F. Gömöry, M. Vojenčiak, E. Pardo, and J. Šouc, "Magnetic flux penetration and AC loss in a composite superconducting wire with ferromagnetic parts," *Supercond. Sci. Technol.*, vol. 22, no. 3, p. 34017, 2009.

[203] A. Stenvall and T. Tarhasaari, "An eddy current vector potential formulation for

estimating hysteresis losses of superconductors with FEM," *Supercond. Sci. Technol.*, vol. 23, no. 12, p. 125013, 2010.

[204] Z. Chen, G. Geng, and J. Fang, "Influence of AC loss on stress and strain of superconducting coils," *J. Supercond. Nov. Magn.*, vol. 32, no. 3, pp. 549–555, 2019.

[205] F. Liang, W. Yuan, C. A. Baldan, M. Zhang, and J. S. Lamas, "Modeling and experiment of the current limiting performance of a resistive superconducting fault current limiter in the experimental system," *J. Supercond. Nov. Magn.*, vol. 28, no. 9, pp. 2669–2681, 2015.

[206] F. Liang *et al.*, "AC loss modelling and experiment of two types of low-inductance solenoidal coils," *Supercond. Sci. Technol.*, vol. 29, no. 11, p. 115006, 2016.

[207] Z. Hong, A. M. Campbell, and T. A. Coombs, "Numerical solution of critical state in superconductivity by finite element software," *Supercond. Sci. Technol.*, vol. 19, no. 12, p. 1246, 2006.

[208] P. Zhou *et al.*, "Frequency-Dependent Transport AC Losses of Coated Superconductors Up To Tens of Kilohertz," *IEEE Trans. Appl. Supercond.*, vol. 29, no. 5, pp. 1–5, 2019.

[209] A. Kumar, A. Agrawal, and J. M. L. Jeyan, "A Numerical Model Comprising the Effect of Number of Turns on AC Losses in 2G HTS Coated Conductor at 77K using H-formulations," in *2019 IEEE 2nd International Conference on Power and Energy Applications (ICPEA)*, 2019, pp. 115–118.

[210] B. Shen *et al.*, "Power Dissipation in the HTS Coated Conductor Tapes and Coils Under the Action of Different Oscillating Currents and Fields," *IEEE Trans. Appl. Supercond.*, vol. 29, no. 5, pp. 1–5, 2019.

[211] K. Kajikawa, T. Hayashi, R. Yoshida, M. Iwakuma, and K. Funaki, "Numerical Evaluation of AC Losses in HTS Wires With 2D FEM Formulated by Self Magnetic Field," vol. 13, no. 2, pp. 3630–3633, 2003.

[212] R. Pecher, "3D-modelling of bulk type II superconductors using unconstrained H-formulation," *Proc. 6th EUCAS, Sorrento, Italy, 2003*, 2003.

[213] R. Brambilla, F. Grilli, and L. Martini, "Development of an edge-element model for AC loss computation of high-temperature superconductors," vol. 16, 2007.

[214] Y. Zhang *et al.*, "AC Loss Reduction in Filamentized YBCO Coated Conductors With Virtual Transverse Cross-Cuts," *IEEE Trans. Appl. Supercond.*, vol. 21, no. 3, pp. 3301–3306, 2011.

[215] N. Amemiya *et al.*, "AC loss reduction of YBCO coated conductors by multifilamentary structure," vol. 1464.

[216] J. R. Clem, J. H. Claassen, and Y. Mawatari, "AC losses in a finite Z stack using an anisotropic homogeneous-medium approximation," *Supercond. Sci. Technol.*, vol. 20, no. 12, p. 1130, 2007.

[217] M. D. Ainslie, V. M. Rodriguez-Zermeno, Z. Hong, W. Yuan, T. J. Flack, and T. A. Coombs, "An improved FEM model for computing transport AC loss in coils made of RABiTS YBCO coated conductors for electric machines," *Supercond. Sci. Technol.*, vol. 24, no. 4, p. 45005, 2011.

[218] D. N. Nguyen, S. P. Ashworth, J. O. Willis, F. Sirois, and F. Grilli, "A new finite-element method simulation model for computing AC loss in roll assisted biaxially textured substrate YBCO tapes," *Supercond. Sci. Technol.*, vol. 23, no. 2, p. 25001, 2009.

[219] V. M. R. Zermeno, A. B. Abrahamsen, N. Mijatovic, and B. Bogi, "Calculation of AC losses in stacks and coils made of second generation high temperature superconducting tapes for large scale applications," pp. 1–19.

[220] M. Ainslie, "Transport AC loss in high temperature superconducting coils, Doctor of Philosophy, Thesis," no. May 2012, 2016.

[221] Y. Tong, M. Guan, and X. Wang, "Theoretical estimation of quench occurrence and propagation based on generalized thermoelasticity for LTS/HTS tapes triggered by a spot heater," *Supercond. Sci. Technol.*, vol. 30, no. 4, p. 45002, 2017.

[222] J. Nugteren, "Normal zone propagation in a YBCO superconducting tape: Measurement and analysis of quasi-adiabatic normal zone propagation in a YBCO coated conductor." University of Twente, 2012.

[223] G. Escamez, C. Lorin, T. Wu, and P. J. Masson, "Quench propagation in ybco racetrack of a rotor winding," 2013.

[224] T. Benkel, Y. Miyoshi, X. Chaud, A. Badel, and P. Tixador, "REBCO tape performance under high magnetic field," *Eur. Phys. J. Appl. Phys.*, vol. 79, no.

3, p. 30601, 2017.

[225] M. J. Wolf, R. Heller, W. H. Fietz, and K.-P. Weiss, “Design and analysis of HTS subsize-conductors for quench investigations towards future HTS fusion magnets,” *Cryogenics (Guildf).*, p. 102980, 2019.

[226] X. Zhang *et al.*, “Active Quenching Technique for YBCO Tapes: Quench Acceleration and Protection,” *J. Supercond. Nov. Magn.*, vol. 31, no. 11, pp. 3465–3474, 2018.

[227] Y. Wang, J. Zheng, Z. Zhu, M. Zhang, and W. Yuan, “Quench behavior of high temperature superconductor (RE)BCO CORC cable,” *J. Phys. D. Appl. Phys.*, 2019.

[228] C. Lacroix and F. Sirois, “Concept of a current flow diverter for accelerating the normal zone propagation velocity in 2G HTS coated conductors,” *Supercond. Sci. Technol.*, vol. 27, no. 3, p. 35003, 2014.

[229] L. Ren *et al.*, “Experimental Analysis of Quench Characteristic in HTS Tapes and Coils,” *IEEE Trans. Appl. Supercond.*, vol. 29, no. 5, pp. 1–6, 2019.

[230] J. Pelegrín *et al.*, “Experimental and numerical analysis of quench propagation on MgB2 tapes and pancake coils,” *Supercond. Sci. Technol.*, vol. 26, no. 4, p. 45002, 2013.

[231] S. Awaji *et al.*, “Hot spot behavior of Y123 coated conductors,” *IEEE Trans. Appl. Supercond.*, vol. 22, no. 3, p. 6601004, 2011.

[232] P. Tixador and N. T. Nguyen, “Design of ReBaCuO-coated conductors for FCL,” *Supercond. Sci. Technol.*, vol. 25, no. 1, p. 14009, 2011.

[233] D. Colangelo and B. Dutoit, “Inhomogeneity effects in HTS coated conductors used as resistive FCLs in medium voltage grids,” *Supercond. Sci. Technol.*, vol. 25, no. 9, p. 95005, 2012.

[234] X. Wang, U. P. Trociewitz, and J. Schwartz, “Self-field quench behaviour of YBa2Cu3O7− δ coated conductors with different stabilizers,” *Supercond. Sci. Technol.*, vol. 22, no. 8, p. 85005, 2009.

[235] Y. Fu, O. Tsukamoto, and M. Furuse, “Copper stabilization of YBCO coated conductor for quench protection,” *IEEE Trans. Appl. Supercond.*, vol. 13, no. 2, pp. 1780–1783, 2003.

[236] L. Dresner, *Stability of superconductors*. Springer Science & Business Media,

2006.

[237] X. Wang, U. P. Trociewitz, and J. Schwartz, “Near-adiabatic quench experiments on short Y Ba 2 Cu 3 O 7− δ coated conductors,” *J. Appl. Phys.*, vol. 101, no. 5, p. 53904, 2007.

[238] L. Antognazza *et al.*, “Comparison between the behavior of HTS thin film grown on sapphire and coated conductors for fault current limiter applications,” *IEEE Trans. Appl. Supercond.*, vol. 19, no. 3, pp. 1960–1963, 2009.

[239] C. Lacroix, J.-H. Fournier-Lupien, K. McMeekin, and F. Sirois, “Normal zone propagation velocity in 2G HTS coated conductor with high interfacial resistance,” *IEEE Trans. Appl. Supercond.*, vol. 23, no. 3, p. 4701605, 2013.

[240] G. A. Levin, K. A. Novak, and P. N. Barnes, “The effects of superconductor–stabilizer interfacial resistance on the quench of a current-carrying coated conductor,” *Supercond. Sci. Technol.*, vol. 23, no. 1, p. 14021, 2009.

[241] G. A. Levin, W. A. Jones, K. A. Novak, and P. N. Barnes, “The effects of superconductor–stabilizer interfacial resistance on quenching of a pancake coil made out of coated conductor,” *Supercond. Sci. Technol.*, vol. 24, no. 3, p. 35015, 2011.

[242] T. A. Friedmann, M. W. Rabin, J. Giapintzakis, J. P. Rice, and D. M. Ginsberg, “Direct measurement of the anisotropy of the resistivity in the a-b plane of twin-free, single-crystal, superconducting YBa 2 Cu 3 O 7− δ,” *Phys. Rev. B*, vol. 42, no. 10, p. 6217, 1990.

[243] J. Lu, E. S. Choi, and H. D. Zhou, “Physical properties of Hastelloy® C-276™ at cryogenic temperatures,” *J. Appl. Phys.*, vol. 103, no. 6, p. 64908, 2008.

[244] Y. S. Touloukian and E. H. Buyco, “Thermophysical Properties of Matter (New York: IFI/Plenum),” 1970.

[245] W. M. Haynes, *CRC handbook of chemistry and physics*. CRC press, 2014.

[246] J. E. Gordon, R. A. Fisher, S. Kim, and N. E. Phillips, “Lattice and electronic specific heat of YBa2Cu3O7,” *Phys. C Supercond. its Appl.*, vol. 162, pp. 484–485, 1989.

[247] S. J. Hagen, Z. Z. Wang, and N. P. Ong, “Anisotropy of the thermal conductivity of YBa 2 Cu 3 O 7− y,” *Phys. Rev. B*, vol. 40, no. 13, p. 9389, 1989.